FABRICATION AND CHARACTERISATION OF HIGHLY ALIGNED FIBROUS ASSEMBLIES

TAN CHIN JOO

FACULTY OF ENGINEERING
UNIVERSITY OF MALAYA
KUALA LUMPUR

2020

FABRICATION AND CHARACTERISATION OF HIGHLY ALIGNED FIBROUS ASSEMBLIES

TAN CHIN JOO

THESIS SUBMITTED IN PARTIAL FULFILMENT OF
THE REQUIREMENTS FOR THE DEGREE OF
[DOCTOR OF PHILOSOPHY]

FACULTY OF ENGINEERING
UNIVERSITY OF MALAYA
KUALA LUMPUR

2020

UNIVERSITY OF MALAYA
ORIGINAL LITERARY WORK DECLARATION

Name of Candidate: TAN CHIN JOO

Matric No: KHA150041, 17020477/2

Name of Degree: Doctor of Philosophy

Title of Project Paper/Research Report/Dissertation/Thesis ("this Work"): Fabrication and Characterisation of Highly Aligned Fibrous Assemblies

Field of Study: Engineering Materials (Materials Engineering)

I do solemnly and sincerely declare that:

(1) I am the sole author/writer of this Work;
(2) This Work is original;
(3) Any use of any work in which copyright exists was done by way of fair dealing and for permitted purposes and any excerpt or extract from, or reference to or reproduction of any copyright work has been disclosed expressly and sufficiently and the title of the Work and its authorship have been acknowledged in this Work;
(4) I do not have any actual knowledge nor do I ought reasonably to know that the making of this work constitutes an infringement of any copyright work;
(5) I hereby assign all and every rights in the copyright to this Work to the University of Malaya ("UM"), who henceforth shall be owner of the copyright in this Work and that any reproduction or use in any form or by any means whatsoever is prohibited without the written consent of UM having been first had and obtained;
(6) I am fully aware that if in the course of making this Work I have infringed any copyright whether intentionally or otherwise, I may be subject to legal action or any other action as may be determined by UM.

Candidate's Signature Date: 31 / 10 / 2020

Subscribed and solemnly declared before,

Witness's Signature Date:

Name:

Designation

ABSTRACT

Vascular grafting has been an effective remedy to vascular diseases for decades. Autografting by using the veins or arteries in the patient's body is found to have patency rate for years. However, autografting may not be possible when compatible vessels are not available. In this case, synthetic vascular grafts are found to be effective replacements. Nevertheless, synthetic grafts with diameter less than 4 mm becomes challenging due to thrombogenicity and mismatch of mechanical properties with the native vessels. Along this line, the ability to develop new biostable synthetic materials suitable for smaller grafts and the ability to evaluate their resulting mechanical properties in view of minimizing properties mismatch become essential. The present thesis can be regarded as a first step toward integrated design of new biostable synthetic materials suitable for small diameter vascular grafts, i.e. less than 4 mm. While biological considerations are equally important, the emphasis of the present work is laid on the fabrication and evaluation of mechanical properties of materials using both experimental and numerical works. Owing to its wide use in biomedical applications, thermoplastic polyurethane elastomer is considered. To this end, the first stage of the work consists in fabricating single layer highly aligned thermoplastic polyurethane fibrous assemblies using dry spinning technique assisted by a weak electrical field. Simple biostability characterizations are conducted on the fibrous samples after immersing them in simulated body fluid for 24 weeks. Results indicate that the polyurethane fibres show no observable or significant deteriorations in physical, mechanical and chemical properties. The second stage of the work deals with the mechanical responses of single and multilayer highly aligned fibrous assemblies. The multilayer assemblies are obtained by weaving two single layer highly aligned assemblies at various woven angles during the spinning: 0°, 16° and 26°. Tensile samples are extracted from these assemblies and subjected to a number of mechanical tests. Results show that single layer assemblies are

strongly anisotropic and exhibit inelastic mechanical responses along fibre direction such as hysteresis, stress-softening, stress relaxation and residual strain. For multilayer woven assemblies with average fibre's diameters of approximately 8 and 15 μm, the dependences of effective elastic modulus on woven angle and fibre average diameter are investigated. The last stage of the work consists in evaluating the applicability of the classical linear elastic laminate theory to multilayer fibrous assemblies in view of predicting their elastic properties. The final aim is to propose new designs of vascular graft consisting of multilayer highly aligned fibrous assemblies whose mechanical properties match with those of native vessels. Results predicted using the classical laminate theory show that the polyurethane fibrous assemblies with fibres diameter approximately 8 μm, woven angle close to 100^{o} and thickness ranges between 0.5 to 0.7 mm could be suitable as the grafts of carotid arteries.

ABSTRAK

Cantuman vaskular telah menjadi rawatan yang berkesan untuk penyakit vaskular selama beberapa dekad. Autograf dengan menggunakan urat atau arteri di badan pesakit didapati mempunyai kadar patensi selama bertahun-tahun. Walau bagaimanapun, autograf tidak mungkin dilakukan apabila saluran yang serasi tidak tersedia. Dalam kes ini, cantuman vaskular sintetik didapati sebagai cantuman yang berkesan. Walau bagaimana pun, cantuman dengan diameter kurang dari 4 mm menjadi cabaran kerana trombogenenisiti dan ketidakcocokan sifat mekanik dengan saluran asli. Oleh itu, kemampuan untuk menghasilkan bahan sintetik biostabil baru yang sesuai untuk cantuman yang lebih kecil dan berkesan untuk menilai sifat mekanik yang dihasilkannya dengan meminimumkan ketidakcocokan sifat menjadi penting. Tesis ini boleh dianggap sebagai langkah pertama ke arah reka bentuk bersepadu bahan sintetik biostabil baru yang sesuai untuk cantuman vaskular berdiameter kecil, iaitu kurang dari 4 mm. Walaupun pertimbangan biologi sama pentingnya, penekanan tesis ini diletakkan pada fabrikasi dan penilaian sifat mekanik bahan menggunakan kedua-dua teknik eksperimen dan berangka. Oleh kerana penggunaannya yang luas dalam aplikasi bioperubatan, elastomer poliuretana termoplastik dipertimbangkan. Untuk tujuan ini, peringkat pertama kerja merangkumi pembuatan satu lapisan berserat poliuretana termoplastik yang sangat sejajar menggunakan teknik putaran kering yang dibantu oleh medan elektrik yang lemah. Struktur yang sangat sejajar diperoleh dengan menyiasat terlebih dahulu hubungan antara parameter pemintalan dan topologi pemasangan berserabut yang dihasilkan. Pencirian biostabiliti dilakukan pada sampel berserabut setelah direndam dalam simulasi cecair badan selama 24 minggu. Hasil pencirian menunjukkan bahawa serat poliuretana tidak menunjukkan kemerosotan sifat fizikal, mekanikal dan kimia yang ketara.Tahap kedua tesis ini berkaitan dengan tindak balas sifat mekanikal berserat tunggal dan multilayer yang sejajar. Perhimpunan berbilang lapisan diperoleh dengan menenun dua lapisan tunggal yang sangat sejajar pada pelbagai sudut tenunan semasa pemintalan: 0 °, 16 ° dan 26 °. Sampel tegangan diekstraksi dari unit ini dan menjalani sejumlah ujian mekanikal. Hasil kajian menunjukkan bahawa pemasangan lapisan tunggal sangat anisotropik dan menunjukkan tindak balas mekanikal inelastik sepanjang arah serat seperti histeresis, pelembutan tekanan, kelonggaran tekanan dan ketegangan sisa. Untuk sifat tenunan pelbagai lapisan dengan diameter gentian rata-rata kira-kira 8 dan 15 μm, pergantungan modulus elastik berkesan pada sudut tenunan dan diameter rata-rata serat disiasat. Tahap terakhir tesis ini adalah untuk menilai kebolehlaksanaan teori laminasi elastik linier klasik kepada pemasangan berserat multilayer dengan tujuan meramalkan sifat elastiknya. Tujuan akhir adalah untuk mencadangkan reka bentuk baru cantuman vaskular yang terdiri daripada susunan berserat berlapisan yang sifat mekaniknya sesuai dengan saluran asli. Hasil yang diramalkan menggunakan teori lamina klasik menunjukkan bahawa kumpulan gentian poliuretana dengan diameter gentian kira-kira 8 μm, ditenun dengan sudut hampir 100^{o} dan ketebalan antara 0.5 hingga 0.7 mm didapati sesuai sebagai cantuman arteri karotid.

ACKNOWLEDGEMENT

In completing my thesis, I received assistances and advices from many people. Thus, I would like to express my greatest gratitude to them here.

First of all, I would like to thank Assoc. Prof. Dr. Andri Andriyana and Assoc. Prof. Ir. Dr. Ang Bee Chin, my supervisors for sacrificing their precious time in guiding me through problems and obstacles in my project. Their advices and guidance not only help in my professional development, but also my personal development. I really learnt a lot from them.

Next, I would like to thank all my seniors for their selfless acts in assisting me to overcome the hardships faced by me in completing this project. Without their assistance, my project would not progress smoothly.

I would also like to thank the Department of Mechanical Engineering, Faculty of Engineering, University of Malaya for the facilities provided to me throughout my project and financial support from PPP grant (PG109-2016A).

Last but not the least, I would like to thank all the laboratory technicians and people that were directly or indirectly involved in my project.

TABLE OF CONTENTS

LIST OF FIGURES

LIST OF TABLES

LIST OF SYMBOLS AND ABBREVIATIONS

PAN	:	Polyacrylonitrile
PEO	:	Polyethylene oxide
PCU	:	Polycarbonate-urethane
PVA	:	Polyvinyl alcohol
NaCl	:	Sodium chloride
P(LLA-CL)	:	Poly(L-lactide)-co-poly (ε-caprolactone)
PHBV	:	Poly(3-hydroxybutyrate-co-3-hydroxyvalerate)
CA	:	Cellulose acetate
PVP	:	Polyvinylpyrrolidone
ACY	:	Acyclovir
PLA	:	Poly(lactic acid)
PGA	:	Polyglycolide
PVB	:	Polyvinyl butyral
PCL	:	Polycaprolactone
SEM	:	Scanning electron microscope
IR	:	Infrared radiation
LVDT	:	Linear variable differential transformer
SBF	:	Simulated body fluid
FTIR	:	Fourier transform infrared spectroscopy

CHAPTER 1: INTRODUCTION

The overview of this study along with the objectives will be discussed in this chapter.

1.1 Background of Study

Vascular grafting has been an effective remedy to vascular diseases for decades. Autografting by using the veins or arteries in the patient's body with high patency rate for years is common in United States where 400,000 operations are conducted yearly (Baim, 2003).

In some cases, autografting is not possible due to the unavailability of suitable arteries or veins (Desai, Seifalian, & Hamilton, 2011). This is when the synthetic vascular grafts come in handy. At the early stage, inert materials with the least interaction with the blood and tissues are the choices for these synthetic vascular grafts. Polyethylene terephthalate (PET) and expanded polytetrafluoroethylene (ePTFE) are the most common materials in vascular grafting with good performance for decades. However, the good performances of the PET and ePTFE are only limited to large vascular grafts with diameter more than 6 mm. It is found that the both materials mentioned are not suitable for small vascular grafts with diameter less than 4 mm (Kannan, Salacinski, Butler, Hamilton, & Seifalian, 2005; Xue & Greisler, 2003). As a result, researches are conducted to sought for more appropriate small diameter synthetic vascular grafts.

The most commonly encountered problems in vascular grafting are compliance mismatch and thrombogenicity. The compliance mismatch can lead to intimal hyperplasia which ends up narrowing the lumen and thus affecting the flow of blood. In order to overcome these problems, homogenous functional endothelization on the vascular grafts can be an effective solution (Daum et al., 2020; Sánchez, Brey, & Briceño, 2018). Thus, the initial design philosophy of synthetic vascular graft by using inert materials is deemed to be unrealistic. This is because the vascular grafts need to allow the attachment of endothelial cells for endothelization to occur. In the literature, highly aligned fibrous morphology which is similar to the extracellular matrix of our bodies is found to be effective in the endothelization process (He et al., 2013; Wong, Liu, Xu, Lin, & Wang, 2013; Xu, Inai, Kotaki, & Ramakrishna, 2004).

Apart from the morphology, the mechanical properties and behaviours of these fibrous assemblies is also an important factor to be considered when they are going to be practically implemented in vascular grafting. It is found that the variations in the mechanical properties between the grafts and the native vessels can induce serious intimal hyperplasia (Favreau et al., 2014; Jeong, Yao, & Yim, 2020). The mechanical responses of the graft under loading may also affect the endothelization process as literature studies show that tissues cultured in scaffolds under static, cyclic or dynamic mechanical loadings have better organisation, more mature and denser (Deng et al., 2009; Jiang et al., 2011; Wang et al., 2008). Hence, it is essential to tailor and study the mechanical properties and behaviours of the grafts in accordance to the targeted vessels.

In the literature, there are many studies on the mechanical properties of the fibrous assemblies (Amoroso, D'Amore, Hong, Wagner, & Sacks, 2011; Lee et al., 2005; Meng, Hu, Zhu, Lu, & Liu, 2007). These mechanical properties are often dictated by their topology such as fibres alignment, beads, and fusion between the fibres. Indeed, during stretching, randomly orientated fibres are found to align in the direction of tensile force by sliding against each other and unfolding from the entanglement (Guo et al., 2017; Kumar & Vasita, 2017; Lee, Andriyana, Ang, Huneau, & Verron, 2018; Lee et al., 2005; Lu et al., 2008; Wong, Andriyana, Ang, & Verron, 2016). This fibre re-alignment due to stretching would modify the assembly properties. Samples with beaded fibres are found to have lower mechanical strength as compared to fibres with no beads (Inai, Kotaki, &

Ramakrishna, 2005) whereas fibres fusion improve the films load bearing capacity (Guo et al., 2017; Lee et al., 2005). Based on all these findings discussed, it is clear that the mechanical properties and behaviours of the fibrous assemblies are complex and details study on a newly designed fibrous assemblies are undoubtedly needed.

Following the discussions from all the previous paragraphs in this section have brought to a conclusion that grafts with highly aligned fibrous morphology and mechanical compliance to the native vessels are needed for effective small calibre vascular grafting. These criteria have motivated this study to fabricate highly aligned polymeric fibrous assemblies for the potential application of small vascular grafting. Although the biological aspects of the grafts are important as well and deserve further investigation, this study only focuses on the mechanical compliance of the grafts. Thus, the emphasis of the present thesis is laid on the evaluation of mechanical response of highly aligned fibrous assemblies.

1.2 Problem Statement

Heart diseases with blocked blood vessels are the most common and deathly diseases worldwide. The most effective treatment to cure this disease is to bypass the blood flow from the clogged blood vessels by using suitable grafts. Autografting by using the patient own blood vessels is often the first and best option to do the grafting due to the biocompatibility. Nonetheless, it is difficult to get a suitable blood vessel from the patient to do the grafting. Consequently, synthetic grafts are needed. While these synthetic grafts are useful and effective in larger diameters, more than 6 mm, they cannot perform as effective in smaller diameters, less than 4 mm. Complications such as thrombogenicity and intima hyperplasia tend to occur. Therefore, there is in need of a competent small calibre vascular graft.

1.3 Objectives of Study

The main aim of this study is to fabricate highly aligned fibrous assemblies as potential small calibre grafts for mechanical characterisations. A thermoplastic polyurethane elastomer is selected as the model polymer in this study as many polyurethanes are found to be applicable in the vascular grafting. To achieve this aim, the following objectives are set:

1. To fabricate highly aligned polyurethane fibrous assemblies.
2. To study the biostability of the assemblies in terms of chemical, physical and mechanical properties.
3. To evaluate the mechanical responses of the single and multilayers woven fibrous assemblies under complex uniaxial tensile loading sequences.
4. To propose a new design of vascular graft with mechanical compliance with the help of classical composite laminate theory.

1.4 Scope of Study

The ultimate goal in this study is to design a competent small calibre vascular graft. There are three main criteria to be considered in designing the graft, which are the biocompatibility, biostability and the ability to avoid complications such as thrombogenicity and intima hyperplasia. While these three criteria are equally important, only two criteria, biostability and the ability to avoid complications are considered in this study. In order to have a graft that is able to avoid complications, the graft needs to have highly aligned fibrous morphology and mechanical properties that is similar to the native vessels. Therefore, the focus here is to study the mechanical properties and behaviours of the highly aligned fibrous assemblies. Although in the process of optimizing the spinning parameters, many fibrous assemblies with interesting morphologies are also fabricated, the mechanical properties of these fibrous assemblies are not studied. Finally, in the designing of the small vascular graft with mechanical properties compliance, only the elastic properties are considered. The is due to the fact that the mechanical responses of the polyurethane fibrous assemblies are very complex which inclusive of hyperelasticity, inelasticity and viscoelasticity. More in deep and lengthy studies are needed to incorporate these complex mechanical responses in designing the grafts and shall be considered for future studies.

1.5 Thesis Organization

The organization of this thesis is briefly described here to ease the comprehensions of the readers. There is a total of five chapters in this thesis. The first chapter is to give the readers an overview of this thesis which include the background, problem statement, objectives and scope of this study. In the following second chapter, a literature review is conducted to study the previous relevant works. After that, the methodology devised to achieve the objectives in this study is elaborated thoroughly in the third chapter. Consequently, results obtained in this study through the methodology described in the third chapter are presented and discussed in the fourth chapter. Finally, the conclusion and recommendations for future works are made in the fifth chapter.

CHAPTER 2: LITERATURE REVIEW

2.1 Small Calibre Polyurethane Vascular Grafts

In applying the small calibre vascular grafts with diameter less than 6 mm, complications such as the intimal hyperplasia and thrombogenicity tend to occur. These complications are mainly due to the lack of hemocompatibility (Adipurnama, Yang, Ciach, & Butruk-Raszeja, 2017) and compliance matching (Salacinski et al., 2001). In simpler explanations, hemocompatibility can be understood as the blood-grafts compatibility whereas compliance matching is the matching of the deformation between native vessels and grafts due to blood pressures. Following these issues, the approaches to synthesize or fabricate competent small calibre polyurethane vascular grafts are discussed in this section.

Initially, vascular grafts are designed such that the grafts are bioinert by coating inorganic or organic layers on the grafts. While these bioinert grafts are effective in grafting large diameter blood vessels, they are incompetent as small calibre vascular grafts with diameters less than 6 mm due to the blood incompatibility and compliance mismatch as discussed in the previous paragraph. Thus, in contrast to the bioinert grafts, bioactive grafts are found to be more suitable for the applications of small calibres vascular grafting. The main approach to fabricate these bioactive vascular grafts is to coat bioactive layers such as anticoagulant molecules, drugs and cells on the grafts to prevent unwanted blood coagulation and promote endothelization to greatly reduce the risks of complications (Sánchez et al., 2018). In order to further improve the vessels and grafts compatibility, the idea of bioactive grafts evolves into biomimic grafts where bioinspired materials are used to mimic the extracellular friendly environment for self-endothelization to occur (Qi, Maitz, & Huang, 2013). This evolution path of vascular grafts as discussed are summarized in Figure 2.1 for better illustration.

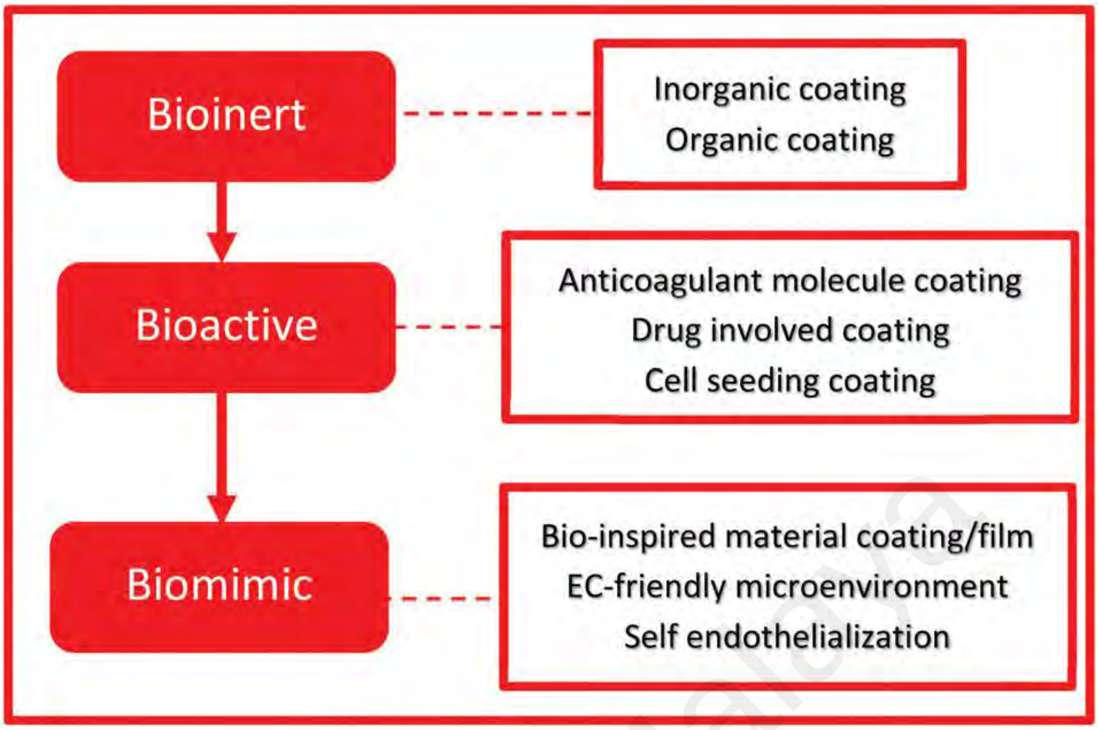

Figure 2.1: The evolution path of bioinert grafts to biomimic grafts for effective small calibre vascular grafting (Adipurnama et al., 2017).

Although polyurethanes exhibit elastomeric behaviours such as hyperelasticity, viscoelasticity and hysteresis which are similar to the mechanical behaviours of most biological tissues (Chen, Liang, & Thouas, 2013), they are mostly still insufficient to be applicable as small calibre vascular grafts due to the inability to allow homogenous and functional endothelization to occur. In the literature, efforts to synthesize or fabricate biomimicking polyurethane vascular grafts for effective endothelization are being conducted vigorously.

For the purpose of effective endothelization, Zhu et al. (Zhu, Gao, He, & Shen, 2004) chemically modify an inert polyurethane. The polyurethane is aminolysed with free NH_2 groups to increase its hydrophilicity and enable the grafting of bioactive components such as gelatin, chitosan and collagen through the coupling agent, glutaraldehyde (Zhu, Gao, Liu, & Shen, 2002). Further cell compatibility tests show that the polyurethanes before and after chemical modification have similar human umbilical vein endothelial cells attachment capabilities. Nevertheless, only the gelatin grafted polyurethane has better cell proliferation capabilities and thus promote better endothelization. Another chemical modification by polymerizing the polyurethane with another bioactive component, lysine-based divinyl oligomers can also improve the cells attachment and proliferation (Sharifpoor, Labow, & Santerre, 2009). However, a later study on the lysine-based polyurethane reported that it is not suitable for small calibre vascular grafting due to compliance mismatch issues (Castillo-Cruz et al., 2019). A more ideal small calibre vascular graft is proposed by blending the polyurethane with ferulic acid (Asadpour et al., 2018). The ferulic acid is found to be released from the polyurethane in a sustained manner in an in vitro assay. Aside from the effectiveness in endothelization on the polyurethane-ferulic acid blends, a series of hemocompatibility tests is conducted on the polyurethane-ferulic acid blends and the results show that the polymer is antithrombogenic. In addition, the polymer also possesses good compliance matching to the coronary artery. Other bioactive components to enhance endothelization that are blended into the polyurethane grafts physically or chemically include heparin (Fang et al., 2016; Lu et al., 2013), fibroin (Yu, Zhang, Thomson, & Turng, 2016), dietary virgin coconut oil (Jaganathan, M, Fauzi Ismail, A, & N, 2017) and polycaprolactone (Mi et al., 2018).

Apart from chemical modifications, introducing porosities to the polyurethane grafts can also enhance the cells attachment, proliferation and antithrombogenicity (Grenier, Sandig, & Mequanint, 2007; Sharifpoor et al., 2009; Zhang, Wang, Liu, & Kodama, 2004). Additional plasma treatment to the porous polyurethane grafts can improve the cells attachment and proliferation as well (Kaibara, Takahashi, Kurotobi, & Suzuki, 2000). However, it is found that only the porosities on the inner surface of grafts matter in the cell attaching and proliferating (Wang, Liu, Guidoin, & Kodama, 2004).

Homogenous endothelizations occur on the grafts with throughout and inner porosities but not outer porosities as illustrated in Figure 2.2. The thickening of the wall or intimal hyperplasia tends to happen at both ends of the grafts as shown in Figure 2 (b).

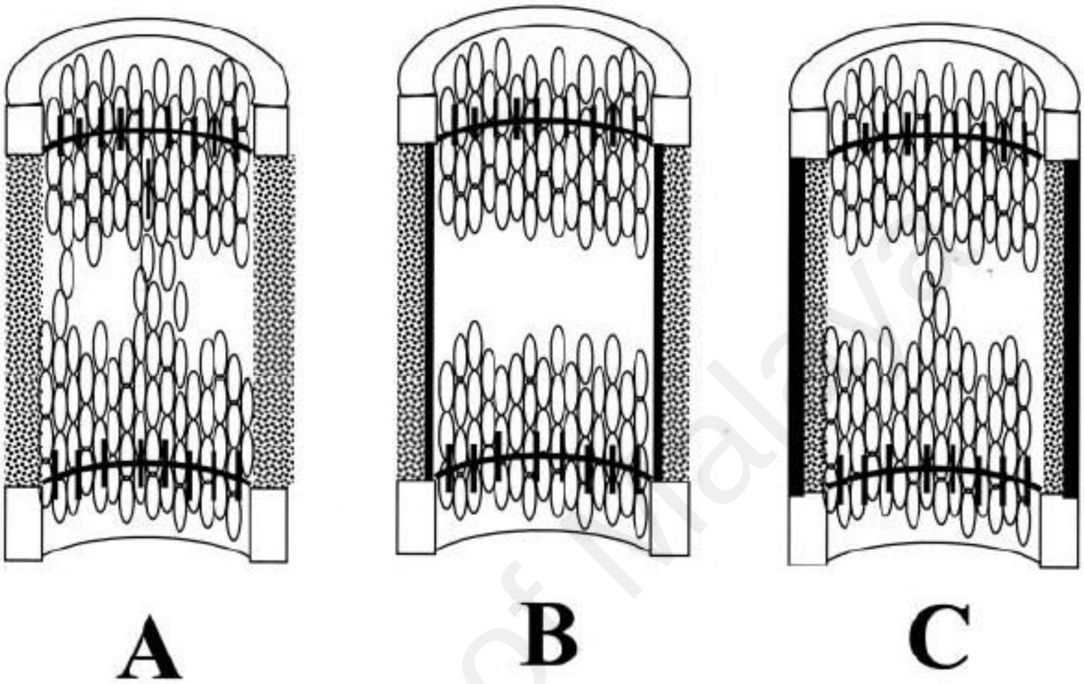

Figure 2.2: Illustration of endothelization on polyurethane grafts with a) thorough, b) outer and c) inner porosities (Wang et al., 2004).

In addition to porosities, the fibrous morphology of small calibre polyurethane graft is being researched in the literature. Nanofibrous grafts are found to have good mechanical properties, high surface to volume aspect ratio, high porosity and most importantly, similar to the extracellular matrix in the body. All these qualities mentioned are desirable for tissue engineering including endothelizations. Most studies in the literature are conducted on the fibrous grafts with random fibres orientations (Bergmeister et al., 2012; Grasl, Bergmeister, Stoiber, Schima, & Weigel, 2010; Karapınar et al., 2004). In order to avoid compliance mismatch, Mi et al. (Mi et al., 2018) fabricate a polyurethane fibrous graft with special structure to address the low and high stiffnesses of the native blood vessels correspond to low and high blood pressures respectively. Basically, the graft is electrospun using a bundled of copper rods as a collector as illustrated in Figure 2.3 (a). As a result, the graft has the structure in Figure 2.3 (b) that can change according to the magnitude of the blood pressure. The stiffness of the graft then changes with the structural change.

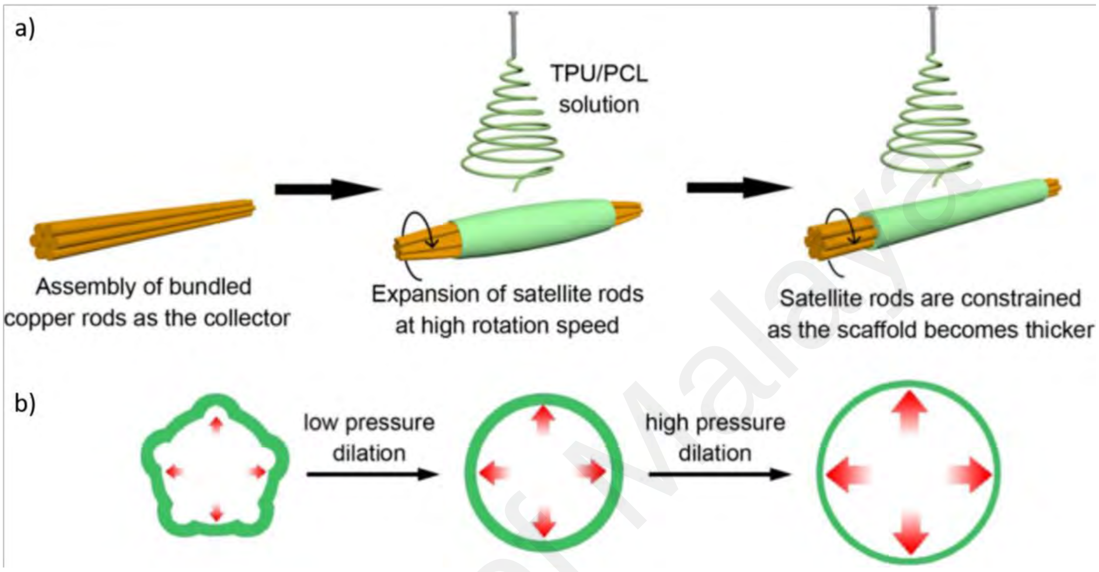

Figure 2.3: a) Electrospinning of fibrous grafts using bundled of copper rods as collectors; b) Dilation of the grafts according to blood pressure (Mi et al., 2018).

Although the orientation of fibres does not affect much on the cells attachment and proliferation, highly aligned fibrous morphology can create a directional microenvironment to guide the cells growth to the desirable morphology (He et al., 2013). The compliance mismatch of these highly aligned fibrous grafts can be reduced by making the fibres crimp, similar to the crimped collagen fibres in the blood vessels where the stiffness is low under a low blood pressure and high under a high blood pressure (Yu et al., 2016). Otherwise, blending the polyurethane with elastin and collagen can also mimic the mechanical properties of the blood vessels as elastin and collagen are major components in blood vessels contributing to their mechanical properties (Wong et al., 2013).

Following the literature studies as discussed in previous paragraphs, many approaches are conducted to synthesize or fabricate competent polyurethane grafts. Nevertheless, porous polyurethane fibrous grafts seem to be the most effective grafts. This is because the fibrous morphology has the similar morphology to the extracellular matrix, a good starting point for the grafts. Then, further modification can be done to promote endothelization and reduce compliance mismatch as elaborated in the previous paragraphs.

2.1.1 Effective Small Calibre Vascular Grafts with Highly Aligned Fibrous Morphology

As mentioned in the previous section, a competent graft is a graft that has similar morphology to the extracellular matrix to allow homogenous functional endothelization to occur. This homogenous functional endothelial layer on the grafts can largely reduce the risks of complications. The studies of the effects of the fibrous morphology on the endothelization process in the literature are discussed in the following paragraphs.

In the study conducted by Uttayarat et al. (Uttayarat et al., 2010), the endothelial cells are found to grow in the direction within 20^o parallel to the axes of the fibres in the fibrous sample as shown in Figure 2.4. This preferential growth of endothelial cells in the direction parallel to the axes of fibres is in agreement with many studies (Han et al., 2008; Meng, Han, et al., 2010; Mi et al., 2015; Whitton, Flint, & Black, 2010).

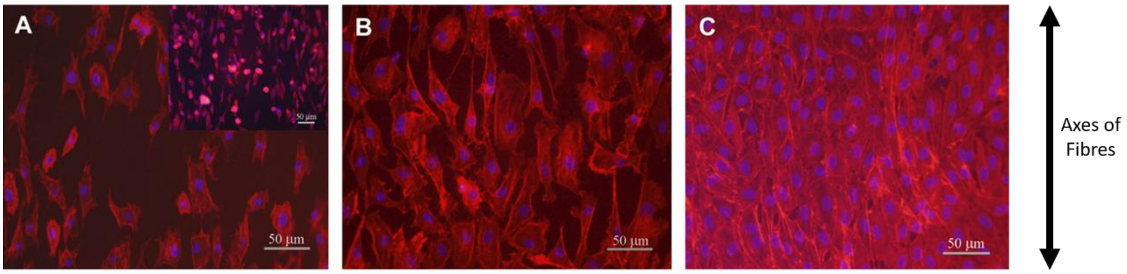

Figure 2.4: Overlays of fluorescently stained actin filaments (red) and cell nuclei (blue) of endothelial cells (inset) at (A) 2 h, (B) day 3 and (C) day 5 post-seeding (Uttayarat et al., 2010).

In the aspect of the morphology of the endothelial cells, it is found that the cells grown on the highly aligned polyurethane fibrous film are different from the cells grown on the polyurethane smooth cast film as shown in Figure 2.5. It can be clearly observed that the cells grown on the fibrous film are more elongated and stretched in the axis directions of the fibres whereas the cells grown on the smooth cast film are less elongated (Han et al., 2008; Meng, Han, et al., 2010). The elongated morphology of the cells on the fibrous film is similar to the cells in natural vascular medial layers. Hence, it can be inferred that the fibrous film can guide the cells to grow in a manner which mimicking the morphology of the native cells.

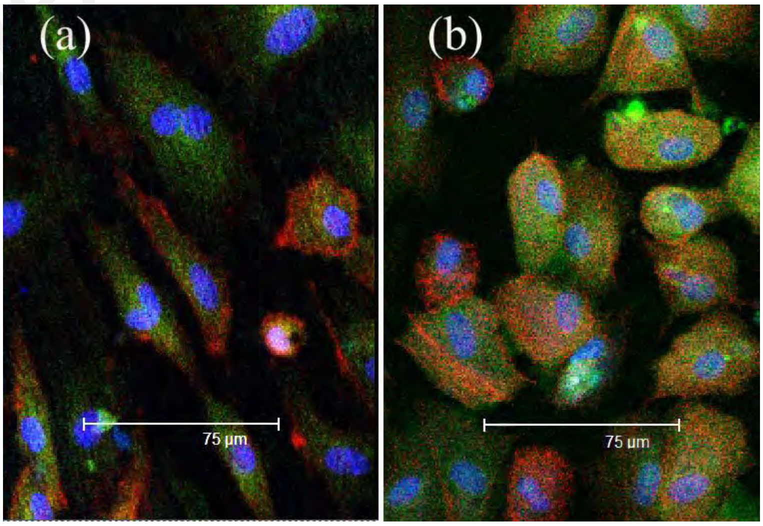

Figure 2.5: Endothelial cells growing on (a) highly aligned polyurethane fibrous film and (b) smooth cast film (Han et al., 2008).

Additionally, Mi et al. (Mi et al., 2015) found that the alignment of the fibres can significantly affect the migrations of cells. The findings on the effects of the fibres alignment on the cell migration are as summarized in Figure 2.6. Aside from orientating to the directions of the fibre axes, the cells are also found to be able to migrate from one fibre to another fibre. For the unidirectional aligned fibres, the cells migrate along the fibres in one direction, which is the direction of the fibre axis. On the other hand, on the orthogonally aligned fibres, the cells are able to migrate to the perpendicular directions via the intersections of two orthogonally aligned fibres. These directional migrations of cells are not observed on random aligned fibres and tissue culture plastic. It appears that the alignment of the fibres can control the migration direction of the cells. In fact, the migration velocity and distance of the cells are also affected by the alignment of the fibres. It is found that aligned fibres can move faster and further. This ability of the aligned fibres to control the cell migration can act as the biological cues for the cell differentiation and gene expression.

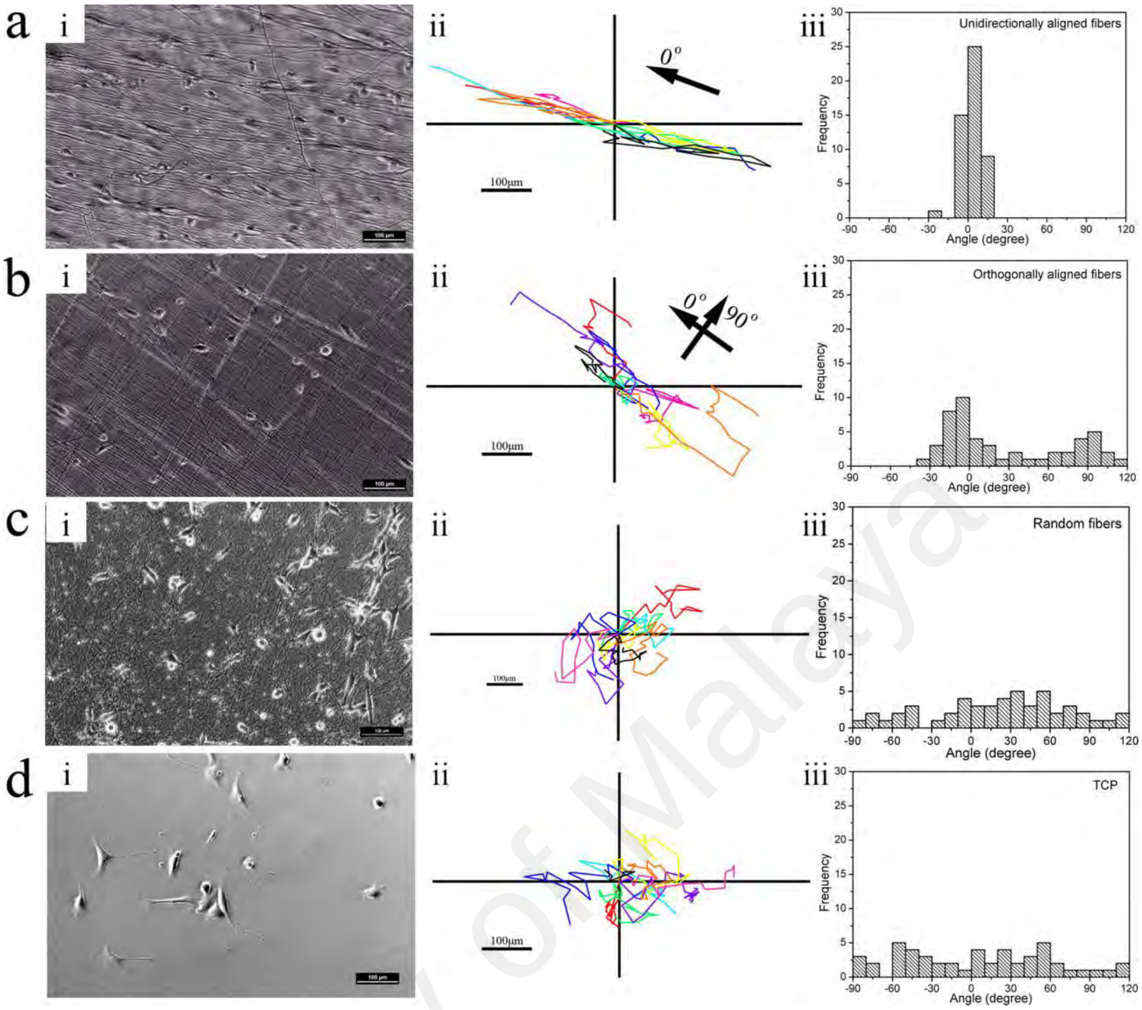

Figure 2.6: Cell migration results on (a) aligned fibres, (b) orthogonal fibres, (c) random fibres, and (d) tissue culture plastic from day 2 to day 5. (i) The initial state images of cell migration, (ii) traces of tracked cells, and (iii) cell orientation angle distribution frequency (Mi et al., 2015).

The hemocompatibility of the highly aligned polyurethane fibres is studied by Liu et al. (Liu, Qin, et al., 2013). This hemocompatibility is evaluated based on the number of platelets that adhered on the fibres as blood flows on the fibres. Results show that platelets adhesion rate of the fibrous vessel is 0.12%, much lower than the smooth polyurethane vessel which is 0.35%. It is found that the higher the platelets adhesion rate of the vessel, the lower the patency rate, the state of being open or unobstructed for the flowing of blood. This is because the adhered platelets would trigger the formation of blood clotting or thrombus on the vessels, thus, obstructing the blood to flow. Due to the low platelets adhesion rate, the patency rate of the highly aligned fibres reaches 100%, much higher than the smooth polyurethane vessel, 28.60%. The thrombus formations on both the smooth and highly aligned polyurethane vessels are presented in Figure 2.7.

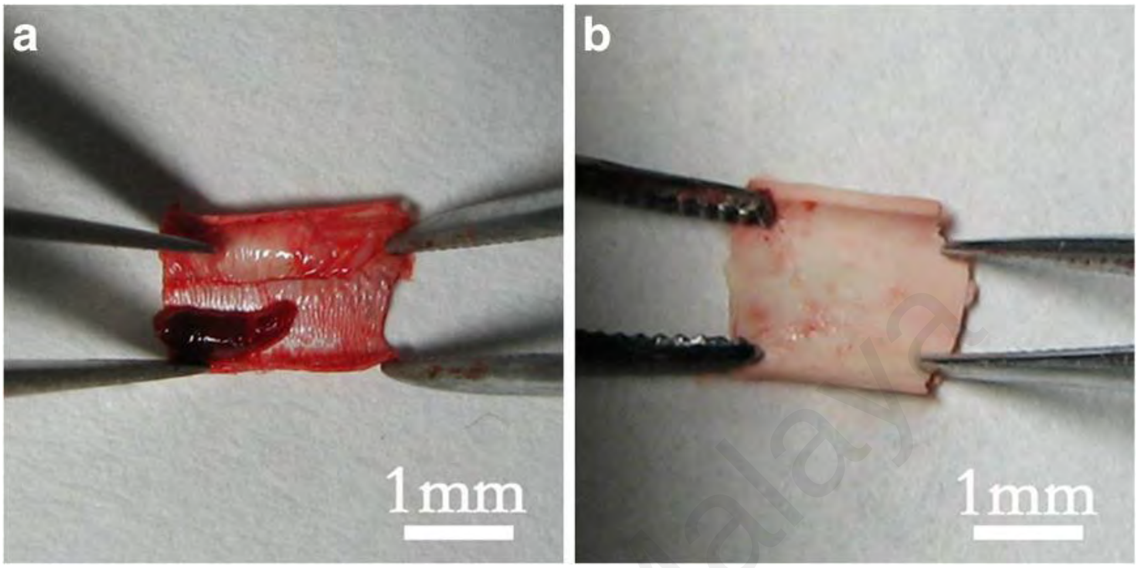

Figure 2.7: (a) Obvious thrombus formation on smooth morphology substrate and (b) much lesser thrombus formation on highly aligned fibrous morphology (Liu, Qin, et al., 2013).

In summary, the highly aligned polyurethane fibres are competent vascular grafts due to their self-endothelization ability and hemocompatibility. Homogenous functional endothelial layers can form on the fibres because of their ability to allow the endothelial cells to attach, grow and migrate on them in a controllable manner by arranging the fibres in desirable orders. As for the hemocompatibility, the highly aligned polyurethane fibres have low platelets adhesion rates which consequently reduce the risks thrombogenicity, promoting high patency rate.

2.2 Electrospinning

Electrospinning is a rapidly emerging nanofibres fabrication technique in the past decades. It has the ability to fabricate fibres with the diameter range from sub – micron to nanometre scale from a wide range of materials, including polymers, composites and ceramics (Raghavan et al., 2012; Tebyetekerwa & Ramakrishna, 2020). Hence, this technique is frequently applied to fabricate fibrous vascular grafts in the literature.

Nanofibres or microfibres are drawn by applying high electrical potential between the polymer solution and collector. As compare to other techniques, electrospinning has better control in the morphology of the membranes by varying the solution parameters, processing parameters and ambient parameters (Bhardwaj & Kundu, 2010). Figure 2.8 shows the schematic diagram of a simple electrospinning set up.

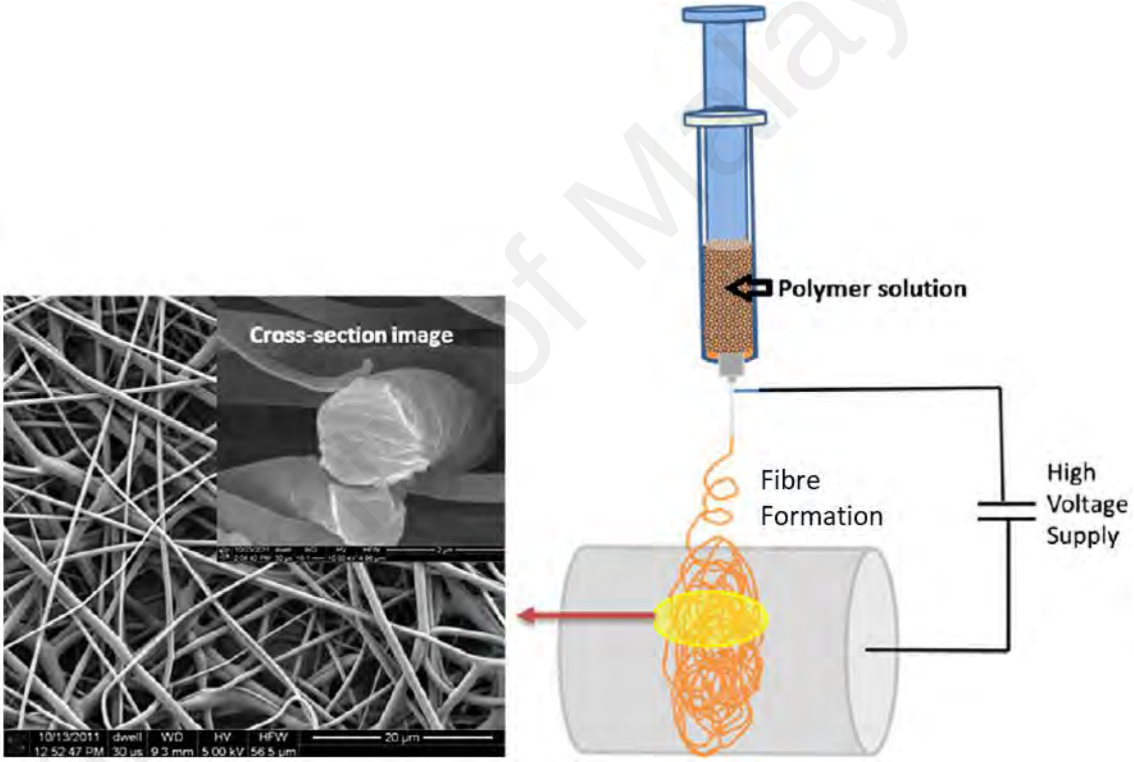

Figure 2.8: Schematic showing electrospinning of polymer solution (Lalia, Kochkodan, Hashaikeh, & Hilal, 2013)

This technique requires high voltage supply to induce charge to the polymer melt or solution in order to draw fibres out of the fluid in the spinneret. Electrostatic drawing of these fibres will occur if the electrical charges are strong enough to overcome the viscosity and surface tension of the fluid. The electrostatic force generated by the high voltage supply will pull the solution out of the spinneret tip and form a droplet at the tip.

After a critical voltage is applied, the droplet will form into conical shape or commonly known as Taylor cone as shown in Figure 2.9. Subsequently, a jet of fluid will be drawn out of the Taylor cone. Solvent in the polymer solution will dry up as the jet reaches the collector, leaving the solid polymeric fibres (Haider, Haider, & Kang, 2015; Raghavan et al., 2012).

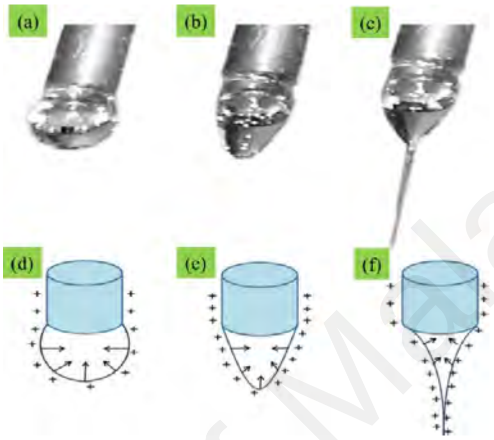

Figure 2.9: (a – c) Digital images to show the deformation of polyvinvylpyrrolidone droplet with the increment in electric field. Effects of electrical charges on the droplet are shown in (d – f) (Haider et al., 2015).

A simple electrospinning system consists of three major components. These components are a high voltage supply, a spinneret and a grounded collector as shown in Figure 2.10. By altering or manipulating this electrospinning system, nanofibrous membranes with the desired characteristics can be obtained. Nevertheless, an ideal electrospun fibres should generally exhibit three properties as shown below (Raghavan et al., 2012).

1. Uniform and controllable diameter distribution.
2. Free from defects or defect – controllable.
3. Continuous single or aligned fibres.

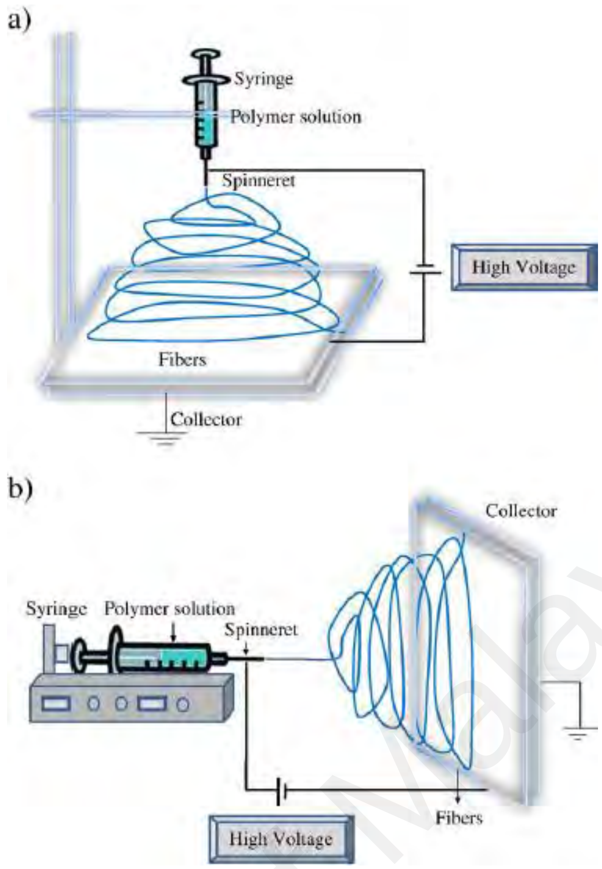

Figure 2.10: (a) vertical set up and (b) horizontal set up of electrospinning apparatus (Bhardwaj & Kundu, 2010).

2.2.1 Electrospinning Parameters

To achieve the ideal nanofibres, many studies have been done to optimise the parameters used in this electrospinning system. These parameters can be grouped into two main categories, solution parameters and processing parameters (Bhardwaj & Kundu, 2010; Raghavan et al., 2012).

2.2.1.1 Solution Parameters

The solution parameters affecting the outcome of the electrospinning includes concentration, viscosity, surface tension and conductivity or surface charge density.

(a) ***Concentration***

It is widely known that the concentration of the polymer solution needs to reach a critical value to obtain optimum fibre’s morphology. At low concentration, formation of beads is obvious. As the concentration increases until an optimum value, the beads will diminish from spherical shape to spindle like shape until disappear to form uniform fibres as shown in Figure 2.11 (Teo, Kotaki, Mo, & Ramakrishna, 2005). However, beads will start to form again beyond the critical concentration due to the drying of the polymer solution at the tip of the spinneret and continuous uniform fibres will not able to form (Sukigara, Gandhi, Ayutsede, Micklus, & Ko, 2004).

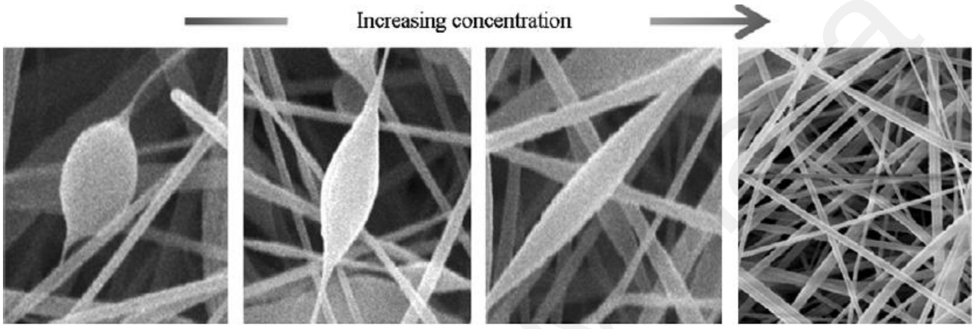

Figure 2.11: Bead morphology of electropspun PAN fibres under the influence of solution concentration (Raghavan et al., 2012).

Researchers also tried to relate the diameter of the nanofibres and the concentration. As a result, they found a power law relationship between the average fibre diameter, AFD and concentration, C (Demir, Yilgor, Yilgor, & Erman, 2002) as shown in Eq. 2.1.

$$AFD = C^3 \qquad \text{Eq. 2.1}$$

(b) ***Viscosity***

Viscosity of the polymer solution is a vital parameter in electrospinning. Solutions with low viscosity may not able to form continuous fibres, whereas solutions with high viscosity is hard to eject the jet out of it. Thus, polymer solution with the optimal viscosity is essential (Bhardwaj & Kundu, 2010). Nevertheless, the optimal viscosity varies depending on the type of polymer. PEO fibres were successfully fabricated using the solution viscosity in the range of 8 poise to 40 poise, while PCU fibres were fabricated using the solution viscosity of 100 poise (Doshi & Reneker, 1995; Nezarati, Eifert, & Cosgriff-Hernandez, 2013).

(c) ***Surface Tension***

Surface tension is basically a function of solution composition. By changing the solvent used, the surface tension can be altered. Ethanol was added to the water soluble PEO solution with the water to ethanol ratio of 0.702 to reduce its surface tension in order to electrospin fibres without beads (Fong, Chun, & Reneker, 1999). Low surface tension solution can be used to electrospin fibres with lesser beads.

(d) ***Conductivity / Surface Charge Density***

The diameter of the fibres can be reduced by increasing the conductivity of the solution as it can increase the charge carriers in the jet, consequently enhance the tensile force pulling the jet in the presence of an electrical field. The conductivity of the polymer solution contributed by the solvent used, amount of ionisable salts available and the polymer itself (Bhardwaj & Kundu, 2010). PVA nanofibres' diameter was reduced from 214 nm to 159 nm by increasing the amount of NaCl in the PVA solution from 0.05 % to 0.2 % (Zhang, Yuan, Wu, Han, & Sheng, 2005).

2.2.1.2 Processing Parameters

The processing parameters in electrospinning are applied voltage, feed rate / flow rate, tip to collector distance and ambient conditions.

(a) ***Applied Voltage***

As electrospinning is a method to draw fibres using strong electrostatic force, the applied voltage is essentially affecting the whole process. The Coulombic force stretches the jet out from the Tylor cone, elongates it until reaches the collector. Stronger applied voltage is said to impart stronger stretching force on the jet and thus further reducing the diameter of the fibres. A study shows that by doubling the applied voltage, the diameter of the fibres decreased by approximately half (Larrondo & St. John Manley, 1981).

However, not all studies show that higher applied voltage promote the formation of lower fibres diameter. The diameter of PEO fibres was not much affected by the applied voltage done in a study (Reneker & Chun, 1996). Another study shows that increasing the applied voltage increased the diameter of the PVA fibres due to the increment in the polymer solution ejection (Zhang et al., 2005). Beads formation on P(LLA-CL) fibres is also reported in a studies when using high applied voltage in electrospinning (Mo, Xu, Kotaki, & Ramakrishna, 2004).

(b) ***Feed Rate / Flow Rate***

Feed rate or flow rate is the speed of mass transfer of the polymer solution from the spinneret to the collector. It is preferable to be as slow as possible for the solvent to evaporate completely during electrospinning (Yuan, Zhang, Dong, & Sheng, 2004). Beaded fibres were fabricated with high feed rate because of the incomplete drying of the PHBV fibres prior to reaching the collector (Zuo et al., 2005).

(c) ***Tip to Collector Distance***

An optimum tip to collector distance is essential to ensure the complete evaporation of the solvent in the fibres. Flattened fibres were fabricated with low tip to collector distance while cylindrical fibres were fabricated with further tip to collector distance (Buchko, Chen, Shen, & Martin, 1999). With constant electric field, the electrospinnability of gelatin fibres decreased with the increment in the tip to collector distance (Teo et al., 2005).

(d) ***Ambient Conditions***

Electrospinning process is always subjected to the ambient conditions. Considering the ambient conditions are not constant and always changing, the electrospun fibres may change in different ambient conditions. This ambient condition is mainly determined by the temperature and the humidity.

Humidity is found to affect the diameter of the fibres fabricated. Nonetheless, different polymer reacts differently with the humidity. The average diameter of CA fibres increased but the average diameter of PVP fibres decreased with the increment of humidity (Vrieze et al., 2009).

In a high temperature condition, the polymer solution will decrease in viscosity with the increase in the evaporation rate and electrical conductivity, resulting in smaller fibres and uniform morphology. ACY – loaded PAN ultrafine fibres were found to be without beads and the diameter distribution was in a narrow range of 400 nm to 700 nm when the electrospinning was done at 80 ^{o}C (Chen & Yu, 2010).

2.2.1.3 Summary

Optimization study on the parameters of electrospinning is essential to fabricate the desirable fibres. Table 2.1 shows the general observation on the fibres by altering the parameters. However, the effects of the parameters may differ from one polymer to another due to the different nature of the polymer.

Table 2.1: Influences of various parameters on the morphology of electrospun fibres (Tijing, Choi, Lee, Kim, & Shon, 2014)

Parameter	Effect / Observation
Solution parameters	
Concentration	• Increasing concentration results in bigger fibres • Very low concentration can form beads on fibres
Molecular weight	• More bead formation at low molecular weight • Increasing molecular weight produces bigger and smoother fibres
Viscosity	• Increasing fibre diameter with the increase of viscosity
Conductivity / surface charge density	• Thinner fibres are formed with increase of conductivity
Surface tension	• Low surface tension generates smooth and uniform fibres at low electric fields
Process parameters	
Applied voltage	• Generally, fibre diameter is decreased with the increase in applied voltage
Feed rate	• Very high feed rate produces bead on fibres while very low feed rate cannot continuously produce fibres • Typical feed rate is below 1 mL / h
Collector	• Different collector shapes are available depending in desired morphology • More uniform thickness of mat can be obtained using a rotating drum
Tip to Collector Distance	• Too far or too near distance would result in bead formation • Needs sufficient time to elongate and dry
Other parameters	
Temperature	• Increased temperature results in decreased fibre diameter
Humidity	• High humidity can induce internal porosity of fibre
Post – spinning treatment	• Drying temperature should be below the boiling temperature of the solvent to avoid bubble and eventually pore formation in the fibre

2.3 Electrospinning of Highly Aligned Fibrous Assemblies

There are quite a number of studies in fabricating highly aligned nanofibrous membranes by modifying the conventional electrospinning set up in the literature. These modifications can be broadly categorized into three main groups which are the electrostatic approaches, mechanical approaches and the combination of both approaches.

2.3.1 Electrostatic Approaches

Fibres are driven to a specific direction at the collector by the electrostatic steering force. This can be achieved by using electrodes or wire drum collectors.

2.3.1.1 Electrodes

When the fibres are ejected from the spinneret, they will undergo whipping instability which causing them to move randomly. This movement is dominated by three electrostatic forces from the external applied voltage, among the fibres and the collector respectively. In fabricating non – woven nanofibrous membranes, flat continuous conductive collectors are usually used. This collector does not have an electric field in preferential direction and thus fibres will deposit on the collector in a random manner (Li, Wang, & Xia, 2004).

Highly aligned nanofibrous membranes can be fabricated by replacing the flat collector with a pair of electrodes with a void gap in between. The width of the gap can be varied from hundreds of micrometres to several centimetres. The interaction between the highly charged fibres and electrodes will encourage the alignment of the fibres in the direction across the gap, steered by the electric field (Li et al., 2004). Please refer to Figure 2.12 for better illustration.

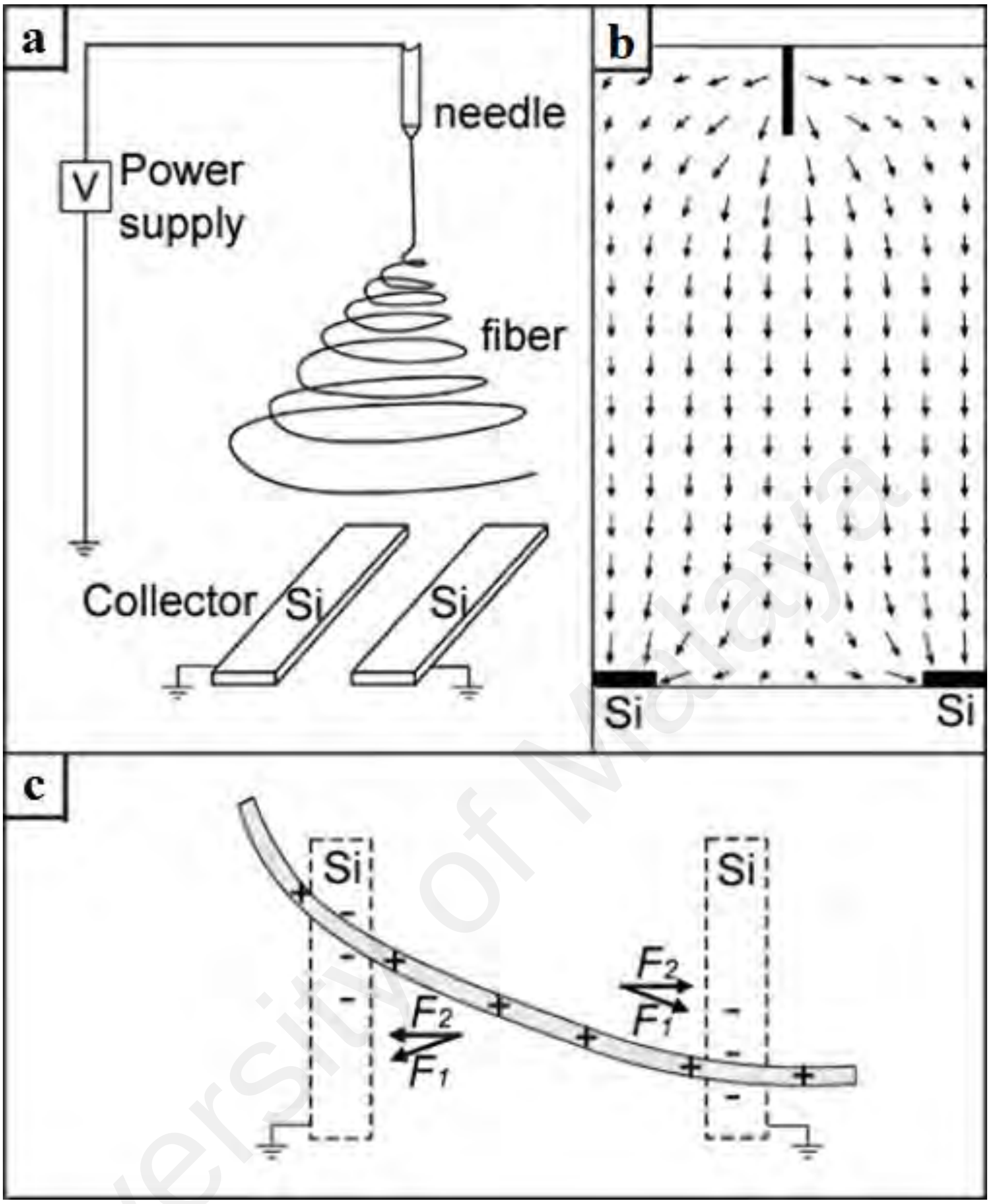

Figure 2.12: (a) Electrospinning set up consists of two conductive collectors, silicon stripes with a gap in between. (b) Illustration of the electrical field strength between the needle and collector. The direction of the electrostatic field lines is indicated by arrows. (c) Interaction of electrostatic force on a charged nanofibre across the gap. F_1, electrostatic force resulted from the electric field, whereas F_2, Coulombic force resulted from the interaction between positively charged nanofibres and the negatively induced charged grounded electrodes (Li, Wang, & Xia, 2003).

Highly aligned PVP nanofibres were successfully synthesized using two parallel gold electrodes with a quartz wafer in between which acted as a non – conductive collector. In the study, it was found that the alignment of the fibres increased as the collection time increased. This is because the fibres deposited across the gap remain highly charged and repel the incoming fibres, forcing them to be aligned in the same direction (Li et al., 2004). Figure 2.13 shows the orientation distribution of the PVP fibres.

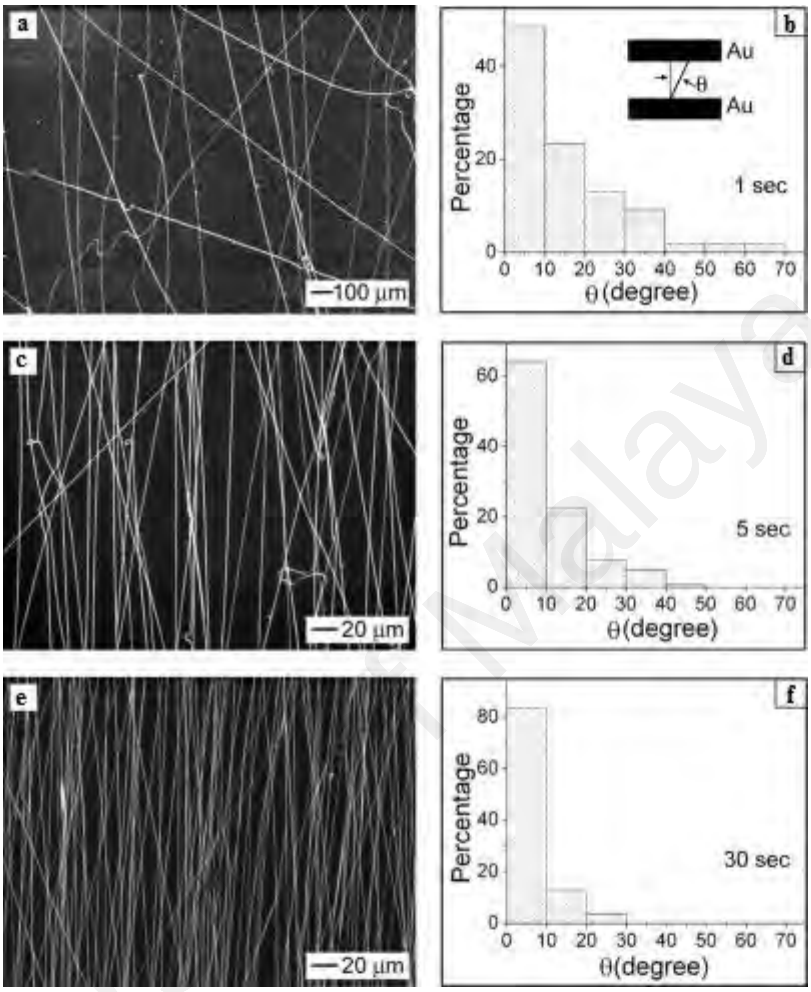

Figure 2.13: a, c, e) Images of PVP nanofibres collected on a quartz wafer located between two gold electrodes under optical microscope. Collection duration of the samples: a) 1 s; c) 5 s; e) 30 s. b, d, f) Orientation of the fibres in the longitudinal direction with respect to the edges of two parallel gold electrodes (Li et al., 2004).

2.3.1.2 Wire Drum Collectors

The concept of using the wire drum collectors is similar to the electrode's method. Gaps exist in between the wire on the drum collector as shown in Figure 2.14. Then, the electrostatic forces will steer the fibres to be deposited across the gaps (Katta, Alessandro, Ramsier, & Chase, 2004).

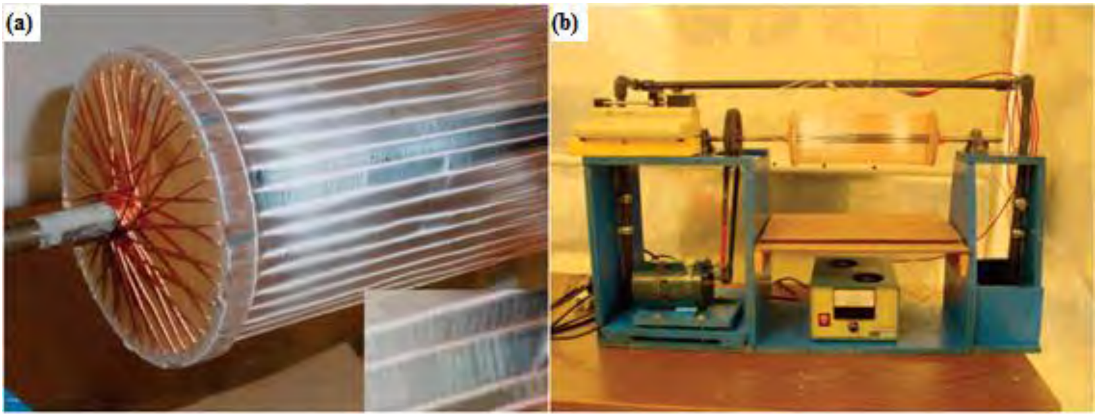

Figure 2.14: (a) Copper wire drum. Collected nylon nanofibres shows alignment in the magnified image. (b) Full set up of the wire drum for electrospinning (Katta et al., 2004).

Unlike the electrodes set up, the wire drum collector set up did not increase the alignment of nylon – 6 fibres as the collection time increased as indicated in Figure 2.15. It is suggested that the fibre mat will become thicker as time goes and it will act as the collector itself, causing the electrostatic steering effect of the wires to diminish (Katta et al., 2004).

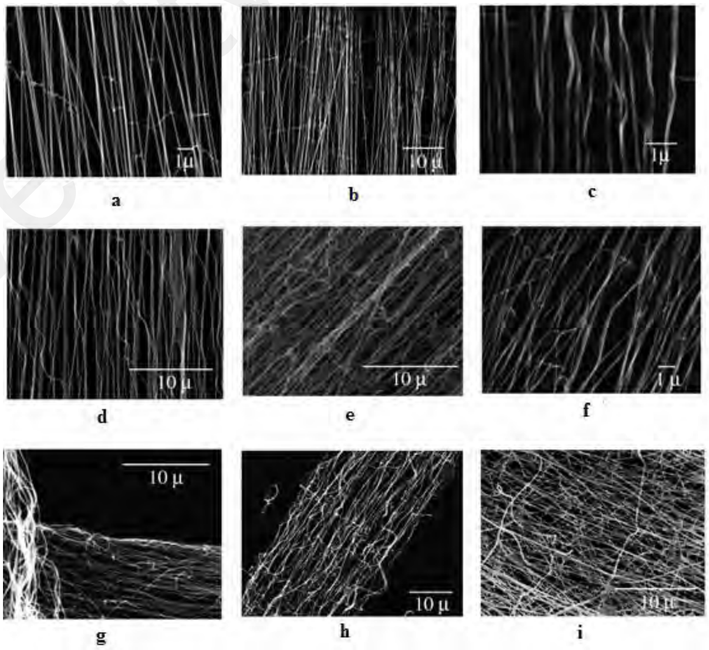

Figure 2.15: (a, b, c) show the polymer nanofibres aligned uniaxially collected on conductive copper wire drum after 5 minutes. (d, e) are after 15 minutes. (f, g, h) are after 40 minutes. (i) is after 2.5 hours (Katta et al., 2004).

2.3.2 Mechanical Approaches

Mechanical approaches utilise very high rotational speed to draw the fibres in one direction. Two types of collectors are typically used, which are the rotating discs and rotating drums.

2.3.2.1 Rotating Discs

A sharp edge rotating disc was used to fabricate highly aligned PEO fibres. The rotational speed of the disc was 1070 rpm with the linear speed of 22 ms^{-1} at the tip of the disc. The jet from the Taylor's cone underwent whipping instability and followed the path with the shape of envelope cone initially. Then, the path changed to an inverted envelop cone shape due to the changing of the electric field caused by the rotating disc. Finally, the fibres were drawn along the circumference of the disc by the high speed rotation (Theron, Zussman, & Yarin, 2001). The drawing process of the fibres is as shown in Figure 2.16.

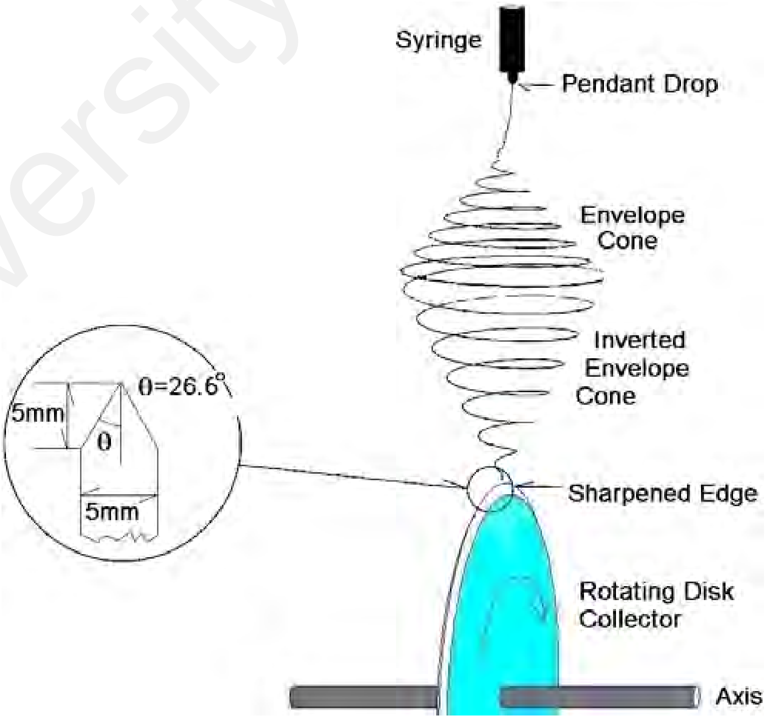

Figure 2.16: Schematic diagram of the jet path. The aluminium disc has a diameter of 200 mm with thickness of 5 mm (Theron et al., 2001).

2.3.2.2 Rotating Drums

Figure 2.17 shows the electrospinning set up with the rotating drum. Similar to the rotating disc, the rotating drum needs to rotate at high speed in order to obtain highly aligned fibres. PLA and PGA blends fibres were randomly oriented when the electrospinning was done using rotating drum with the rotational speed of 360 rpm. Further increasing the rotational speed to 850 rpm improved the alignment of the fibres (Ramdhanie et al., 2006).

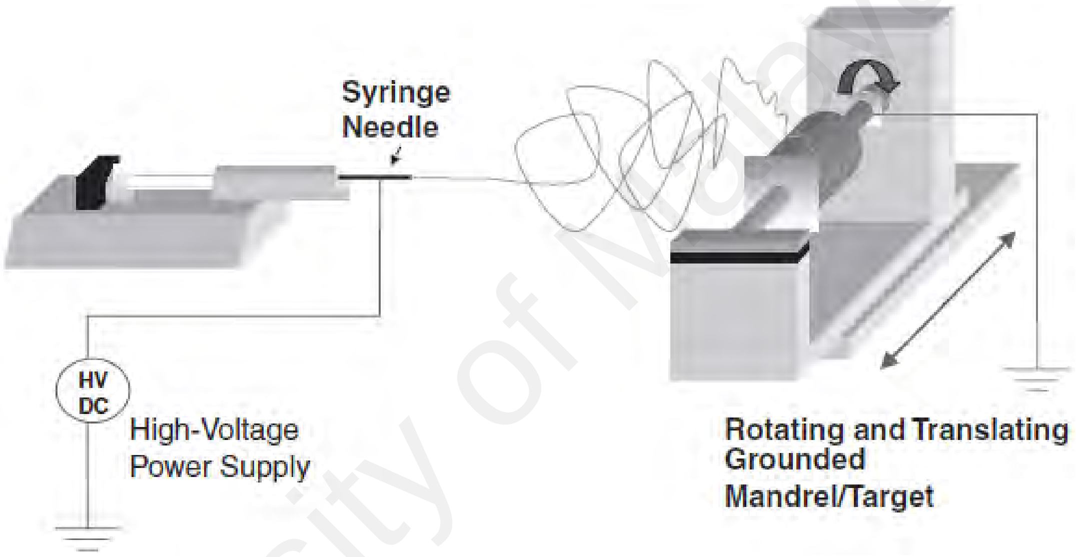

Figure 2.17: Schematic of an electrospinning apparatus (Ramdhanie et al., 2006).

In a study, the alignment of PVB fibres increased by incorporating inorganic salt as the additive in the polymer solution. Fibres with inorganic salts favoured to deposit on a narrower region than the fibres without organic salts as illustrated in Figure 2.18. It was suggested that fibres with inorganic salts as additives were more conductive and highly charged when in an electric field. These highly charged fibres will selectively choose the shortest path to reach the collector for the discharging purpose and thus narrowing the fibres deposition region. With the help of high speed rotating drum, the fibres were further aligned (Song, Cui, & Chang, 2011).

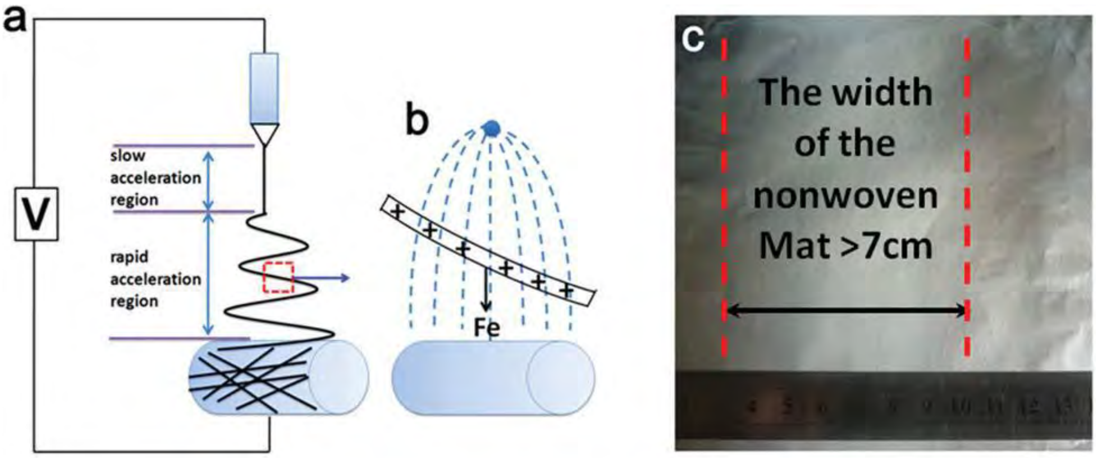

without inorganic salts

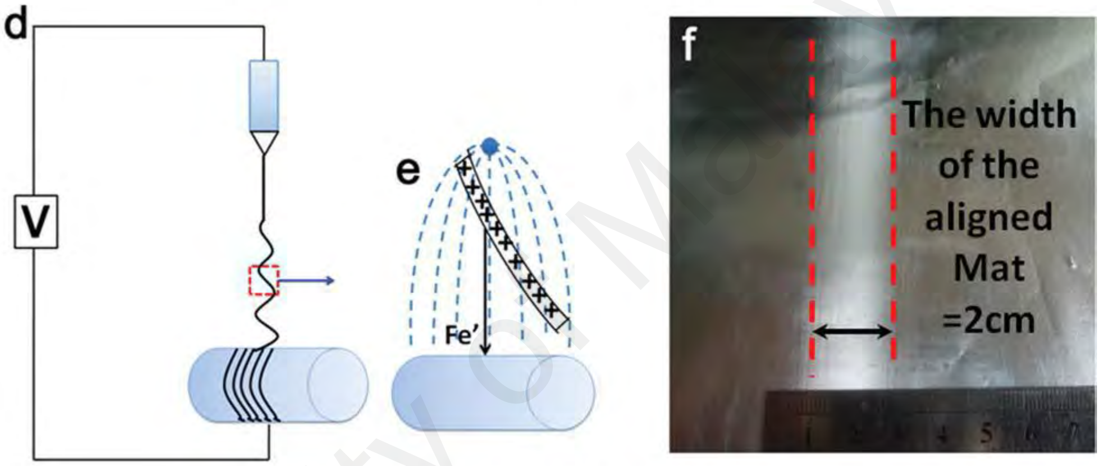

with inorganic salts

Figure 2.18: Schematic showing the path travelled by the jet and the F_e, force resulted from the interaction between the electrical field and charged jet, while the digital images showing the width of the collected mats under the different conditions: (a, b, and c) without inorganic salts; (d, e, and f) with inorganic salts (Song et al., 2011).

In addition to the rotating drum, a back electrode was added to the set up to improve the fibres' alignment as shown in Figure 2.19. The function of the back electrode was to eliminate the whipping motion of the polymer jet completely. Highly aligned PEO fibres was fabricated by using the back electrode and rotating drum with the surface speed of 4.71 ms^{-1} (Kiselev & Rosell-Llompart, 2012).

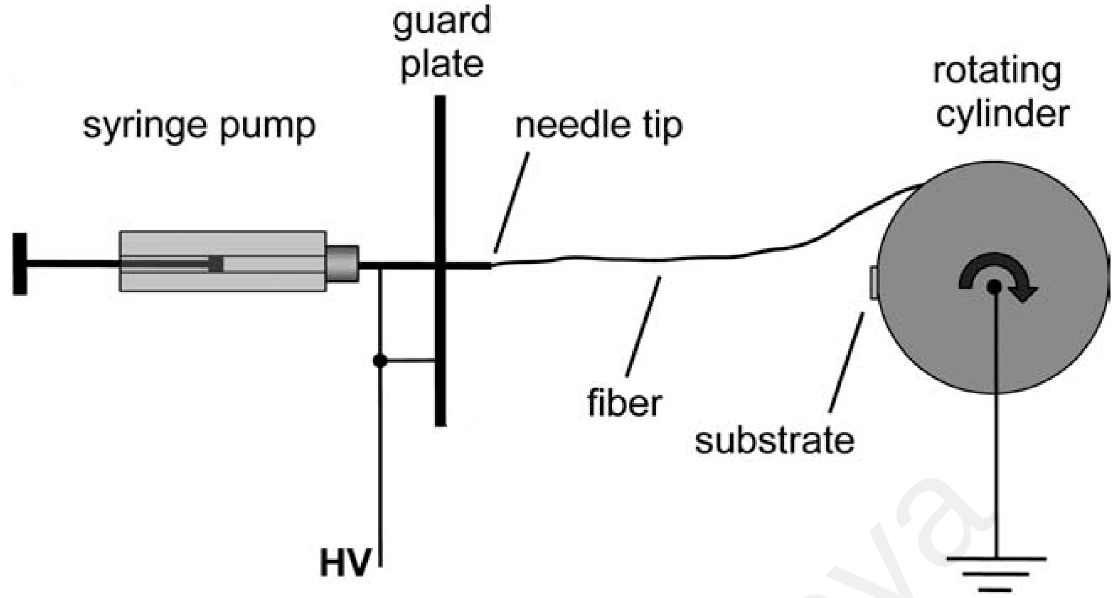

Figure 2.19: Experimental arrangement for electrospinning. Back electrode is labelled ‘‘guard plate’’ (Kiselev & Rosell-Llompart, 2012).

2.3.3 Combination of Electrostatic and Mechanical Approaches

The electrospinning set up with the combination of electrostatic and mechanical approaches is shown in Figure 2.20. Sharp edged bars were used as electrodes for electrostatic steering purpose as mentioned in the earlier session and the rotating drum was to draw the fibres in the circumferential direction with high rotational speed. Highly aligned PCL fibres were fabricated using this set up (Teo et al., 2005).

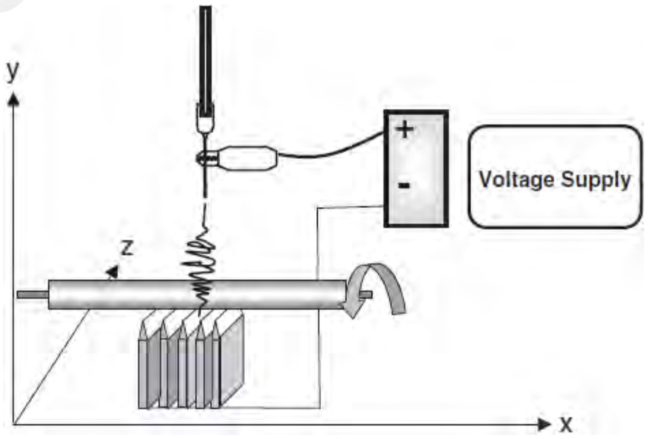

Figure 2.20: Electrospinning with knife-edged bars used (Teo et al., 2005)

2.4 Other Spinning Techniques

While the electrospinning is widely used in the fabrication of polyurethane fibres, there are some other solution spinning techniques used to fabricate these fibres, such as wet spinning and solution blow spinning in the literature. These two techniques will be discussed briefly in the following sections.

2.4.1 Wet Spinning

The fabrication of polyurethane fibres through wet spinning is by drawing solution jets from the polymer solution and directly immersed the jets into a coagulation bath to form the fibres (Duarte, Pereira, Habert, & Borges, 2008; Kim, Kwon, & Na, 2019; Liu et al., 2008; Lu et al., 2018; Reddy, Deopura, & Joshi, 2010; Xiao, Zhu, & Gu, 2010). The set ups of wet spinning can be illustrated in Figure 2.21.

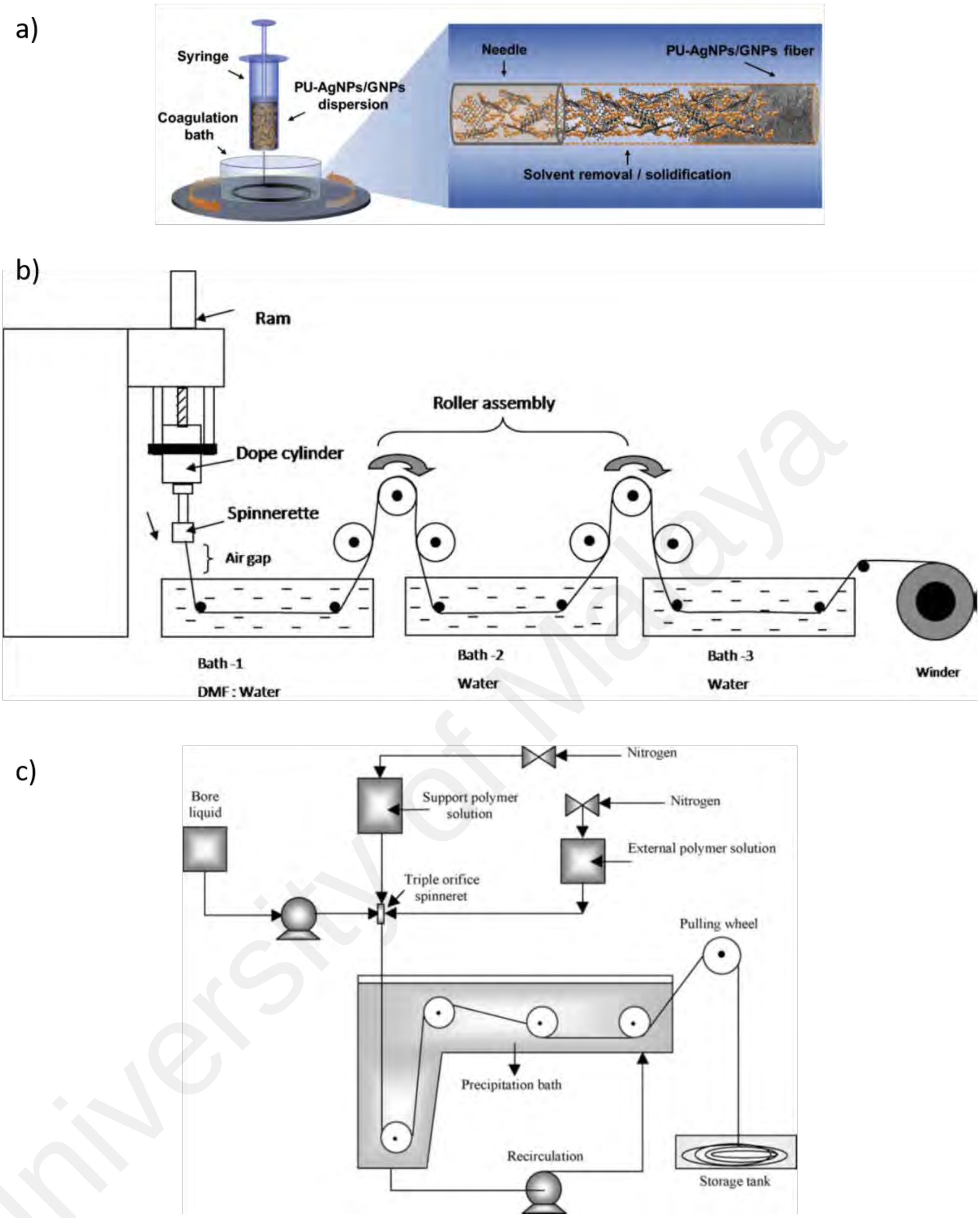

Figure 2.21: (a) Simple (Kim et al., 2019) and (b) complex (Reddy et al., 2010) and hollow fibres (Duarte et al., 2008) wet spinning setups.

In the Figure 2.21 (a), the simple setup consists of a polymer solution source and a coagulation bath. The solution jet is immediately immersed into the coagulation bath to form the solid fibres. This coagulation bath is a non-solvent to the polymer solution. Once the polymer solution jet is in contact with the non-solvent coagulation bath, a solvent exchange occurred, where the solvent of the polymer jet diffuses out to the coagulation bath and the non-solvent in the coagulation bath diffuses into the polymer jet until an equilibrium is achieved (Paul, 1968). The diffusion of the solvent out of and non-solvent into the polymer solution jets causes the solution jet to coagulate and solidify into a fibre instantaneously. If a smaller diameter fibre is desired, a roller assembly system is normally employed to further stretch the fibres as shown in Figure 2.21 (b).

Aside from the normal fibres, the wet spinning techniques can be used to fabricate hollow fibres. However, the spinneret with more than one orifice is needed in the wet spinning setup as illustrated in Figure 2.22 (c). The extra orifice is used to allow the bore liquid to fill in the hollow part of the polymer solution jet (Duarte et al., 2008). This bore liquid is also a non – solvent to the polymer solution like the coagulation bath. The solvent exchanges of the hollow solution jet can be illustrated in Figure 2.22. The mentioned bore liquid plays an important role to prevent the structural collapse of the hollow section by filling in the hollow section to provide the structural rigidity and also accelerate the solidification of the solution jet through the solvent exchange process.

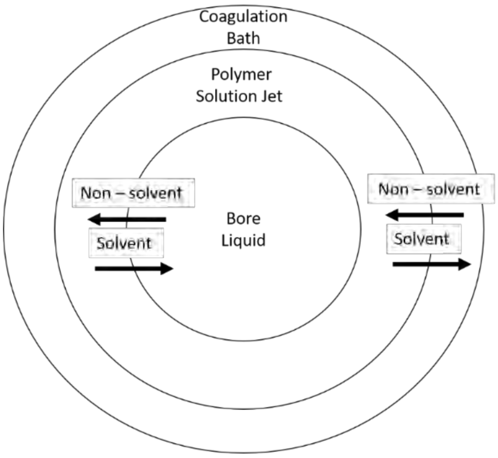

Figure 2.22: The fluxes of the solvent and non – solvent during the fabrication of hollow fibres due to concentration gradient by the wet spinning technique (Duarte et al., 2008).

2.4.2 Solution Blow Spinning

The solution blow spinning technique is another polyurethane fibres fabrication technique (Kuk et al., 2016; Tomecka et al., 2017) found in the literature. This technique is a relatively new technique as compared to the electrospinning. Similar to the electrospinning, the solution blow spinning can produce fibres with diameters in the range from micro to nanometres. It is first developed by Medeiros et al. (Medeiros, Glenn, Klamczynski, Orts, & Mattoso, 2009) in the year of 2009.

The basic setup of the solution blow spinning is as shown in Figure 2.23 (a) which consists of a polymer solution pressurized gas source and collector. The pressurized gas is analogues to the high voltage supply used in the electrospinning, where the high-pressure gas is used to draw and stretch fibres out of the polymer solution. In order to do so, a specially designed nozzle as illustrated in Figure 2.23 (b) is needed. It is designed such that the different in gas pressure, P_1 and the atmospheric pressure, P_{atm} can create a resultant pressure, P_2 to draw and stretch the polymer solution jet. Finally, the fibres solidify and deposit on the collector.

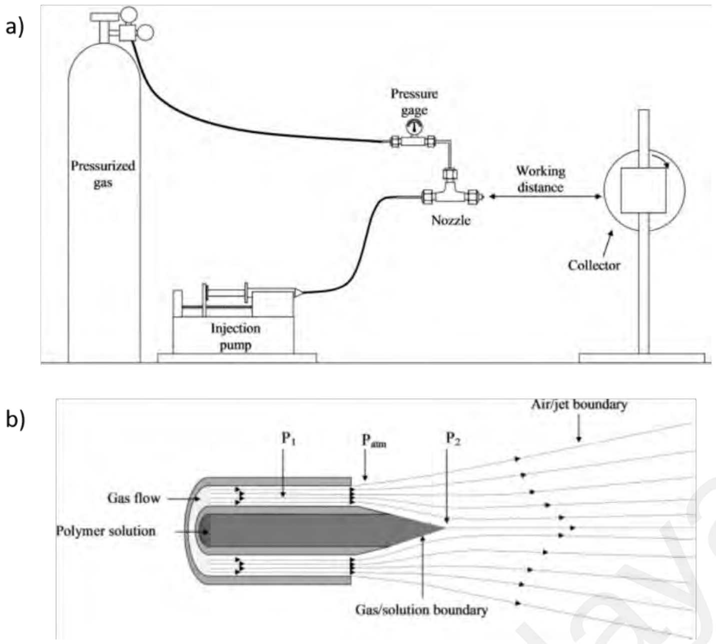

Figure 2.23: (a) Setup and (b) nozzle design of the solution blow spinning (Medeiros et al., 2009).

2.5 Mechanical Characterisation of Fibres

The studies on the mechanical properties of the fibrous samples are important and proper testing methods or equipment are crucial to cater the mechanical testing on the fibrous samples. Hence, some of the common testing methods in the literature are reviewed to understand the mechanisms, advantages and challenges of using these methods.

For the sake of nomenclature clarity in the following sections, the term “fibrous assemblies” is defined as samples with an assembly of fibres, while the term “single fibre” is defined as an individual fibre.

2.5.1 Uniaxial Testing Machines

The universal testing machine is the most versatile and common machine used to study the mechanical properties of a sample. As the name implies, this machine can perform mechanical tests on almost all kinds of materials. Despite of that, only the mechanical testing on the polymeric fibrous samples will be further discussed in this study.

2.5.1.1 Fibrous Assemblies

(a) ***Sample Preparation***

(i) Compressive Mechanical Tests

Fibrous assemblies are usually in the form of thin films or membranes with thickness less than 1 mm (Baker et al., 2008; Deng et al., 2011; Ifkovits et al., 2009; Liu, Ashcraft, et al., 2013; Matsuda & Kawahara, 2008). Compressive mechanical tests are not usually feasible to be conducted on these thin fibrous films or membranes directly as the samples need to be thick or in large amount. In this point of view, Poquillon et al. (Poquillon, Viguier, & Andrieu, 2005) are able to conduct compressive mechanical tests on fibrous samples by packing the fibres into an enclosed tube as shown in Figure 2.24. This may not able to reflect the actual compressive mechanical properties of the fibres since the samples are not as fabricated or extracted. This is because the packing of fibres into an enclosed tube may introduce extra porosity or defects which may affect the mechanical testing results.

Another compressive mechanical test was conducted by Deng et al. (Deng et al., 2011). In that study, the 250 μm thickness membrane was rolled into a 1 cm height cylindrical shape sample. Compressive force was imposed in the direction of the cylindrical axis where it is thick enough to be compressed by the universal testing machine.

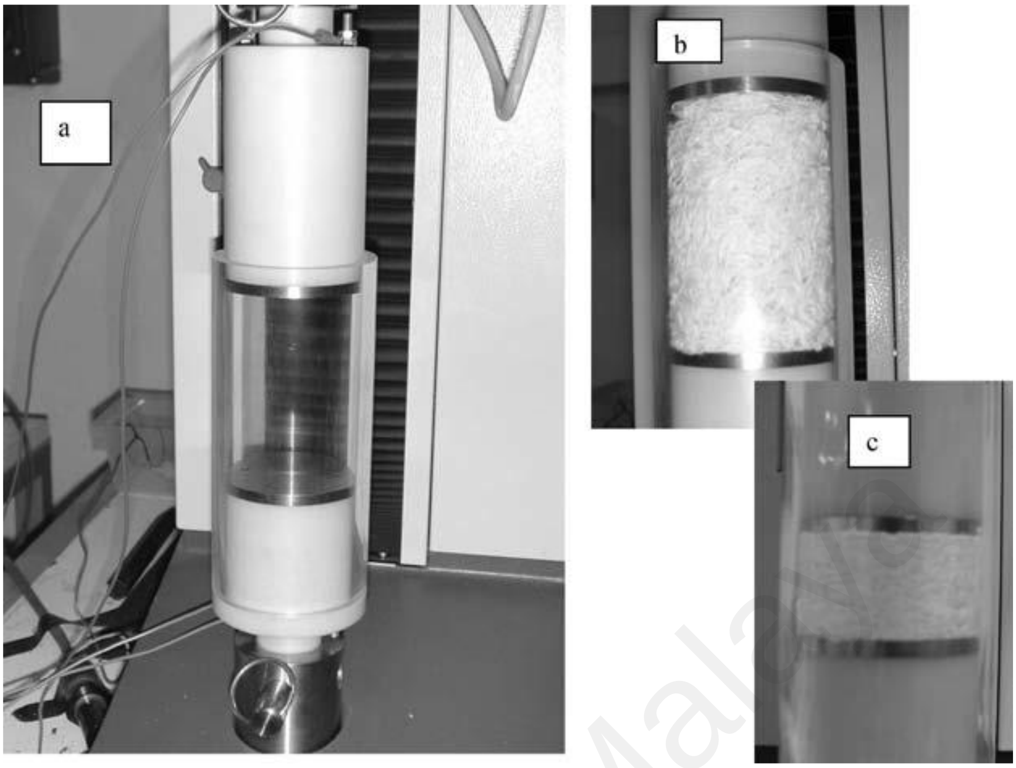

Figure 2.24: Mechanical compressive testing on enclosed fibres in plexiglass tube with diameter of 60 mm (Poquillon et al., 2005).

(ii) Tensile Mechanical Tests

Tensile mechanical tests are typically conducted directly on the polymeric fibrous assemblies in the literature (Baker et al., 2008; Benitez et al., 2013; Brown, Litvinov, Discher, Purohit, & Weisel, 2009; Bulota, Michud, Hummel, Hughes, & Sixta, 2016; Deng et al., 2011; Drexler & Powell, 2011; Huang, Chen, Reneker, Lai, & Hou, 2006; Ifkovits et al., 2009; Li, Song, et al., 2016; Liu, Ashcraft, et al., 2013; Matsuda et al., 2005; Matsuda & Kawahara, 2008; Metter et al., 2010; Nerurkar, Elliott, & Mauck, 2007; Qiao et al., 2016; Rubina, Pradeep, Yahya, Lisa, & Viness, 2012; Song, Ling, Ma, Yang, & Chen, 2013; Stachewicz, Peker, Tu, & Barber, 2011; Wanasekara, Matolyak, & Korley, 2015; Xie et al., 2012; Zhao, Jiang, Pan, Zhu, & Chen, 2007). As it is commonly known, the mechanical properties of a sample do not depend on its geometry, size or dimension. However, for the tensile mechanical tests, dog bone shape samples are preferable as the load bearing will be concentrated within the gauge length, instead of the regions near the grips, giving a more accurate measurement of the mechanical properties, such as the moduli, tensile strengths and strains at break (Bardelcik, Vowles, & Worswick, 2018).

Similarly, the tensile mechanical tests on fibrous samples are also preferable in dog bone shape to avoid premature failure at the grips of the universal testing machines. Indeed, there are studies in the literature that used dog bone shape fibrous samples for tensile mechanical testing (Drexler & Powell, 2011; Wanasekara et al., 2015). Wanasekara et al. (Wanasekara et al., 2015) conducted the tensile mechanical tests complying with the ASTM D638, where the fibrous assemblies samples were cut into dog bone shape. This ASTM D638 is a standard test method for the tensile properties of plastics. It is highly relevant to use a standard when it comes to the comparisons of mechanical properties between different types of samples. For an example, the same ASTM D638 Standard was applied on both woven oriented polypropylene fibres and tapes to do comparisons on their mechanical properties (Hine, Ward, Jordan, Olley, & Bassett, 2003).

Despite of that, in the literature, most studies did not have dog bone shape fibrous samples for tensile mechanical testing. Instead, the samples were in the shape of cuboid (Benitez et al., 2013; Huang et al., 2006; Ifkovits et al., 2009; Li, Song, et al., 2016; Liu, Ashcraft, et al., 2013; Matsuda et al., 2005; Matsuda & Kawahara, 2008; Qiao et al., 2016; Rubina et al., 2012; Song et al., 2013; Stachewicz et al., 2011; Xie et al., 2012; Zhao et al., 2007). This may be due to the difficulty in cutting the soft and delicate fibrous samples into dog bone shape without damaging the samples. Cutting the samples into cuboid shape, on the other hand, is easier. However, the cuboid shape samples do not have the stress concentrated at the gauge length region. The stress would be more concentrated at the mounting region of the samples that possibly lead to premature failure at the clamping region. Additional precautions are sometimes needed to prevent this premature failure, such as the usage of the specially designed brackets (Rubina et al., 2012) or paper frame (Huang, Zhang, Ramakrishna, & Lim, 2004; Xie et al., 2012) to mount the samples properly without imposing excessive stress concentration to the samples at the mounting regions.

(b) *Mechanical Loading Program*

A fibrous sample may present different mechanical responses under different mechanical loadings. Mechanical loading programs such as the compressive and tensile mechanical loadings as mentioned in the previous session can reveal different mechanical properties of the samples. For instance, a study by Stachewicz et al. (Stachewicz et al., 2011) conducted tensile mechanical loadings on notched samples to study the stress delocalization in crack tolerant electrospun nanofibre networks. In this study, the crack tolerant properties can only be manifested under tensile mechanical loadings since crack opening occurs under tensile mechanical loadings (Tong & Wu, 2014).

(i) Strain Rate

The strain rate is another important factor in the mechanical loading program, especially in testing polymers with viscoelasticity, a time dependent mechanical behaviour (Khan, Lopez-Pamies, & Kazmi, 2006). As a matter of fact, many studies had showed that strain rate is actually affecting the mechanical properties of polymers (Li & Lambros, 2001; Mulliken & Boyce, 2006; Richeton, Ahzi, Vecchio, Jiang, & Adharapurapu, 2006).

However, the viscoelasticity or the strain rate effect of the polymeric fibrous samples is not commonly studied. Most studies are only focusing on the efficacy of the fibrous samples in their respective applications, such as biomedical (Baker et al., 2008; Benitez et al., 2013; Deng et al., 2011; Drexler & Powell, 2011; Ifkovits et al., 2009; Li, Song, et al., 2016; Matsuda et al., 2005; Matsuda & Kawahara, 2008; Metter et al., 2010; Rubina et al., 2012; Song et al., 2013; Xie et al., 2012; Zhao et al., 2007) and electronic application (Liu, Ashcraft, et al., 2013) despite having constant strain rate monotonic mechanical tests as complementary tests. Although there are also studies focusing in the mechanical properties of the fibrous samples, they are mainly about the change in tensile strengths and moduli of the samples at a constant strain rate due to fibres orientation (Nerurkar et al., 2007), microstructure (Brown et al., 2009; Wanasekara et al., 2015), crack (Stachewicz et al., 2011) and chemical cross-linking (Qiao et al., 2016).

(ii) Precondition Loadings

The usual practice of conducting monotonic tensile mechanical test on a fibrous sample is to directly mount the sample to the universal testing machine and stretch it until failure (Benitez et al., 2013; Brown et al., 2009; Drexler & Powell, 2011; Li, Song, et al., 2016; Liu, Ashcraft, et al., 2013; Matsuda et al., 2005; Matsuda & Kawahara, 2008; Qiao et al., 2016; Rubina et al., 2012; Song et al., 2013; Stachewicz et al., 2011; Wanasekara et al., 2015; Xie et al., 2012; Zhao et al., 2007).

Nonetheless, in some studies, precondition loadings were imposed to the fibrous samples before stretching it until failure (Baker et al., 2008; Ifkovits et al., 2009; Metter et al., 2010; Nerurkar et al., 2007). Initially, the samples were stretch and held for 1 minute or 5 minutes to ensure proper mounting and engagement of the sample to the grips of the universal testing machines. Then, 10 or 15 cycles of loading with maximum strain less than 1 % strain were imposed to the samples. These preconditioning relaxation and cyclic loadings are important to impart a similar loading history to all the samples, allowing more consistent and reproducible results for the mathematical evaluation of the mechanical properties (de Gelidi, Tozzi, & Bucchi, 2016). Despite that, these precondition loadings imposed to the samples should be small enough to avoid any damage to the samples before the subsequent mechanical tests. However, in doing precondition loadings, certain deformation mechanisms occurring during these precondition loadings such as the significant fibres realignment cannot be captured (Miller, Edelstein, Connizzo, & Soslowsky, 2012). This fibres realignment is an important attribute in a fibrous sample that contribute largely to the mechanical behaviours and properties of the sample.

2.5.1.2 Single Fibre Samples

The mechanical tests on the single fibre samples will only characterise the intrinsic mechanical properties of the fibres, different from the fibrous assemblies, where the extrinsic architecture or structure of the fibres assembly, such as the orientation (Nerurkar et al., 2007) and chemical cross-linking (Qiao et al., 2016) are taken into account when evaluating the mechanical properties.

Like fibrous assemblies, compressive mechanical tests are not applicable to single fibre samples. Thus, the following discussions in this section will be based on the tensile mechanical tests of single fibre samples using universal testing machines.

(a) *Samples Preparation*

Unlike fibrous assemblies samples, the geometry or shape of single fibre samples for tensile mechanical tests is not controllable since a single fibre is always cylindrical in shape (Blackledge & Hayashi, 2006; Blackledge, Swindeman, & Hayashi, 2005; Hunsaker, Price, & Bai, 1992; Kong & Eichhorn, 2005; Shi, Wan, Wong, Chen, & Blackledge, 2010; Shojaei, Li, & Voyiadjis, 2012). Despite of that, it is difficult to extract or spin a fibre with a uniform diameter along the axis. In addition, the variation in the diameter between fibres is also common. Thus, statistical analyses are often conducted to get a representative diameter for the calculation of stress, which is an important factor in evaluating the mechanical properties of the fibre.

The process for mounting the single fibres to the universal testing machines is actually like the fibrous assemblies samples. Before mounting the single fibre to the universal testing machines, the procedure is basically just to transfer the single fibre to a frame and use epoxy or adhesive to fix the both ends of the single fibre to the frame (Hunsaker et al., 1992; Kong & Eichhorn, 2005; Neugirg, Burgard, Greiner, & Fery, 2016; Shi et al., 2010). An illustration of the mounting of a single fibre to the universal testing machine is as shown in Figure 2.25.

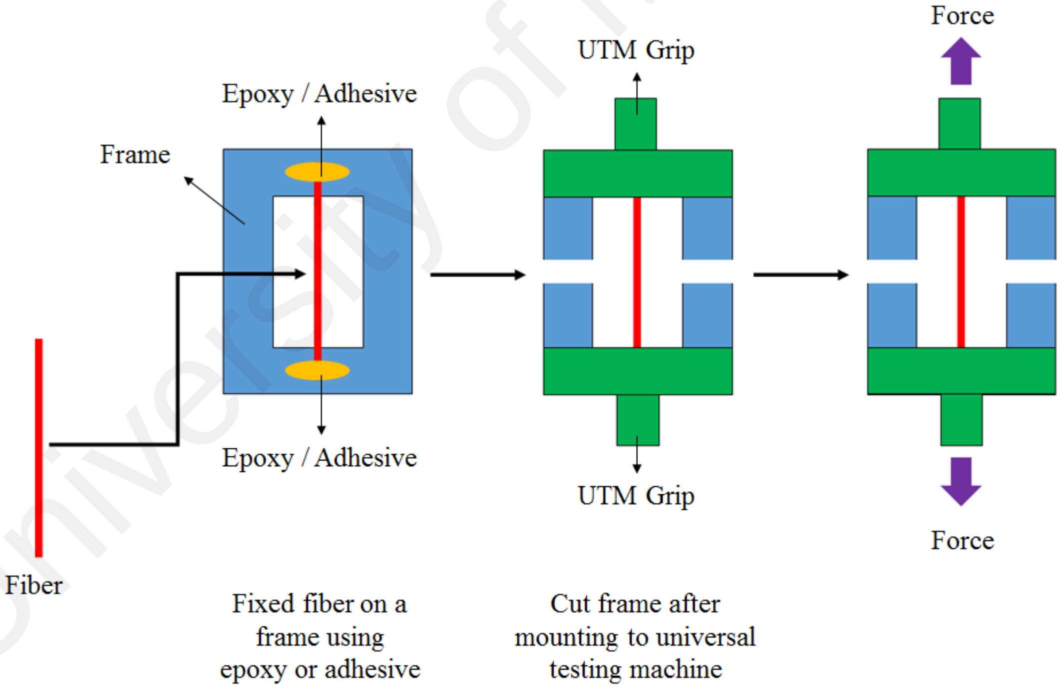

Figure 2.25: Mounting of a single fibre on a frame to the universal testing machine (Hunsaker et al., 1992; Neugirg et al., 2016; Shi et al., 2010).

As for the mechanical tests on the single fibres in the nano to micro scale, the load cells in the universal testing machines must have low maximum force detection, as low as 2 N (Hunsaker et al., 1992; Kong & Eichhorn, 2005). However, a bundle of fibres in

10 can be used for conducting mechanical tests to compensate for a higher maximum force detection load cell, similar to a study done by Boluta et al. (Bulota et al., 2016).

(b) ***Mechanical Loading Program***

Aside from the monotonic tensile mechanical tests at a constant strain rate conducted on the single fibre samples to determine the moduli and tensile strengths (Blackledge & Hayashi, 2006; Blackledge et al., 2005; Hunsaker et al., 1992; Kong & Eichhorn, 2005; Neugirg et al., 2016), others mechanical tests, such as continuous dynamic analysis (Basu, Hay, Swindeman, & Oliver, 2014; Blackledge & Hayashi, 2006; Blackledge et al., 2005), cyclic loadings (Shojaei et al., 2012) and interfacial fibres adhesion test (Shi et al., 2010) were also conducted on single fibre samples in the literature.

(i) Continuous Dynamic Analysis

Although there are studies that conducted dynamic mechanical analysis on single fibre samples, the dynamic moduli retrieved from the test are at a constant strain under a harmonic force (Kim et al., 2015; Steinmann et al., 2011). The evolution of these dynamic moduli with strain is not really studied.

Realizing the complexity in the mechanical properties of the viscoelastic polymeric fibres and the dynamic moduli of these viscoelastic materials may change with strain, Basu et al. (Basu et al., 2014) conducted the continuous dynamic analyses on PET fibres and silk fibres. Indeed, the study shows that the dynamic mechanical behaviours of the fibres change with strain due to the realignment of polymeric chains during the stretching process in mechanical test. These findings are in agreement with two studies conducted by Blackledge et al. (Blackledge & Hayashi, 2006; Blackledge et al., 2005) on silk fibres spun by spiders. Hence, the continuous dynamic analysis on the polymeric fibres is important to have a deeper study on the dynamic mechanical behaviours of the fibres.

The idea of this continuous dynamic analysis is to conduct the tensile mechanical test until failure and dynamic mechanical analysis simultaneously on a sample. In this way, the storage modulus and lost modulus of the sample can be retrieved instantaneously during the tensile mechanical test from 0 strain to failure. An additional remark in this test is to use a very small harmonic force, 4.5 mN in the studies of Basu et al. (Basu et al., 2014) and Blackledge et al. (Blackledge & Hayashi, 2006; Blackledge et al., 2005), so that the resulting harmonic strain will not exceed the linear viscoelastic regime.

(ii) Cyclic Loadings

Based on the previous discussion, it is now clear that monotonic tensile mechanical tests are not able to fully characterise the mechanical properties of a fibre.

In a study conducted by Shojaei et al. (Shojaei et al., 2012), cyclic tensile mechanical tests were conducted on polyurethane fibres to study their shape memory properties. Other mechanical behaviours of the polyurethane fibres, such as hysteresis, stress softening, and permanent set are manifested in these cyclic loadings. These behaviours are important defining traits for polymers, especially for elastomers (Nunes, Fonseca, & Pereira, 2000).

(iii) Interfacial Fibres Adhesion Tests

Interfibres fusions are found to affect the mechanical properties of the fibrous assemblies samples in the literature (Huang, Manickam, & McCutcheon, 2013; Tang & Mukhopadhyay, 2006). Specifically, the mechanical strength of polyacylonitrile and polysulfone nanofibrous membranes is improved with the fusions between fibres (Huang et al., 2013). Thus, the interfacial properties between the fibres are also contributing to the mechanical properties of the fibrous assemblies.

Shi et al. (Shi et al., 2010) conducted a simple adhesion test between two fibres as illustrated in Figure 2.26. Two fibres were fixed to two independent cardboard frames respectively before they were mounted to the universal testing machine. The mountings were done in a way that the two axes of the fibres were perpendicular to each other. Finally, the two fibres were brought together until they adhered to each other before pulling them apart by the universal testing machine. Through conducting this test, the adhesion force between the fibres can be retrieved.

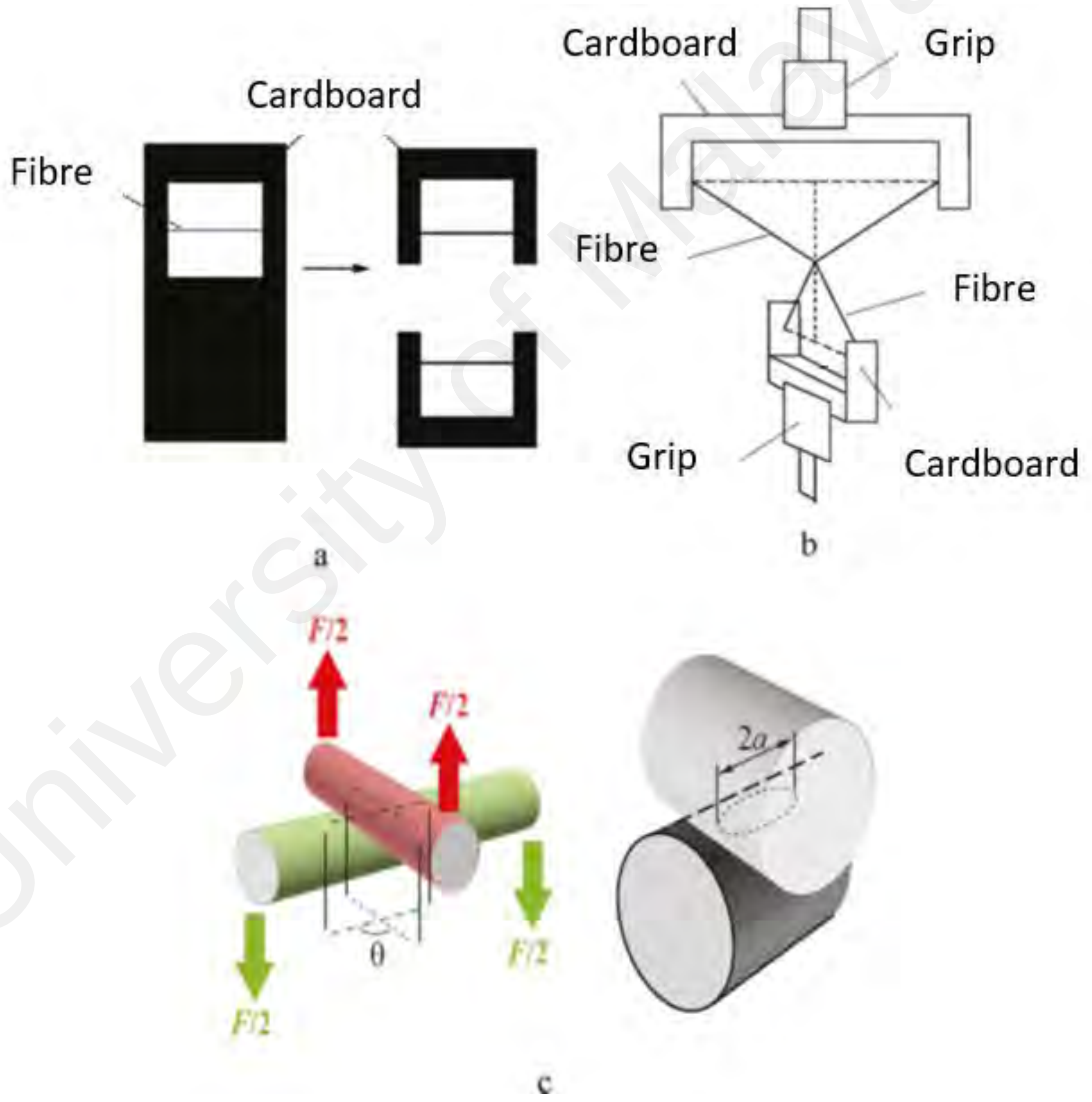

Figure 2.26: Schematic illustration of interfacial fibres adhesion test (Shi et al., 2010).

Indeed, using this method to determine the interfacial fibres adhesion is easy and effective. However, it cannot accurately reflect the actual fusion or interfacial force between fibres in some cases. This is because the fibres fabricated for this testing is by electrospinning using parallel electrodes (Li et al., 2004). The as spun fibres existed separately, where the adhesion was imposed to the two fibres later. On the contrary, the fusion between fibres in some fibrous assemblies is as fabricated (Mit‑uppatham, Nithitanakul, & Supaphol, 2004; Tang & Mukhopadhyay, 2006). Thus, the different in the adhesion mechanisms may lead to different adhesion properties between the fibres.

2.6 Morphology-Mechanical Behaviours Relations of Polyurethane Fibrous Assemblies

Thermoplastic polyurethane elastomer is a biphasic polymer possessing both thermoplastic properties and elastomeric behaviours (Drobny, 2014). From the microscopic perspective, thermoplastic polyurethane elastomers have microphase separated microstructure, which comprises of hard and soft domains or segments (Kojio, Kugumiya, Uchiba, Nishino, & Furukawa, 2008). This unique microstructure is originated from the thermodynamic incompatibility of the two domains. Hard domains are having higher glass transition temperature, contributing to the strength of the polyurethane and sites of thermoreversible physical cross linking to ease the fabrication process like the typical thermoplastics. On the other hand, soft domains which have lower glass transition temperature are responsible for the rubbery properties (Christenson, Anderson, Hiltner, & Baer, 2005).

Owing to the thermoplastic property, polyurethane can be processed into articles with various shapes and structures for many useful applications. Among all these shapes and structures, polyurethane foams are the most fabricated structure for the applications of thermal insulation (Kotresh et al., 2009; Mikelis, Ugis, Viesturs, Laura, & Andris, 2014), sound insulation (Soto et al., 2017; Sung, Kim, Kim, & Kim, 2016) and impact absorbance (Koohbor, Kidane, & Lu, 2016; Maji, Schreyer, Donald, Zuo, & Satpathi, 1995). Besides foams, polyurethane films with biocompatibility are also used extensively in the biomedical field (Matsui, Ono, & Akcelrud, 2012; Savan et al., 2016; Zhang, Woodruff, Clark, Martin, & Minchin, 2016). Some polyurethane films are also found suitable for the electronic applications (Li, Wang, et al., 2016; Su, Zhang, Wang, MacDiarmid, & Wynne, 1998) and special application in telecommunication (Chen, Kuang, Sargent, & Wang, 2003). Apart from the foams and films, polyurethane fibres with high aspect ratio are also gaining more and more interest and attention. Polyurethane fibrous assemblies are often being used in the water purification (Lee, Heo, et al., 2017; Zhu et al., 2017) and biomedical applications (Han, Farah, Domb, & Lelkes, 2013; Tonda-Turo, Boffito, Cassino, Gentile, & Ciardelli, 2016) due to the high porosity and surface area to volume ratio. Other applications include energy storage (Ke et al., 2016), polymer electrolyte (Peng et al., 2016), protective clothing (Sheng, Zhang, Luo, Yu, & Ding, 2016) and shape memory polymer (Safranski et al., 2016).

Different forms or structures of polyurethane may possess different mechanical properties or behaviours as the microstructure of the polyurethane may change according to the fabrication process. For instance, polyurethane foams, films and fibres are found to have dissimilar mechanical properties due to different microstructures (Pedicini & Farris, 2003; Stirna et al., 2012; Sunada, Kuriyagawa, Kawamura, & Nitta, 2011). While there are many studies on the mechanical behaviours of polyurethane in the literature, the main focus is on polyurethane foams due to the crashworthiness property (Briody, Duignan, Jerrams, & Ronan, 2012; Marsavina, Linul, Voiconi, & Sadowski, 2013; Weißenborn, Ebert, & Gude, 2016; Whisler & Kim, 2015). The mechanical behaviours studies on the polyurethane fibres, are relatively less and not in details, mainly in the form of non-woven fibrous assemblies (Amoroso et al., 2011; Lee et al., 2005; Meng et al., 2007).

In short, investigations into the mechanical properties and behaviours of the polyurethane fibrous assemblies can be crucial to avoid failures during their services. Hence, in this section, the studies on the mechanical properties and behaviours of polyurethane fibres assemblies are reviewed along with the factors affecting their mechanical properties and behaviours.

2.6.1 Intrinsic Molecular Morphology of Polyurethane Fibres

The microphase separated molecular morphology of a polyurethane fibre can be illustrated in a simple diagram as shown in Figure 2.2 (a). According to Kaursoin et al. (Kaursoin & Agrawal, 2007) and Ding et al. (Ding, Hu, Tao, & Hu, 2006), the soft segments in the polyurethane tend to align in the stretching direction while the hard segments remain perpendicular to the direction. However, the continuous stretching or drawing of the fibres to a greater extent can force the hard segments to fully align in the stretching direction (Kaursoin & Agrawal, 2007) as illustrated in Figure 2.27 (b). In other words, the alignment of the soft and hard segments will be higher if the diameters of the fibres are smaller. The confinement of the polymeric chains into smaller diameters fibres can also induce stronger hydrogen bonding among the hard segments as the chains are closer together. Both the alignment of the hard and soft domains together with the stronger hydrogen bonds among the hard segments can synergistically improve the mechanical properties of the fibres (Kaursoin & Agrawal, 2007; Pedicini & Farris, 2003).

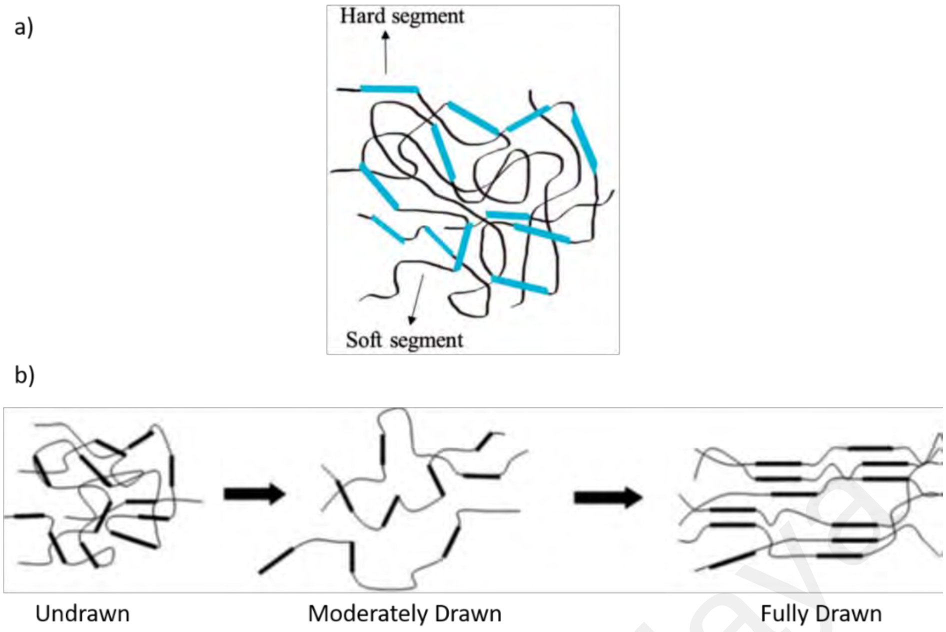

Figure 2.27: (a) Schematic diagram of a microphase separated polyurethane fibre (Sáenz-Pérez et al., 2018); (b) Evolution of the microphase separated morphology of polyurethane fibres under different degree of drawing (Kaursoin & Agrawal, 2007)

The microstructure of the fully drawn polyurethane fibres with aligned soft and hard segments are similar to the Pervosek Model (Herrera Ramirez, R. Bunsell, & Colomban, 2006; Philippe, 2013; Prevorsek, Tirpak, Harget, & Reimschuessel, 1974; Ramirez, Colomban, & Bunsell, 2004) and Oudet Model (Colomban, 2013; Herrera Ramirez et al., 2006; Le Clerc, Bunsell, & Piant, 2006; Oudet & Bunsell, 1987; Ramirez et al., 2004) proposed for semicrystalline polymeric microfibres, such as polyamides and polyesters fibres. The two models mentioned are as illustrated in Figure 2.28. These two models are similar as both models are consisting of crystallites embedded inside the amorphous domains. The crystallites are connected or linked together in series by the polymeric chains in the amorphous domains to form microfibrils.

In the Pervorsek Model, a fibre is consisting of an assembly of microfibrils. Although the crystallites are embedded within the amorphous domains, these domains are different within the fibrils and between the fibrils. The intrafibrillar regions are the typical amorphous domains, where the chains are randomly oriented. On the contrary, the polymeric chains in the interfibrillar amorphous domains are aligned. This type of amorphous domains with aligned polymeric chains are named as mesomorphous domains. As for the Oudet Model, the microfibrils described in the Pervosek Model are constituents of a bigger entity, macrofibril. Similar to Pervosek Model, this Oudet Model has the mesomorphous domains between the microfibrils and also the macrofibrils.

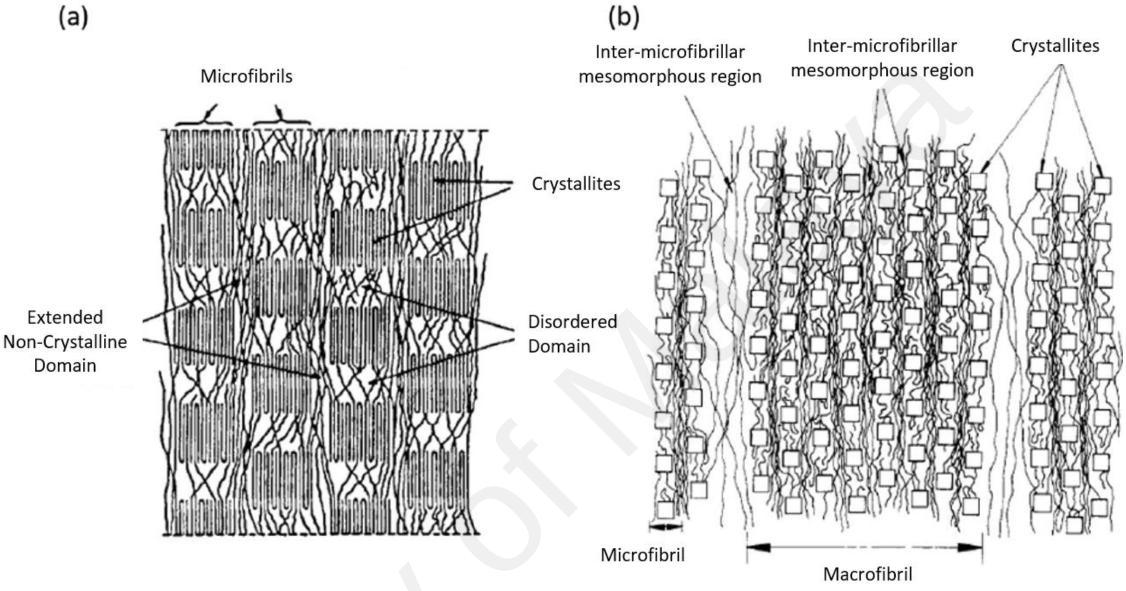

Figure 2.28: (a) Pervorsek Model (Prevorsek et al., 1974) and (b) Oudet Model (Oudet & Bunsell, 1987).

Oudet and Bunsell (Oudet & Bunsell, 1987) explain that the mesomorphous domains in the fibres are responsible for the mechanical behaviours of the fibres. Since the crystallites are already well compacted, only the polymeric chains in the mesomorphous domains can undergo deformations during mechanical loadings. The strain hardening occurs when the polymeric chains in the mesomorphous domains are stretched and failure occurs when these polymeric chains connecting the crystallites ruptures during mechanical loadings. Thus, the anchorages between the crystallites and the polymeric chains in the mesomorphous domains play important roles in determining the mechanical strength and damage to the fibres. In the case of polyurethane fibres, the crystallites and mesomorphous domains can be analogue to the hard and soft phases respectively.

In a nutshell, the deformation and failure mechanisms of polyurethane fibres at the molecular level can largely influence the macro mechanical behaviours and properties of the fibres. Despite of that, there are only a handful of studies in the literature. The studies are mostly focusing on the effects of hard segments morphology to the mechanical properties of the polyurethane fibres (Zhu, Hu, Lu, Yeung, & Yeung, 2008; Zhu et al., 2006; Zhu et al., 2007). It is found that the higher the content of the hard segments or domains in the polyurethane fibres, the higher the mechanical strengths and moduli. This is because the hard domains can evolve into isolated hard domains, inter-connected hard domains and ultimately to a continuous hard domains as the composition of the hard domains increases, contributing to the strength and moduli of the polyurethane (Hong, Yu, Youk, & Cho, 2007; Lin & Chen, 1998). In addition, high pressure steaming and heat treatment to the high hard segments content polyurethane fibres can induce higher crystallinity in the hard segments, further increasing the maximum strain with significant reduction in the thermal shrinkage (Zhu et al., 2006; Zhu et al., 2007).

Aside from the hard segments, the soft segments can also influence the mechanical properties of the polyurethane fibres despite being less studied in the literature (Hong et al., 2007; Meng et al., 2007). Polyurethane fibres with higher content of soft segments are more flexible with longer elongation. Nevertheless, the flexibility of the fibres can be reduced with the increment in the crystallinity of the soft segments.

2.6.2 Extrinsic Surface Morphology of Polyurethane Fibrous Assemblies

In the previous section, the roles of molecular morphology in dictating the mechanical properties and behaviours of polyurethane fibres are highlighted. Nonetheless, it is still not enough to fully describe or characterise the mechanical behaviours and properties of the polyurethane fibrous assemblies. This is because a polyurethane fibrous assembly is an entity comprises of a collection of polyurethane fibres. The interactions between the fibres within the assembly can have significant impacts to the mechanical behaviours and properties of the whole assembly. Thus, the relations between the extrinsic surface morphology and mechanical behaviours and properties of the polyurethane fibrous assembly are discussed in the following paragraphs.

Pedicini and Farris (Pedicini & Farris, 2003) compare the mechanical behaviours of polyurethane fibrous assembly with the typical bulk polyurethane sample. It is found that the bulk sample behaves like a typical elastomer where a sigmodal stress-strain curve is observed under the monotonic tensile mechanical loading. In the contrary, despite being an elastomer in nature, the fibrous sample have a monotonic stress-strain relation without an inflection in the slope as observed in bulk sample. Instead, an upturn in stress at high strain is observed for the fibrous sample. This finding is in agreement with the study conducted by Lee et al. (Lee et al., 2005). The stress-strain curves of both bulk and fibrous samples are as shown in Figure 2.29.

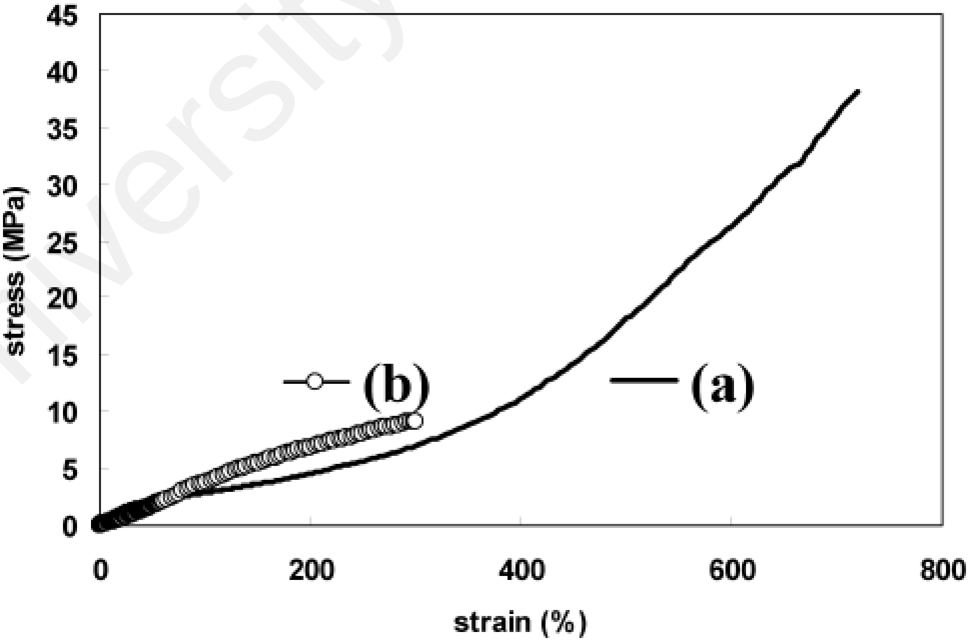

Figure 2.29: Engineering stress-strain curve of (a) bulk and (b) fibrous polyurethane samples (Pedicini & Farris, 2003).

With the reference to the micrographs in Figure 2.30, Pedicini and Farris (Pedicini & Farris, 2003) further explain that the stress-strain behaviour of the fibrous sample is due to its surface morphology. The relatively low stress at small strain is due to the low density of the porous fibrous sample. However, as the strain increases, the fibres in the sample align themselves to the direction of the stretching. Consequently, the amount of fibres sustaining the loads increases and thus, the stress increases.

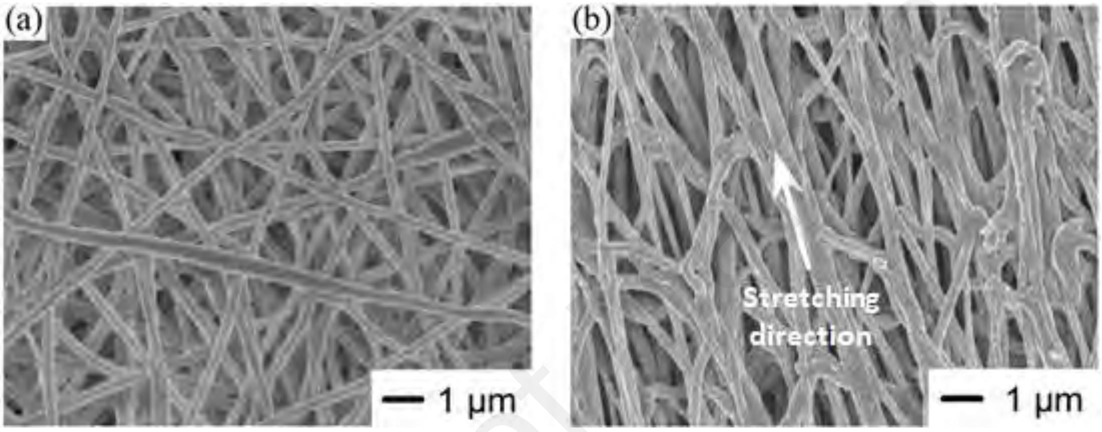

Figure 2.30: Micrographs of polyurethane fibrous samples (a) before and (b) after monotonic mechanical tensile loading (Pedicini & Farris, 2003).

Beside the sigmodal stress-strain behaviour under monotonic mechanical tensile loading, an elastomer like the polyurethane also exhibit mechanical hysteresis and stress softening behaviours under cyclic loadings as illustrated in Figure 2.31. In the figure, there are stress-strain curves for three cycles of loading imposed to an elastomer. The 1st, 2nd and 3rd cycle are denoted by ①, ②, and ③ respectively. Mechanical hysteresis is formed when the unloading curves do not follow the same path as the loading curves. On the other hand, stress softening can be observed when the loading stress level is lower than the previous loading stress level despite being at the same strain level. Both of these behaviours are often interrelated and being named as Mullins effect (Diani, Fayolle, & Gilormini, 2009).

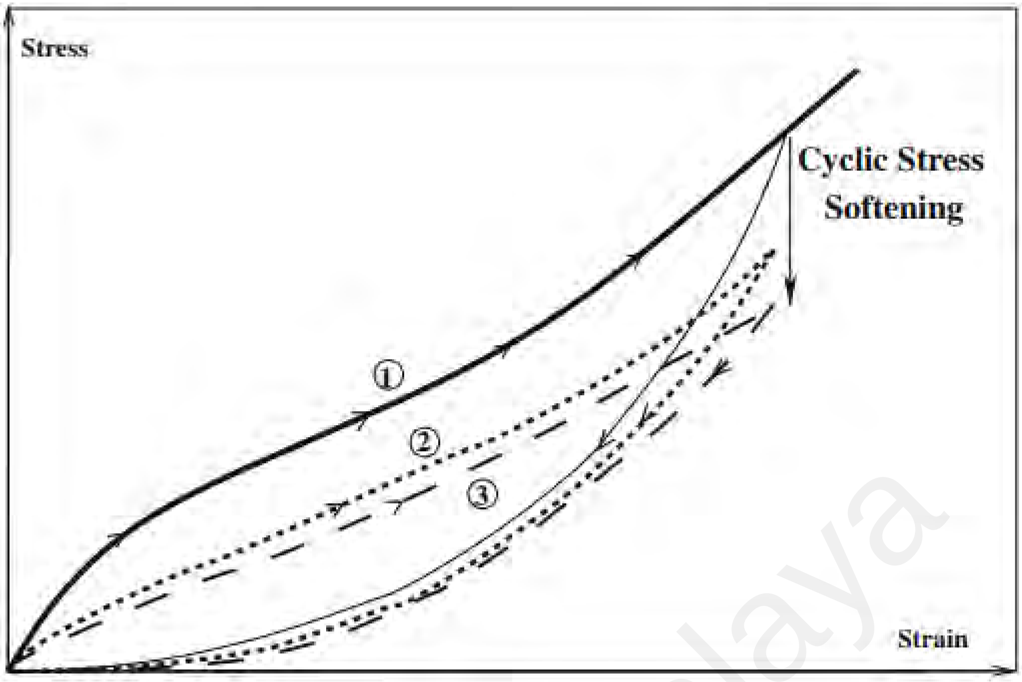

Figure 2.31: Engineering stress-strain curves of typical elastomers under cyclic loadings (Cantournet, Desmorat, & Besson, 2009).

While it is undeniable that this Mullins effect is originated from the nature of the polyurethane as an elastomer (Qi & Boyce, 2005; Sui et al., 2017), the extrinsic fibrous surface morphology can also contribute to the Mullins effect of the polyurethane fibrous assembly (Lee et al., 2005). Figure 2.32 shows the evolution of the surface morphology of a polyurethane fibrous assembly from 0% strain, then loaded to 200% strain and finally back to the unloaded state. Despite being at the same unloaded state, the morphology of the fibrous sample after and before the loading are not the same. The mechanical loading has changed the morphology of the fibrous sample.

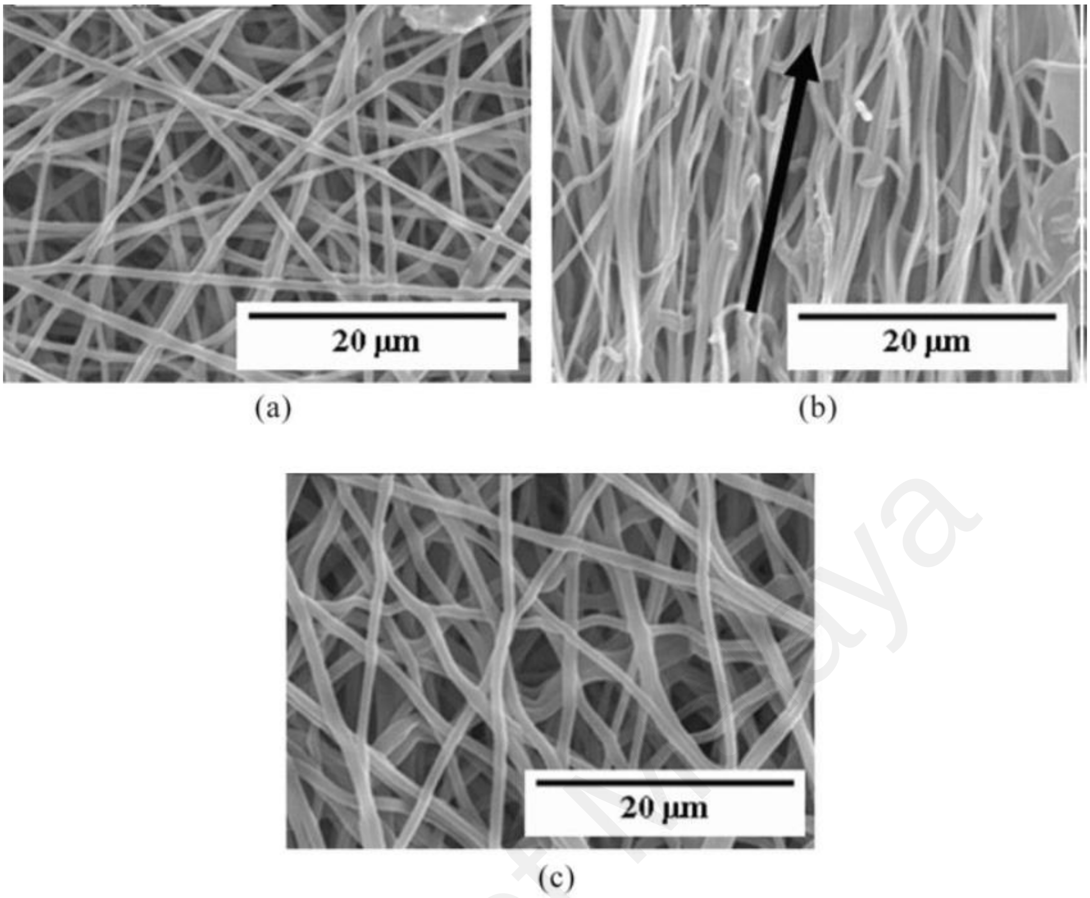

(a) (b)

(c)

Figure 2.32: Surface morphology of the polyurethane fibrous assembly at (a) 0 % strain, (b) 200 % strain and (c) unloaded state (Lee et al., 2005).

Lee et al. (Lee et al., 2005) propose that there are many junction points among the fibres in the polyurethane fibrous assembly. Some of these points are bonding points while the other are non-bonding points as illustrated in Figure 2.33. Most of the mechanical loads will be sustained by the bonding points to resist deformation as these points are effective sites for local physical or frictional entanglement (Bai et al., 2012; Kidoaki, Kwon, & Matsuda, 2006; Mondal, 2014). Still, the fibrous morphology maybe damaged due to the slippage of the fibres or alteration of the fibrous structure since the non-bonding points can be easily broken upon loadings. This damage to the morphology can be viewed as a kind of energy dissipation mechanism which is the source of the hysteresis loss and stress softening of the polyurethane fibrous assembly. At higher strain, the energy dissipation will be exaggerated along with higher hysteresis lost and stress softening as the bonding points can be broken too. The significance of these junction points to the mechanical properties and behaviours of the polyurethane fibrous assemblies is also highlighted in a more recent study conducted by Amoroso et al. (Amoroso et al., 2011). These points are said to impart high strain energy and mechanical anisotropy to the polyurethane fibrous assemblies.

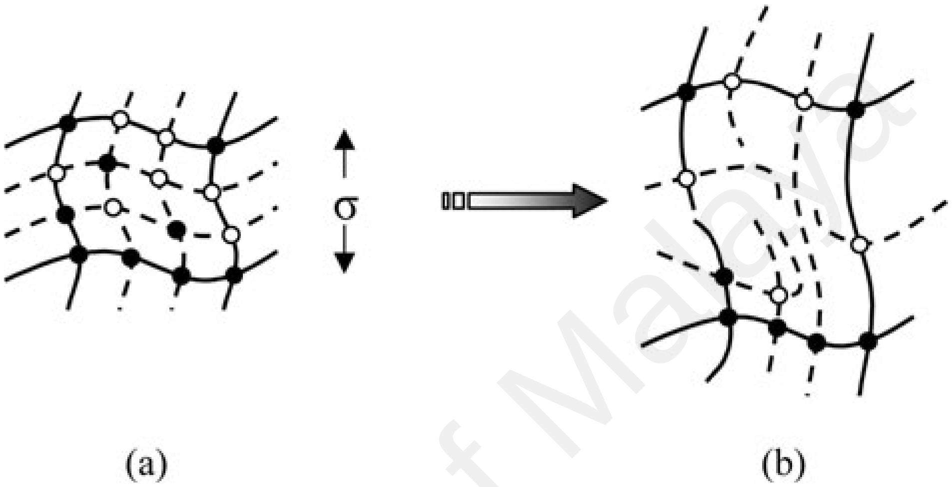

Figure 2.33: Illustration of polyurethane fibrous assembly with bonding points denoted by • and non-bonding points denoted by ◦ (a) before and (b) after loading (Lee et al., 2005).

2.7 Summary

Thermoplastic polyurethane elastomers are polymers synthesized from the polycondensation of isocyanate and polyol, resulting in the formation of urethane linkage. Depending on the types of the monomers used in the polycondensation process, these thermoplastic polyurethanes elastomers can have different characteristics, behaviours and properties. Additionally, from the perspective of processing, thermoplastic polyurethane elastomers can be shaped into articles with different geometries easily due to the thermoplastic behaviours. Consequently, thermoplastic polyurethane elastomers are suitable in many applications such as biomedical, shape memory, impact absorbance and so on.

Despite the versatility of thermoplastics polyurethane elastomers as mentioned in the previous paragraph, this study only focuses on the application of thermoplastic polyurethane elastomers in the small vascular grafting. Researchers are fond of employing thermoplastic polyurethane elastomers in the small vascular grafting application due to their tailorable properties.

As discussed in the Section 2.1, the core idea to have a competent small vascular graft is to have a biomimetic graft with extracellular friendly microenvironment for self-endothelization to occur readily. Researches are conducted to chemically and physically modify the polyurethanes to achieve this objective. However, the mechanical behaviours of these polyurethane grafts are seldom studied although the mechanical incompatibility of the grafts and vessels can lead to intimal hyperplasia and thrombogenicity due to the compliance mismatch.

Mechanical behaviours and properties of the polyurethane grafts can be complex due to their unique phase separated molecular microstructures. This complexity increases when the polyurethane grafts are having fibrous morphology. The combined effects of the intrinsic phase separated molecular and extrinsic fibrous morphology of the polyurethane fibres to their mechanical behaviours can be sophisticated. Detail discussions on the mechanical behaviours of these polyurethane fibres can be found in the Section 2.6.

Lack of studies despite the importance of the complex mechanical behaviours and properties of the polyurethane fibrous grafts have led the author to the objectives of this study as described in Section 1.2. To achieve these objectives, the polyurethane fibrous assemblies need to be fabricated as the samples of the polyurethane small vascular grafts. As it is well known, electrospinning is a very common technique to fabricate fibrous samples. Nevertheless, many parameters are involved in fabricating the fibrous samples. Tedious parameter optimizations are often needed to electrospin the ideal samples, especially for the highly aligned fibrous assemblies. In fact, the author tries optimizing the parameters to fabricate highly aligned fibrous assemblies but unsuccessful. Further elaborations can be found in the later sections. Consequently, to avoid all the difficulties of electrospinning, the author uses a facile dry spinning technique to fabricate the highly aligned fibrous samples for further biostability and mechanical characterisation.

In the literature, the mechanical testing on these soft and delicate fibres with the diameters ranges from a few micrometres to less than 100 nanometres using the universal testing machines are difficult and tedious, no matter from the aspect of sample handling or the testing itself, especially for the one single fibre as discussed in Section 2.5.1.2. Mechanical testing on the fibrous assemblies or a collection of fibres, on the other hand are much easier as compared to the single fibres. The detail discussion of the mechanical testing of single fibres and fibrous assemblies can be found in Section 2.5. In this study, investigations are carried on the mechanical behaviours of the polyurethane fibrous assemblies under complex mechanical loadings instead of just the single polyurethane fibre. This is because the author intends to capture the complex combined effects of the intrinsic molecular and extrinsic surface morphology on the mechanical behaviours of the polyurethane fibrous assemblies such as the viscoelasticity, stress softening and hysteresis.

CHAPTER 3: METHODOLOGY OF STUDY

The methodology in this study consists of three parts. The first part is on the fabrication of highly aligned fibres, whereas the second part is on the biostability study of the samples and the third part is on the mechanical testing of the highly aligned and woven fibrous assemblies. The last part which will be on mechanical simulation of the woven fibrous assemblies using classical laminate theory.

3.1 Materials

MDI-polyester/polyether polyurethane (a thermoplastic elastomer) pellets with CAS number of 68084-39-9 were used as the base material to fabricate the polymeric fibres. These thermoplastic elastomer pellets have the density of 1.18 g/ml and glass transition temperature of -40 ^{o}C as stated in the specification sheet. The chemical structure of the polyurethane is shown in the Figure 3.1. Soft domains of the polyurethane are comprised of the polyester (Chen, Yu, Chen, Lin, & Liu, 2001) and polyether (Gallagher et al., 2016) groups, whereas the hard domains are comprised of the methylene diphenyl diisocyanate (MDI) (Chen et al., 2001) groups.

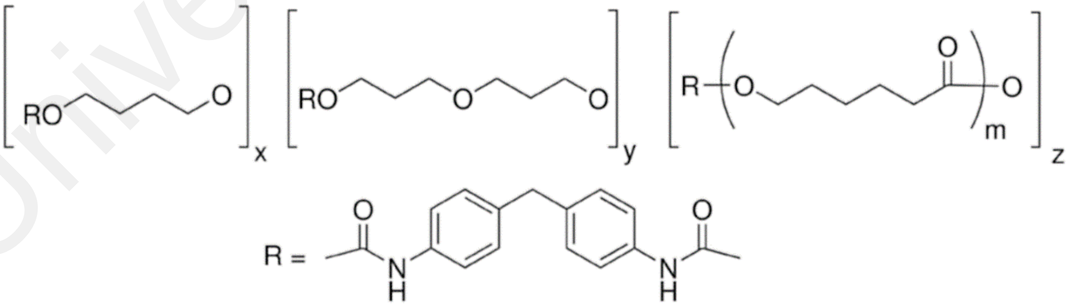

Figure 3.1: Chemical structure of MDI-polyester/polyether polyurethane obtained from the specification sheet.

N,N-Dimethylformamide (DMF) and Tetrahydrofuran (THF) with purity more than 99 % were used as solvents to dissolve the MDI-polyester/polyether polyurethane pellets.

The base material and all chemicals were purchased from Sigma Aldrich. They were used as received without further processing.

Three polymer solutions with different polymer concentrations and solvent ratios, denoted by Solution A, B and C are prepared as shown in Table 3.1. These polyurethane pellets and solvents are purchased from Sigma Aldrich and used directly without further processing.

Table 3.1: Polymer solution parameters.

Solution	Solvent Ratio (DMF:THF)	Polymer Concentration (wt %)
A	1:0	10
B	1:0	15
C	1:1	15

After dissolving the polyurethane pellets, the viscosity and electrical conductivity of the solutions are measured using Brookfield DV-II + Pro EXTRA viscometer with S18 spinneret and Mettler Toledo Seven Compact Benchtop Meter respectively.

3.2 Spinning of Fibres

Two spinning techniques are used to fabricate the fibres in this study, which are the electrospinning and dry spinning as illustrated in Figure 3.2. The two are detailed in the following sections.

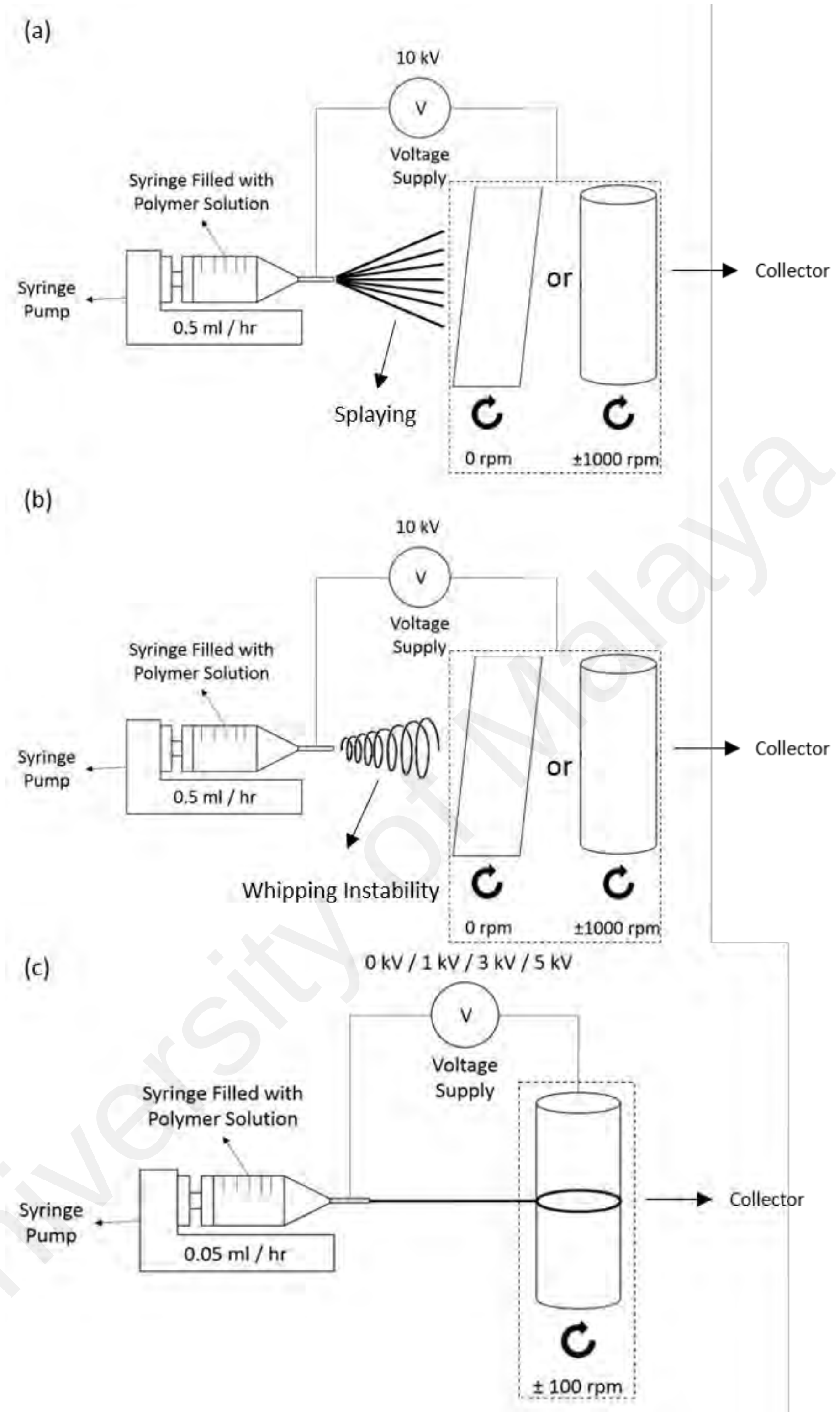

Figure 3.2: Electrospinning of fibres with (a) splaying (Dhakate, Singla, Uppal, & Mathur, 2010; Shin, Hohman, Brenner, & Rutledge, 2001) and (b) whipping instability (Bagchi, Brar, Singh, & Ghanshyam, 2015; Shin et al., 2001); (c) Dry spinning assisted by weak electrical field (Tan, Andriyana, Ang, & Chagnon, 2018; Tan et al., 2019).

3.2.1 Electrospinning

The basic setup of electrospining is presented in Figure 3.2 (a, b). It consists of three main components, a high voltage supply, a syringe pump and a collector. In this study, syringes with 27 gauge size needles are used to contain the polymer solution while the syringe pump is used to control the solution injection rate. A 10 kV of electrical potential difference is applied between the tip of the syringe needle and the collector. The fibres are drawn from the syringe to the collector by the strong electrical force. Two types of collectors are used, a stationary and rotating collector as shown in Figure 3.2 (a) and (b) respectively. For the rotating collector, a high rotating speed of ± 1000 rpm is applied to increase the alignment of the fibres (Al-Ajrah, Lafdi, Liu, & Le Coustumer, 2018; Maciel et al., 2018; Song et al., 2018). The processing parameters of the electrospinning techniques are as shown in Table 3.2.

Table 3.2: Processing parameters of electrospinning.

Sample	Solution	Applied Voltage (kV)	Tip to Collector Distance (cm)	Rotational Speed (rpm)	Solution Injection Rate ($mlhr^{-1}$)
PU1	A	10	15	0	0.5
PU2	B	10	15	0	0.5
PU3	B	10	15	± 1000	0.5
PU4	C	10	15	0	0.5
PU5	C	10	15	± 1000	0.5

3.2.2 Dry Spinning

Dry spinning is a less complicated technique in the fabrication of fibres as compared to electrospinning. It uses mechanical force to draw fibres out of the solution to the collector (Jin, Zhang, Hang, Shao, & Hu, 2013; Tan et al., 2018). The setup of dry spinning in this study only comprises of a syringe pump and a rotating collector as shown in Figure 3.2 (c). Similar to the electrospinning, syringes with 27 gauge size needles are used to contain the polymer solution while a syringe pump is used to control the solution injection rate.

3.2.2.1 Highly Aligned Fibrous Assemblies

In order to start the dry spinning process, a fibre is drawn manually from the syringe to the rotating collector. Then, the rotating collector takes up the spinning of the fibres by mechanical drawing force. The polyurethane solution must be viscous and volatile enough, so that a fibre can be continuous drawn from the solution in the syringe. In this case, Solution C is used to be dry spun. The rotational speed used in this dry spinning is very low, ± 100 rpm as compared to the ± 1000 rpm of rotational speed used in electrospinning. This is to ensure that the rotational force is not too strong to break the continuous drawn fibres. If the continuous fibre break, manual drawing of the fibres has to be repeated. A weak voltage is also applied between the tip of the syringe needle and collector during the spinning process to study the effect of the electrical force on the dry spun samples. However, it is important to note that the applied voltage is not strong enough to initiate the electrospinning process. The processing parameters are listed in the Table 3.3.

Table 3.3: Processing parameters of dry spinning.

Sample	Solution	Applied Voltage (kV)	Tip to Collector Distance (cm)	Rotational Speed (rpm)	Solution Injection Rate (mlhr^{-1})
PU6	C	0	15	± 100	0.05
PU7	C	1	15	± 100	0.05
PU8	C	3	15	± 100	0.05
PU9	C	5	15	± 100	0.05

3.2.2.2 Woven Fibrous Assemblies

Basically, the fabrication of the woven polyurethane fibrous assemblies is actually like the fabrication of the highly aligned polyurethane fibrous assemblies as described in

Section 3.2.2.1 except that, in order to spin the woven fibres, the syringe pump with the syringe fixed on it is allowed to reciprocate along the axis of the cylindrical collector. The reciprocation speeds are varied to enable the deposition of woven fibrous assemblies with different woven angles, θ. Figure 3.3 illustrates the set up and mechanisms to dry spin the woven fibrous assemblies.

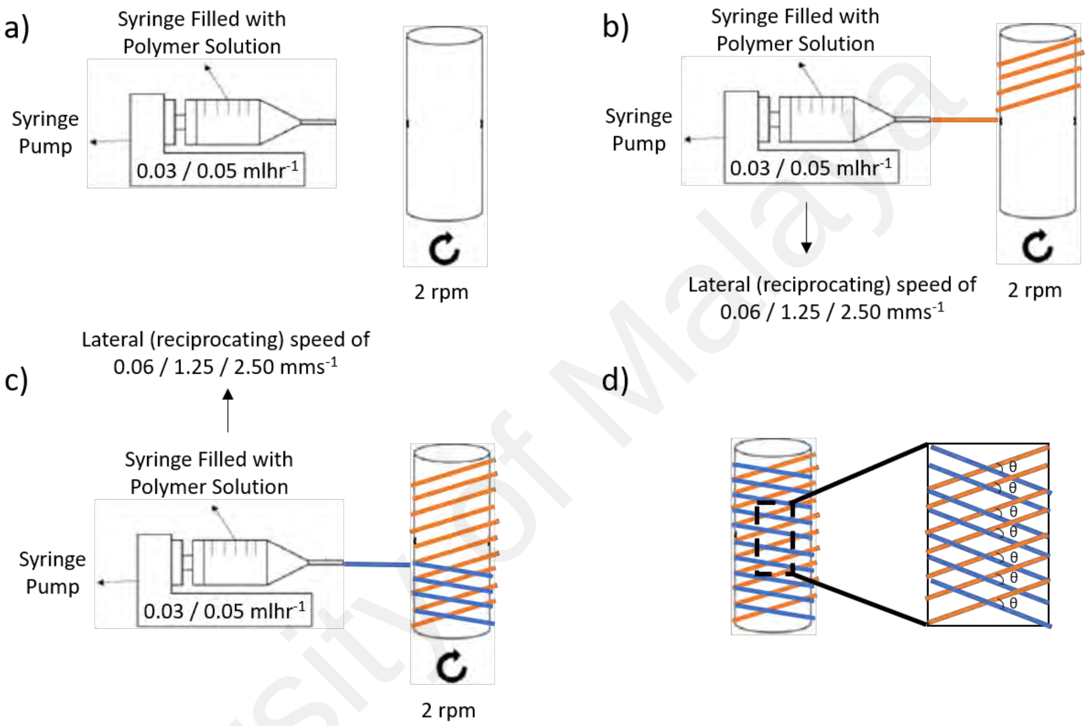

Figure 3.3: a) Dry spinning set up; b) and c) Reciprocating of the syringe pump along the axis of the cylindrical collector during dry spinning with the speed of 0.06, 1.25 and 2.50 mms^{-1} respectively; d) A sheet of woven fibrous assemblies deposited on the collector with the woven angle, θ.

The processing parameters in dry spinning the woven fibrous assemblies are stated in the Table 3.4. In order to minimize the breakage of the continuous drawn fibres, the tip to collector distance is changed to 2.5 cm and the rotational speed is reduced to 2 rpm. Two different solution injection rates of 0.03 and 0.05 mlhr^{-1} are used with the aim to fabricate fibres with different diameters.

Table 3.4: Processing parameters in dry spinning of woven fibrous assemblies.

Sample	Solution	Tip to Collector Distance (cm)	Rotational Speed (rpm)	Solution Injection Rate (mlhr^{-1})	Reciprocation Speed (mms^{-1})
PU10	C	2.5	2	0.03	0.63
PU11					1.25
PU12					2.50
PU13				0.05	0.63
PU14					1.25
PU15					2.50

3.2.3 Surface Characterizations

The fibres surface morphology was observed under the Phenom ProX desktop scanning electron microscope (SEM) with 1000 × magnification and 5000 × magnification. The micrographs with the magnification of 1000 × were used for fibres orientation analysis. Similarly to the work of Wong et al. (Wong et al., 2016), two assumptions were made: the fibre orientation was in plane and the orientation at the top layer was considered to represent the average fibre orientation of the whole sample. The diameter of 100 fibres from the 5000 × magnification micrographs were measured to get the mean value and the standard error. Both the orientation analysis and diameter measurement were done using the ImageJ 1.48v software. OrientationJ Distribution processing method in OrientationJ plugin was used for orientation analysis, whereas the diameter measurement was evaluated using the measuring tools in the software.

3.3 Biostability Study on the Highly Aligned Fibrous Assemblies

In this section, the sample preparations and procedures for the biostability study on the samples are described in detail. Since all the dry spun samples have similar alignment and diameter in topology as shown in the Section 4.1.3.1, PU7 is chosen arbitrarily for subsequent testing.

In order to study the biostability of PU7, the fibres are immersed into a simulated body fluid. This simulated body fluid (SBF) is prepared by dissolving Hank's balanced salt (without sodium bicarbonate and phenol red, Sigma Aldrich) and sodium bicarbonate (reagent grade) in distilled water (Zainal Abidin, Atrens, Martin, & Atrens, 2011). The durations of immersion are 2, 4, 8, 12 and 24 weeks respectively. All these simulated body fluids with samples immersed inside are kept at body temperature, 37 ^{o}C using a water bath.

3.3.1 Mass Change Measurement

The initial masses of the samples denoted by M_i are measured, whereas the masses of the samples after immersion in SBF, M_f are measured before and after removing all the absorbed water by drying in oven at 40 ^{o}C for every immersion duration. Then, the percentages change in mass, $M_{\%}$ are calculated based on this equation, $M_{\%} = \frac{M_f - M_i}{M_i} \times 100\%$.

3.3.2 pH Measurement

The pH values of the stimulated body fluids are measured after every immersion duration using a pH meter.

3.3.3 Surface Characterisation

The surface characterisations of the dried fibres before and after every immersion duration are conducted using SEM as described in Section 3.2.3.

3.3.4 Fourier Transform Infrared Spectroscopy (FTIR)

FTIR is used to detect the chemical interactions between the fibres and SBF. Both the fibres and SBF before and after every immersion duration are characterised using Nicolet iS10 FTIR spectrometer from Thermo Scientific. The spectra range from 400 to 4000 wavenumber with a resolution of 4 cm^{-1}.

3.3.5 Initial Tensile Modulus and Ultimate Tensile Strength Measurement

Monotonic tensile mechanical tests under the strain rate of 0.001 s^{-1} are conducted on the dried samples after every immersion duration in the SBF. The procedures are similar to the procedures described in Section 3.4. However, the average surface area to mass ratio in Section 3.4.1.1 cannot be obtained as only two samples are available for each immersion duration. The cross-sectional areas of the samples are just estimated by using the average value from the 12 equivalent diameters measured.

3.4 Mechanical Testing

3.4.1 Highly Aligned Fibrous Assemblies

Similar to Section 3.3, PU7 is chosen arbitrarily for the mechanical testing. The testing procedures are described in the following sections.

3.4.1.1 Estimation of Initial Sample Cross-sectional Area

In view of analysing the mechanical test results, information on tensile specimen cross-sectional area is needed. Due to the irregular shape and small size of fibres, obtaining a precise sample cross-sectional area is a daunting task. Furthermore, since thermoplastic polyurethane elastomeric fibres are soft materials, the cross-sectional shape may be easily distorted under slight excessive force which might occur during the measurement. To overcome this difficulty, indirect measurement was conducted. First, the fabricated bundles of fibres were cut into 6 cm length, with 4 cm as the gauge length and 1 cm each at both ends of the sample to be clamped during the tensile test. Then, the mass of the sample was measured before clamping it to the uniaxial tensile machine. Additional precaution was taken by casting water soluble poly(vinyl alcohol), PVA at the clamping region of the sample to prevent premature failure and slipping of the sample through the grip of the tensile machine during the test. After properly clamping the sample as shown in Figure 3.4 (a), dino-lite digital microscope was used to capture perpendicularly the image at the middle of the gauge length of the samples. For each sample, an image was taken from every 30° angle of viewing, starting from 0° to 360°. Thus, a total of 12 images were obtained from each sample. An example of image taking at several angles of 0°, 30°, 90° and 120° is illustrated in Figure 3.4 (b). By assuming circular cross-sectional area, diameters measurement was done in these 12 images. The equivalent diameter, D for the irregular cross-sectional area was calculated to compensate for the lack of circularity of the cross-sectional area using equation $D = \sqrt{D_1 D_2}$, where D_1 and D_2 are two perpendicular diameters as previously measured (Sun, Han, Wang, & Lim, 2008). A total of 12 equivalent circular diameters were measured for each sample and the average value was computed.

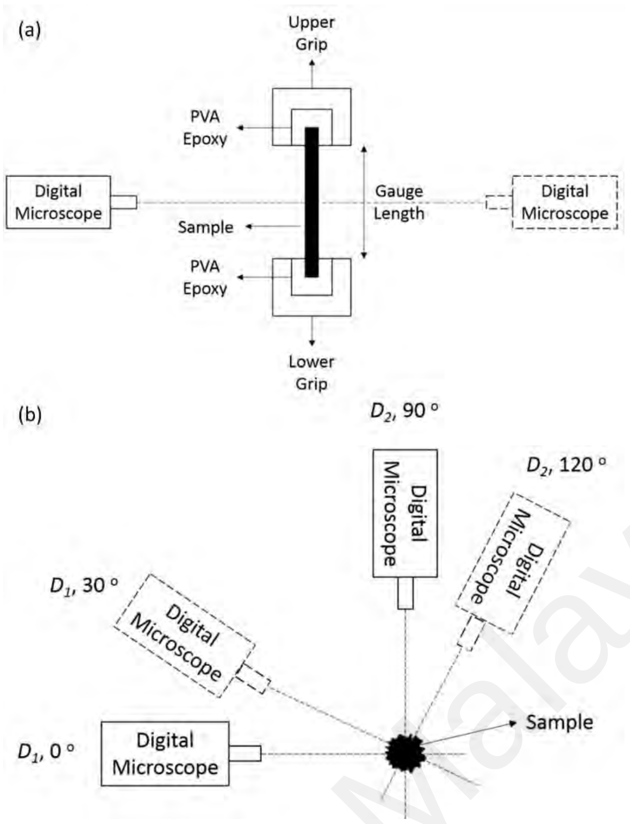

Figure 3.4: Illustration of (a) front view of the sample gripped at the tensile machine and (b) top view of the sample.

For the sake of simplicity, the indirect measurements of initial cross-sectional area were only conducted on 8 representative samples used for monotonic tensile test. The ratio between initial cross-sectional area and mass was subsequently calculated for each sample and the corresponding average over 8 samples was computed. It was found that the average cross-sectional area to mass ratio, denoted α, was 93.4 mm^2g^{-1}. Finally, since all the samples are produced from the same precursor, by assuming that all samples have the same density, the initial cross-sectional area, A of any other tensile sample can be easily estimated by multiplying the above average ratio with the sample mass, m, i.e. $A = \alpha m$. The sizes of the 8 samples are tabulated in Table 3.5.

Table 3.5: Sizes of the tensile samples.

Sample	Cross-sectional Area / mm^2	Gauge Length / cm
1	14.8	4
2	13.7	4
3	20.4	4
4	19.3	4
5	20.3	4
6	13.0	4
7	13.6	4
8	12.8	4

3.4.1.2 Uniaxial Tensile Mechanical Testing

The mechanical tests were conducted using Shimadzu AGS-X Series Universal Tensile Testing Machine equipped with a 5 kN load cell. Three mechanical tests were conducted: uniaxial monotonic tensile test, cyclic tensile test with increasing maximum strain and relaxation tensile test. They were performed at two different strain rates of 0.1 and 0.001 s^{-1}. The loading profiles for the uniaxial cyclic tensile test and relaxation tensile test are illustrated in Figure 3.5. During the cyclic test, the unloading was set to stop when the force was 0 N instead of 0 % strain before starting the next cycle as shown in Figure 3.5 (a) to prevent the sample from buckling. In the case of relaxation tensile test, the samples were held at strains of 20 % and 40 % as shown in Figure 3.5 (b). Please note that only uniaxial monotonic tensile test at 0.001 s^{-1} were conducted for 8 times due to the reason mentioned in the Section 3.4.1.1. All other tests were conducted twice to ensure the consistency of the results.

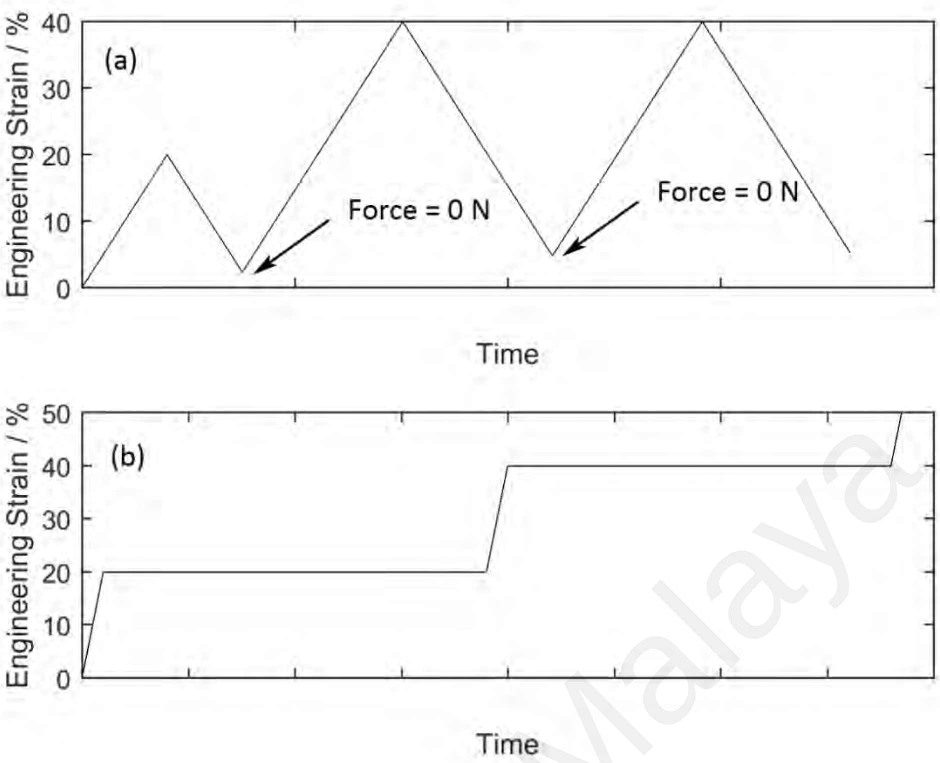

Figure 3.5: Loading profile for (a) cyclic tensile test and (b) relaxation tensile test.

3.4.2 Woven Fibrous Assemblies

The mechanical testing on the woven fibrous assemblies is rather easier than the mechanical testing of the highly aligned fibrous assemblies in the Section 3.4.1, where the estimation of the initial sample cross-sectional area in Section 3.4.1.1 is not required as the woven fibrous assemblies are in mats.

3.4.2.1 Samples Preparation

For mechanical testing, the mats are cut into smaller cuboid specimens with area dimension of 5.0 × 0.5 cm^2, where the 0.5 cm is in the axial direction and the 5.0 cm is in the circumferential direction of the collector as illustrated in Figure 3.6. The gauge length is 3 cm allocating 1 cm at the both ends of the specimens to be clamped on the uniaxial tensile machine grips. The thicknesses of the samples are measured by using a thickness gauge.

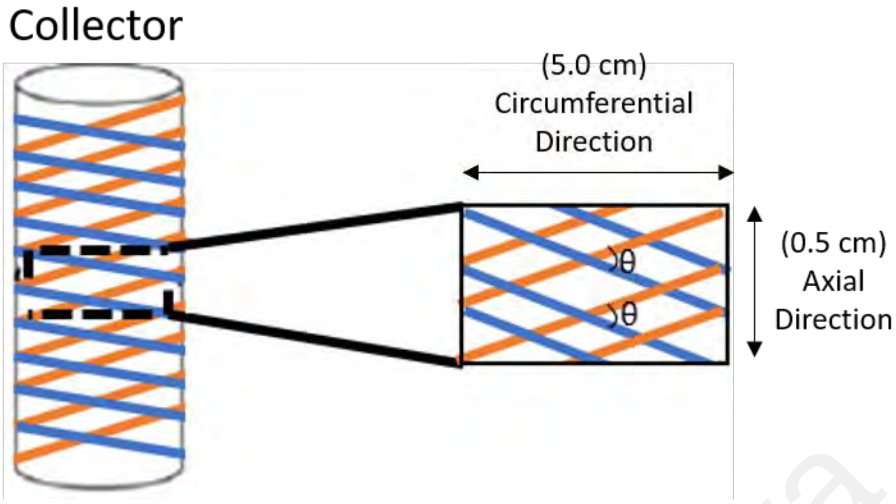

Figure 3.6: The area dimension of a mechanical testing specimen.

3.4.2.2 Uniaxial Tensile Mechanical Testing

The uniaxial tensile testing machine used in Section 3.4.1 are used to probe the mechanical responses of the woven fibrous assemblies in the circumferential direction as labelled in Figure 3.6. Similarly, three types of mechanical tests, which are the uniaxial monotonic tensile test, cyclic tensile test and relaxation tensile test are conducted on the samples with two different strain rates of 0.001 s^{-1} and 0.1 s^{-1}. The mechanical loading programs for the cyclic and relaxation tensile tests at the strain rate of 0.001 s^{-1} are as shown in Figure 3.7. In the case of cyclic tensile test, the samples are loaded to 200 % strain before unloading to 0 N force as shown in Figure 3.7 (a) to prevent the samples from buckling. On the other hand, for the relaxation tensile test, the samples are loaded to 100 % and 200 % strain respectively before holding for 30 minutes as shown in Figure 3.7 (b) and (c).

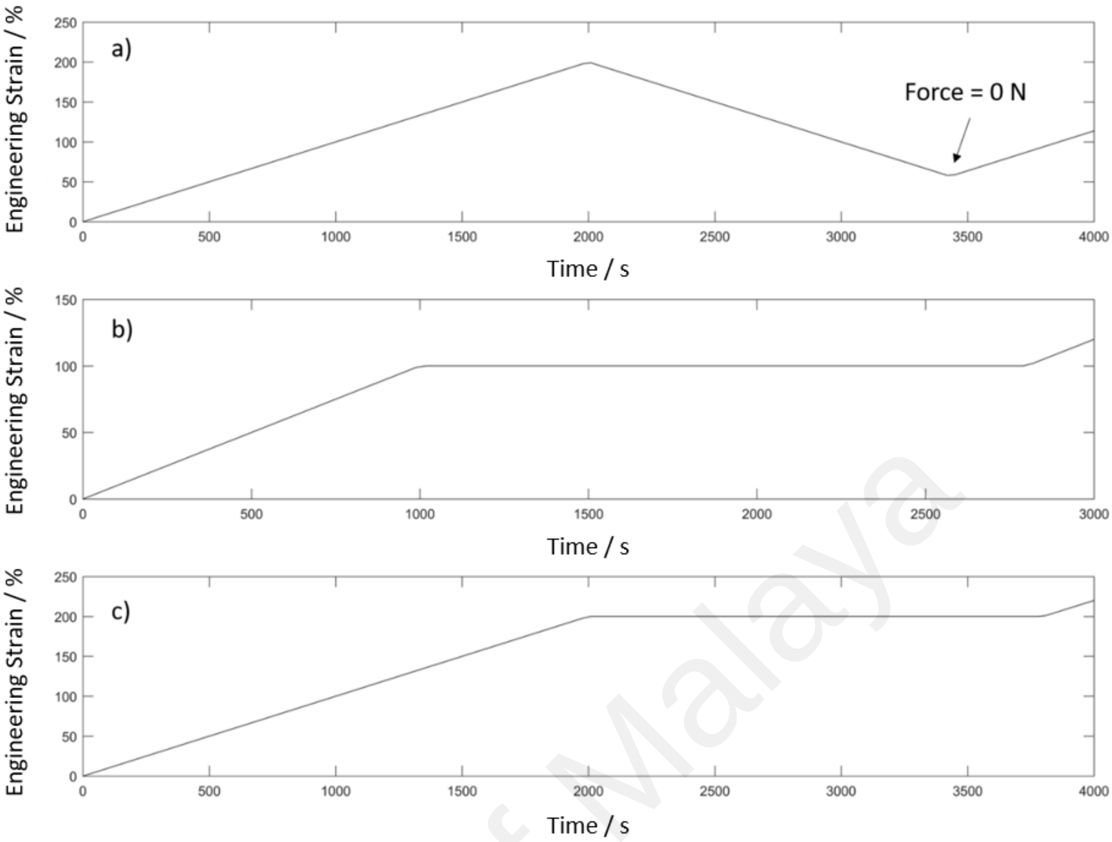

Figure 3.7: Loading profiles at 0.001 s^{-1} strain rate for (a) cyclic tensile test at 100 % strain, (b) relaxation tensile test at 100 % and (c) 200 % strain respectively.

3.5 Prediction of Elastic Properties of Woven Fibrous Assemblies

In this section, the elastic properties or the initial moduli of the woven fibrous assemblies are predicted using the classical laminate theory. However, unlike the conventional fibres reinforced composites, the fibrous assemblies in this study consist of only fibres without matrices. Despite of that, this laminate theory is widely used in the literature to predict the elasticity of the fibrous assemblies (Huang, 2002a, 2002b; Sry, Mizutani, Endo, Suzuki, & Todoroki, 2018).

As commonly known, a laminate is composed of multiple layers stacked together with certain configurations. In this study, the highly aligned fibrous assemblies with woven angle, 0^{o} are the layers in the two layers stacked laminates. These two layers with the same thicknesses are stacked such that fibre's axes between layers are having the same angles as the woven angles, θ in this study as illustrated in Figure 3.8.

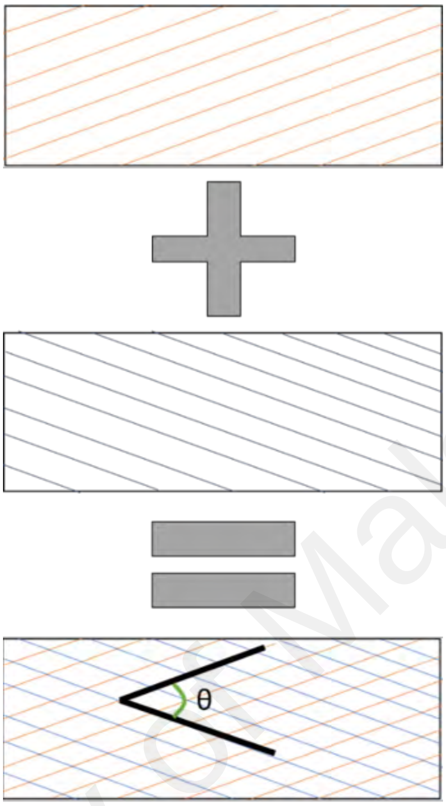

Figure 3.8: Illustration of a laminate composed of two layers of highly aligned fibrous assemblies stacking together.

The first step in applying the classical laminate theory to the fibrous assemblies is to find out the constitutive equations for the single layer highly aligned fibrous assemblies under the loading in the direction of the fibre's axis, x as shown in Figure 3.9. The fibrous assemblies are transversely isotropic with plane stress assumption. Four material parameters of the highly aligned fibrous assembly, which are the longitudinal initial modulus, E_x, transversal initial modulus E_y, Poisson's ratio due to the longitudinal loading, v_{xy} and shear modulus, G_{xy} are needed. The equation is expressed in Equation 3.1, where σ_{xx}, σ_{yy}, τ_{xy}, ε_{xx} and ε_{yy} correspond to the longitudinal stress, transversal stress, shear stress, longitudinal strain and transversal strain respectively. v_{yx} is the Poisson's ratio due to the transversal loading and can be computed based on Equation 3.2.

For the sake of simplicity, the Equation 3.1 can be expressed as Equation 3.3 with a stiffness matrix, $[Q_{ij}]$ where γ_{xy} is the shear strain.

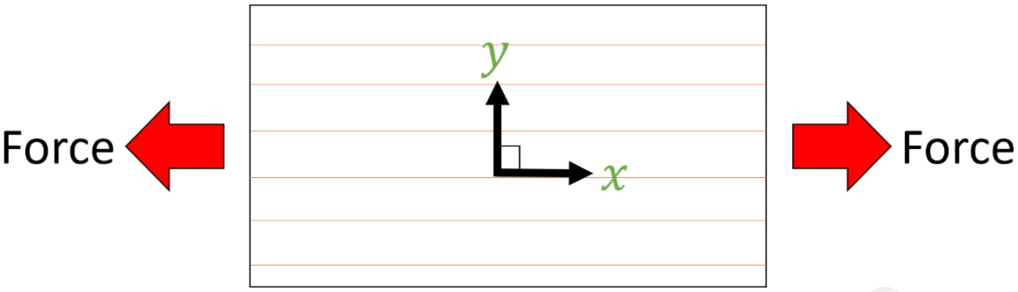

Figure 3.9: A layer of highly aligned fibrous assembly loaded in the $\boldsymbol{x}$ direction.

$$\begin{bmatrix} \sigma_{xx} \\ \sigma_{yy} \\ \tau_{xy} \end{bmatrix} = \begin{bmatrix} \frac{E_x}{1 - v_{xy}v_{yx}} & \frac{v_{yx}E_x}{1 - v_{xy}v_{yx}} & 0 \\ \frac{v_{yx}E_x}{1 - v_{xy}v_{yx}} & \frac{E_y}{1 - v_{xy}v_{yx}} & 0 \\ 0 & 0 & G_{xy} \end{bmatrix} \begin{bmatrix} \varepsilon_{xx} \\ \varepsilon_{yy} \\ 2\varepsilon_{xy} \end{bmatrix} \qquad 3.1$$

$$v_{yx} = \frac{v_{xy}}{E_x} \times E_y \qquad 3.2$$

$$\begin{bmatrix} \sigma_{xx} \\ \sigma_{yy} \\ \tau_{xy} \end{bmatrix} = \begin{bmatrix} Q_{11} & Q_{12} & Q_{13} \\ Q_{21} & Q_{22} & Q_{23} \\ Q_{31} & Q_{32} & Q_{33} \end{bmatrix} \begin{bmatrix} \varepsilon_{xx} \\ \varepsilon_{yy} \\ \gamma_{xy} \end{bmatrix} \qquad 3.3$$

Subsequently, the next step is to establish the constitutive equations for the fibrous assembly under the off axis loading in the direction X as shown in Figure 3.10 where σ_{XX}, σ_{YY}, τ_{XY}, ε_{XX}, ε_{YY} and γ_{XY} correspond to the longitudinal stress, transversal stress, shear stress, longitudinal strain, transversal strain and shear strain respectively. The equation is expressed in Equation 3.4 with an off axis loading stiffness matrix, $[\bar{Q}_{ij}]$.

$$\begin{bmatrix} \sigma_{XX} \\ \sigma_{YY} \\ \tau_{XY} \end{bmatrix} = \begin{bmatrix} \bar{Q}_{11} & \bar{Q}_{12} & \bar{Q}_{13} \\ \bar{Q}_{21} & \bar{Q}_{22} & \bar{Q}_{23} \\ \bar{Q}_{31} & \bar{Q}_{32} & \bar{Q}_{33} \end{bmatrix} \begin{bmatrix} \varepsilon_{XX} \\ \varepsilon_{YY} \\ \gamma_{XY} = 2\varepsilon_{XY} \end{bmatrix} \qquad 3.4$$

This $[\bar{Q}_{ij}]$ is related to $[Q_{ij}]$ by a transformation matrix, $[T]$ where $c = \cos \propto$ and $s = \sin \propto$ as shown in Eq. 3.5 and 3.6.

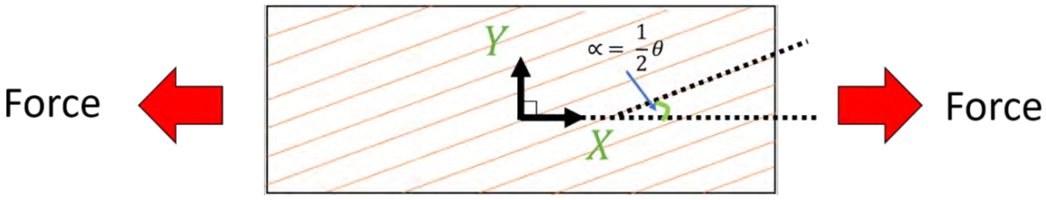

Figure 3.10: A layer of highly aligned fibrous assembly loaded in the ***X*** direction.

$$[\bar{Q}_{ij}] = [T][Q_{ij}][T]^{Transpose} \tag{3.5}$$

$$T = \begin{bmatrix} c^2 & s^2 & -2sc \\ s^2 & c^2 & 2sc \\ sc & -sc & c^2 - s^2 \end{bmatrix} \tag{3.6}$$

Finally, since the thicknesses of the two layers highly aligned fibrous assemblies are the same, the stiffness matrix of the woven fibrous assembly loaded in the X direction, $[\bar{Q}_{ij}]_{woven}$ is contributed equally by the stiffness matrices of the two layers of highly aligned fibrous assemblies and can be calculated based on Eq. 3.7. An illustration is provided in Figure 3.11. Consequently, by considering only the uniaxial extension along the X direction, the apparent Poisson's ratio and initial longitudinal moduli can be computed by using Equation 3.8 and 3.9 respectively.

$$[\bar{Q}_{ij}]_{woven} = \frac{1}{2}\left([\bar{Q}_{ij}]_{1^{st}\ layer} + [\bar{Q}_{ij}]_{2^{nd}\ layer}\right) \tag{3.7}$$

$$v_{XY} = -\frac{\varepsilon_{YY}}{\varepsilon_{XX}} = \frac{\bar{Q}_{12_{woven}}}{\bar{Q}_{22_{woven}}} \tag{3.8}$$

$$E_X = \bar{Q}_{11_{woven}} - \frac{\bar{Q}_{12_{woven}}{}^2}{\bar{Q}_{22_{woven}}} \tag{3.9}$$

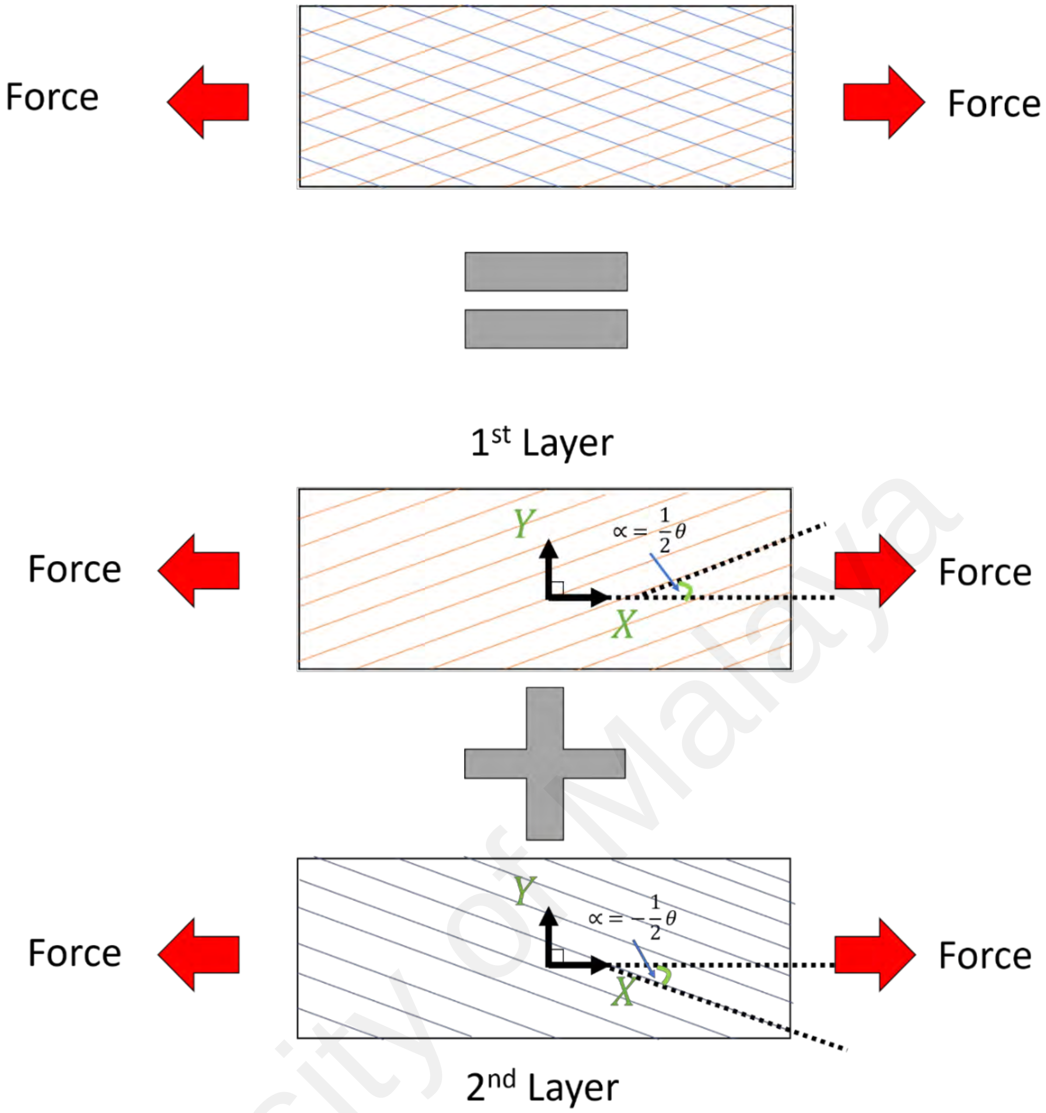

Figure 3.11: Two layers of highly aligned fibrous assemblies contributed equally to the elasticity of the woven fibrous assemblies.

CHAPTER 4: RESULTS & DISCUSSION

This chapter will discuss the result obtained from the morphology and mechanical characterisations of the fabricated fibres.

4.1 Spinning of Fibres

4.1.1 Properties of the Polymer Solutions

The viscosities and electrical conductivities of the polyurethane solutions with different concentrations and solvent ratios are as shown in Table 4.1.

Table 4.1: Viscosities and electrical conductivities of the polymer solutions.

Solution	Solvent Ratio (DMF:THF)	Polymer Concentration (wt %)	Viscosity (Pa.s)	Electrical Conductivity (μScm^{-1})
DMF	1:0	0	0.71	4.650
THF	0:1	0	0.37	0.029
THF and DMF	1:1	0	0.50	1.481
A	1:0	10	1.50	1.822
B	1:0	15	8.16	1.550
C	1:1	15	8.20	1.380

With reference to Table 4.1, the viscosity of the polyurethane solution is highly dependent on the concentration of the solution. An obvious increase in the viscosity of the polyurethane solution from 1.50 to 8.16 Pa.s is measured when the solution concentration increases just from 10 to 15 wt %. The solvent used in the solution does not affect much in the viscosity. Solution B and C with the same concentration are having similar viscosity, 8.16 and 8.20 Pa.s respectively despite having different solvent ratios.

Although having not much effects in the viscosity of the solution, the solvent ratio seems to affect the electrical conductivity of the solution. Solution C has lower electrical conductivity than Solution B as the THF in Solution C is having lower electrical conductivity than DMF. Besides solvent ratio, the electrical conductivity of the polymer solution seems to be affected by the polymer concentration as well. Solution B with higher polymer concentration, 15 % are having lower electrical conductivity than Solution A with lower polymer concentration, 10 % despite having the same solvent ratio.

4.1.2 Surface Analysis of Electrospun Fibres

All the electrospun samples are in the form of mat or film made up of assemblies of fibres. The main characteristics of all the electrospun samples can be summarized in Table 4.2, while Figure 4.1 shows the representative SEM micrographs of 5 electrospun samples.

Table 4.2: Surface morphology, structure and alignment of the fibres.

Sample	Alignment of Fibres	Beads on Fibres	Structure of Fibre	Diameter of Fibres (µm)	Variance (%)
PU1	Random	Present	Straight	0.712 ± 0.026	3.65
PU2	Random	Absent	Partially straight and partially coiled	1.915 ± 0.162	8.46
PU3	Partially	Absent	Straight	1.064 ± 0.080	7.52
PU4	Random	Absent	Coiled	1.238 ± 0.014	1.13
PU5	Partially	Absent	Wavy	0.618 ± 0.019	3.07

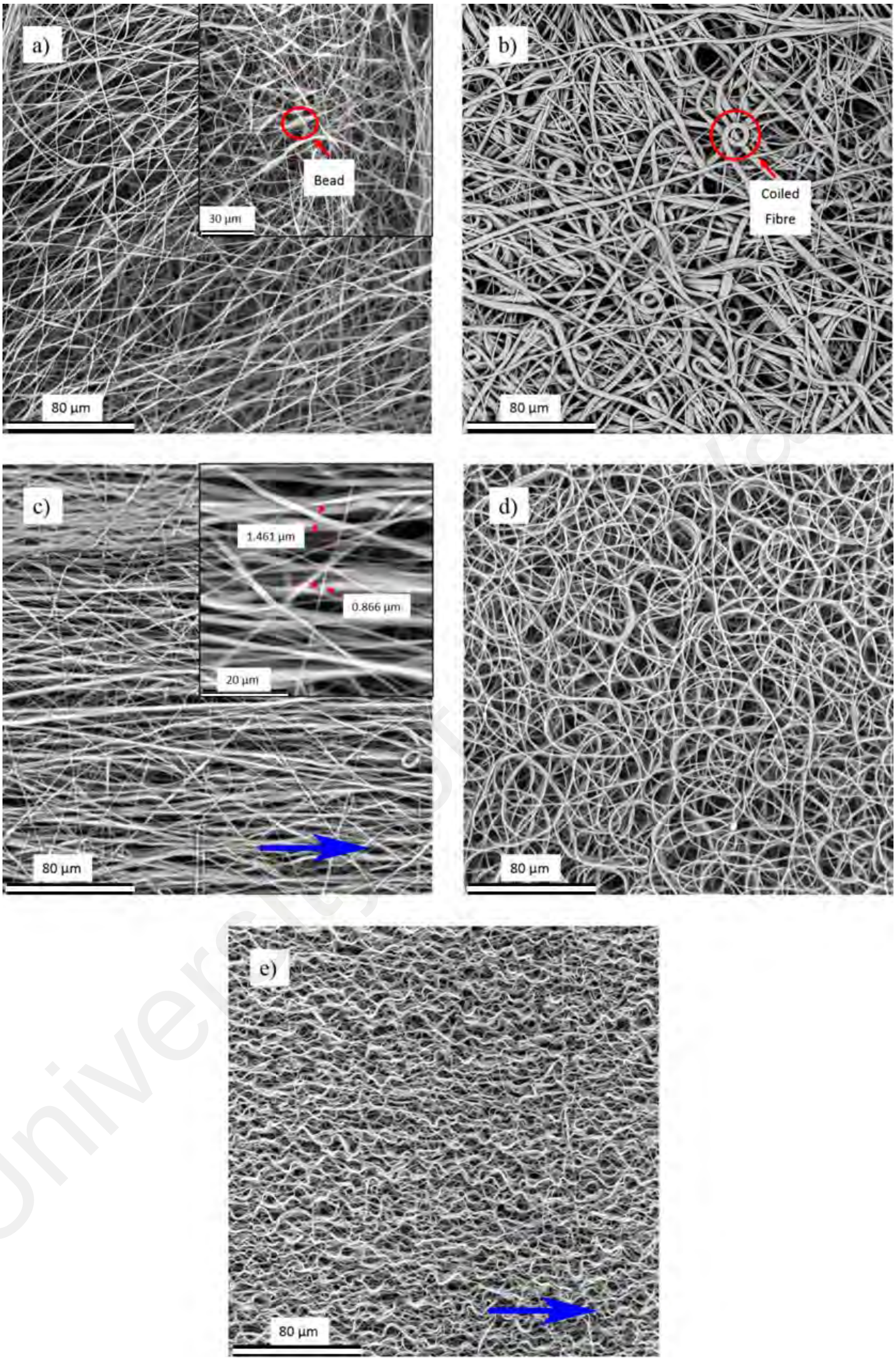

Figure 4.1: SEM micrographs of (a) PU1, (b) PU2, (c) PU3, (d) PU4 and (e) PU5. The features of the fibres are circled in red whereas the blue arrow indicates the circumferential direction of the rotating collector.

4.1.2.1 Orientation of Fibres

Figure 4.2 shows the orientation distribution curves of the electrospun fibres. PU1, PU2 and PU4 fabricated using stationary collector have very small or no peak in the orientation distribution curves, indicating the random orientation of the fibres similar to the study of Wong et al. (Wong et al., 2016).

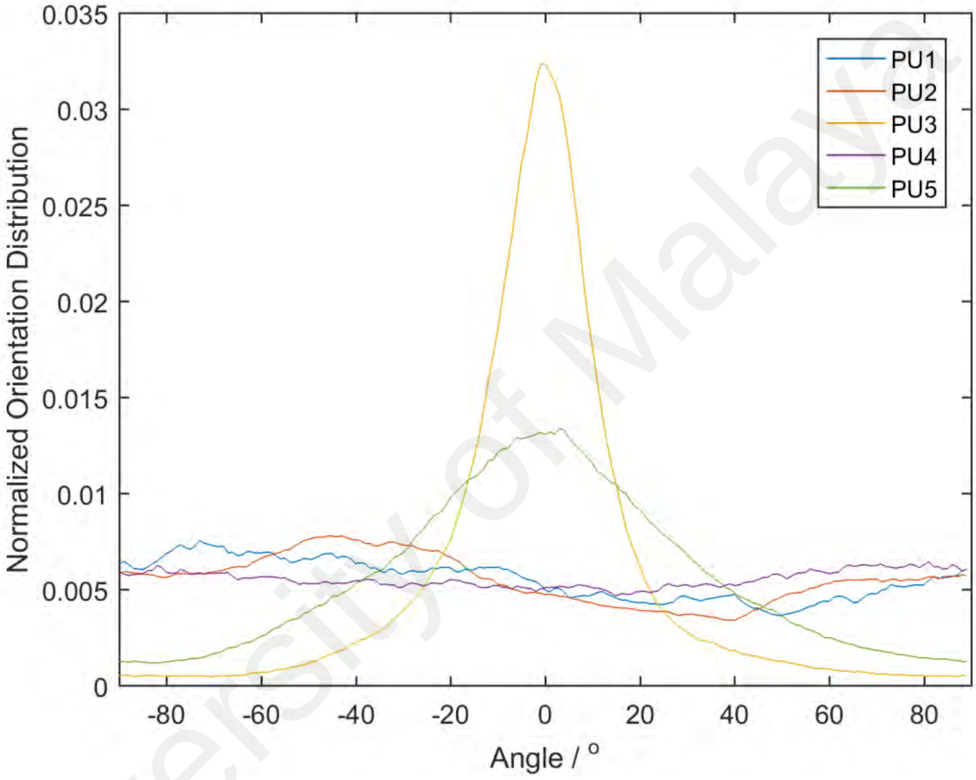

Figure 4.2: Orientation distribution curves of fibres in electrospun samples.

An obvious peak can be observed in the orientation distribution curves of PU3 and PU5 at around 0^{o} angle, which corresponds to the horizontal direction of the micrographs indicated by the blue arrow in Figure 4.1 (c, e). The fibres are partially oriented in the horizontal direction as shown in Figure 4.1 (c, e). This is due to the usage of high speed rotating collector in electrospinning (Al-Ajrah et al., 2018; Maciel et al., 2018; Song et al., 2018). The strong rotational force can drive the fibres to align in the circumferential direction of the rotation indicated by the blue arrow as shown in Figure 4.1 (c, e).

The peak in the orientation distribution curve of PU3 is much sharper than PU5 although both samples are fabricated using the rotational speed of ± 1000 rpm. This is due to the wavy structure of the fibres in PU5 which will be discussed further in the later session. In this fibres orientation analysis by ImageJ software, a straight fibre is considered to be oriented in one direction whereas a wavy fibre is considered to be oriented in more than one direction. Therefore, the peak in the curve of PU5 is not as sharp as PU3 although the overall orientation is similar.

4.1.2.2 Beads on Fibres

If a fibre does not have a uniform diameter along its axis, beads can be observed as shown in the micrograph of PU1 in Figure 4.1 (a). The beads appear to be swollen segments along the axes of fibres. These beads can reduce the cohesions or interactions between fibres in the sample (Huang et al., 2004) and act as stress concentrations during mechanical loadings (Hajiali, Shahgasempour, Naimi-Jamal, & Peirovi, 2011), resulting in poorer mechanical properties.

Low viscosity of the Solution A may be the cause of the beads on the fibres. It is found that solution with low viscosity encourages the formation of the beads (Fong et al., 1999; Gu et al., 2018; Krifa, Hammami, & Wu, 2015; Nezarati et al., 2013). This is due to the insufficient viscoelastic force to overcome the surface tension of the solution jet from the syringe, favouring the formation of larger beads. Thus, by using polyurethane Solution B and C with much higher viscosities, the electrospun fibres do not possess beads.

4.1.2.3 Structure of Fibres

Regarding the structures of fibres, 3 types of structures can be observed: straight, coiled and wavy fibres.

(a) ***Straight Fibres***

The straight fibres in PU1 could be originated from the splaying of the polymer solution jet, where multifilament are split out from a single solution jet (Dhakate et al., 2010; Shin et al., 2001). This splaying of the solution jet is likely to be attributed to the DMF solvent in Solution A as stated in Table 3.1. It is found that DMF can increase the electrical conductivity of a polymer solution along with the reduction of surface tension, thus encourages the splaying of the solution jet (Hsu & Shivkumar, 2004). The split-out fibres are in a straight manner and deposited on the stationary collector as illustrated in Figure 4.3. On the contrary, the straight fibres in PU3 is not originated from the splaying effect mentioned. Instead, it is due to the usage of rotating collector. Without considering the type of collector, PU2 and PU3 have the same solution and processing parameters. Hence, the fibres in PU3 should have the same coiled structures as in PU2. However, the rotating collector stretches the supposedly coiled fibres in PU3 into straight fibres (Kiselev & Rosell-Llompart, 2012; Tong & Wang, 2007; Zhao et al., 2017).

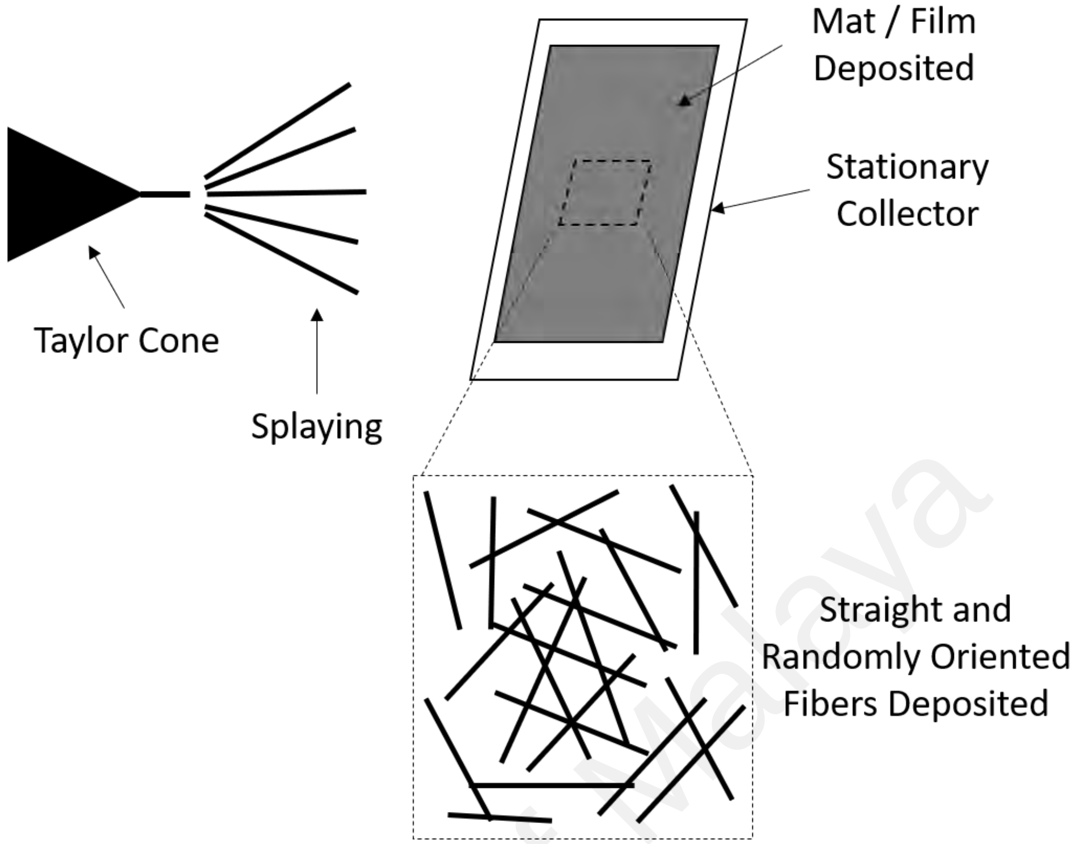

Figure 4.3: Illustration of deposition of straight and randomly oriented fibres on the stationary collector due to the splaying of the solution jet.

(b) ***Coiled Fibres***

Most electrospun fibres are straight (Al-Ajrah et al., 2018; Dhakate et al., 2010; Hajiali et al., 2011; Huang et al., 2004; Maciel et al., 2018; Song et al., 2018; Wang et al., 2009; Wong et al., 2016) and only small traces of coiled fibres can be found in some studies (Lee, Ang, Andriyana, Shariful, & Amalina, 2017; Nezarati et al., 2013; Park & Rutledge, 2018; Tong & Wang, 2007). It is unique to have all coiled fibres in PU4 and high portion of coiled fibres in PU2.

According to a study conducted by Bagchi et al. (Bagchi et al., 2015), this coiled fibres originate from the whipping instability of the polymer solution jet. Whipping instability causes the fibres to travel in a spiral path and deposit as coiled fibres on the collector (Zhao et al., 2017) as illustrated in Figure 4.4. The polymer solution jet travels in a straight path before the chaotic motion of whipping instability starts. In the cases of PU2 and PU4, it is hypothesized that the degree of whipping instability is low, where the straight path is long with very small diameter of spiral motion before reaching the collector. This may be due to the highly viscous Solution B and C as high viscosity solution is found to decrease the degree of chaotic motion in whipping instability (Guerrero, Rivero, Gundabala, Perez-Saborid, & Fernandez-Nieves, 2014).

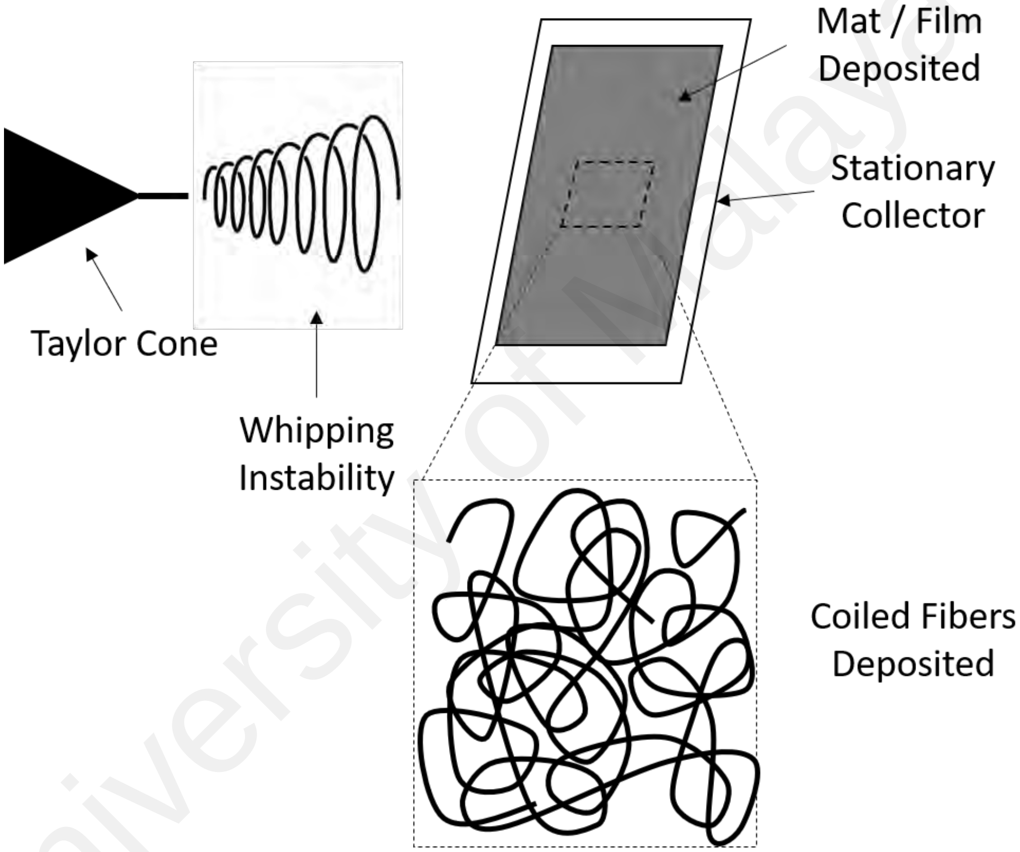

Figure 4.4: Illustration of deposition of coiled fibres on the stationary collector due to the whipping instability of the solution jet.

As shown in Figure 4.5, these coiled fibres tend to stack up to form tower like structures in PU4. The diameter of the spiral motion of polymer jet could be as small as 24.6 µm as evidenced by the diameter of the hollow section of the tower like structure. However, this structure is only observed in certain areas of the sample. It is most likely caused by the disruption of orderly organisation of the fibres due to the repulsions between fibres (Liu & Dzenis, 2008) since electrospun fibres are found to have residual charges (Catalani, Collins, & Jaffe, 2007; Collins, Federici, Imura, & Catalani, 2012). As the stacking of coiled fibres increases, the packing of fibres becomes denser and the accumulation of residual charges increases. To a certain extent, the electrical repulsive force is strong enough to repel the incoming fibres. Thus, stacking is no longer possible. Then, fibres start to scatter all around the surface of collector away from the tower like structures as clear gaps are observed between the tower like structures and scattered fibres.

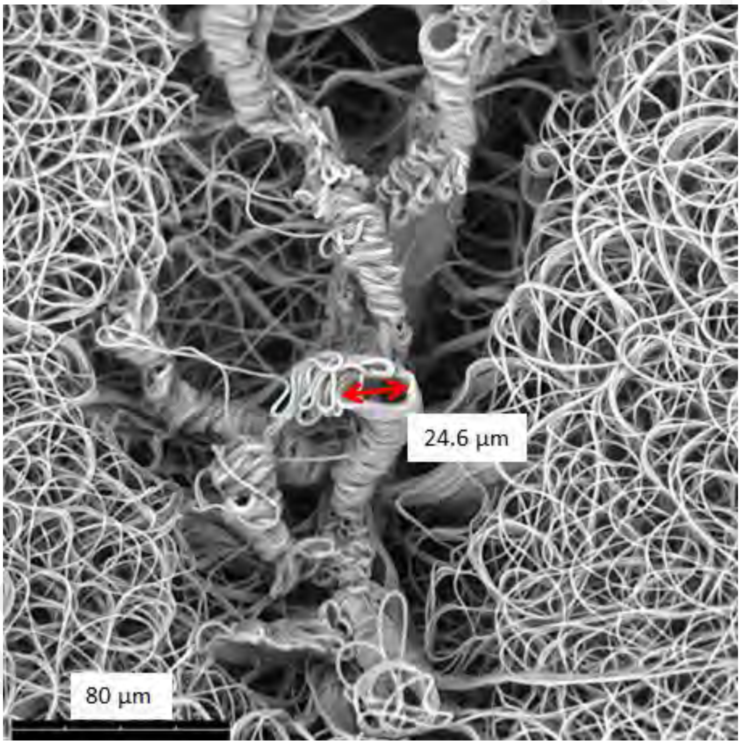

Figure 4.5: Tower like structures in PU4.

(c) ***Wavy Fibres***

Wavy fibres are found in PU5 similar to a study conducted by Kiselev et al. (Kiselev & Rosell-Llompart, 2012) but not in PU3 despite that both samples are actually fabricated using a rotating collector with ± 1000 rpm. However, PU3 is spun using Solution B whereas PU5 is spun using Solution C as stated in Table 3.1. In Solution B, polyurethane is dissolved in DMF only, but polyurethane is dissolved in a mixture of DMF and THF in Solution C. It is known that THF is more volatile than DMF (Erdem et al., 2015; Shawon & Sung, 2004). Hence, Solution C is more volatile than Solution B. The solution jet of Solution C may dry and solidify into fibres earlier than Solution B. As a result, the fibres spun from Solution C may experience greater stretching forces by the rotating collector. Thus, greater contraction maybe experienced by the fibres in PU5 when they are removed from the collector, which manifested into the wavy fibre structure (Liu, Zhang, Xia, & Yang, 2010).

(d) ***Diameter of Fibres***

Based on the micrographs in Figure 4.1, an obvious non-uniformity in the fibre diameters of PU2 and PU3 can be observed in Figure 4.1 (b, c) respectively.

Two fibres in PU3 which have apparent difference in diameters are measured. The diameters are 1.461 and 0.866 μm respectively as shown in Figure 4.1 (c). The reason for this observation is unaccountable.

Observations in Figure 4.1 (b), however, show that coiled fibres have relatively larger diameters than the straight fibres in PU2. Thus, further analysis on the fibre diameters are carried out. 100 diameter measurements are taken from coiled fibres and straight fibres respectively. Coiled fibres have an average diameter of 2.897 ± 0.16 μm, whereas straight fibres have an average diameter of 0.933 ± 0.048 μm. The separate diameter measurements of coiled and straight fibres could not be done on PU3 since the rotating collector stretched the coiled fibres into straight fibres.

As mentioned in the previous session, coiled fibres are due to the whipping instability of polymer solution jet while straight fibres are due to the splaying of polymer solution jet. Both fibres structures present in PU2 indicate that both whipping instability and splaying of polymer solution occurred during the fabrication of this sample. With reference to the diameter measurements of coiled fibres and straight fibres, it can be inferred that the splaying of polymer solution jet can fabricate smaller diameter fibres than the whipping instability of polymer solution jet.

In the literature, high electrical conductivity polymer solutions help in reducing the fibre diameter (Erdem et al., 2015; Jun, Hou, Andreas, Wendorff, & Greiner, 2003) and this reduction in diameter may be due to the splaying of polymer solution jet (Hsu & Shivkumar, 2004) as mentioned in the previous paragraph. The electrical conductivity of the polyurethane solution is in the order of Solution A, B to C from the highest to lowest magnitude as shown in Table 4.1. By using Solution A with the highest electrical conductivity, the fabricated fibres in PU1 are all straight due to splaying of solution jet. Solution B has the intermediate electrical conductivity and therefore, the fabricated fibres in PU2 are partially coiled and straight due to both phenomena. Lastly, Solution C with the lowest electrical conductivity is used to fabricate coiled fibres in PU4 due to the whipping instability of the solution jet.

The average diameters of all the electrospun fibres are tabulated in Table 4.2. In this study, two concentrations of polyurethane solution, 10 and 15 wt % are used for electrospinning. Many studies have reported that electrospun fibres with lower concentration of polymer solution have smaller diameters (Demir et al., 2002; Dhakate et al., 2010; Lee, Ang, et al., 2017; Wong et al., 2016). PU1 is the only sample electrospun from 10 wt % polyurethane solution and it has smaller average diameter than all the samples, except for PU5. This is because PU5 is fabricated using a high speed rotating collector of ± 1000 rpm despite being spun from 15 wt % polyurethane solution. The high rotational speed can stretch the fibres further and therefore, decreases the diameters of the fibres (Kołbuk, Sajkiewicz, Maniura-Weber, & Fortunato, 2013; Meng, Wang, et al., 2010). Electrospun fibres using rotating collector in PU3 shows 44.4 % of reduction in average diameter as compared to the electrospun fibres in PU2 using stationary collector although the other processing and solution parameters are the same. Similar reduction in average diameter of fibres can also be observed between PU5 and PU4, where the reduction is 50.1 %.

4.1.3 Dry Spinning

The idea of Kiselev et al. (Kiselev & Rosell-Llompart, 2012) is adapted in this study. It is proposed that the polymer solution jet should travel in a straight path to reach the rotating collector, so that the fibres fabricated would align following the rotation.

Parameters optimization on the electrospinning set up in this study is conducted to drive the polymer solution jet to travel in a linear manner before depositing onto the rotating collector. Consequently, the splaying in electrospinning is successfully eliminated and the whipping instability is reduced to a minimum extent through the parameter optimization. However, only partial alignment can be observed in PU3 and PU5 as shown in Figure 4.2.

Due to the difficulties to completely eliminate the whipping instability in electrospinning due to the high voltage application, a dry spinning technique is opted to fabricate highly aligned polyurethane fibres in this study. The polymer solution jet can travel in the straight manner to reach the rotating collector without the application of high voltage as illustrated in Figure 4.6. Nonetheless, the dry spun fibres are in bundles, unlike the electrospun fibres, are in mats.

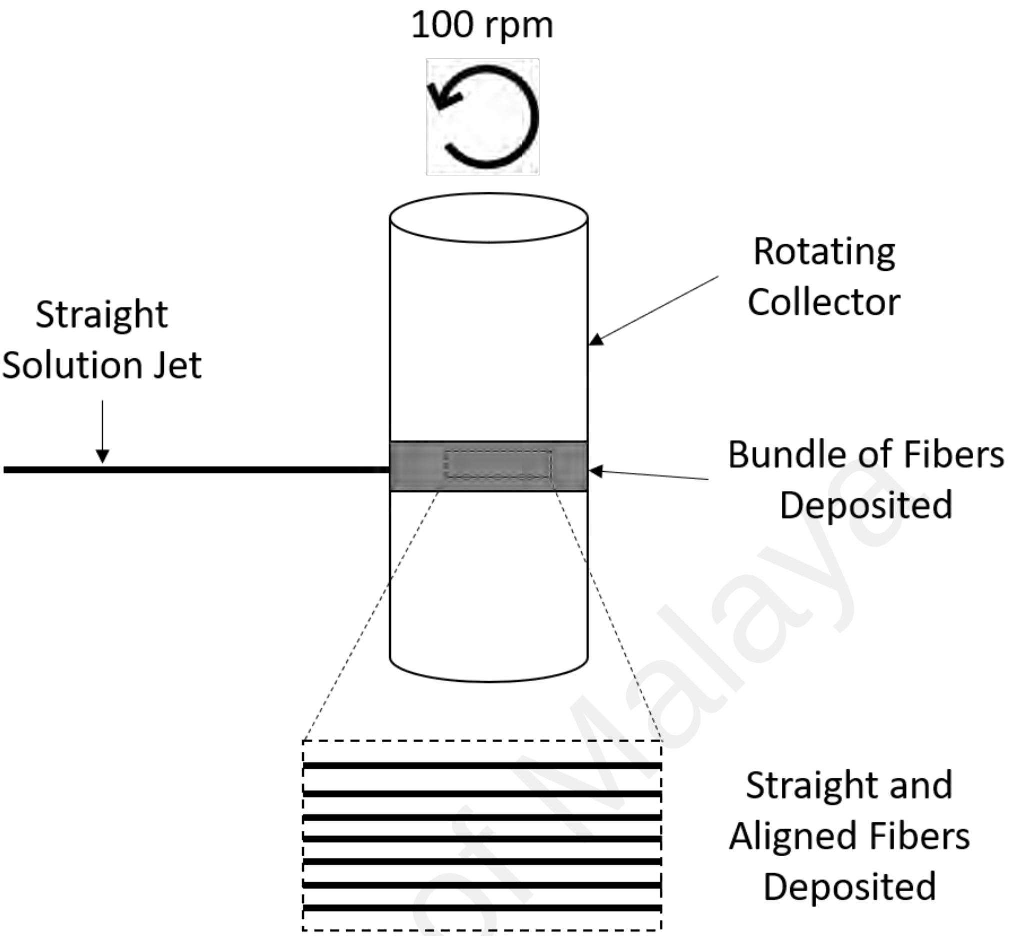

Figure 4.6: Illustration of deposition of straight and aligned fibres on the rotating collector as the solution jet is travelling in a straight manner.

4.1.3.1 Surface Analysis of Dry Spun Fibres

(a) ***Highly Aligned Fibrous Assemblies***

The micrographs of dry spun samples, PU6, PU7, PU8 and PU9 are as shown in Figure 4.7. All the samples have the similar topology. The observed fibres are without beads, highly aligned, and uniform in diameters. Although these fibres are dry spun, the three characteristics mentioned are ideal for electrospun fibres as described by Raghavan et al. (Raghavan et al., 2012).

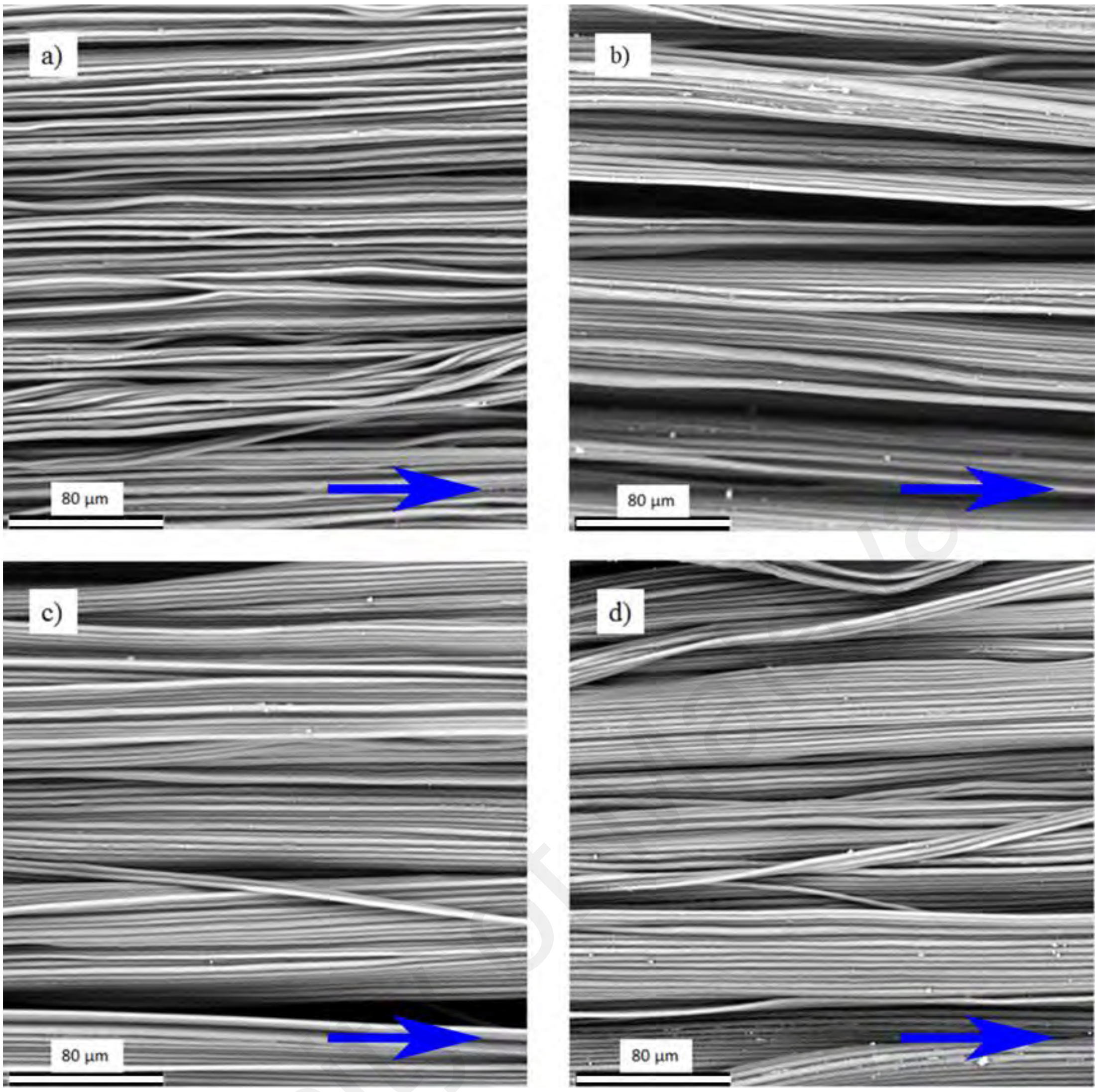

Figure 4.7: SEM micrographs of (a) PU6, (b) PU7, (c) PU8 and (d) PU9 where the blue arrows correspond to the circumferential direction of the rotating collector.

(i) Orientation of Fibres

The orientation distribution curves of all the dry spun samples are plotted in Figure 4.8 (a). All the distribution curves show a sharp peak, in line with the observations on the SEM micrographs in Figure 4.7. The blue arrows correspond to the direction of the 0^o angle.

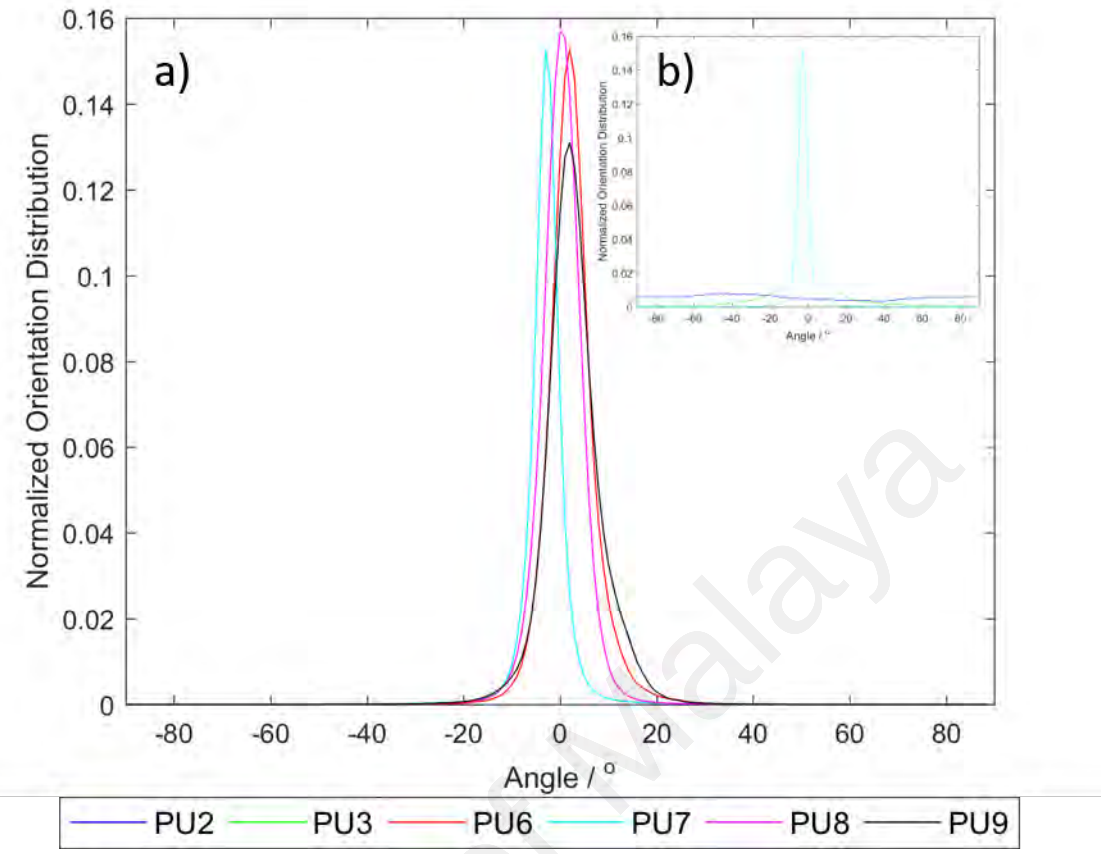

Figure 4.8: Orientation distribution curves of (a) dry spun samples; (b) PU2, PU3 and PU7.

Orientation distribution curves of PU2, PU3 and PU7, corresponding to not aligned, partial aligned and highly aligned fibres are plotted in Figure 4.8 (b) for comparison purpose. The orientation distribution curve of PU7 is a representative of all the dry spun fibres as the orientation distributions are similar as shown in Figure 4.8 (a). It is obvious that dry spun fibres have the sharpest peak and thus, the fibres are highly aligned as compared to the electrospun fibres in this study.

(ii) Diameter of Fibres

The average diameters of the dry spun fibres range from 2.620 to 2.799 µm are much larger as compared to the electrospun fibres, which range from 0.618 to 1.915 µm. Nevertheless, the diameters of these dry spun fibres still fall into the range of the diameters fabricated through electrospinning which is ranged from nanometre to micrometre (Silva, Vistulo de Abreu, & Godinho, 2017).

Despite the application of 0 to 5 kV voltage during the dry spinning process respectively, the diameters of the fibres do not change much as shown in Figure 4.9. It is common that the diameter of fibres changes with the change in the applied voltage during electrospinning (Lee, Ang, et al., 2017; Raghavan et al., 2012; Shawon & Sung, 2004). Apparently, the applied voltages in this dry spinning are too low to have significant effects on the diameter of the fibres.

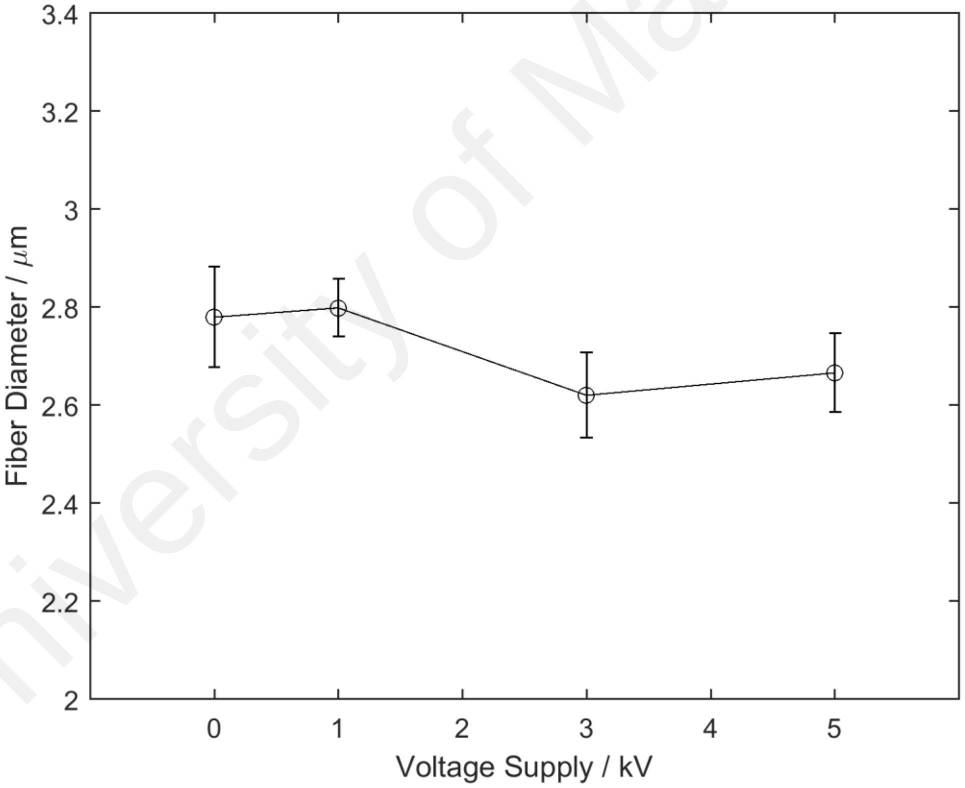

Figure 4.9: Variation of the fibre diameter with the applied voltage.

(b) ***Woven Fibrous Assemblies***

The SEM micrographs of the six woven fibrous assemblies are as shown in Figure 4.10. All the fibres in the assemblies are smooth in morphology without beads identical to the fibres in the highly aligned dry spun fibres as shown in Figure 4.7.

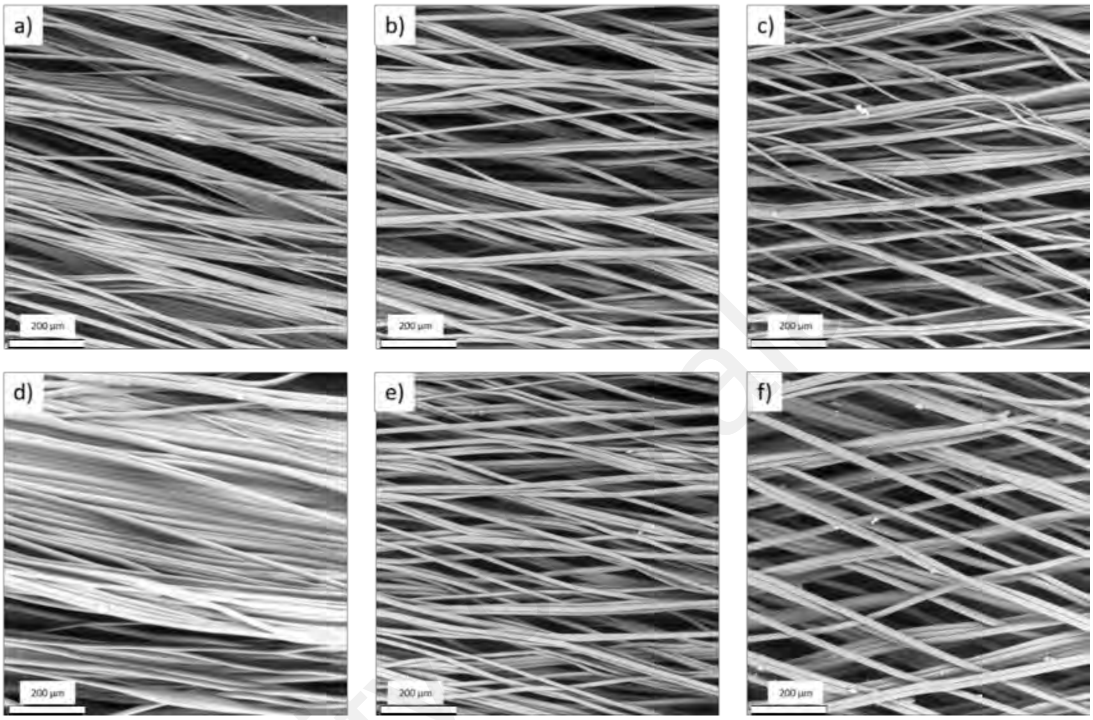

Figure 4.10: The SEM micrographs of a) PU10, b) PU11, c) PU12, d) PU13, e) PU14 and f) PU15 with scale bars corresponds to 200 μm.

Further analyses are conducted on the SEM micrographs to evaluate the diameters and the woven angles of the fibres in the six woven fibrous assemblies. The results are tabulated in Table 4.3. With reference to the Table 4.3, it is obvious that these woven fibres have much larger diameter than the highly aligned fibres in PU7 with the average diameter of 2.80 μm as shown in Figure 4.9. This is because in fabricating the PU7, higher tip to collector distance, 15 cm and rotational speed, 100 rpm are applied as shown in Table 3.3, thus the fibres stretch to lower diameters. However, in the view to have a better control in the woven angle and reduce the stress softening effect during the fibres spinning process due to excessive stretching which will be discussed further in the later section, the tip to collector distance is reduced to 2.5 cm and the rotational speed is reduced to 2 rpm. As a result, fibres assemblies with different woven angles of 0°, 16° and 26° are successfully fabricated with the expense of larger fibre's diameters as shown in Table 4.3. Another inference can be made that the higher the solution injection rate, the larger the diameters of fibres. By changing the solution injection rate from 0.03 to 0.05 mlhr^{-1}, the diameters of the fibres change from approximately 8 to 15 μm according to Table 4.3.

Table 4.3: Average diameters and woven angles of the fibrous assemblies.

Sample	Solution Injection Rate (mlhr^{-1})	Average Diameter (μm)	Reciprocation Speed (mms^{-1})	Average Woven Angle (°)
PU10	0.03	7.85 ± 0.27	0.63	0
PU11		8.39 ± 0.31	1.25	16
PU12		8.35 ± 0.27	2.50	26
PU13	0.05	15.4 ± 0.4	0.63	0
PU14		14.9 ± 0.4	1.25	16
PU15		15.1 ± 0.4	2.50	26

4.2 Biostability of Highly Aligned Fibrous Assemblies

4.2.1 Physical Characterisations

The most obvious change in the polyurethane fibrous samples after immersing in the SBF is the swollen effect. According to Figure 4.11, the increment in the mass immediately after removing from the SBF bathes of the fibrous samples without any drying is within the range of 100% to 140% regardless of the immersion durations. In other words, the fibres swell more than 1 time of their initial mass after immersing into the SBF bathes due to the absorption of the SBF. As a result, these SBF rich fibrous samples can be favourable sites for the body cells attachment for endothelization purpose.

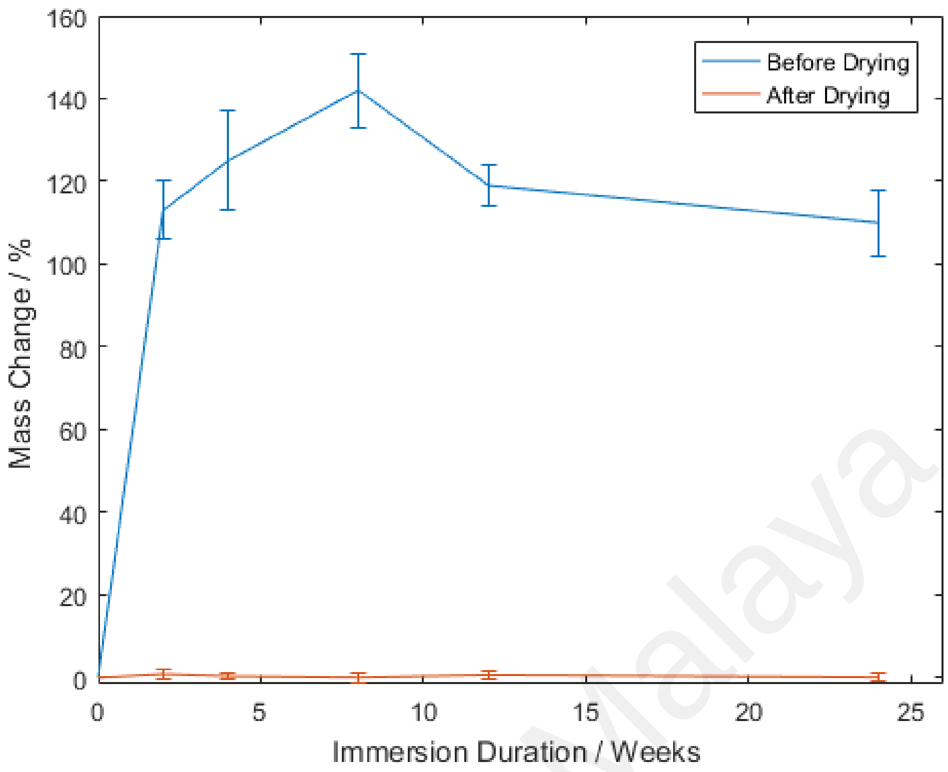

Figure 4.11: Mass change of the highly aligned polyurethane fibres.

In the view of evaluating physical degradation, the amount of mass lost is deemed to be the easiest and the most direct indication in most studies (Breche et al., 2016; Brzeska, Heimowska, Janeczek, Kowalczuk, & Rutkowska, 2014; Żenkiewicz, Richert, Malinowski, & Moraczewski, 2013; Zhou, Yi, Liu, Liu, & Liu, 2009). Normally, the lost in mass is accompanied with the loss of molecular weight, crystallinity and mechanical strength. Along this line, in order to evaluate physical degradation, the mass loss measurement should be conducted after all moistures have been removed from the samples. This is achieved by drying the samples before mass loss measurement. It appears that the mass loss in the polyurethane fibrous samples is negligible, less than 1% regardless of the SBF immersion durations as shown in Figure 4.12 (a) which agrees with the average diameters of the fibres that do not change significantly in the range of 2.66 to 3.24 µm as shown in Figure 4.12 (b). This negligible mass lost may suggest that no observable degradation has occurred. Nevertheless, further tests are needed to verify this suggestion. In this study, the mechanical properties of the polyurethane fibrous samples are evaluated for validation which will be further discussed in the next section.

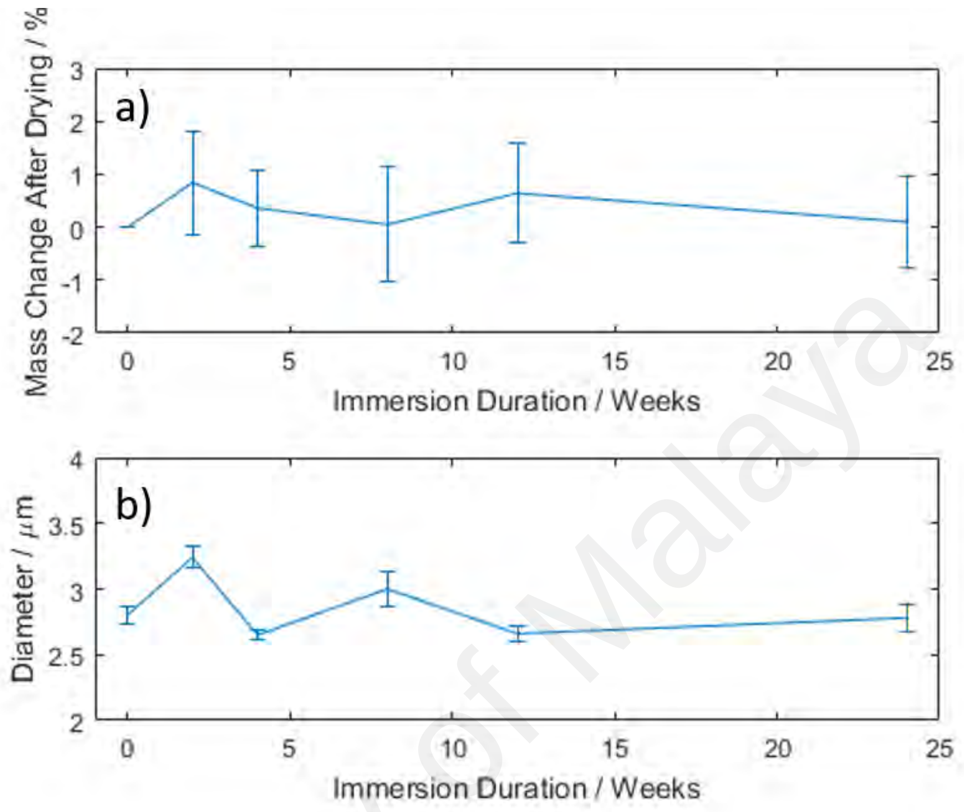

Figure 4.12: (a) Mass change of the highly aligned polyurethane fibres after drying and (b) average diameter of the fibres at different SBF immersion durations.

4.2.2 Mechanical Characterisations

Effects of the moisture on the mechanical properties of polyurethane is noteworthy in the literature (Huang, Yang, An, Li, & Chan, 2005; Yang, Huang, Li, Lee, & Li, 2003; Yang, Huang, Li, & Li, 2006). The glass transition temperature is found to be lowered with moisture trapped inside the microstructure of the polyurethane, which in turn changes the mechanical properties and behaviours of the polyurethane. Despite of that, the effects of moisture are not permanent. The glass transition temperature will return to the initial value after the moistures are removed totally. However, the mechanical properties of the wet samples are undeniably crucial in the operating environment of the vascular grafting.

As discussed in the previous paragraph, the effects of moisture on the mechanical properties of the polyurethane are temporarily which is not in the interest of this study. Instead, the permanent damage to the polyurethane fibrous samples due to the hydrolytic degradation in SBF (Brzeska et al., 2014) is of the interest in this study. Hence, the fibrous samples are dried totally before the mechanical tests and validated using FTIR spectra as shown in Figure 4.16. The peaks of hydroxyl groups in water molecules are not found in the spectra of all the dried fibres which indicates the absence of moisture on or in the fibres.

The initial moduli and ultimate tensile strengths of the polyurethane fibrous samples after different SBF immersion durations are plotted in Figure 4.13. The initial moduli of the polyurethane fibrous samples range from 7.63 to 8.00 MPa, whereas the ultimate tensile strengths range from 6.54 to 6.98 MPa. These ultimate tensile strengths are similar to the longitudinal ultimate tensile strength of Saphenous vein with the average value of 5.38 MPa (Hamedani, Navidbakhsh, & Tafti, 2012). Both the initial moduli and ultimate tensile strengths are having insignificant changes after different SBF immersion durations in agreement with the insignificant mass lost in the fibrous samples as shown in Figure 4.12. It is clear now that there is no observable degradation in terms of mass lost and mechanical properties at the macroscopic level.

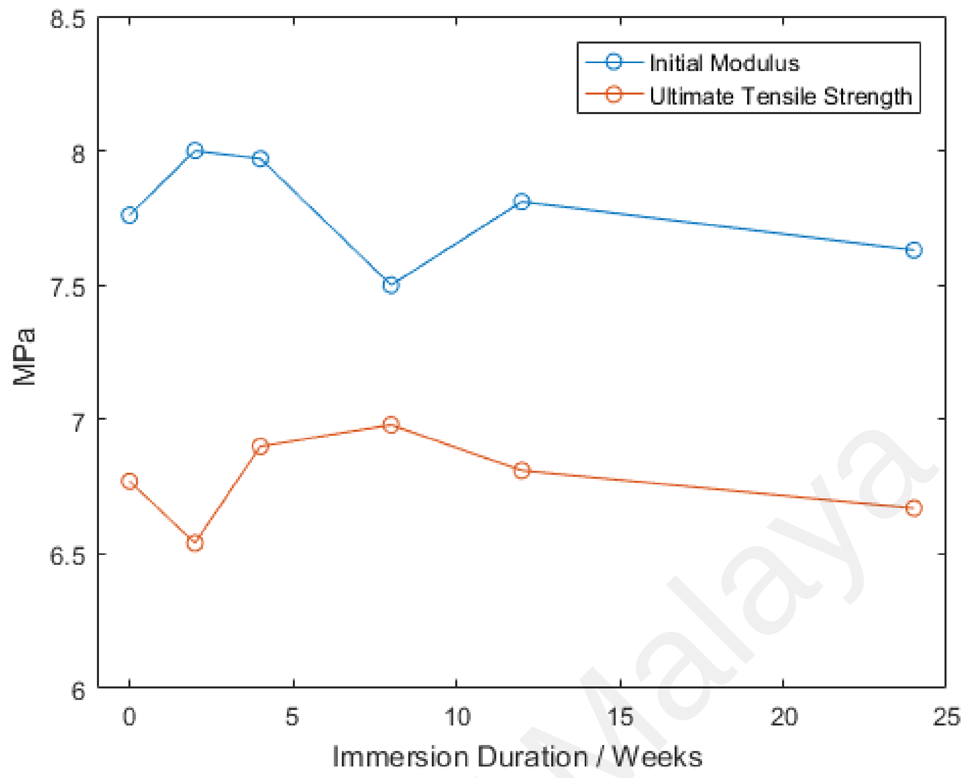

Figure 4.13: Evolution of initial modulus and ultimate tensile strength of the highly aligned polyurethane fibres with the increment in SBF immersion durations.

4.2.3 Chemical Characterisations

4.2.3.1 Simulated Body Fluid (SBF)

The pH value of the SBF is measured after every immersion duration. As a control, the pH value of a SBF sample without polyurethane fibrous sample immersed in it is also measured. The results are plotted in Figure 4.14. It is observed that both the SBF with or without the fibrous samples immersed in them are having similar pH values after every immersion duration. The pH values fluctuate between pH 6 to 7 which are almost neutral. This can be another indication that the polyurethane fibres do not undergo hydrolytic degradation as the process would have released acidic groups into the SBF due to the breakage of ester or urethane bonds causing the pH values to drop (Ruan et al., 2014; Wang et al., 2011).

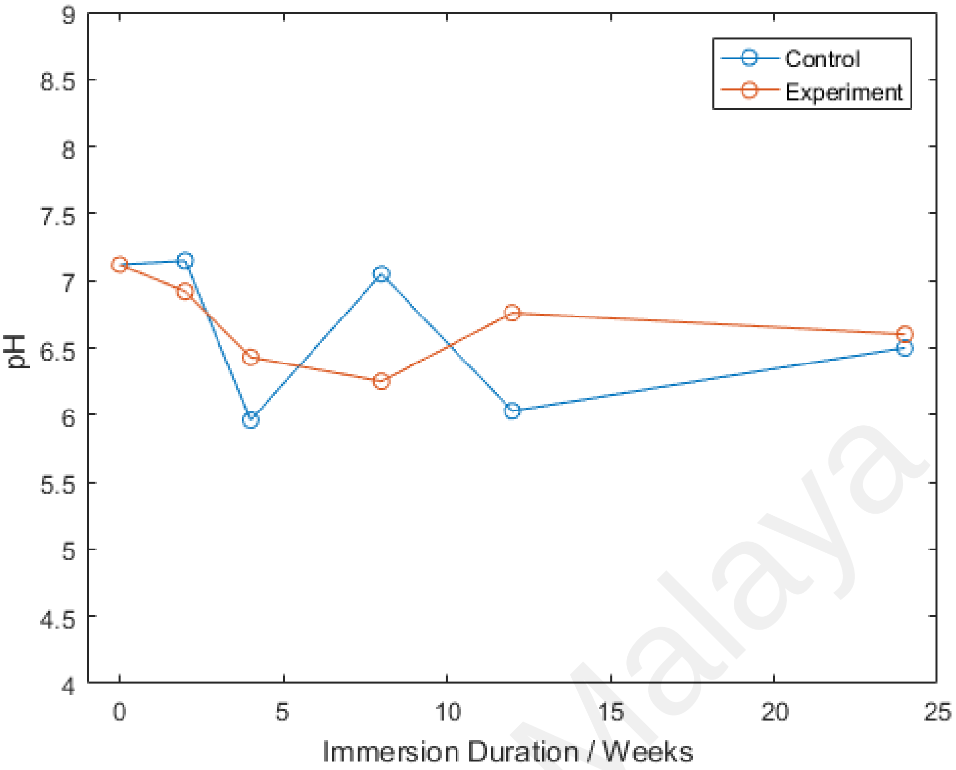

Figure 4.14: pH of the SBF after different immersion durations.

Further analysis on SBF is conducted by using FTIR. The FTIR spectra of the SBF at different immersion durations are as shown in Figure 4.15. There are 3 distinctive peaks can be observed in the spectra at the wavenumbers, 602/604, 1635 and 3335/3337 cm^{-1}. These peaks are corresponding to the hydroxyl bonds in the water molecules (Litvak, Anker, & Cohen, 2018) which consists of more than 90% of the content in the SBF. The difference of 2 cm^{-1} of the peaks with wavenumber 602/604 cm^{-1} and 3335/3337 cm^{-1} is insignificant because it is less than the FTIR scanning resolution, 4 cm^{-1} as stated in the Section 3.3.4. No additional peak is observed in the spectra after every immersion duration which suggests that no degraded products from the polyurethane fibres are found in the SBF.

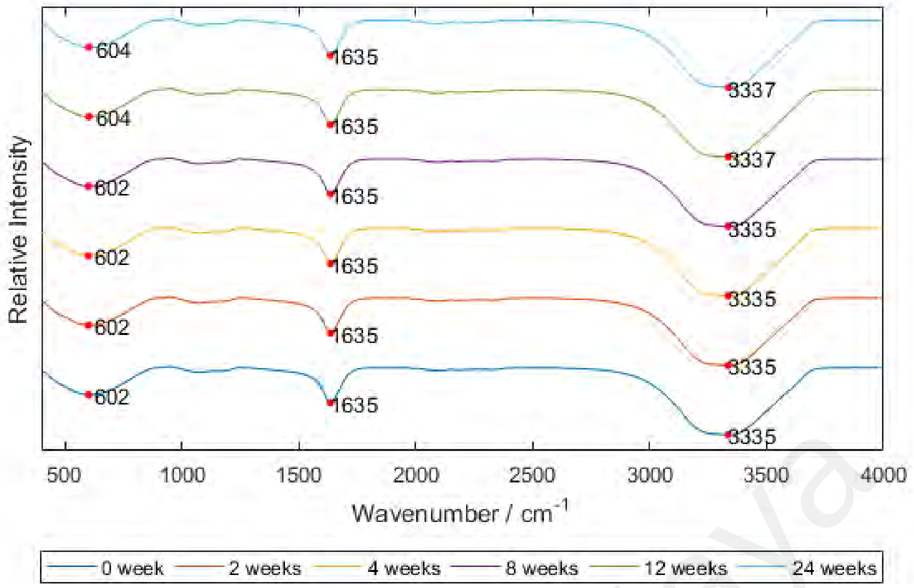

Figure 4.15: FTIR spectra of SBF after different immersion durations.

4.2.3.2 Highly Aligned Polyurethane Fibres

Polyurethane with solvents trapped inside the microstructure is found to have lower modulus (Monaghan & Pethrick, 2012). This external factor may influence the initial moduli in Section 4.2.2 and go against the objective to study the mechanical properties of the polyurethane fibres due to hydrolytic degradation solely. In order to prevent the incomplete drying of the solvent, THF with much higher volatility are mixed with DMF (Erdem et al., 2015; Shawon & Sung, 2004) to spin the fibres in this study. The absence of the residual solvents in the polyurethane fibres is verified by FTIR. Figure 4.16 shows the FTIR spectra of a polyurethane pellet before being processed into fibres and the polyurethane fibres after all the SBF immersion durations. According to Figure 4.16, it can be suggested that there is no residual solvent in the polyurethane fibres as the FTIR spectra of the polyurethane pellet and fibres match each other perfectly without any extra peak that may exist due to the residual DMF or THF solvent.

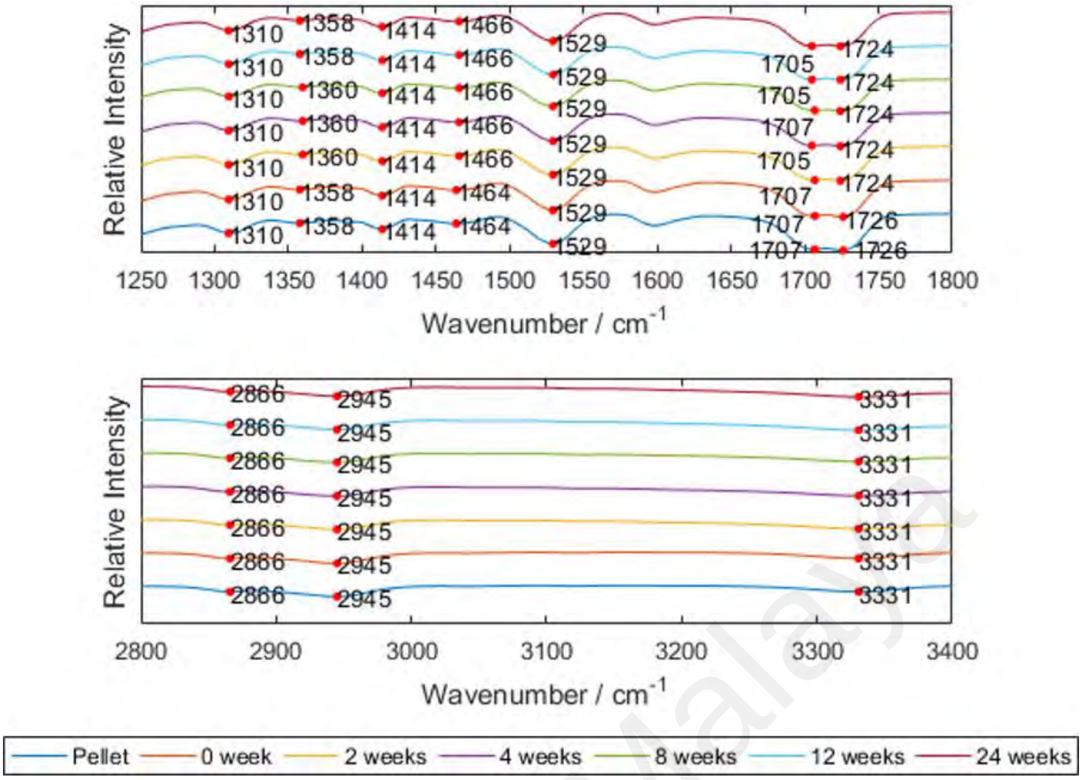

Figure 4.16: FTIR spectra of a polyurethane pellet and the highly aligned polyurethane fibres after different immersion durations.

In the literature, the degradation of the polyurethane is due to breakage of the urethane linkages which correspond to the C=O and NH functional groups. The wavenumbers corresponding to some characteristic peaks of the bonds in polyurethanes are tabulated in Table 4.4. Due to the breakage of the urethane linkages, the intensity of the transmittance peaks corresponds to the C=O and NH groups would become lower than the undegraded polyurethane (Luo, Miao, & Xu, 2011; Sahoo, Kalita, Mohanty, & Nayak, 2018). With the reference to Figure 4.16, the FTIR spectra of the dried polyurethane fibres match each other in terms of intensities and peaks regardless of the immersion durations. This means that the chemical structure of the polyurethane fibres remains intact even after 24 weeks of immersion in the SBF bath.

Table 4.4: Bonds corresponding to the FTIR spectra wavenumbers of the polyurethane (Asefnejad, Khorasani, Behnamghader, Farsadzadeh, & Bonakdar, 2011; Bonakdar et al., 2010; Kurimoto et al., 2000).

Wavenumber / cm^{-1}	Bond
1310	$-CH_2$
1358 / 1360	
1414	
1466 / 1464	
1529	NH
1705 / 1707	H-bond between NH and C=O
1724 / 1726	C=O
2866	$-CH_2$
2945	
3331	NH

4.2.4 Summary

Biostability tests are conducted on the fibres due to the potential of the fibres in the application of vascular grafting. The fibres are immersed in SBF for different durations of 2, 4, 8, 12 and 24 weeks. Then, the biostability of the fibres after immersing in SBF is evaluated from three aspects, physical, mechanical and chemical properties. Physical characterisations show that the mass change and the average diameter change of the fibres are negligible. In term of mechanical properties, the initial modulus and ultimate tensile strength of the fibres are having insignificant changes as well. Lastly, the chemical structures of the fibres also remain intact after immersing in SBF. As a conclusion, the fibres fabricated in this study are biostable even after 24 weeks of immersion in SBF.

4.3 Mechanical Responses

4.3.1 Highly Aligned Fibrous Assemblies

4.3.1.1 Uniaxial Monotonic Tensile Test

Monotonic tensile test with the strain rate of 0.001 s^{-1} was carried out on 8 samples fabricated from different batches of production. The force-displacement curves are presented in Figure 4.17 (a) to study the consistency among different batches of samples. It is observed that the 8 curves do not coincide with each other which suggest that each tensile sample does not contain the same number of fibres, i.e. the mass varies from one sample to another. Nevertheless, their diameters are found to be similar. Consequently, samples with different masses will have different amount of fibres and sustain different magnitude of load although undergoing the same condition of mechanical test.

Using the estimation of sample initial cross-sectional area as detailed in Section 3.4.1.1, the engineering stress-strain curves of 8 samples are plotted in Figure 4.17 (b), showing closer agreement between them. In the following discussion, for the sake of simplicity, the terms “stress” and “strain” refer to “engineering stress” and “engineering strain” respectively.

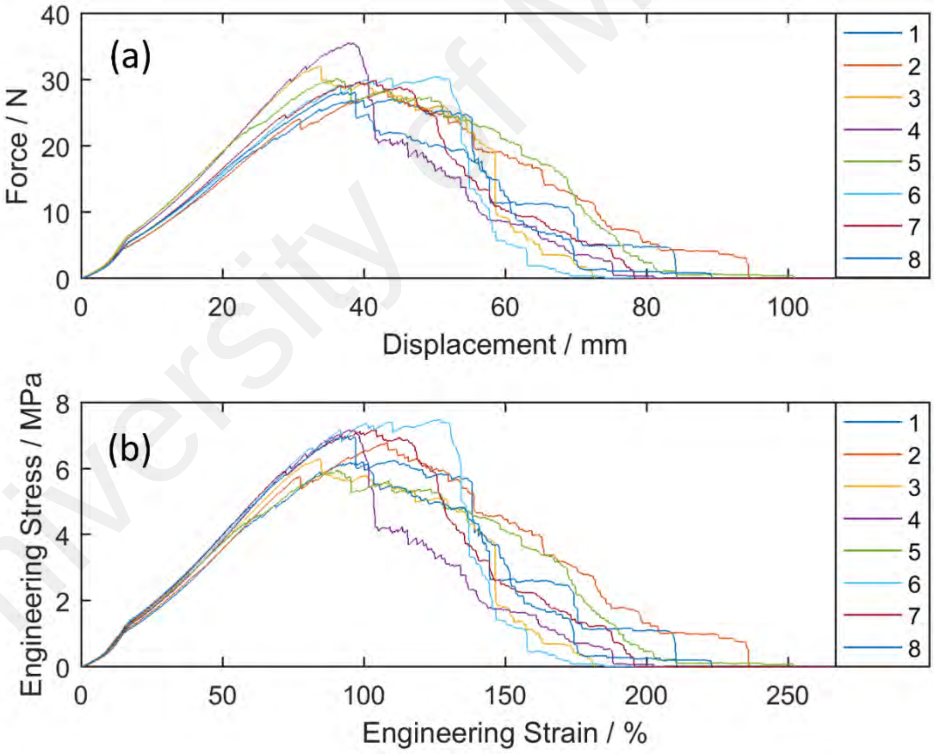

Figure 4.17: (a) Force versus displacement curves of eight samples under monotonic tensile tests; (b) Engineering stress-strain curves of monotonic tensile tests.

According to Figure 4.17, the samples fail or fracture gradually rather than abruptly after reaching the ultimate tensile strength. An illustration of the gradual fracture of the samples is shown in Figure 4.18, transitioning from (a) to (d). Initially, the width of the sample continuously decreases, changing from (a) to (b). After reaching the ultimate tensile strength, the sample starts to fracture bit by bit as shown by (c) and (d). This may be due to the fact that all the fibres in a bundle do not have the same diameter but instead a distribution of diameters as indicated in Figure 4.19 (a). Thus, the fibres fail according to the size of diameter as small diameter fibres can withstand lower load than large diameter fibres. This gradual fibre failure is in line with the work of Wei et al. (Wei, Xia, Wong, & Baji, 2009). The ultimate tensile strength, defined as the highest stress level achieved during the monotonic tensile test, is found to be 6.77 ± 0.17 MPa at the strain rate of 0.001 s^{-1}.

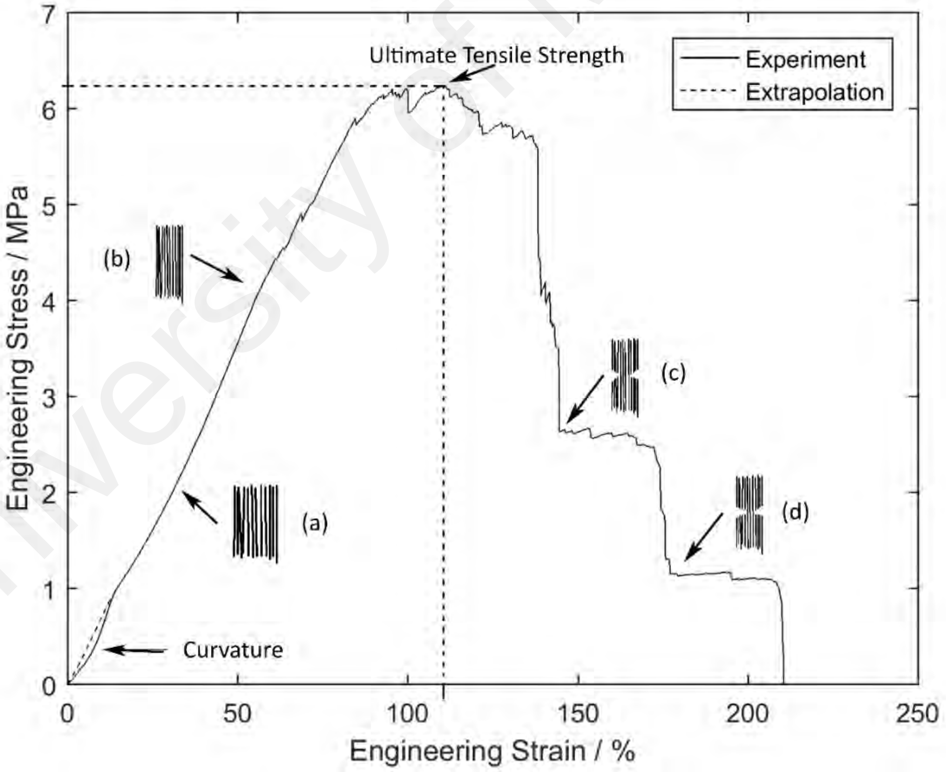

Figure 4.18: Representative engineering stress-strain curve of monotonic tensile tests with extrapolation (in dashed line) at the beginning of the engineering stress-strain curve under monotonic tensile test.

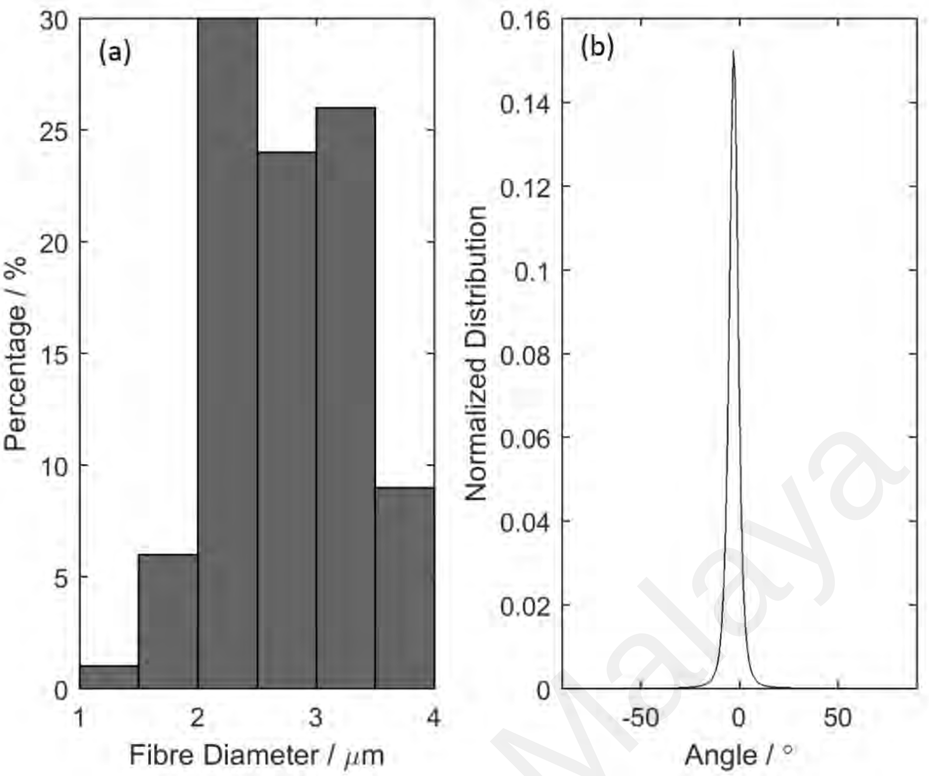

Figure 4.19: (a) Diameter distribution and (b) orientation distribution of polyurethane fibres.

A small curvature at the beginning of every stress-strain curves before the strain of 20 % can be observed and labelled in Figure 4.18. This non-linear phenomenon before the linear stress-strain behaviour of the samples is similar to the crimped collagen fibres in tendons and ligaments (Szczesny et al., 2016). Nevertheless, the nature of this non-linearity or toe region of these crimped collagen fibres is different from the polyurethane fibres in the present study. The toe region of the collagen fibres is originated from the straightening of the fibres (Johnson et al., 1994; Shah, Jayson, & Hampson, 1979). By referring to Figure 4.8, the fabricated polyurethane fibres have straight structure instead of crimp one. In fact, due to the nature of dry spinning process, the fibres are subjected to a pre-stretch during the processing, marked by the shrinkage of the fibres during the removal from the collector. The corresponding pre-stretch yields to a stress-softening in the materials as can be observed during the tensile test. The stress-softening is commonly found in an elastomer (Mullins, 1969; Qi & Boyce, 2005). Extrapolation is done as illustrated in Figure 4.18 (represented by a dashed line in the beginning of stress-strain curve) to compensate for the stress-softening effect. Ignoring the corresponding stress-softening due to pre-stretch during fibre fabrication, the initial modulus is found to be 7.76 ± 0.15 MPa.

The stress-strain curve of polyurethane fibres in Figure 4.18 does not show a sigmoidal shape like a typical elastomer. It is known that sigmoidal shape stress-strain curve of bulk polyurethane will change to nearly linear trend once processed into fibres (Pedicini & Farris, 2003).

Monotonic tensile test with higher strain rate of 0.1 s^{-1} were also conducted. Figure 4.20 shows the representative stress-strain curves taken from two samples for strain rates of 0.001 s^{-1} and 0.1 s^{-1} respectively. It is found that the sample tested with the higher strain rate has higher initial modulus and ultimate tensile strength of 8.15 ± 0.21 MPa and 9.32 ± 0.85 MPa respectively. This finding is similar to a study on a bulk polyurethane by Fan et al. (Fan, Weerheijm, & Sluys, 2015) in which the transition of rubbery to glassy state occurs as the strain rate increases. Another study by Yi et al. (Yi, Boyce, Lee, & Balizer, 2006) shows that polyurethane will mechanically recognise higher glass transition temperature under higher strain rate making it stiffer and stronger.

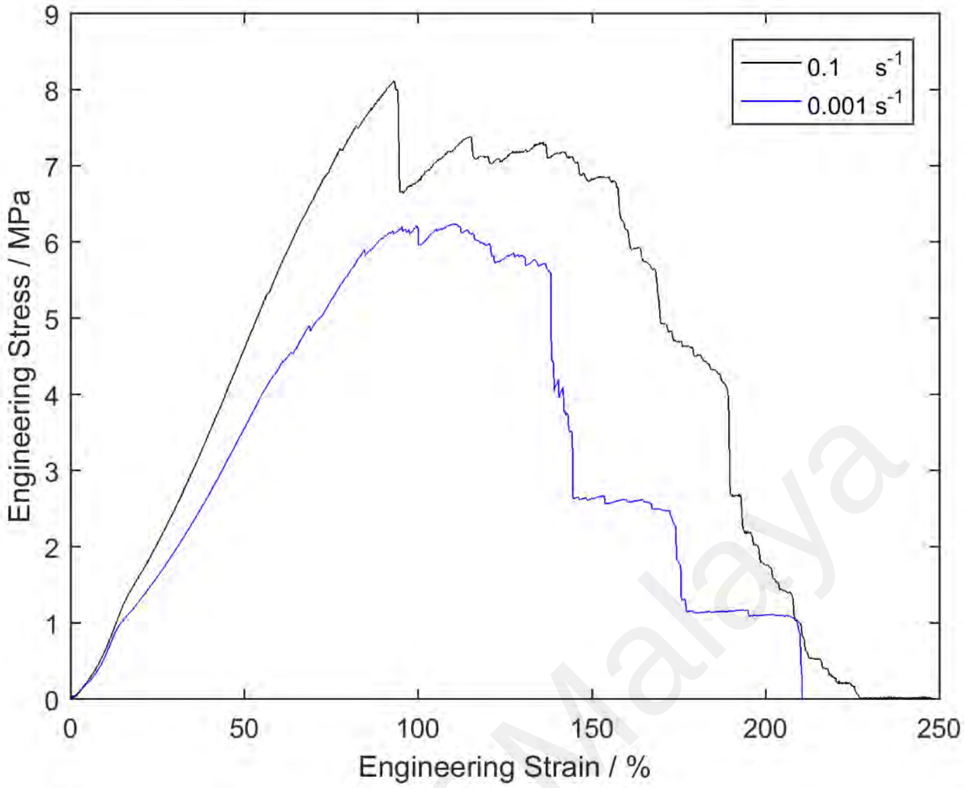

Figure 4.20: Representative engineering stress-strain curves of tensile samples undergoing monotonic tensile at two different strain rates

The mechanical strength of polyurethane is generally attributed to the hard domains of polyurethane (Qi & Boyce, 2005). In our study, the hard domains correspond to the MDI groups. According to Buckley et al. (Buckley, Prisacariu, & Martin, 2010), the tensile moduli of bulk MDI based polyurethanes range from 39.2 MPa to 85.7 MPa at the strain rate of 0.03 s^{-1}, much higher than the initial moduli of the MDI based polyurethane fibres fabricated in this study, which are 7.76 ± 0.15 MPa and 8.15 ± 0.21 MPa at 0.001 s^{-1} and 0.1 s^{-1} respectively. This may be due to the overestimation of the effective cross-sectional area where the porosity within the fibres and the voids between the fibres in the bundles were not explicitly excluded in the measurement of cross-sectional area.

4.3.1.2 Uniaxial Cyclic Tensile Test

Figure 4.21 shows the representative stress-strain curves of materials under cyclic tensile loading at 0.1 s^{-1} and 0.001 s^{-1} strain rates. For each curve, a hypothetical 1st cycle curve is extrapolated to remove the effect of softening due to pre-stretch during processing. Similar to the monotonic tensile test, cyclic tensile tests with higher strain rate yield to stiffer and stronger material responses than those at lower strain rate. Obvious inelastic responses, such as stress-softening, hysteresis, and residual deformation are observed. Another inelastic mechanical behaviour can be observed at the cycles to maximum strain of 40 %. For the same maximum strain, lower maximum stress level is observed at the 2nd cycle than the 1st cycle. This phenomenon is named as permanent stress set (Cheng & Chen, 2003). In the literature, these unique mechanical behaviours of polyurethane are attributed to the microstructural changes during the cyclic test. Indeed, the restructuring of the hard domains is found to impart the inelastic mechanical properties to polyurethane in cyclic mechanical loading (Christenson et al., 2005).

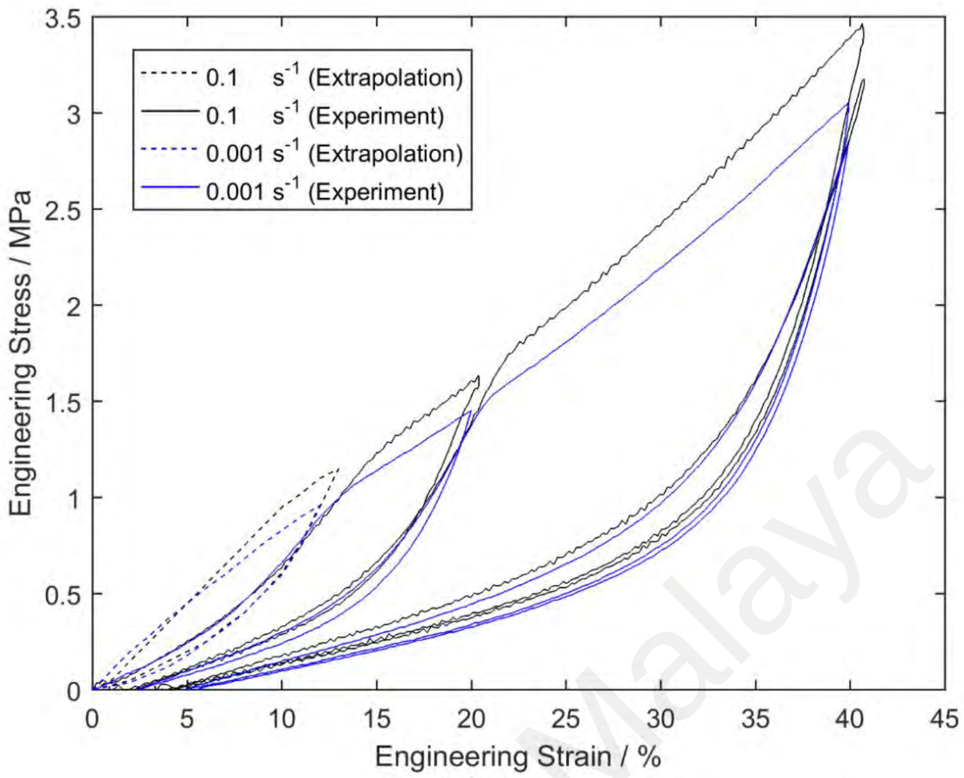

Figure 4.21: Representative engineering stress-strain curves of tensile samples undergoing cyclic tensile test at two different strain rates.

(a) ***Residual Deformation***

During unloading, polyurethane fibres do not completely return to 0 % strain. Instead, they retain certain amount of residual strain after unloading the material to 0 N force during uniaxial cyclic tensile tests. These residual strains are tabulated in Table 4.5. The extrapolated first cycle is assumed to have no residual strain since no experimental data is available as the pre-stretch occurred during the fabrication process before the mechanical test.

Table 4.5: Residual deformation of the samples at different strain rates and maximum strains.

Strain Rate / s^{-1}	Maximum Engineering Strain / %	Residual Deformation / %
0.1	20	1.05 ± 0.12
	40	3.45 ± 0.12
0.001	20	2.61 ± 0.14
	40	5.29 ± 0.27

The results in Table 4.5 suggest that the residual deformation depends on maximum strain and strain-rate. The residual strain increases with the maximum strain and decreases as the strain rate increases. Nonetheless, the residual strain remains almost constant if the loading does not exceed the previous cycle's maximum strain.

(b) ***Hysteresis***

Hysteresis formed when the unloading path does not follow the loading path in a cyclic loading. The cycles in the cyclic test are separated individually for better illustration of hysteresis in Figure 4.22. Polyurethane fibres have significant hysteresis as shown in Figure 4.22 (a)-(c). However, it is noteworthy that the hysteresis is very small if the maximum strain of the cycle does not exceed the maximum strain of the previous cycle as shown in Figure 4.22 (d). Based on Figure 4.22 also, the unloading curves are found to be identical irrespective to the strain rate, consistent with the unloading behaviour found in the compressive cyclic loading of bulk polyurethane (Qi & Boyce, 2005).

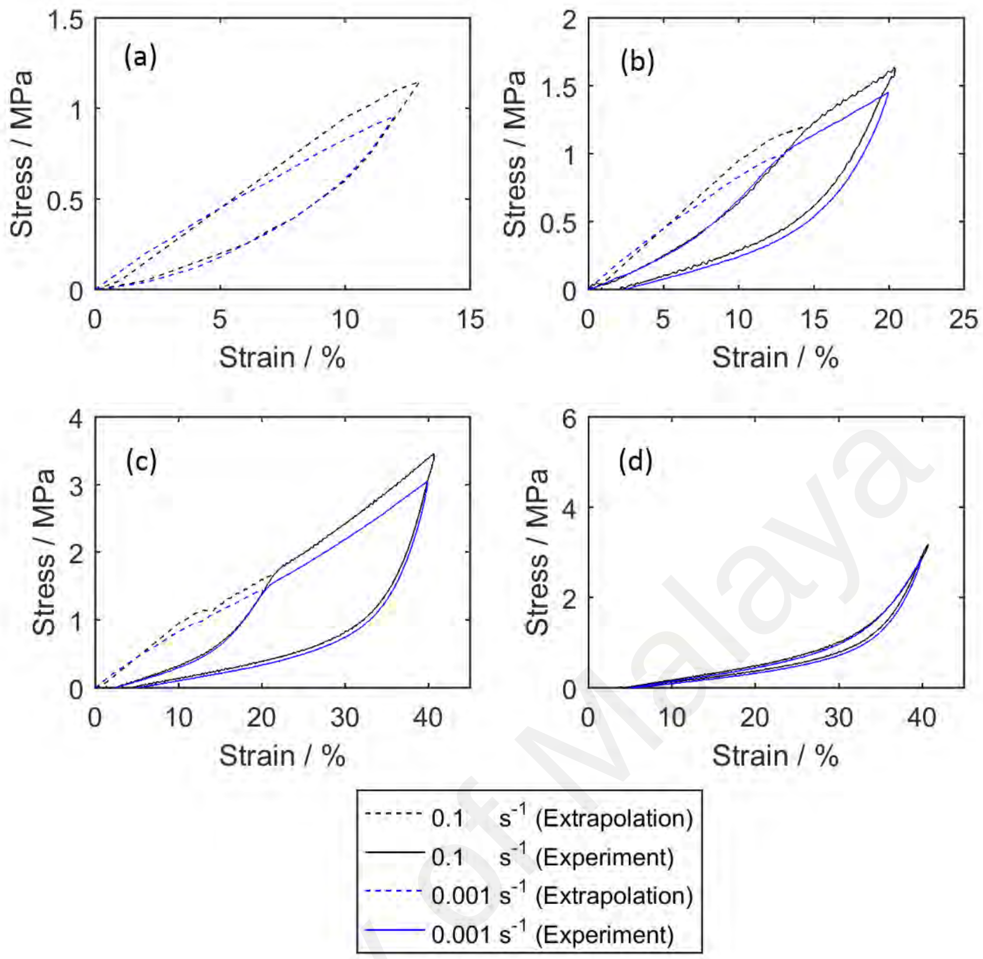

Figure 4.22: Hysteresis of sample under cyclic loading at: (a) hypothetical 1st cycle due to pre-stretch during processing, (b) 1st cycle of 20 % maximum strain, (c) 1st cycle of 40 % maximum strain, (d) 2nd cycle of 40 % maximum strain

The hysteresis loss ratio is calculated following the work of Bergstrom and Boyce (Bergstrom & Boyce, 1998) as shown in Eq. 4.1. It is the ratio of the stabilised hysteresis, H after 5 or more cycles (area of the hysteresis) and the energy supplied during loading, E (area under the loading curve). H and E are represented by the Eq. 4.2 and 4.3 respectively where the loading stress, σ_L and unloading stress, σ_{UL} are functions of strain, ε. and plotted against maximum strain in Figure 4.23.

$$HLR = \frac{H}{E} \qquad 4.1$$

$$H = E + \int_{\varepsilon_2}^{\varepsilon_1} \sigma_{UL}(\varepsilon)\, d\varepsilon \qquad 4.2$$

$$E = \int_{\varepsilon_1}^{\varepsilon_2} \sigma_L(\varepsilon)\, d\varepsilon \qquad 4.3$$

However, only one cycle is considered into the calculation in this study. All cycles are treated as if the stress-softening effect from prior loading is not existed as extrapolated in Figure 4.22 (a)-(c). Generally, the hysteresis and hysteresis lost ratio increase as the maximum strain increases as shown in Figure 4.23. Nevertheless, the hysteresis lost ratio is higher at lower strain rate at any strain, attributed to the similar amount of hysteresis but higher energy supplied during loading. As for the 2nd cycle with same maximum strain with the 1st cycle, 40 %, the hysteresis is considerably small, having low hysteresis loss ratios of 0.221 ± 0.007 at 0.001 s^{-1} and 0.157 ± 0.003 at 0.1 s^{-1} strain rate respectively. In this study, the hysteresis property of this particular polyurethane is opposite to the typical elastomers, such as natural rubber and styrene-butadiene rubber where the hysteresis loss ratio increases with strain rate (Kar & Bhowmick, 1997).

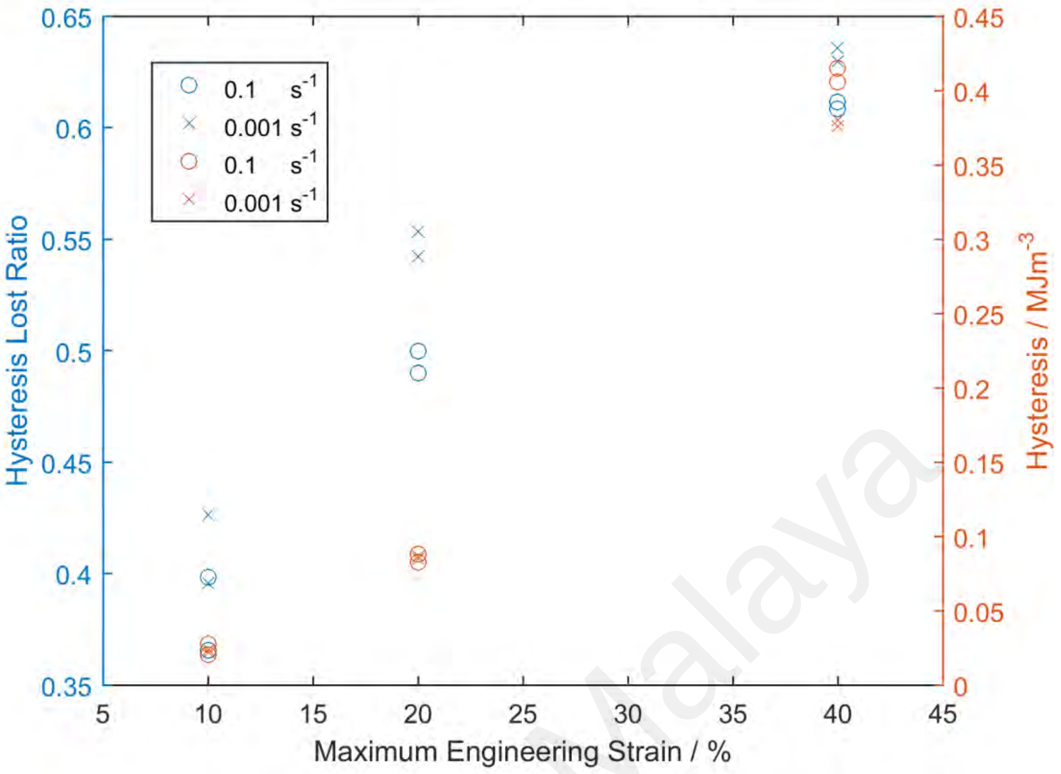

Figure 4.23: Hysteresis lost ratio and hysteresis against maximum engineering strain.

It is observed that almost the same amount of hysteresis at the two strain rates, except for 40 % strain, where the amount of hysteresis is slightly higher at 0.1 s^{-1} strain rate. As for the energy supplied during the loading, it is higher at higher strain rate due to the higher stiffness and strength as shown in Figure 4.20 and 4.21. Mechanical properties of the polyurethane can be altered by changing the chemical formulation and morphology, allowing greater flexibility in hysteresis and other mechanical properties. The amount and shape of hysteresis may vary even from one and another (Yi et al., 2006). This existence of hysteresis is often related to the irreversible damage to the hard domains and weakening of the hydrogen bonds in the microstructure of thermoplastic polyurethane elastomer (Christenson et al., 2005; Gorce, Hellgeth, & Ward, 1993).

(c) ***Stress Softening***

The stress softening of the polyurethane fibres is clearly noticeable after every cycle as shown in Figure 4.22. In order to evaluate the extent of stress-softening, only the loading curves to the same strain are considered as shown in Figure 4.24. The degree of stress-softening is evaluated in two ways: overall and instantaneously. Overall stress-softening is computed by finding the ratio of the difference between supplied energy during the 1st uploading curve and the 2nd uploading curve to the energy supplied during the 1st uploading curve. Energy supplied is defined as the area under the loading curve as shown in Eq. 4.3 previously. As for the instantaneous stress-softening, it is defined as the ratio of the difference between the two stress levels at the 1st and 2nd loading curves to the stress level at the 1st loading curve during every strain level, adopted from the study of Chai et al. (Chai, Andriyana, Verron, & Johan, 2013).

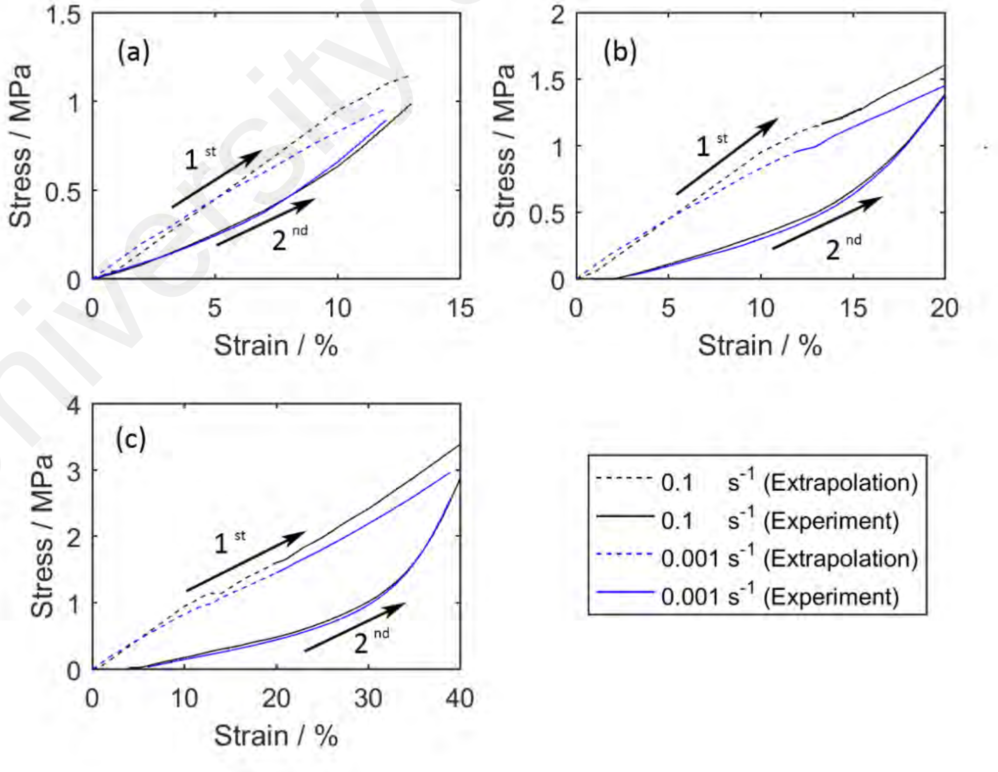

Figure 4.24: 1st and 2nd loading curves at (a) 10 % strain, (b) 20 % strain and (c) 40 % strain.

The overall and instantaneous stress-softening effects are shown in Figure 4.25. In general, the stress-softening appears to be strongly dependent on the maximum strain but nearly independent of the strain rate. Stress-softening in elastomers is often associated to the polymeric chains disentanglement, bond or cross-linking and filler rupture (Bueche, 1960; Diani et al., 2009; Hanson et al., 2005; Kraus, Childers, & Rollmann, 1966). Hard domains and the hydrogen bonding in thermoplastic polyurethane elastomer are analogous to the typical fillers and chemical cross-linking in elastomers respectively (Sui, Baimpas, Dolbnya, Prisacariu, & Korsunsky, 2015). Thus, stress-softening and hysteresis are actually similar in nature since both phenomena in polyurethane fibres are nearly unaffected by strain rate as shown in Figure 4.23 and Figure 4.25.

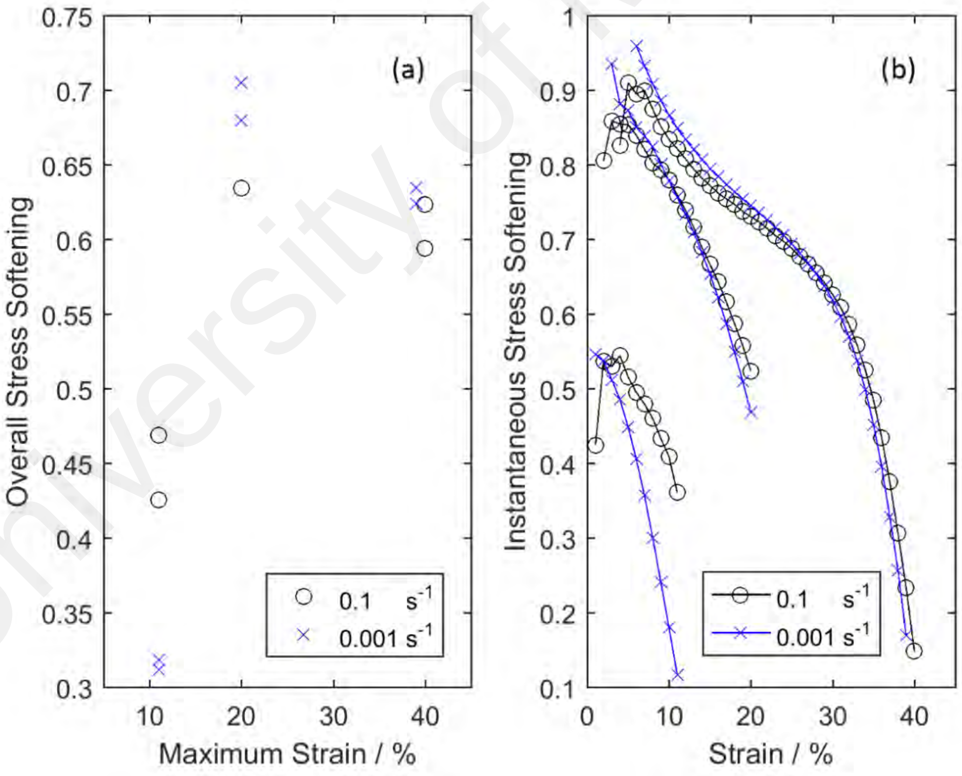

Figure 4.25: (a) Overall and (b) representative instantaneous stress softening at maximum strain level of 10 %, 20 % and 40 % under two different strain rates.

In the case of instantaneous softening, its value is initially high before decreases significantly as the strain approach its maximum independently of strain-rate or maximum strain. This suggests that most instantaneous stress-softening occurs at the beginning of the 2nd uploading. In addition, the rate of instantaneous stress-softening appears to become lower when the maximum strain increases as shown in Figure 4.25 (b). Very distinctive reduction in the instantaneous stress-softening rate along to the maximum strain of approximately 40 % can be seen at the region around strain of 15 % to 30 % strain. As for the maximum strain of approximately 20 %, this region where the reduction of the rate of instantaneous stress softening occurs is still observable but not as obvious as in the case of 40 % maximum strain. Finally, this phenomenon is not observed at 10 % maximum strain.

4.3.1.3 Stress Relaxation Tensile Test

Two steps stress relaxation tensile test was held at 20 % and 40 % strain at 0.1 s^{-1} and 0.001 s^{-1} strain rates respectively for the duration of 3600 s. The representative stress-strain curves from two samples are shown in Figure 4.26 (a). As expected, the sample with higher strain rate shows higher stiffness and strength. During the relaxation, the evolution of normalized stress with respect to the holding duration is also plotted in Figure 4.26 (b). Similarly to the work of Xia et al. (Xia, Song, Zhang, & Richardson, 2007) and Abouzahr and Wilkes (Abouzahr & Wilkes, 1984) on bulk polyurethane, it appears that most stress relaxation happens before the 500 s of holding period, indicated by a steep curvature as shown in Figure 4.26 (b). Sample tested under higher strain rate are further from the relaxation equilibrium path regardless of the holding strain. At lower strain rate, sample with holding strain of 40 % are further from the relaxation equilibrium state than the 20 % holding strain, similar to bulk polyurethane (Abouzahr & Wilkes, 1984). Nonetheless, sample with the higher strain rate is having similar distance from the relaxation equilibrium state independent of holding strain. The holding strain effects on the distance from the equilibrium path seem to diminish at higher strain rate.

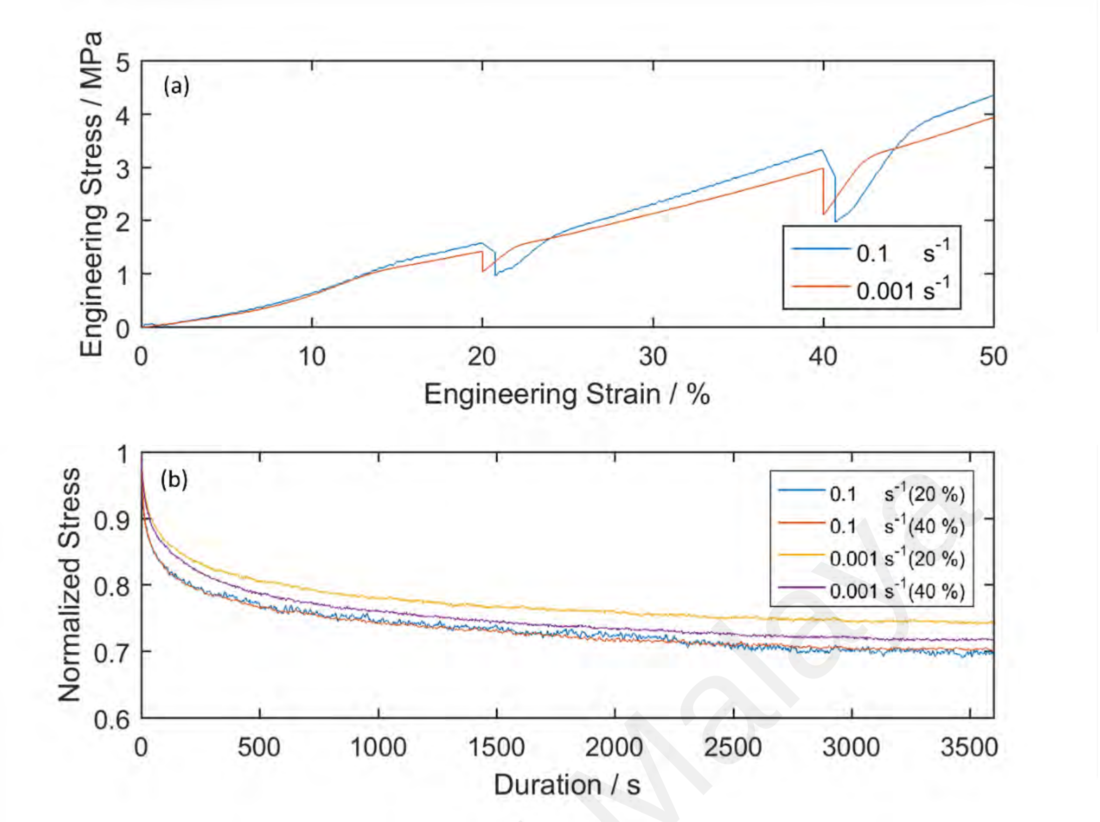

Figure 4.26: Stress relaxation tensile test: Representative (a) engineering stress-strain curve (b) normalized stress against time.

4.3.2 Highly Aligned Fibrous Assemblies with Different Fibre's Diameters

The monotonic engineering stress-strain curves of the woven fibrous assemblies with woven angle, 0° but different average diameters under the strain rates of 0.001 and 0.1s^{-1} respectively are plotted in Figure 4.27. Pedicini and Farris (Pedicini & Farris, 2003) reported that the polyurethane fibres with diameters about 0.5 µm have linear stress-strain responses under monotonic mechanical tensile tests. This linear response is only observed in the fibrous assemblies with the smallest average diameter, 2.80 ± 0.06 µm in this study. The fibrous assemblies with higher average diameters of 7.85 ± 0.27 and 15.4 ± 0.4 µm are showing sigmoidal stress-strain responses like typical elastomers instead of linear responses. It appears that polyurethane fibrous assemblies only show linear stress-strain responses when the fibre's diameters are below a certain threshold value.

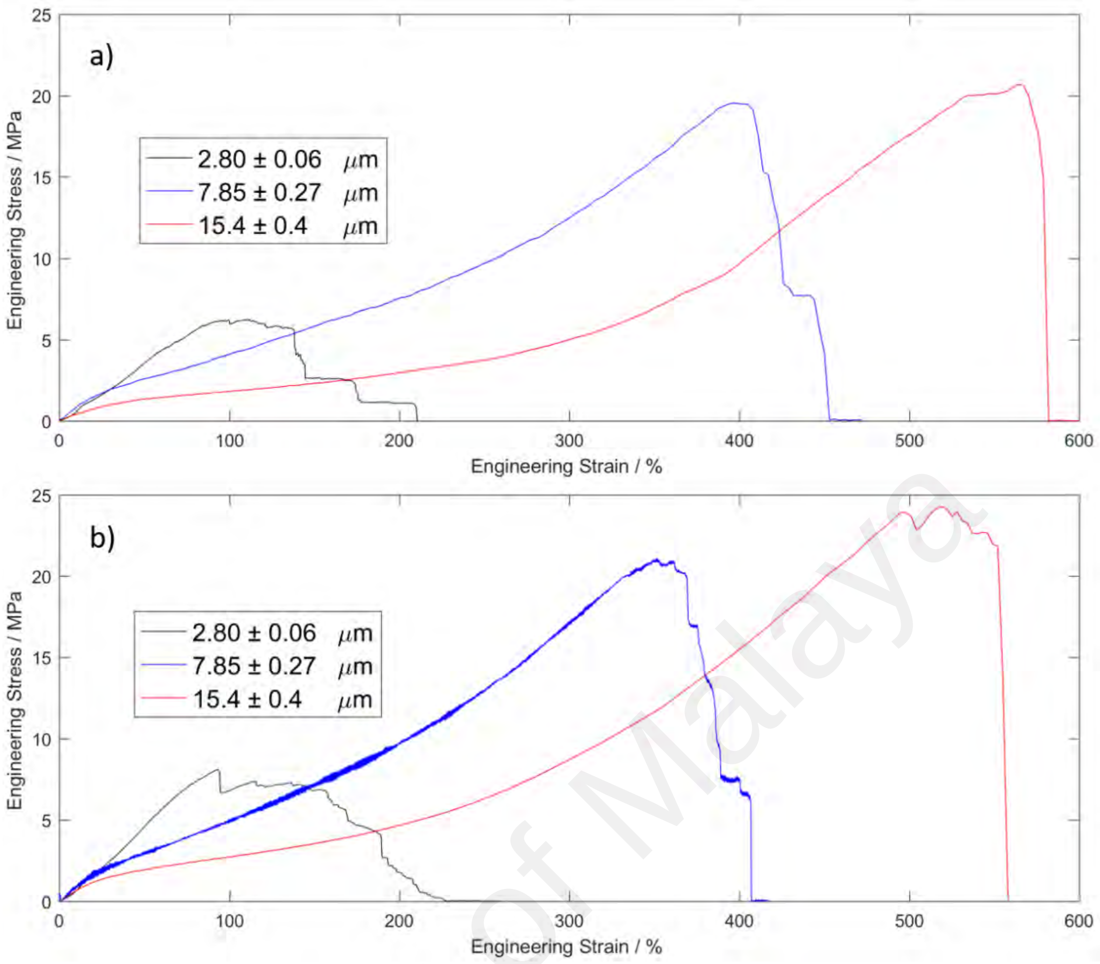

Figure 4.27: Representative monotonic engineering stress-strain curves of the fibrous assemblies with woven angle, 0° under the strain rate a) 0.001 and b) 0.1 s^{-1}.

Depending on the diameter of the fibres, the fibrous assemblies can have different mechanical properties in term of the initial modulus, ultimate tensile strength and elongation at break according to Figure 4.27. The variations of these properties due to different fibre's diameters are shown in the Figure 4.28. It is found that all the fibrous assemblies regardless of fibre's diameters have higher initial moduli and ultimate tensile strengths but lower elongations at break at higher strain rates. This is because polyurethanes can transform from ductile to brittle state at high strain rates as discussed in the Section 4.3.1.1.

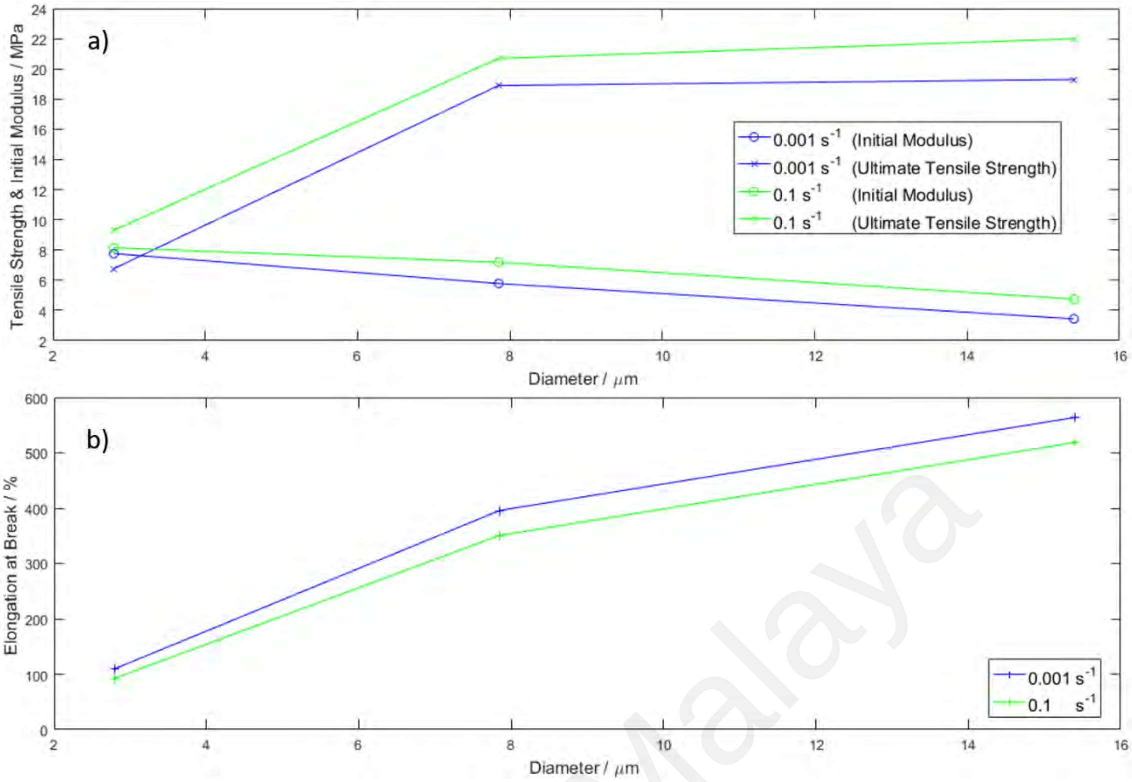

Figure 4.28: Variation of a) initial moduli, ultimate tensile strengths and b) elongations at break due to different fibre's diameters.

The initial modulus is observed to increase as the diameter of the fibres in the assemblies decreases. In the perspective of molecular microstructure, when the polyurethanes are spun into fibres, the soft and hard domains in the polyurethane will align in the fibres axial direction. As the fibres are drawn or stretched to smaller diameters, the alignment of the domains will become greater. In addition, smaller diameters fibres can confine the polymeric chains inside them and thus promoting stronger hydrogen bonding among the hard domains as the chains are closer together. As a result, the alignment of the domains together with the stronger hydrogen bonds among the hard segments can synergistically improve the mechanical properties of the fibrous assemblies (Kaursoin & Agrawal, 2007; Pedicini & Farris, 2003).

Another interesting observation is that the PU10 and PU13 with diameters of 7.85 ± 0.27 and 15.4 ± 0.4 μm respectively are having higher ultimate tensile strengths than the

PU7 with diameters, 2.80 ± 0.06 µm although having lower initial moduli. While the reason for this observation is not known, a study conducted by Pedicini and Farris (Pedicini & Farris, 2003) shows that the bulk polyurethane has a higher tensile strength than the polyurethane fibres with diameters about 0.5 µm. Hence, together with the sigmoidal stress-strain responses as shown in Figure 9 and the higher ultimate tensile strengths of the PU10 and PU13, it is reasonable to believe that polyurethane fibrous assemblies with larger diameters behave similar like the typical bulk elastomers in term of mechanical properties.

In the case of elongations at break, an increment is observed as the diameter of the fibres in the assemblies increases. This is due to the low draw ratio of the fibres during fabrication. Larger diameter fibres which are less drawn during fabrication have more allowances to be elongated or stretched during the tensile mechanical tests and therefore higher elongations at break (Tascan, 2014).

4.3.3 Woven Fibrous Assemblies

4.3.3.1 Uniaxial Monotonic Tensile Test

In this section, the evolution of the mechanical properties of fibrous assemblies due to different woven angles will be discussed. For this study, only the fibrous assemblies with diameters of approximately 8 and 15 µm are considered without the assemblies with diameter approximately 3 µm. This is because the 3 µm diameter fibrous assemblies with different woven angles are not possible to be fabricated by using the dry spinning technique in this study as all the attempts in optimizing the processing parameters to fabricate the fibrous assemblies with different woven angles are unsuccessful.

The stress-strain responses of the woven fibrous assemblies, PU11, PU12, PU14 and PU15 are similar to the sigmoidal trends observed in the highly aligned fibrous assemblies, PU10 and PU13 as shown in Figure 4.27. Thus, to avoid redundancy, the stress-strain responses are not presented in this section. As replacements, the woven fibrous assemblies are characterized by their initial moduli, ultimate tensile strengths and elongations at break in this section.

The variations of the ultimate tensile strengths and elongations at break due to the woven angles of the fibres in the fibrous assemblies are plotted in Figure 4.29 and 4.30. Generally, the ultimate tensile strengths and elongations at break of the woven fibrous assemblies have the same trend as the highly aligned fibrous assemblies if comparisons are being made between the diameters of the fibres and tensile test strain rates respectively. The observations can be elaborated as follows.

a) For the fibrous assemblies with the same diameter, the ultimate tensile strengths are always higher under the higher strain rate of tensile loading, whereas the elongations at break are always lower regardless of the woven angles.
b) For the tensile loading under the same strain rate, both the ultimate tensile strengths and elongations at break are always higher for the fibrous assemblies with the larger diameter regardless of the woven angles.

The effect of woven angles can only be observed in the ultimate tensile strengths as the elongations at break of the fibrous assemblies remain almost constant despite having different woven angles. Based on the Figure 4.29 and 4.30, the ultimate tensile strength of the fibrous assemblies decreases as the woven angle increases. It is in line with the study conducted by Whelan et al. (Whelan et al., 2019) where the less aligned fibrous samples in the direction of the loading have lower tensile strengths. This may be due to the fact that when the woven angle increases, the fibre’s axes deviate more from the tensile loading direction. Consequently, the fibrous assemblies have lower resistance to bear the load and thus, lower ultimate tensile strength.

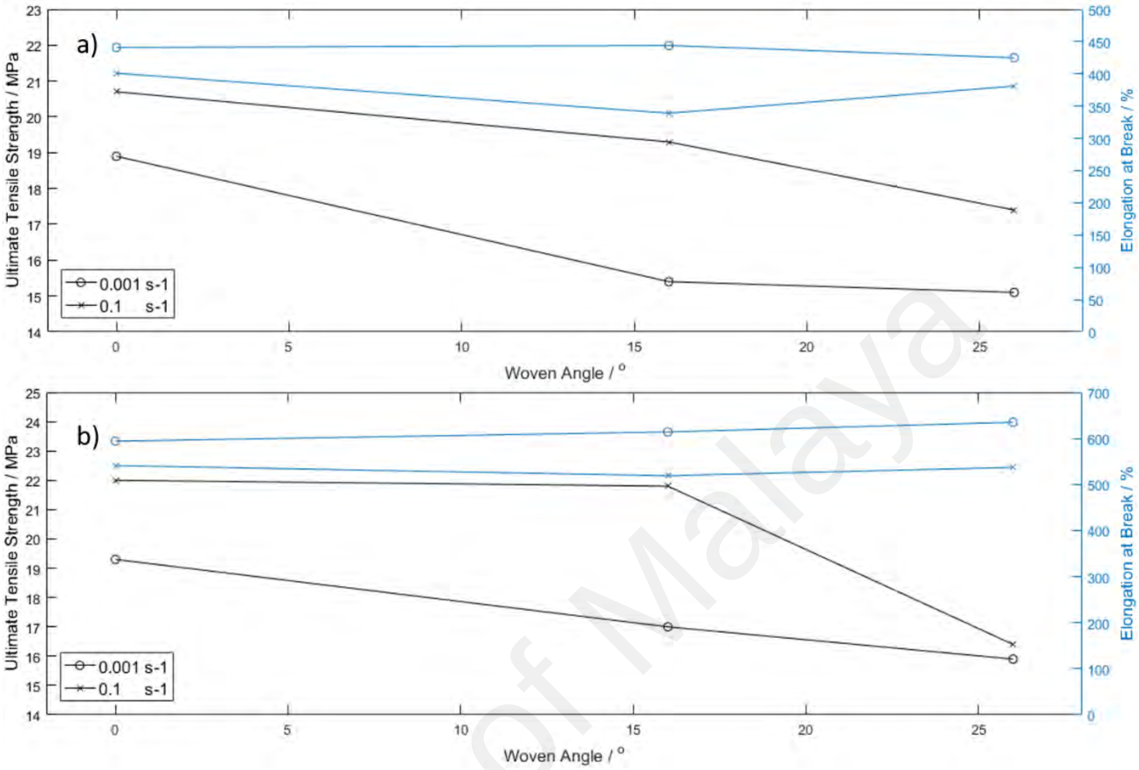

Figure 4.29: Variation of ultimate tensile strengths and elongations at break for fibrous assemblies with diameter approximately a) 8 and b) 15 µm respectively.

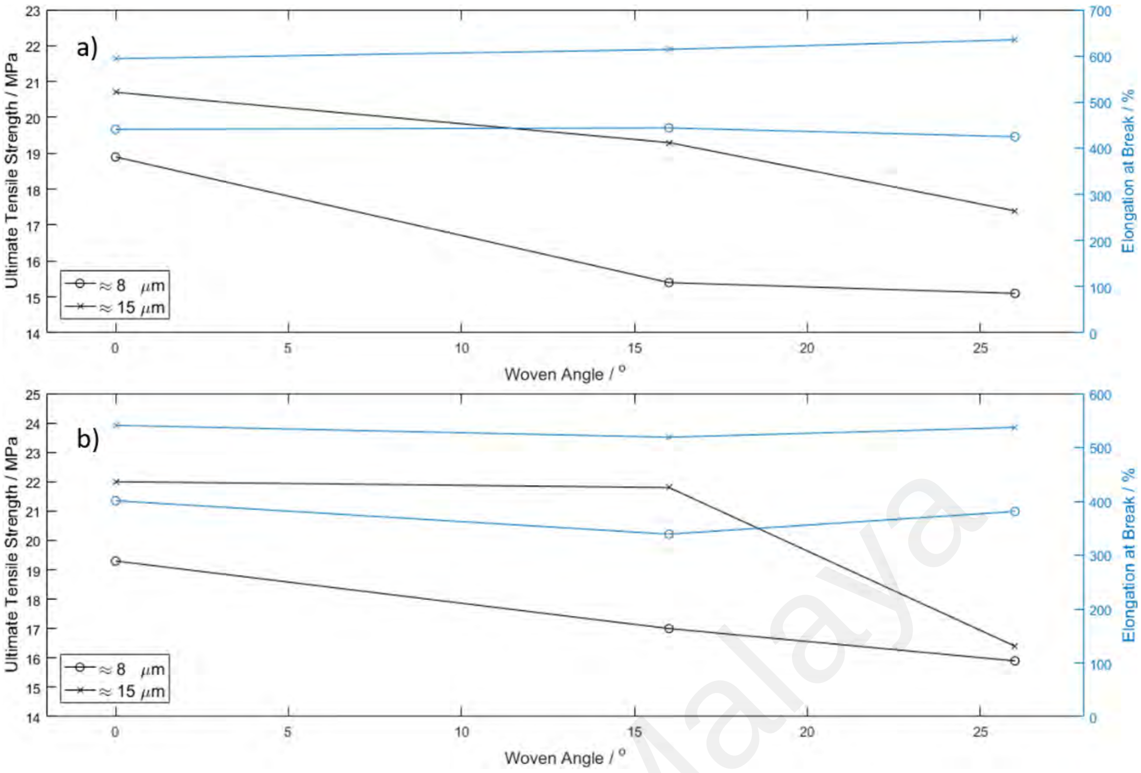

Figure 4.30: Variation of ultimate tensile strengths and elongations at break for fibrous assemblies tested under strain rates of a) 0.001 and b) 0.1 s^{-1} respectively.

Figure 4.31 shows the variation of initial moduli with the woven angles of the fibrous assemblies. It seems that the initial moduli of fibrous assemblies behave similarly to the ultimate tensile strengths, where initial moduli increase with strain rates but decrease with diameters.

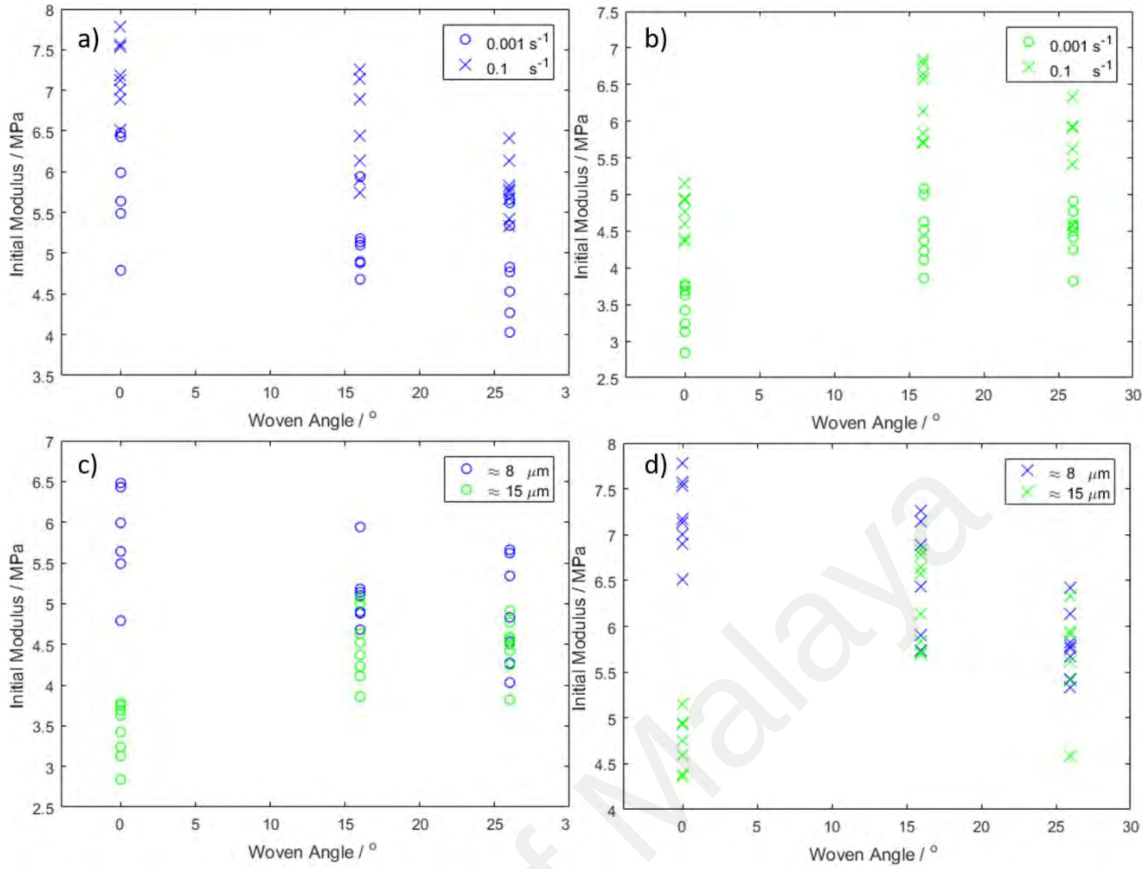

Figure 4.31: Initial moduli versus woven angles of fibrous assemblies for different strain rates with diameters approximately (a) 8 and (b) 15 µm; Initial moduli versus woven angles of fibrous assemblies for different diameters with strain rates (c) 0.001 and (d) 0.1 s^{-1}.

In the Figure 4.31 also, the initial moduli are observed to vary with the woven angles. For the fibrous assemblies with diameters approximately 8 µm, the initial modulus decreases steadily as the woven angle increases as shown in Figure 4.31 (a). Similar to the ultimate tensile strengths, this reduction is most probably due to the off axis of the fibres from the loading direction as the woven angles increase. On the contrary, fibrous assemblies with diameters approximately 15 µm show an increment in the initial modulus before decreasing with the increment in the woven angles as shown in Figure 4.31 (b). The strengthening effect from the woven angle, 0^{o} to 16^{o} is probably caused by the interfibres fusions due to incomplete solvent evaporation during the fibres fabrication. It is well documented in the literature that spun fibrous assemblies may have fused fibres that enhance the mechanical properties of the assemblies (Bai et al., 2012; Kidoaki et al., 2006; Lee et al., 2005; Mondal, 2014). An attempt to illustrate this phenomenon is given in Figure 4.32. This strengthening effect is more apparent in higher woven angles because the fusion can resist deformation better in higher woven angle. Since the strengthening only happens on the fibrous assemblies with diameters approximately 15 μm but not 8 μm, it is speculated that larger diameter fibres have more solvent content as highlighted in a study conducted by Liang et. al (Liang, Prasad, Wang, Wu, & Lu, 2019) and thus take more time to completely evaporate. As a result, the fibres fused at the junction points (Mondal, 2014).

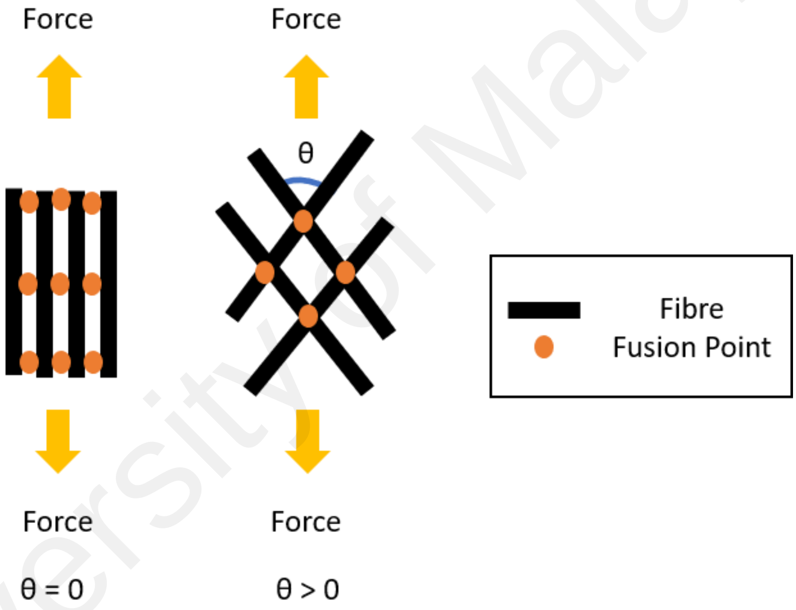

Figure 4.32: Interfibres fusions with different woven angles.

4.3.3.2 Uniaxial Cyclic Tensile Test

The general features of the stress-strain responses of the woven fibrous assemblies under uniaxial cyclic tensile tests are similar to the highly aligned fibrous assemblies discussed in Section 4.3.1.2. For further analyses on the mechanical behaviours of the woven fibrous assemblies with different woven angles at 100 % strain, three aspects, which are the hysteresis lost ratio, stress softening, and residual deformation are evaluated. The plots of the three aspects mentioned against the woven angles of the fibrous assemblies are as shown in the Figure 4.33.

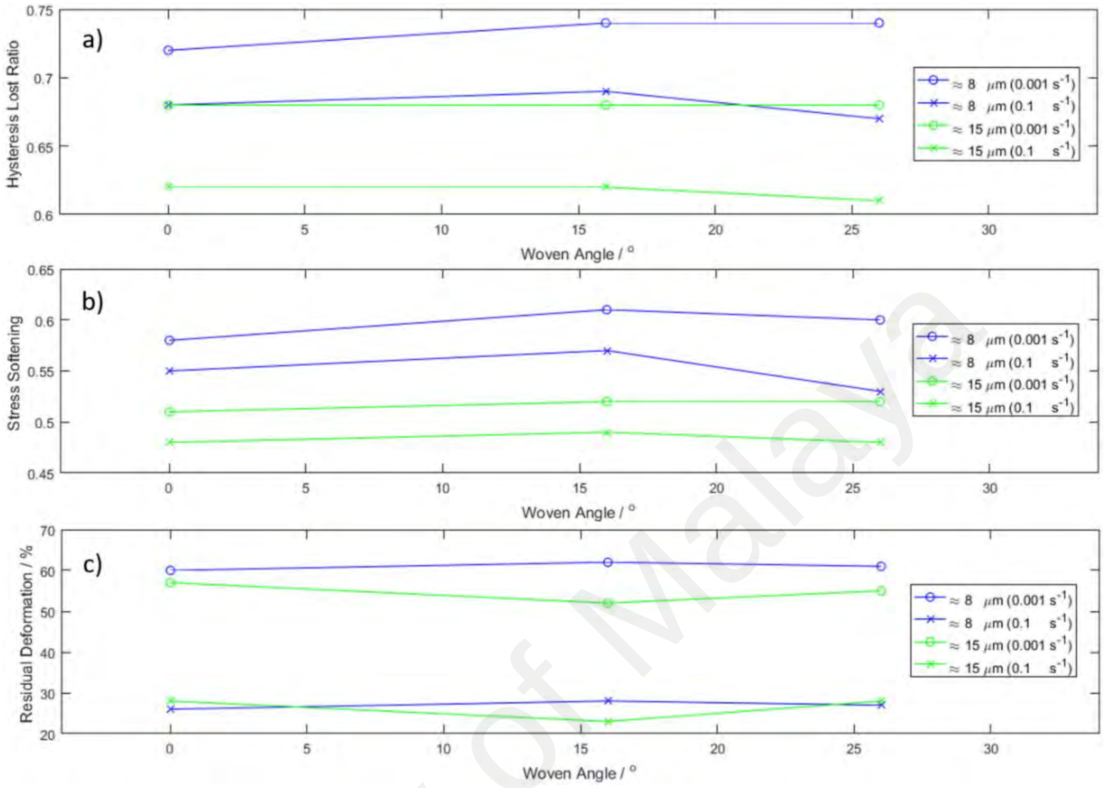

Figure 4.33: Plots of a) hysteresis lost ratio, b) stress softening and c) residual deformation of the woven fibrous assemblies versus woven angles with different fibre's diameters and strain rates respectively.

With reference to Figure 4.33, unlike the initial moduli and ultimate tensile strengths, the hysteresis lost ratio, stress softening and residual deformation appear to be insensitive to the woven angles of the fibrous assemblies as the variations of these three aspects are insignificant with woven angles. Obvious variations can only be observed in fibrous assemblies with different fibre's diameters and strain rates respectively. Nonetheless, the trends are the same as the highly aligned fibrous assemblies in the previous sections, where the hysteresis lost ratio, stress softening and residual deformation are higher with higher strain rate regardless of woven angles. As for the fibrous assemblies with different fibre's diameters, except for the residual deformation, the other two quantities mentioned are higher with the smaller diameter irrespective of the woven angles. The residual deformation seems to be similar despite of having different diameters fibrous assemblies identical to the trend in elongation at break.

4.3.3.3 Uniaxial Relaxation Tensile Test

The stress relaxation of the woven fibrous assemblies is evaluated from the amount of stress reduction after holding for 30 minutes at the strain of 100 % and 200 % respectively. All the results are plotted in Figure 4.34.

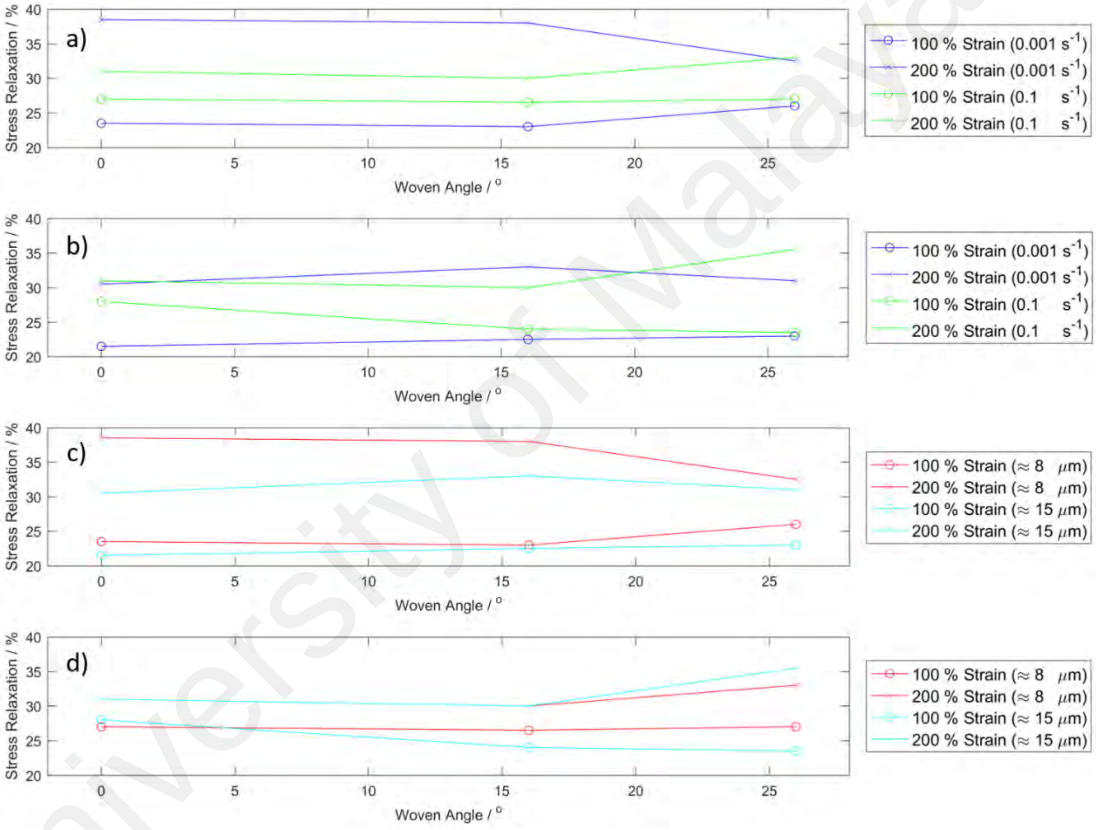

Figure 4.34: Amount of stress relaxation versus the woven angle of the fibrous assemblies with different fibre's diameters of (a) 8 and (b) 15 µm under the strain rates of (c) 0.001 s^{-1} and (d) 0.1 s^{-1}. The percentage of stress relaxation is defined by the ratio between the stress at the end of 30 min relaxation and the initial stress before relaxation at that strain.

A general trend can be observed in Figure 4.34, that is the amount of stress relaxation of the fibrous assemblies is higher at higher holding strain irrespective of the fibre's diameters, strain rates and woven angles. However, under the higher strain rate of 0.1 s^{-1}, the difference in amount of stress relaxation is smaller between the two different holding strains as compared to the strain rate 0.001 s^{-1} according to Figure 4.34 (a, b). Besides that, the amount of stress relaxation is also found to be similar under higher strain rate of 0.1 s^{-1} regardless of woven angles and fibre's diameters as shown in Figure 4.34 (d).

4.4 Elasticity of Woven Fibrous Assemblies

As described in Section 3.5, four material parameters of the highly aligned fibrous assembly, which are the longitudinal initial modulus, E_x, transversal initial modulus E_y, Poisson's ratio due to the longitudinal loading, v_{xy} and shear modulus, G_{xy} are needed to do elasticity prediction using the classical laminate theory. E_x and v_{xy} are obtained experimentally, where E_x is shown in Figure 4.31 and v_{xy} is listed in Table 4.6. It is assumed here that v_{xy} does not change with strain rate. On the contrarily, the E_y and G_{xy} are determined through the parametric study.

Table 4.6: Poisson ratio of woven fibrous assemblies due to longitudinal loading.

Diameter of Fibres (μm)	Woven Angle (°)	Poisson's Ratio, v_{xy}
≈ 8	0	0.27 ± 0.09
	16	0.45 ± 0.11
	26	0.52 ± 0.13
≈ 15	0	0.17 ± 0.05
	16	0.44 ± 0.12
	26	0.52 ± 0.17

4.4.1 Parametric Study of the Classical Laminate Theory on Woven Fibrous Assemblies

In order to do the parametric study in this section, E_x and v_{xy} of highly aligned fibrous assemblies with diameter approximately 8 μm which are experimentally obtained under the loading strain rate of 0.001 s^{-1} are applied into the laminate theory. The E_y and G_{xy}

are varied to understand how these two material parameters affect the predicted Poisson's ratios and initial moduli.

4.4.1.1 Shear Modulus, G_{xy}

Since the fibre's axes are in the direction of the loading axis for the highly aligned fibrous assemblies, it is assumed that the E_y of the fibrous assemblies is very low as compared to the E_x. For parametric study on the G_{xy}, the E_y is assumed to be 0.01 MPa. The variations of the Poisson's ratio and longitudinal initial modulus of the woven fibrous assemblies with different values of shear moduli predicted by the classical laminate theory are plotted in Figure 4.35.

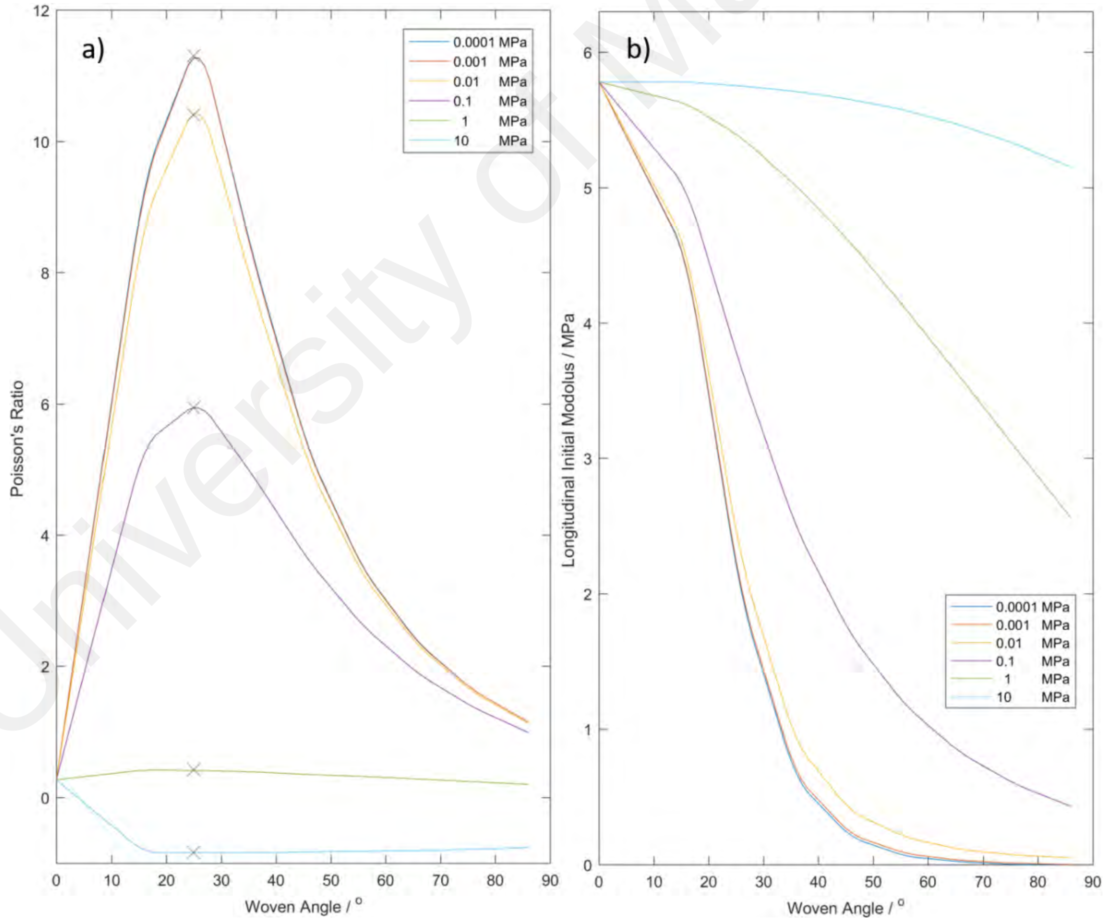

Figure 4.35: Evolution of a) Poisson's ratio and b) longitudinal initial modulus of woven fibrous assemblies as a function of woven angles for various values of shear moduli.

It is clearly noticeable in Figure 4.35 (a) that there are peaks in the curves of Poisson's ratio against the woven angle regardless of the values of the shear modulus. These peaks are all corresponding to the woven angle, 25° as indicated by the "×" marks in the curves. Except for the shear modulus of 10 MPa, the curves with other shear moduli are showing maximum peaks where the Poisson's ratio increases until a maximum value as the woven angle increases before starting to drop. As the shear modulus decreases, the maximum peak increases in value until a certain extent where the curves coincide and no longer showing different maximum peaks. On the other hand, if the shear modulus is large, the Poisson's ratio becomes negative value where the sample elongates in both the lateral and longitudinal directions. Yeh et al. (Yeh, Yeh, & Zhang, 1999) explain that the negative Poisson's ratio is caused by the shear extension coupling characteristic of fibrous laminated structures. The lateral widening occurs during longitudinal extension when two layers with different fibres orientations are forced to deform similarly as the two layers are bounded together according to the study conducted by Chen et al. (Chen, Scarpa, Farrow, Liu, & Leng, 2013).

The predicted longitudinal initial moduli of the fibrous assemblies show a general decrement as the woven angles increase regardless of the shear moduli as shown in Figure 4.35 (b). Nevertheless, the initial moduli of the fibrous assemblies are found to decrease faster with lower shear moduli. As the shear modulus is further decreased to a greater extent, the initial modulus shows no dependency on the shear modulus. Apart from that, it can be observed that when the shear modulus is large, 10 MPa in this case, the predicted longitudinal initial modulus does not decrease much with the increment in the woven angles. It seems that the fibrous laminates with greater shear moduli are more rigid to resist deformation, unaffected by the woven angles.

4.4.1.2 Transversal Initial Modulus, E_y

Similar to the previous section, the parametric study on the E_y is conducted by assuming a small value for G_{xy}, 0.01 MPa. The variations of Poisson's ratio and longitudinal initial modulus with the woven angle are presented in Figure 4.36. Again, the maximum peaks of the Poisson's ratio are marked with "×" in Figure 4.36 (a). The peak value increases as the E_y decreases until a maximum value where decreasing the E_y would not further increase the peak value, having same trend as decreasing the G_{xy}. In addition, it is observed that the peak shifts from higher woven angles to lower woven angles until it remains at a constant woven angle, 25° as the E_y decreases.

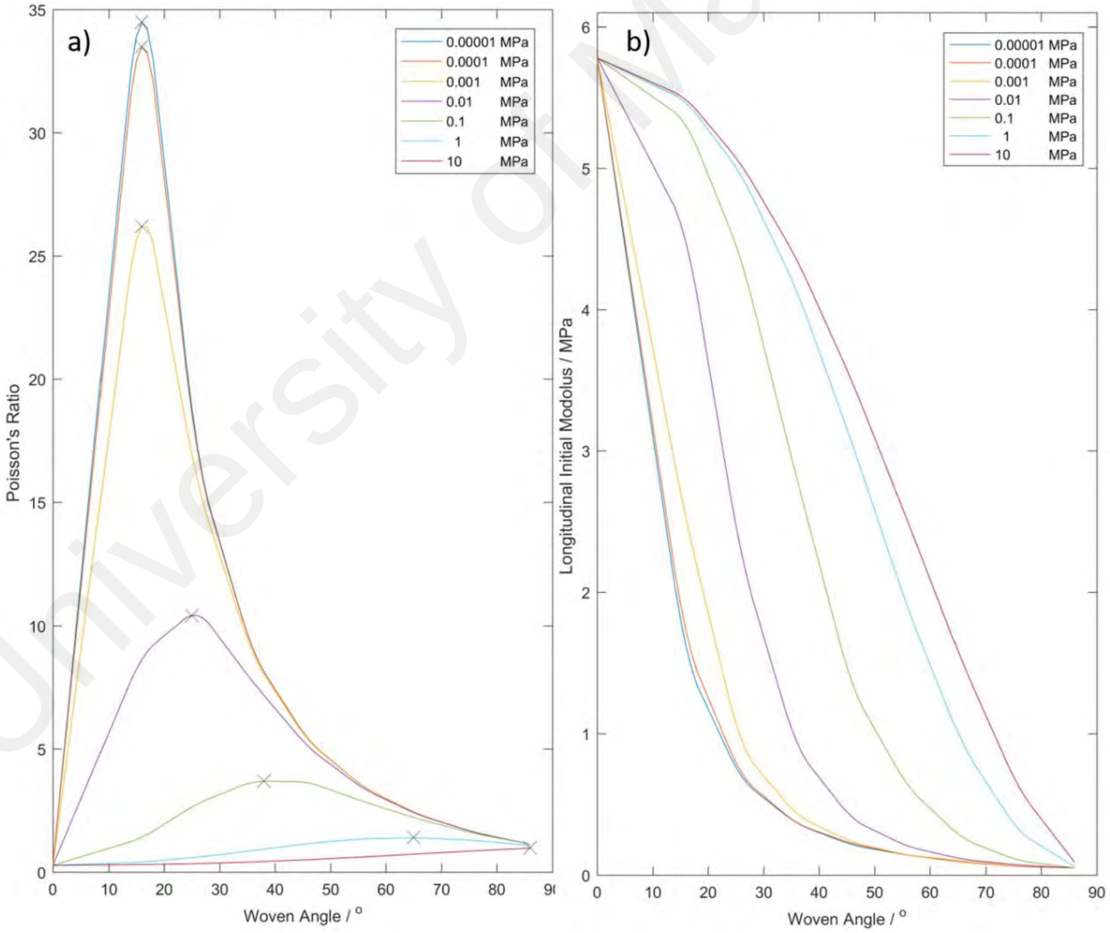

Figure 4.36: Evolution of a) Poisson's ratio and b) longitudinal initial modulus of woven fibrous assemblies as a function of woven angles for various values of transversal initial moduli.

As for the longitudinal initial modulus, decreasing the $\boldsymbol{E_y}$ increases the rate of initial modulus decrement with woven angle until the rate becomes constant at certain $\boldsymbol{E_y}$ according to Figure 4.36 (b), behaving in the same manner as decreasing the $\boldsymbol{G_{xy}}$ in the previous section. It is also observed that the predicted longitudinal initial modulus diminishes close to 0 MPa as the woven angle approaches 90^o irrespective of the $\boldsymbol{E_y}$.

4.4.2 Curves Fitting with the Experimental Data

The previous section focused on the theoretical prediction on how E_y and G_{xy} would affect the E_X and v_{XY}. In order to determine E_y and G_{xy} of our materials, a curve fitting procedure is needed. Along this line, in this section, the unknown material parameters E_y and G_{xy} are identified using an optimization technique with fmincon solver in MATLAB. While the optimization for the fibrous assemblies with the fibres diameter of approximately 8 µm is conducted using both the longitudinal initial moduli and Poisson's ratio experimental data, only Poisson's ratio is used for the optimization of the fibrous assemblies with the fibres diameter approximately 15 µm. This is because the classical laminate theory is not able to simulate the stiffening of the fibrous assemblies with fibres diameter approximately 15 µm from the woven angle, 0^o to 16^o as shown in Figure 4.31 (b). The optimized $\boldsymbol{E_y}$ and $\boldsymbol{G_{xy}}$ are tabulated in Table 4.7.

Table 4.7: Optimized material parameters, $\boldsymbol{E_y}$ and $\boldsymbol{G_{xy}}$.

Average Diameter of Fibres (µm)	Woven Angle (^{o})	Strain Rate (s^{-1})	E_y (MPa)	G_{xy} (MPa)
≈ 8	0	0.001	0.64	0.19
		0.1	0.71	0.22
≈ 15	0	0.001	0.03	0.5
		0.1	0.16	0.61

Figure 4.37 shows the comparison between the simulated and experimental longitudinal initial moduli and Poisson's ratios respectively. Generally, the classical laminate theory agrees well with the experimental results, except for the longitudinal initial moduli of the fibrous assemblies with larger fibres diameter of approximately 15 µm. This discrepancy is most probably due to the fusion between fibres which is elaborated previously in Section 4.3.3.1.

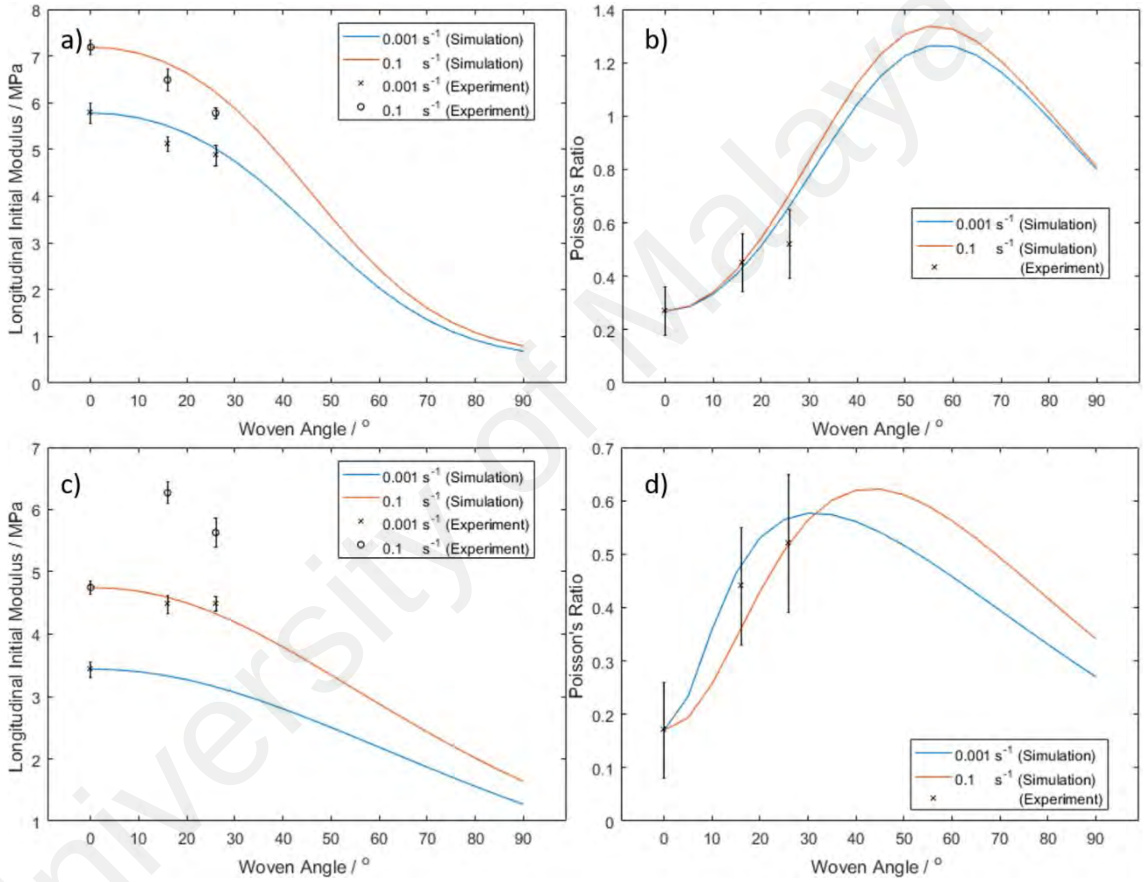

Figure 4.37: Simulated longitudinal initial moduli and Poisson's ratio versus woven angles for fibrous assemblies with the fibre's diameters approximately a, b) 8 and c, d) 15 µm respectively.

4.4.3 Designing Elasticity Compliance Vascular Grafts

In this section, designs of elasticity compliance vascular grafts where the deformation of the grafts is similar to the native vessels are proposed based on the classical laminate theory in the Section 4.2.2. However, it is noteworthy that the morphology of the vascular grafts is an important element to promote the endothelization process. Hence, the morphology is taken into consideration as well in designing these elasticity compliance vascular grafts.

The blood vessels are having complex microstructures which comprise of three different layers, intima, media and adventitia layers. It is well known that endothelialisation is more effective in grafts mimicking the morphology of the native blood vessels (He et al., 2013; Wong et al., 2013; Xu et al., 2004). Nevertheless, it is difficult to design grafts with complex microstructure totally similar to the native blood vessels as the three different layers have different fibrous morphologies (Schriefl Andreas, Zeindlinger, Pierce David, Regitnig, & Holzapfel Gerhard, 2012). In order to have a simpler design, only the morphology of the inner layer of the blood vessels, intima layer is considered because it is found that the blood compatibility and biofunctionality are merely affected by the inner layers of grafts (Wang et al., 2004).

The morphology of the intima layers in the arteries mainly consists of two families of fibres with an approximate angle of 80^{o} between them (Schriefl Andreas et al., 2012) which corresponds to the woven angle, 80^{o} of the fibrous assemblies in this study. As for the stiffnesses, it is found that the circumferential stiffness is about 1.5 times the longitudinal stiffness of the arteries (Bergel, 1961). In order to mimic the stiffness of the arteries, the classical laminate theory is used to predict the longitudinal and transversal initial modulus of the fibrous assemblies. The transversal initial modulus corresponds to the circumferential stiffness as the sheet of fibrous assemblies will be rolled into the geometry of a cylindrical graft. Ratios of the predicted transversal and longitudinal initial moduli, E_Y/E_X from 0 to 2 are plotted against the woven angles in Figure 4.38.

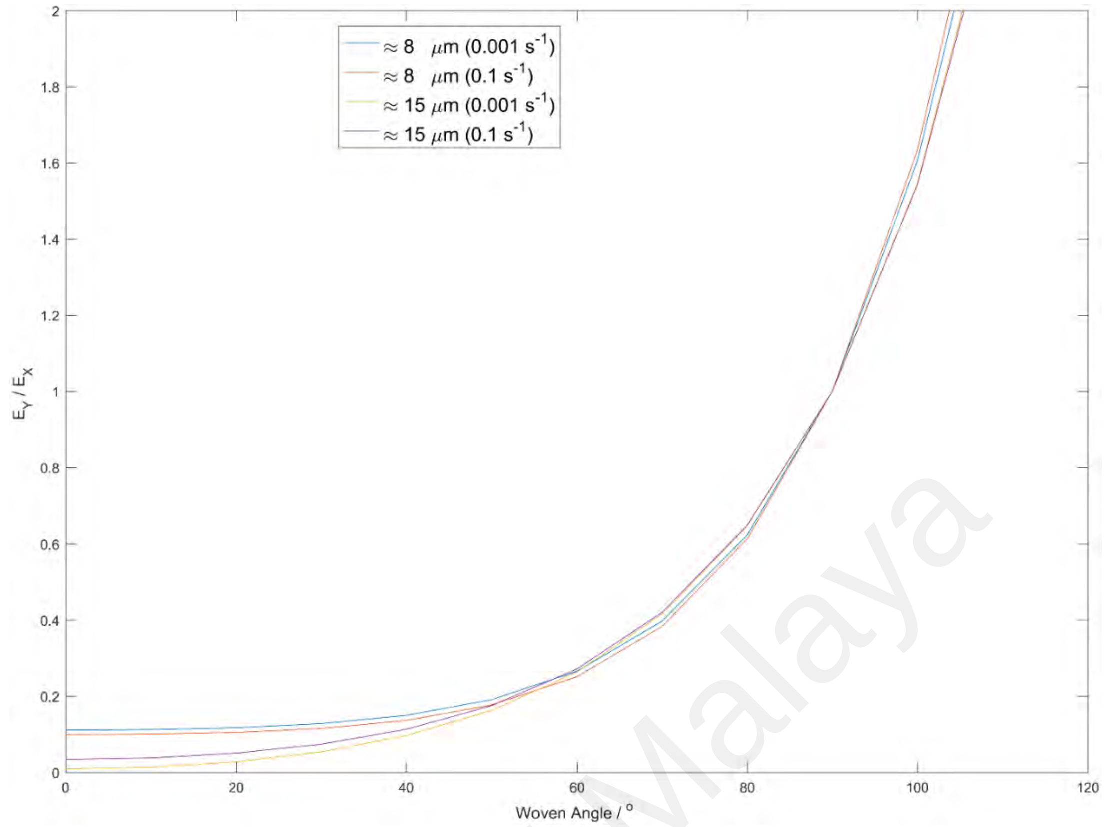

Figure 4.38: Ratios of the predicted transversal and longitudinal initial moduli plotted against the woven angles.

As shown in Figure 4.38, it is clear that the E_Y/E_X are similar in the range of 1.5 to 2.0 regardless of the fibre's diameters and woven angles. The interpolated values of the E_Y/E_X in the interest of designing the vascular grafts are tabulated in Table 4.8. It seems that the polyurethane fibrous assemblies in this study cannot achieve the 1.5 E_Y/E_X value, with the woven angle, 80°. The 1.5 E_Y/E_X value can only be achieved in the fibrous assemblies with the woven angle close to 100°. Based on the studies in the literature (Bergel, 1961; Das, Paul, Taylor, & Banerjee, 2015; Schriefl Andreas et al., 2012), the arteries are stiffer circumferentially than longitudinally despite having less fibres aligned in the circumferential direction due to the higher fibres angle in the circumferential direction. The polyurethane fibrous assemblies in this study cannot behave as such because the arteries comprise of a mixture of elastin and collagen fibres whereas the fibrous assemblies here are only consist of polyurethane fibres alone. Hence, in order to have polyurethane fibrous assemblies that are stiffer in the circumferential direction, the woven angles need to be higher than 80°, so that more fibres are aligned in the circumferential direction.

Table 4.8: $\boldsymbol{E_Y/E_X}$ of the polyurethane fibrous assemblies.

Average Diameter of Fibres (µm)	Strain Rate (s^{-1})	Woven Angle (°)	E_Y/E_X
≈ 8	0.001	80	0.6
	0.1		
	0.001	98	1.5
	0.1		
≈ 15	0.001	80	0.6
	0.1		
	0.001	99	1.5
	0.1		

After obtaining a suitable woven angle for the grafts, the next step is to design the wall thickness of the grafts, t_g. The graft is designed such that it will expand or deform circumferentially similar to the native blood vessel due to the blood pressures.

In order to start the designing, it is first noteworthy to know that the inner diameter of the graft and vessel are the same. Even after the introduction of pressure, the diameters of the graft and vessel will remain the same. Thus, the radial strains, ε are the same for both the graft and vessel as well. The nett radial strains are contributed by the hoop, radial and longitudinal stress. However, with the assumptions that the grafts and vessels are long and open system with thin walls, the radial strain is only contributed by the hoop stress. The radial strains of the grafts and vessels are related by the pressure, P exerted on them, radii, R, thicknesses, t, and hoop moduli, E_θ as shown in Eq. 4.4 and 4.5. The subscripts, g and v correspond to the grafts and vessels respectively. Since the ε_g is equal to ε_v and the P is the same in both the graft and vessel, Eq. 4.6 is derived. Consequently, the thickness of the grafts can be determined using Eq. 4.6.

$$\varepsilon_g = \frac{\frac{PR_g}{t_g}}{E_{\theta_g}} \tag{4.4}$$

$$\varepsilon_v = \frac{\frac{PR_v}{t_v}}{E_{\theta_v}} \tag{4.5}$$

$$\frac{E_{\theta_v}}{E_{\theta_g}} = \frac{t_g}{t_v} \tag{4.6}$$

For a case study, the carotid artery in human is considered. A study conducted by Khamdaeng et al. (Khamdaeng, Luo, Vappou, Terdtoon, & Konofagou, 2012) reported that the hoop modulus of the carotid artery is 0.89 ± 0.27 MPa whereas the wall thickness is 0.61 ± 0.018 mm for adults aged between 30 to 32. The E_Y is considered to be the E_{θ_g} of the fibrous assemblies with woven angle, θ of 98^o or 99^o as illustrated in Figure 4.39. The fibrous sheet is to be rolled into a cylindrical graft. This E_Y is predicted using the classical laminate theory.

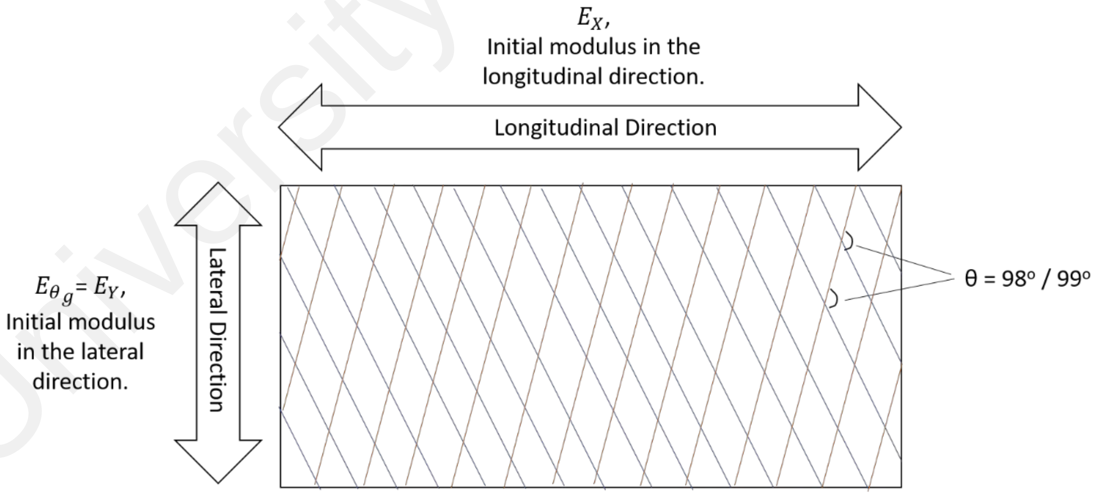

Figure 4.39: Illustration of the designed graft.

By using Eq. 4.6, the t_v can be determined and are presented in Table 4.9. It appears that the fibrous assemblies with diameter approximately 8 μm is more applicable as vascular graft for arteries as the assemblies have similar E_Y/E_X and t_v to the arteries.

Table 4.9: Proposed wall thicknesses for the polyurethane fibrous vascular grafts.

Average Diameter of Fibres (μm)	Strain Rate (s^{-1})	Woven Angle (°)	E_Y/E_X	t_v (mm)
≈ 8	0.001	98	1.5	0.63
	0.1			0.54
≈ 15	0.001	99	1.5	0.35
	0.1			0.28

In this section, the polyurethane fibrous grafts are designed through the application of a simple classical laminate theory to meet the elastic properties of the blood vessels. Based on this theory, the diameters, woven angles and thickness of the grafts are predicted for the carotid arteries. However, it is noteworthy to mention that the woven structure of the grafts is assumed to mechanically response similar to the laminate structure to accommodate the classical laminate theory. Despite of this assumption, the predicted and experimental initial moduli of the fibrous grafts show close proximity as shown in Figure 4.37. With this level of confidence, the predicted initial moduli are further utilised to predict the thickness of the grafts using Eq. 4.6 where the grafts are assumed to behave like open ended thin walled pressure cylindrical vessels. To close the discussion, it is to note that while the more complex and realistic mechanical behaviours of native blood vessels such as hyperelasticity, viscoelasticity, hysteresis and stress softening are not considered in the calculation, the obtained parameters from classical linear elastic laminate theory are useful and could provide important information on the design of vascular grafts.

CHAPTER 5: CONCLUSION & RECOMMENDATION

5.1 Conclusion

Highly aligned fibrous morphology is found to allow homogenous functional endothelization on the surface of a vascular graft to reduce the risk of compliance mismatch and thrombogenicity in the literature. Thus, in the view of designing a competent vascular graft, four main objectives are proposed in this study. The achievements of these mentioned objectives are further elaborated in the following sections.

5.1.1 To Fabricate Highly Aligned Polyurethane Assemblies

The first objective is to fabricate highly aligned polyurethane fibrous assemblies. This fibres fabrication task is achieved by investigating the relationships between the spinning techniques and the topology of the fibrous assemblies.

Through experimental study, it is found that the spinning mechanisms in electrospinning are controllable by altering the solution parameters. By adjusting the solution parameters, the polymer solution jet from the syringe can be controlled before the deposition of fibres on to the collector. Solutions with high viscosity and low electrical conductivity can induce the whipping instability of the solution jet, while solution with low viscosity and high electrical conductivity are able to induce the splaying of the solution jet. In order to obtain highly aligned fibrous sample, the fibres need to be deposited on a high speed rotating collector. However, the high speed rotating collector can impose excessive stretching on the fibres, evidenced by the fibres with wavy structure due to contraction. Subsequently, dry spinning is found to be more suitable technique to be used for the fabrication of highly aligned fibrous sample. Results show that the dry spun fibres are straight and highly aligned although having larger diameters.

In the process of getting the best parameters for the fabrication of highly aligned fibrous assemblies, the spinning techniques are studied in deep. Aside from the highly aligned fibrous sample, other fibrous samples with different topology are successfully fabricated such as the fibres with beads, coiled fibres, fibres with different average diameters and alignments. While these other topologies are not desirable in this study, they could be used in other suitable applications in the future. The spinning mechanisms and parameters to fabricate fibrous assemblies with various topologies are well presented in this study for future references and guidelines. However, further investigations are only conducted on the highly aligned fibrous assemblies complying to the objectives of this study.

5.1.2 To Study the Biostability of the Assemblies in Terms of Chemical, Physical and Mechanical Properties

As for the second objective, the biostability of the highly aligned polyurethane fibrous assemblies are investigated. The results show that the fibrous assemblies do not undergo obvious or significant deterioration in the physical, mechanical and chemical properties even after 24 weeks of immersion in stimulated body fluid. Considering this characteristic, this highly aligned polyurethane fibrous assemblies could be applicable as synthetic vascular grafts.

5.1.3 To Evaluate the Mechanical Responses of the Single and Multilayers Woven Fibrous Assemblies under Complex Uniaxial Tensile Loading Sequences

Consequently, the mechanical responses of the fibrous assemblies are studies to achieve the third objective. These mechanical responses are crucial to ensure the mechanical compliance to the blood vessels for the potential application of vascular grafting. In addition, it is also the fundamental information to simulate the mechanical responses of the multilayers fibrous assemblies using the classical laminate theory.

Subsequently, the mechanical responses of the fibres were investigated under uniaxial monotonic, cyclic and relaxation tensile test.

In the uniaxial monotonic tensile test, the stress-strain behaviour of the fibrous assemblies with average diameter 2.80 μm is nearly linear before reaching the ultimate tensile strength, which is different from the sigmoidal shaped stress-strain behaviour found in typical bulk elastomers. This shows that the mechanical property changes when bulk polyurethane is fabricated into microfibres. However, it seems that there is a minimum threshold diameter for this linear stress-strain behaviour to occur as the fibrous assemblies with average diameters, approximately 8 and 15 μm do not have the linear sigmoidal shaped stress-strain behaviour. Instead, it is a sigmoidal stress-strain behaviour like bulk elastomers. Nevertheless, higher stiffness or initial modulus is observed under higher strain rate in all the fibrous assemblies regardless of the fibres diameter.

Inelastic mechanical responses, such as the hysteresis, stress-softening and residual deformation are revealed in the uniaxial cyclic tensile test. The effect of maximum strain and strain rate on these mechanical responses was studied. Generally, hysteresis increases as the maximum strain increases. However, hysteresis remains almost constant and hysteresis loss ratio decreases as the strain rate increases. As for the stress softening, strain rate seems to have no obvious effect on it. Both hysteresis and stress softening appear to be strain rate independent.

Lastly, two steps uniaxial tensile test with two holding strains is conducted on the fibres. At higher strain rate, the distance from the relaxation equilibrium state is further than the lower strain rate. Nevertheless, similar distance from the relaxation equilibrium state is found at higher strain rate despite having different holding strain.

Further investigations of this study are conducted on the multilayers highly aligned fibrous assemblies. The samples are fabricated by weaving the highly aligned fibrous assemblies with woven angles of 0°, 16° and 26° with diameters approximately 8 and 15 μm respectively. Mechanical testing show that the woven angles greatly influence the initial moduli of the woven fibrous assemblies but not the hysteresis, stress softening, relaxation behaviours under uniaxial cyclic tensile tests.

5.1.4 To Propose a New Design of Vascular Graft with Mechanical Compliance with the Help of Classical Laminate Theory

Ultimately, the initial moduli of the fibrous assemblies are simulated and predicted using classical laminate theories to the end of designing vascular grafts with mechanical compliance to the native blood vessels to achieve the fourth objective. Results predicted from the classical laminate theory show that the polyurethane fibrous assemblies with fibres diameter approximately 8 μm, woven angle close to 100° and thickness ranges between 0.5 to 0.7 mm could be suitable as the grafts of carotid arteries.

5.2 Recommendation

In the end of this study, a plausible design of an elastic compliant small calibre vascular graft for carotid arteries are proposed using the classical laminate theory based on the results of the mechanical testing on the highly aligned polyurethane woven fibrous samples. However, the classical laminate theory is only able to simulate the small strain linear elastic properties of the fibrous assemblies without considering the hyperelasticity, stress softening, hysteresis, viscoelasticity and viscoplasticity of the grafts. These properties are found to be significant as shown in Section 4.3. Hence, for the continuation of this study, apart from the elasticity, the other mechanical behaviours or properties mentioned can be further simulated using appropriate mechanical model such as the large deformation theory with a hyperelastic strain energy function accounting for two preferred directions or anisotropic nonlinear viscoplasticity. Finally, the models can be implemented into finite element code. In this way, the proposed design in this study can be further improved.

As for the biological tests, the fibrous samples in this study are solely tested on their biostability. In order to further verify the biocompatibility of the samples, in vitro cell culturing and later on in vivo cell culturing can be conducted for a longer durations, more than 24 weeks. Additionally, the biomechanics of the grafts can be studied in conjunction with the in vivo cell culturing. The real time mechanical responses of the graft while blood passing through it are an important factor in forming a homogenous functional endothelium layer.

After proper and in deep studies on the polyurethane fibrous samples, the fibres can be embedded into a matrix, further mimicking the real blood vessels with fibres embedded inside extracellular matrices. The studies on the fibres solely without matrices are essential to provide a strong foundation to the studies of the fibres embedded inside a matrix. These fibres embedded inside matrices can be treated as fibres reinforced composites for further studies.

REFERENCES

Abouzahr, S., & Wilkes, G. L. (1984). Structure property studies of polyester- and polyether-based MDI-BD segmented polyurethanes: Effect of one- vs. two-stage polymerization conditions. *J. Appl. Polym. Sci., 29*, 2695-2711.

Adipurnama, I., Yang, M.-C., Ciach, T., & Butruk-Raszeja, B. (2017). Surface modification and endothelialization of polyurethane for vascular tissue engineering applications: A review. *Biomater. Sci., 5*(1), 22-37.

Al-Ajrah, S., Lafdi, K., Liu, Y., & Le Coustumer, P. (2018). Fabrication of ceramic nanofibers using polydimethylsiloxane and polyacrylonitrile polymer blends. *J. Appl. Polym. Sci., 135*(10), 45967-n/a.

Amoroso, N. J., D'Amore, A., Hong, Y., Wagner, W. R., & Sacks, M. S. (2011). Elastomeric electrospun polyurethane scaffolds: The interrelationship between fabrication conditions, fiber topology, and mechanical properties. *Adv. Mater., 23*, 106-111.

Asadpour, S., Ai, J., Davoudi, P., Ghorbani, M., Jalali Monfared, M., & Ghanbari, H. (2018). In vitro physical and biological characterization of biodegradable elastic polyurethane containing ferulic acid for small-caliber vascular grafts. *Biomed. Mater., 13*(3), 035007.

Asefnejad, A., Khorasani, M. T., Behnamghader, A., Farsadzadeh, B., & Bonakdar, S. (2011). Manufacturing of biodegradable polyurethane scaffolds based on polycaprolactone using a phase separation method: physical properties and in vitro assay. *Int. J. Nanomed., 6*, 2375-2384.

Bagchi, S., Brar, R., Singh, B., & Ghanshyam, C. (2015). Instability controlled synthesis of tin oxide nanofibers and their gas sensing properties. *J. Electrost., 78*, 68-78.

Bai, Z., Xu, W., Xu, J., Liu, X., Yang, H., Xiao, S., . . . Chen, L. (2012). Microstructure and mechanical properties of polyurethane fibrous membrane. *Fiber. Polym., 13*(10), 1239-1248.

Baim, D. S. (2003). Percutaneous treatment of saphenous vein graft disease: The ongoing challenge. *J. Am. Coll. Cardiol., 42*(8), 1370-1372.

Baker, B. M., Gee, A. O., Metter, R. B., Nathan, A. S., Marklein, R. A., Burdick, J. A., & Mauck, R. L. (2008). The potential to improve cell infiltration in composite fiber-aligned electrospun scaffolds by the selective removal of sacrificial fibers. *Biomaterials, 29*(15), 2348-2358.

Bardelcik, A., Vowles, C. J., & Worswick, M. J. (2018). A mechanical, microstructural, and damage study of various tailor hot stamped material conditions consisting of martensite, bainite, ferrite, and pearlite. *Metall. Mater. Trans. A, 49*(4), 1102-1120.

Basu, S., Hay, J. L., Swindeman, J. E., & Oliver, W. C. (2014). Continuous dynamic analysis: evolution of elastic properties with strain. *MRS Commun., 4*(1), 25-29.

Benitez, P. L., Sweet, J. A., Fink, H., Chennazhi, K. P., Nair, S. V., Enejder, A., & Heilshorn, S. C. (2013). Sequence-specific crosslinking of electrospun, elastin-like protein preserves bioactivity and native-like mechanics. *Adv. Healthc. Mater., 2*(1), 114-118.

Bergel, D. H. (1961). The static elastic properties of the arterial wall. *J. Physiol., 156*(3), 445-457.

Bergmeister, H., Grasl, C., Walter, I., Plasenzotti, R., Stoiber, M., Schreiber, C., . . . Schima, H. (2012). Electrospun small-diameter polyurethane vascular grafts: Ingrowth and differentiation of vascular-specific host cells. *Artif. Organs, 36*(1), 54-61.

Bergstrom, J. S., & Boyce, M. C. (1998). Constitutive modeling of the large strain time-dependent behavior of elastomers. *J. Mech. Phys. Solids, 46*(5), 931-954.

Bhardwaj, N., & Kundu, S. C. (2010). Electrospinning: A fascinating fiber fabrication technique *Biotechnol. Adv., 28* 325 - 347

Blackledge, T. A., & Hayashi, C. Y. (2006). Silken toolkits: Biomechanics of silk fibers spun by the orb web spider Argiope argentata (Fabricius 1775). *J. Exp. Biol., 209*(13), 2452.

Blackledge, T. A., Swindeman, J. E., & Hayashi, C. Y. (2005). Quasistatic and continuous dynamic characterization of the mechanical properties of silk from the cobweb of the black widow spider Latrodectus hesperus. *J. Exp. Biol., 208*(10), 1937.

Bonakdar, S., Emami, S. H., Shokrgozar, M. A., Farhadi, A., Ahmadi, S. A. H., & Amanzadeh, A. (2010). Preparation and characterization of polyvinyl alcohol hydrogels crosslinked by biodegradable polyurethane for tissue engineering of cartilage. *Mater. Sci. Eng. C, 30*(4), 636-643.

Breche, Q., Chagnon, G., Machado, G., Girard, E., Nottelet, B., Garric, X., & Favier, D. (2016). Mechanical behaviour's evolution of a PLA-b-PEG-b-PLA triblock copolymer during hydrolytic degradation. *J. Mech. Behav. Biomed. Mater., 60*, 288-300.

Briody, C., Duignan, B., Jerrams, S., & Ronan, S. (2012). Prediction of compressive creep behaviour in flexible polyurethane foam over long time scales and at elevated temperatures. *Polym. Test, 31*(8), 1019-1025.

Brown, A. E. X., Litvinov, R. I., Discher, D. E., Purohit, P. K., & Weisel, J. W. (2009). Multiscale mechanics of fibrin polymer: Gel stretching with protein unfolding and loss of water. *Science, 325*(5941), 741.

Brzeska, J., Heimowska, A., Janeczek, H., Kowalczuk, M., & Rutkowska, M. (2014). Polyurethanes based on atactic poly[(R,S)-3-hydroxybutyrate]: Preliminary degradation studies in simulated body fluids. *J. Polym. Environ., 22*(2), 176-182.

Buchko, C. J., Chen, L. C., Shen, Y., & Martin, D. C. (1999). Processing and microstructural characterization of porous biocompatible protein polymer thin films *Polym., 40* 7397 - 7407

Buckley, C. P., Prisacariu, C., & Martin, C. (2010). Elasticity and inelasticity of thermoplastic polyurethane elastomers: Sensitivity to chemical and physical structure. *Polym., 51*, 3213-3224.

Bueche, F. (1960). Molecular basis for the mullins effect. *J. Appl. Polym. Sci., 4*(10), 107-114.

Bulota, M., Michud, A., Hummel, M., Hughes, M., & Sixta, H. (2016). The effect of hydration on the micromechanics of regenerated cellulose fibres from ionic liquid solutions of varying draw ratios. *Carbohydr. Polym., 151*, 1110-1114.

Cantournet, S., Desmorat, R., & Besson, J. (2009). Mullins effect and cyclic stress softening of filled elastomers by internal sliding and friction thermodynamics model. *Int. J. Solid Struct., 46*(11), 2255-2264.

Castillo-Cruz, O., Avilés, F., Vargas-Coronado, R., Cauich-Rodríguez, J. V., Chan-Chan, L. H., Sessini, V., & Peponi, L. (2019). Mechanical properties of l-lysine based segmented polyurethane vascular grafts and their shape memory potential. *Mater. Sci. Eng. C, 102*, 887-895.

Catalani, L. H., Collins, G., & Jaffe, M. (2007). Evidence for molecular orientation and residual charge in the electrospinning of poly(butylene terephthalate) nanofibers. *Macromol., 40*(5), 1693-1697.

Chai, A. B., Andriyana, A., Verron, E., & Johan, M. R. (2013). Mechanical characteristics of swollen elastomers under cyclic loading. *Mater. Des., 44*, 566-572.

Chen, H.-M., & Yu, D.-G. (2010). An elevated temperature electrospinning process for preparing acyclovir-loaded PAN ultrafine fibers *J. Mater. Process. Technol., 210* 1551 - 1555

Chen, K.-S., Yu, T. L., Chen, Y.-S., Lin, T.-L., & Liu, W.-J. (2001). Soft- and hard-segment phase segregation of polyester-based polyurethane. *J. Polym. Res., 8*(2), 99-109.

Chen, Q., Kuang, L., Sargent, E. H., & Wang, Z. Y. (2003). Ultrafast nonresonant third-order optical nonlinearity of fullerene-containing polyurethane films at telecommunication wavelengths. *Appl. Phys. Lett., 83*(11), 2115-2117.

Chen, Q., Liang, S., & Thouas, G. A. (2013). Elastomeric biomaterials for tissue engineering. *Progress in Polymer Science, 38*(3), 584-671.

Chen, Y. J., Scarpa, F., Farrow, I. R., Liu, Y. J., & Leng, J. S. (2013). Composite flexible skin with large negative Poisson's ratio range: numerical and experimental analysis. *Smart Mater. Struct., 22*(4), 045005.

Cheng, M., & Chen, W. (2003). Experimental investigation of the stress–stretch behavior of EPDM rubber with loading rate effects. *Int. J. Solid Struct., 40*, 4749-4768.

Christenson, E. M., Anderson, J. M., Hiltner, A., & Baer, E. (2005). Relationship between nanoscale deformation processes and elastic behavior of polyurethane elastomers. *Polym., 46*, 11744–11754.

Collins, G., Federici, J., Imura, Y., & Catalani, L. H. (2012). Charge generation, charge transport, and residual charge in the electrospinning of polymers: A review of issues and complications. *J. Appl. Phys., 111*(4), 044701.

Colomban, P. (2013). Understanding the nano- and macromechanical behaviour, the failure and fatigue mechanisms of advanced and natural polymer fibres by Raman/IR microspectrometry. *Adv. Nat. Sci.: Nanosci. Nanotechnol., 4*, 1-10.

Das, A., Paul, A., Taylor, M. D., & Banerjee, R. K. (2015). Pulsatile arterial wall-blood flow interaction with wall pre-stress computed using an inverse algorithm. *Biomed. Eng. Online, 14*(1), S18.

Daum, R., Visser, D., Wild, C., Kutuzova, L., Schneider, M., Lorenz, G., . . . Schenke-Layland, K. (2020). Fibronectin adsorption on electrospun synthetic vascular grafts attracts endothelial progenitor cells and promotes endothelialization in dynamic in vitro culture. *Cells, 9*(3). (Accession No. 32210018)

de Gelidi, S., Tozzi, G., & Bucchi, A. (2016). The role of pre-conditioning frequency in the experimental characterization of hyper-elastic materials as models for soft tissue applications. *Int. J. Appl. Mech., 08*(05), 1650066.

Demir, M. M., Yilgor, I., Yilgor, E., & Erman, B. (2002). Electrospinning of polyurethane fibers *Polym., 43* (11), 3303 - 3309

Deng, D., Liu, W., Xu, F., Yang, Y., Zhou, G., Zhang, W. J., . . . Cao, Y. (2009). Engineering human neo-tendon tissue in vitro with human dermal fibroblasts under static mechanical strain. *Biomaterials, 30*(35), 6724-6730.

Deng, M., Kumbar, S. G., Nair, L. S., Weikel, A. L., Allcock, H. R., & Laurencin, C. T. (2011). Biomimetic structures: Biological implications of dipeptide-substituted polyphosphazene–polyester blend nanofiber matrices for load-bearing bone regeneration. *Adv. Funct. Mater., 21*(14), 2641-2651.

Desai, M., Seifalian, A. M., & Hamilton, G. (2011). Role of prosthetic conduits in coronary artery bypass grafting. *Eur. J. Cardio-Thorac. Surg., 40*(2), 394-398.

Dhakate, S. R., Singla, B., Uppal, M., & Mathur, R. B. (2010). Effect of processing parameters on morphology and thermal properties of electrospun polycarbonate nanofibers. *Adv. Mat. Lett., 1*(3), 200-204.

Diani, J., Fayolle, B., & Gilormini, P. (2009). A review on the Mullins effect. *Eur. Polym. J., 45*, 601-612.

Ding, X. M., Hu, J. L., Tao, X. M., & Hu, C. P. (2006). Preparation of Temperature-Sensitive Polyurethanes for Smart Textiles. *Text. Res. J., 76*(5), 406-413.

Doshi, J., & Reneker, D. H. (1995). Electrospinning process and applications of electrospun fibers *J. Electrost., 35* 151 - 160

Drexler, J. W., & Powell, H. M. (2011). Regulation of electrospun scaffold stiffness via coaxial core diameter. *Acta Biomater., 7*(3), 1133-1139.

Drobny, J. G. (2014). 9 - Thermoplastic Polyurethane Elastomers. In J. G. Drobny (Ed.), *Handbook of Thermoplastic Elastomers (Second Edition)* (pp. 233-253). Oxford: William Andrew Publishing.

Duarte, L. T., Pereira, C. C., Habert, A. C., & Borges, C. P. (2008). Polyurethane/polyethersulphone composite hollow fibers produced by simultaneous spinning of two polymer solutions. *J. Membr. Sci., 311*(1), 12-22.

Erdem, R., Usta, İ., Akalin, M., Atak, O., Yuksek, M., & Pars, A. (2015). The impact of solvent type and mixing ratios of solvents on the properties of polyurethane based electrospun nanofibers. *Appl. Surf. Sci., 334*, 227-230.

Fan, J. T., Weerheijm, J., & Sluys, L. J. (2015). High-strain-rate tensile mechanical response of a polyurethane elastomeric material. *Polym., 65*, 72-80.

Fang, J., Zhang, J., Du, J., Pan, Y., Shi, J., Peng, Y., . . . Mo, X. (2016). Orthogonally functionalizable polyurethane with subsequent modification with heparin and endothelium-inducing peptide aiming for vascular reconstruction. *ACS Appl. Mater. Interfaces, 8*(23), 14442-14452.

Favreau, J. T., Liu, C., Yu, P., Tao, M., Mauro, C., Gaudette, G. R., & Ozaki, C. K. (2014). Acute reductions in mechanical wall strain precede the formation of intimal hyperplasia in a murine model of arterial occlusive disease. *J. Vasc. Surg., 60*(5), 1340-1347.

Fong, H., Chun, I., & Reneker, D. H. (1999). Beaded nanofibers formed during electrospinning *Polym., 40* 4585 - 4592

Gallagher, G., Padsalgikar, A., Tkatchouk, E., Jenney, C., Iacob, C., & Runt, J. (2016). Environmental stress cracking performance of polyether and PDMS-based polyurethanes in an in vitro oxidation model. *J. Biomed. Mater. Res. B: Appl. Biomater., 00*(00), 1-15.

Gorce, J.-N., Hellgeth, J. W., & Ward, T. C. (1993). Mechanical hysteresis of a polyether polyurethane thermoplastic elastomer. *Polym. Eng. Sci., 33*(78), 1170-1176.

Grasl, C., Bergmeister, H., Stoiber, M., Schima, H., & Weigel, G. (2010). Electrospun polyurethane vascular grafts: In vitro mechanical behavior and endothelial adhesion molecule expression. *J. Biomed. Mater. Res. A, 93A*(2), 716-723.

Grenier, S., Sandig, M., & Mequanint, K. (2007). Polyurethane biomaterials for fabricating 3D porous scaffolds and supporting vascular cells. *J. Biomed. Mater. Res. A, 82A*(4), 802-809.

Gu, X., Li, N., Luo, J., Xia, X., Gu, H., & Xiong, J. (2018). Electrospun polyurethane microporous membranes for waterproof and breathable application: The effects of solvent properties on membrane performance. *Polym. Bull., 75*(8), 3539-3553.

Guerrero, J., Rivero, J., Gundabala, V. R., Perez-Saborid, M., & Fernandez-Nieves, A. (2014). Whipping of electrified liquid jets. *Proc. Natl. Acad. Sci. U. S. A., 111*(38), 13763-13767.

Guo, F., Wang, N., Hou, L., Liu, J., Wang, L., & Zhao, Y. (2017). Mechanical enhancement of bi-phasic electrospun nanofibrous films by optimizing composition and configuration. *Mater. Chem. Phys., 193*, 220-226.

Haider, A., Haider, S., & Kang, I.-K. (2015). A comprehensive review summarizing the effect of electrospinning parameters and potential applications of nanofibers in biomedical and biotechnology *Arab. J. Chem.*, 1 - 24

Hajiali, H., Shahgasempour, S., Naimi-Jamal, M. R., & Peirovi, H. (2011). Electrospun PGA/gelatin nanofibrous scaffolds and their potential application in vascular tissue engineering. *Int. J. Nanomed., 6*, 2133-2141.

Hamedani, B. A., Navidbakhsh, M., & Tafti, H. A. (2012). Comparison between mechanical properties of human saphenous vein and umbilical vein. *Biomed. Eng. Online, 11*(1), 59.

Han, J., Farah, S., Domb, A. J., & Lelkes, P. I. (2013). Electrospun rapamycin-eluting polyurethane fibers for vascular grafts. *Pharm. Res., 30*(7), 1735-1748.

Han, Z. Z., Kong, H., Meng, J., Wang, C. Y., Xie, S. S., & Xu, H. Y. (2008, 2008//). *Biological responses of endothelial cells to aligned nanofibers of MWNT/PU by electrospinning.* Paper presented at the 7th Asian-Pacific Conference on Medical and Biological Engineering, Berlin, Heidelberg.

Hanson, D. E., Hawley, M., Houlton, R., Chitanvis, K., Rae, P., Orler, E. B., & Wrobleski, D. A. (2005). Stress softening experiments in silica-filled polydimethylsiloxane provide insight into a mechanism for the Mullins effect. *Polym., 46*, 10989-10995.

He, W., Hu, Z., Xu, A., Liu, R., Yin, H., Wang, J., & Wang, S. (2013). The preparation and performance of a new polyurethane vascular prosthesis. *Cell Biochem. Biophys., 66*(3), 855-866.

Herrera Ramirez, J., R. Bunsell, A., & Colomban, P. (2006). *Microstructural mechanisms governing the fatigue failure of polyamide 66 fibres* (Vol. 41).

Hine, P. J., Ward, I. M., Jordan, N. D., Olley, R., & Bassett, D. C. (2003). The hot compaction behaviour of woven oriented polypropylene fibres and tapes. I. Mechanical properties. *Polym., 44*(4), 1117-1131.

Hong, S. J., Yu, W.-R., Youk, J. H., & Cho, Y. R. (2007). Polyurethane smart fiber with shape memory function: Experimental characterization and constitutive modelling. *Fiber. Polym., 8*(4), 377.

Hsu, C.-M., & Shivkumar, S. (2004). N,N-Dimethylformamide additions to the solution for the electrospinning of poly(ε-caprolactone) nanofibers. *Macromol. Mater. Eng., 289*(4), 334-340.

Huang, C., Chen, S., Reneker, D. H., Lai, C., & Hou, H. (2006). High‐strength mats from electrospun poly(p‐phenylene biphenyltetracarboximide) nanofibers. *Adv. Mater., 18*(5), 668-671.

Huang, L., Manickam, S. S., & McCutcheon, J. R. (2013). Increasing strength of electrospun nanofiber membranes for water filtration using solvent vapor. *J. Membr. Sci., 436*, 213-220.

Huang, W. M., Yang, B., An, L., Li, C., & Chan, Y. S. (2005). Water-driven programmable polyurethane shape memory polymer: Demonstration and mechanism. *Appl. Phys. Lett., 86*(11), 114105.

Huang, Z.-M. (2002a). On a general constitutive description for the inelastic and failure behavior of fibrous laminates—Part I: Lamina theory. *Comput. Struct., 80*(13), 1159-1176.

Huang, Z.-M. (2002b). On a general constitutive description for the inelastic and failure behavior of fibrous laminates—Part II: Laminate theory and applications. *Comput. Struct., 80*(13), 1177-1199.

Huang, Z.-M., Zhang, Y. Z., Ramakrishna, S., & Lim, C. T. (2004). Electrospinning and mechanical characterization of gelatin nanofibers. *Polym., 45*(15), 5361-5368.

Hunsaker, M. E., Price, G. E., & Bai, S. J. (1992). Processing, structure and mechanics of fibres of heteroaromatic oxazole polymers. *Polym., 33*(10), 2128-2135.

Ifkovits, J. L., Devlin, J. J., Eng, G., Martens, T. P., Vunjak-Novakovic, G., & Burdick, J. A. (2009). Biodegradable fibrous scaffolds with tunable properties formed from photo-cross-linkable poly(glycerol sebacate). *Appl. Mater. Interfaces, 1*(9), 1878-1886.

Inai, R., Kotaki, M., & Ramakrishna, S. (2005). Deformation behavior of electrospun poly(L-lactide-co-e-caprolactone) nonwoven membranes under uniaxial tensile loading. *J. Polym. Sci.: Part B: Polym. Phys., 43*, 3205-3212.

Jaganathan, S. K., M, M. P., Fauzi Ismail, A., A, M., & N, G. (2017). Production and hemocompatibility assessment of novel electrospun polyurethane nanofibers loaded with dietary virgin coconut oil for vascular graft applications. *J. Bioact. Compat. Polym., 33*(2), 210-223.

Jeong, Y., Yao, Y., & Yim, E. K. F. (2020). Current understanding of intimal hyperplasia and effect of compliance in synthetic small diameter vascular grafts. *Biomater. Sci., 8*(16), 4383-4395.

Jiang, Y., Liu, H., Li, H., Wang, F., Cheng, K., Zhou, G., . . . Zou, H. (2011). A proteomic analysis of engineered tendon formation under dynamic mechanical loading in vitro. *Biomaterials, 32*(17), 4085-4095.

Jin, Y., Zhang, Y., Hang, Y., Shao, H., & Hu, X. (2013). A simple process for dry spinning of regenerated silk fibroin aqueous solution. *J. Mater. Res., 28*(20), 2897-2902.

Johnson, G. A., Tramaglini, D. M., Levine, R. E., Ohno, K., Choi, N.-Y., & Woo, S. L.-Y. (1994). Tensile and viscoelastic properties of human patellar tendon. *J. Orthop. Res., 12*(6).

Jun, Z., Hou, H., Andreas, S., Wendorff, J., H., & Greiner, A. (2003). Poly-L-lactide nanofibers by electrospinning – Influence of solution viscosity and electrical conductivity on fiber diameter and fiber morphology. In *e-Polymers* (Vol. 3).

Kaibara, M., Takahashi, A., Kurotobi, K., & Suzuki, Y. (2000). Proliferation of endothelial cells on the plasma-treated segmented-polyurethane surface: attempt of construction of a small caliber hybrid vascular graft and antithrombogenicity. *Colloids Surf. B: Biointerfaces, 19*(3), 209-217.

Kannan, R. Y., Salacinski, H. J., Butler, P. E., Hamilton, G., & Seifalian, A. M. (2005). Current status of prosthetic bypass grafts: A review. *J. Biomed. Mater. Res. Part B, 74B*(1), 570-581.

Kar, K. K., & Bhowmick, A. K. (1997). High ‐ strain hysteresis of rubber vulcanizates over a range of compositions, rates, and temperatures. *J. Appl. Polym. Sci., 65*(7), 1429-1439.

Karapınar, K., Ulus, A. T., Tütün, U., Aksöyek, A., Apaydın, N., Pamuk, K., . . . Katırcıoğlu, S. F. (2004). Implantation of novel small-diameter polyurethane vascular prostheses interposed in canine femoral and carotid arteries. *Eur. Surg. Res., 36*(4), 241-248.

Katta, P., Alessandro, M., Ramsier, R. D., & Chase, G. G. (2004). Continuous electrospinning of aligned polymer nanofibers onto a wire drum collector *Nano Lett., 4* (11), 2215 - 2218

Kaursoin, J., & Agrawal, A. K. (2007). Melt spun thermoresponsive shape memory fibers based on polyurethanes: Effect of drawing and heat-setting on fiber morphology and properties. *J. Appl. Polym. Sci., 103*(4), 2172-2182.

Ke, H., Ghulam, M. u. H., Li, Y., Wang, J., Peng, B., Cai, Y., & Wei, Q. (2016). Ag-coated polyurethane fibers membranes absorbed with quinary fatty acid eutectics solid-liquid phase change materials for storage and retrieval of thermal energy. *Renew. Energy, 99*, 1-9.

Khamdaeng, T., Luo, J., Vappou, J., Terdtoon, P., & Konofagou, E. E. (2012). Arterial stiffness identification of the human carotid artery using the stress–strain relationship in vivo. *Ultrasonics, 52*(3), 402-411.

Khan, A. S., Lopez-Pamies, O., & Kazmi, R. (2006). Thermo-mechanical large deformation response and constitutive modeling of viscoelastic polymers over a wide range of strain rates and temperatures. *Int. J. Plast., 22*(4), 581-601.

Kidoaki, S., Kwon, I. K., & Matsuda, T. (2006). Structural features and mechanical properties of in situ–bonded meshes of segmented polyurethane electrospun from mixed solvents. *J. Biomed. Mater. Res. Part B, 76B*(1), 219-229.

Kim, J. H., Heckert, N. A., Mates, S. P., Seppala, J. E., McDonough, W. G., Davis, C. S., . . . Holmes, G. A. (2015). Effect of fiber gripping method on the single fiber tensile test: II. Comparison of fiber gripping materials and loading rates. *J. Mater. Sci., 50*(5), 2049-2060.

Kim, S.-W., Kwon, S.-N., & Na, S.-I. (2019). Stretchable and electrically conductive polyurethane- silver/graphene composite fibers prepared by wet-spinning process. *Compos. B: Eng., 167*, 573-581.

Kiselev, P., & Rosell-Llompart, J. (2012). Highly aligned electrospun nanofibers by elimination of the whipping motion. *J. Appl. Polym. Sci., 125* 2433 - 2441

Kojio, K., Kugumiya, S., Uchiba, Y., Nishino, Y., & Furukawa, M. (2008). The microphase-separated structure of polyurethane bulk and thin films. *Polym. J., 41*, 118.

Kołbuk, D., Sajkiewicz, P., Maniura-Weber, K., & Fortunato, G. (2013). Structure and morphology of electrospun polycaprolactone/gelatine nanofibres. *Eur. Polym. J., 49*(8), 2052-2061.

Kong, K., & Eichhorn, S. J. (2005). The influence of hydrogen bonding on the deformation micromechanics of cellulose fibers. *J. Macromol. Sci. Part B, 44*(6), 1123-1136.

Koohbor, B., Kidane, A., & Lu, W.-Y. (2016). Characterizing the constitutive response and energy absorption of rigid polymeric foams subjected to intermediate-velocity impact. *Polymer Testing, 54*, 48-58.

Kotresh, T. M., Indushekar, R., Subbulakshmi, M. S., Vijayalakshmi, S. N., Krishna Prasad, A. S., Padaki, V. C., & Agrawal, A. K. (2009). Heat release and burning behaviour of foam and foam/Basofil fabric combination. *Polym. Test, 28*(5), 511-520.

Kraus, G., Childers, C. W., & Rollmann, K. W. (1966). Stress softening in carbon black-reinforced vulcanizates. Strain rate and temperature effects. *J. Appl. Polym. Sci., 10*, 229-244.

Krifa, M., Hammami, M. A., & Wu, H. (2015). Occurrence and morphology of bead-on-string structures in centrifugal forcespun PA6 fibers. *J. Text. Inst., 106*(3), 284-294.

Kuk, E., Ha, Y.-M., Yu, J., Im, I.-T., Kim, Y., & Jung, Y. C. (2016). Robust and flexible polyurethane composite nanofibers incorporating multi-walled carbon nanotubes produced by solution blow spinning. *Macromol. Mater. Eng., 301*(4), 364-370.

Kumar, P., & Vasita, R. (2017). Understanding the relation between structural and mechanical properties of electrospun fiber mesh through uni-axial tensile testing. *J. Appl. Polym. Sci.*, 1-11.

Kurimoto, Y., Takeda, M., Koizumi, A., Yamauchi, S., Doi, S., & Tamura, Y. (2000). Mechanical properties of polyurethane films prepared from liquefied wood with polymeric MDI. *Bioresour. Technol., 74*(2), 151-157.

Lalia, B. S., Kochkodan, V., Hashaikeh, R., & Hilal, N. (2013). A review on membrane fabrication: Structure, properties and performance relationship *Desalination, 326* 77 - 95

Larrondo, L., & St. John Manley, R. (1981). Electrostatic fiber spinning from polymer melts. III. Electrostatic deformation of a pendant drop of polymer melt *J. Polym. Sci. Polym. Phys. Ed. , 19* 933 - 940

Le Clerc, C., Bunsell, A. R., & Piant, A. (2006). Influence of temperature on the mechanical behaviour of polyester fibres. *J. Mater. Sci., 41*(22), 7509-7523.

Lee, J. J. L., Andriyana, A., Ang, B. C., Huneau, B., & Verron, E. (2018). Electrospun PMMA polymer blend nanofibrous membrane: Electrospinability, surface morphology and mechanical response. *Mater. Res. Express, 5*(6), 065311.

Lee, J. J. L., Ang, B. C., Andriyana, A., Shariful, M. I., & Amalina, M. A. (2017). Fabrication of PMMA/zeolite nanofibrous membrane through electrospinning and its adsorption behavior. *J. Appl. Polym. Sci., 134*(6), n/a-n/a.

Lee, K., Lee, B., Kim, C., Kim, H., Kim, K., & Nah, C. (2005). Stress-strain behavior of the electrospun thermoplastic polyurethane elastomer fiber mats. *Macromol. Res., 13*(5), 441-445.

Lee, S. J., Heo, D. N., Heo, M., Noh, M. H., Lee, D., Park, S. A., . . . Kwon, I. K. (2017). Most simple preparation of an inkjet printing of silver nanoparticles on fibrous membrane for water purification: Technological and commercial application. *J. Ind. Eng. Chem., 46*, 273-278.

Li, D., Wang, Y., & Xia, Y. (2003). Electrospinning of polymeric and ceramic nanofibers as uniaxially aligned arrays *Nano Lett., 3* (8), 1167 - 1171

Li, D., Wang, Y., & Xia, Y. (2004). Electrospinning nanofibers as uniaxially aligned arrays and layer - by - layer stacked films. *Adv. Mater., 16*(4), 361-366.

Li, H., Song, P., Qiao, T., Cui, Q., Song, X., & Zhang, B. (2016). A quaternary composite fiber membrane for guided tissue regeneration. *Polym. Adv. Technol., 27*(2), 178-184.

Li, Y., Wang, H., Zhang, X., Zhang, Q., Wang, X., Cao, D., . . . Cui, Z. (2016). Organic thin film transistors with novel photosensitive polyurethane as dielectric layer. *RSC Adv., 6*(7), 5377-5383.

Li, Z., & Lambros, J. (2001). Strain rate effects on the thermomechanical behavior of polymers. *Int. J. Solids Struct., 38*(20), 3549-3562.

Liang, J.-W., Prasad, G., Wang, S.-C., Wu, J.-L., & Lu, S.-G. (2019). Enhancement of the oil absorption capacity of poly(lactic acid) nano porous fibrous membranes derived via a facile electrospinning method. *Appl. Sci., 9*(5).

Lin, J. R., & Chen, L. W. (1998). Study on shape-memory behavior of polyether-based polyurethanes. II. Influence of soft-segment molecular weight. *J. Appl. Polym. Sci., 69*(8), 1575-1586.

Litvak, I., Anker, Y., & Cohen, H. (2018). On-line in situ determination of deuterium content in water via FTIR spectroscopy. *RSC Adv., 8*(50), 28472-28479.

Liu, D. S., Ashcraft, J. N., Mannarino, M. M., Silberstein, M. N., Argun, A. A., Rutledge, G. C., . . . Hammond, P. T. (2013). Spray layer-by-layer electrospun composite proton exchange membranes. *Adv. Funct. Mater., 23*(24), 3087-3095.

Liu, H., Xu, W., Zou, H., Ke, G., Li, W., & Ouyang, C. (2008). Feasibility of wet spinning of silk-inspired polyurethane elastic biofiber. *Mater. Lett., 62*(12), 1949-1952.

Liu, L., & Dzenis, Y. A. (2008). Analysis of the effects of the residual charge and gap size on electrospun nanofiber alignment in a gap method. *Nanotechnol., 19*, 1-7.

Liu, R., Qin, Y., Wang, H., Zhao, Y., Hu, Z., & Wang, S. (2013). The in vivo blood compatibility of bio-inspired small diameter vascular graft: effect of submicron longitudinally aligned topography. *BMC Cardiovasc. Disord., 13*(1), 79.

Liu, Y., Zhang, X., Xia, Y., & Yang, H. (2010). Magnetic field-assisted electrospinning of aligned straight and wavy polymeric nanofibers. *Adv. Mater. (Deerfield Beach, Fla.), 22*(22), 2454-2457.

Lu, G., Cui, S.-j., Geng, X., Ye, L., Chen, B., Feng, Z.-g., . . . Li, Z.-z. (2013). Design and preparation of polyurethane-collagen/heparin-conjugated polycaprolactone double-layer bionic small-diameter vascular graft and its preliminary animal tests. *126*(7), 1310-1316.

Lu, J.-W., Zhang, Z.-P., Ren, X.-Z., Chen, Y.-Z., Yu, J., & Guo, Z.-X. (2008). High-elongation fiber mats by electrospinning of polyoxymethylene. *Macromol., 41*, 3762-3764.

Lu, Y., Jiang, J., Yoon, S., Kim, K.-S., Kim, J.-H., Park, S., . . . Piao, L. (2018). High-performance stretchable conductive composite fibers from surface-modified silver nanowires and thermoplastic polyurethane by wet spinning. *ACS Appl. Mater. Interfaces, 10*(2), 2093-2104.

Luo, Y.-L., Miao, Y., & Xu, F. (2011). Synthesis, phase behavior, and simulated in vitro degradation of novel HTPB-b-PEG polyurethane copolymers. *Macromol. Res., 19*(12), 1233-1241.

Maciel, M. M., Ribeiro, S., Ribeiro, C., Francesko, A., Maceiras, A., Vilas, J. L., & Lanceros-Méndez, S. (2018). Relation between fiber orientation and mechanical properties of nano-engineered poly(vinylidene fluoride) electrospun composite fiber mats. *Compos. Part B: Eng., 139*, 146-154.

Maji, A. K., Schreyer, H. L., Donald, S., Zuo, Q., & Satpathi, D. (1995). Mechanical properties of polyurethane-foam impact limiters. *121*(4), 528-540.

Marsavina, L., Linul, E., Voiconi, T., & Sadowski, T. (2013). A comparison between dynamic and static fracture toughness of polyurethane foams. *Polym. Test, 32*(4), 673-680.

Matsuda, T., Ihara, M., Inoguchi, H., Kwon, I. K., Takamizawa, K., & Kidoaki, S. (2005). Mechano‐active scaffold design of small‐diameter artificial graft made of electrospun segmented polyurethane fabrics. *J. Biomed. Mater. Res. Part A, 73A*(1), 125-131.

Matsuda, T., & Kawahara, D. (2008). Electrospinning fabrication of high-trackable catheter tip with gradually graded or gradient flexibility. *J. Biomed. Mater. Res. Part B, 87B*(1), 35-41.

Matsui, M., Ono, L., & Akcelrud, L. (2012). Chitin/polyurethane networks and blends: Evaluation of biological application. *Polym. Test, 31*(1), 191-196.

Medeiros, E. S., Glenn, G. M., Klamczynski, A. P., Orts, W. J., & Mattoso, L. H. C. (2009). Solution blow spinning: A new method to produce micro- and nanofibers from polymer solutions. *J. Appl. Polym. Sci., 113*(4), 2322-2330.

Meng, J., Han, Z., Kong, H., Qi, X., Wang, C., Xie, S., & Xu, H. (2010). Electrospun aligned nanofibrous composite of MWCNT/polyurethane to enhance vascular endothelium cells proliferation and function. *J. Biomed. Mater. Res. A, 95A*(1), 312-320.

Meng, Q., Hu, J., Zhu, Y., Lu, J., & Liu, Y. (2007). Morphology, phase separation, thermal and mechanical property differences of shape memory fibres prepared by different spinning methods. *Smart Mater. Struct., 16*, 1192-1197.

Meng, Z. X., Wang, Y. S., Ma, C., Zheng, W., Li, L., & Zheng, Y. F. (2010). Electrospinning of PLGA/gelatin randomly-oriented and aligned nanofibers as potential scaffold in tissue engineering. *Mater. Sci. Eng.: C, 30*(8), 1204-1210.

Metter, R. B., Ifkovits, J. L., Hou, K., Vincent, L., Hsu, B., Wang, L., . . . Burdick, J. A. (2010). Biodegradable fibrous scaffolds with diverse properties by electrospinning candidates from a combinatorial macromer library. *Acta Biomater., 6*(4), 1219-1226.

Mi, H.-Y., Jing, X., Yu, E., Wang, X., Li, Q., & Turng, L.-S. (2018). Manipulating the structure and mechanical properties of thermoplastic polyurethane/polycaprolactone hybrid small diameter vascular scaffolds fabricated via electrospinning using an assembled rotating collector. *J. Mech. Behav. Biomed. Mater., 78*, 433-441.

Mi, H. Y., Salick, M. R., Jing, X., Crone, W. C., Peng, X. F., & Turng, L. S. (2015). Electrospinning of unidirectionally and orthogonally aligned thermoplastic polyurethane nanofibers: fiber orientation and cell migration. *J. Biomed. Mater. Res. A, 103*(2), 593-603.

Mikelis, K., Ugis, C., Viesturs, Z., Laura, S., & Andris, A. (2014). Rigid polyurethane foam thermal insulation protected with mineral intumescent mat. *Autex Res. J., 14*(4), 259-269.

Miller, K. S., Edelstein, L., Connizzo, B. K., & Soslowsky, L. J. (2012). Effect of preconditioning and stress relaxation on local collagen fiber re-alignment: Inhomogeneous properties of rat supraspinatus tendon. *J. Biomech. Eng., 134*(3), 031007-031007.

Mit‐uppatham, C., Nithitanakul, M., & Supaphol, P. (2004). Ultrafine electrospun polyamide‐6 fibers: Effect of solution conditions on morphology and average fiber diameter. *Macromol. Chem. Phys., 205*(17), 2327-2338.

Mo, X. M., Xu, C. Y., Kotaki, M., & Ramakrishna, S. (2004). Electrospun P(LLA-CL) nanofiber: A biomimetic extracellular matrix for smooth muscle cell and endothelial cell proliferation *Biomaterials, 25* 1883 - 1890

Monaghan, S., & Pethrick, R. A. (2012). Solvent effects on cure in a 2K polyurethane—Mechanical and dielectric studies. *Ind. Eng. Chem. Res., 51*(34), 11038-11044.

Mondal, S. (2014). Influence of solvents properties on morphology of electrospun polyurethane nanofiber mats. *Polym. Adv. Technol., 25*(2), 179-183.

Mulliken, A. D., & Boyce, M. C. (2006). Mechanics of the rate-dependent elastic–plastic deformation of glassy polymers from low to high strain rates. *Int. J. Solids Struct., 43*(5), 1331-1356.

Mullins, L. (1969). Softening of rubber by deformation. *Rubber Chem. Technol., 42*(1), 339-362.

Nerurkar, N. L., Elliott, D. M., & Mauck, R. L. (2007). Mechanics of oriented electrospun nanofibrous scaffolds for annulus fibrosus tissue engineering. *J. Orthop. Res., 25*(8), 1018-1028.

Neugirg, B. R., Burgard, M., Greiner, A., & Fery, A. (2016). Tensile versus AFM testing of electrospun PVA nanofibers: Bridging the gap from Microscale to nanoscale. *J. Polym. Sci. Pt. B-Polym. Phys., 54*(23), 2418-2424.

Nezarati, R. M., Eifert, M. B., & Cosgriff-Hernandez, E. (2013). Effects of humidity and solution viscosity on electrospun fiber morphology. *Tissue Eng.: Part C, 19* (10), 810 - 819

Nunes, R. C. R., Fonseca, J. L. C., & Pereira, M. R. (2000). Polymer–filler interactions and mechanical properties of a polyurethane elastomer. *Polym. Test, 19*(1), 93-103.

Oudet, C., & Bunsell, A. R. (1987). Effects of structure on the tensile, creep and fatigue properties of polyester fibres. *J. Mater. Sci., 22*(12), 4292-4298.

Park, J. H., & Rutledge, G. C. (2018). Ultrafine high performance polyethylene fibers. *J. Mater. Sci., 53*(4), 3049-3063.

Paul, D. R. (1968). Diffusion during the coagulation step of wet-spinning. *J. Appl. Polym. Sci., 12*(3), 383-402.

Pedicini, A., & Farris, R. J. (2003). Mechanical behavior of electrospun polyurethane. *Polym., 44*(22), 6857-6862.

Peng, X., Zhou, L., Jing, B., Cao, Q., Wang, X., Tang, X., & Zeng, J. (2016). A high-performance electrospun thermoplastic polyurethane/poly(vinylidene fluoride-co-hexafluoropropylene) gel polymer electrolyte for Li-ion batteries. *J. Solid State Electrochem., 20*(1), 255-262.

Philippe, C. (2013). Understanding the nano- and macromechanical behaviour, the failure and fatigue mechanisms of advanced and natural polymer fibres by Raman/IR microspectrometry. *Adv. Nat. Sci.-Nanosci Nanotechnol, 4*(1), 013001.

Poquillon, D., Viguier, B., & Andrieu, E. (2005). Experimental data about mechanical behaviour during compression tests for various matted fibres. *J. Mater. Sci., 40*(22), 5963-5970.

Prevorsek, D. C., Tirpak, G. A., Harget, P. J., & Reimschuessel, A. C. (1974). Effects of thermal contraction on structure and properties of PET fibers. *J. Macromol. Sci. Part B, 9*(4), 733-759.

Qi, H. J., & Boyce, M. C. (2005). Stress–strain behavior of thermoplastic polyurethanes. *Mech. Mater., 37*, 817-839.

Qi, P., Maitz, M. F., & Huang, N. (2013). Surface modification of cardiovascular materials and implants. *Surf. Coat. Tech., 233*, 80-90.

Qiao, T., Song, P., Guo, H., Song, X., Zhang, B., & Chen, X. (2016). Reinforced electrospun PLLA fiber membrane via chemical crosslinking. *Eur. Polym. J., 74*, 101-108.

Raghavan, P., Lim, D.-H., Ahn, J.-H., Nah, C., Sherrington, D. C., Ryu, H.-S., & Ahn, H.-J. (2012). Electrospun polymer nanofibers: The booming cutting edge technology *React. Funct. Polym., 72* 915 - 930

Ramdhanie, L. I., Aubuchon, S. R., Boland, E. D., Knapp, D. C., Barnes, C. P., Simpson, D. G., . . . Bowlin, G. L. (2006). Thermal and mechanical characterization of electrospun blends of poly(lactic acid) and poly(glycolic acid) *Polym. J., 38* (11), 1137 - 1145

Ramirez, J. M. H., Colomban, P., & Bunsell, A. (2004). Micro‐Raman study of the fatigue fracture and tensile behaviour of polyamide (PA 66) fibres. *J. Raman Spectrosc., 35*(12), 1063-1072.

Reddy, G. V. R., Deopura, B. L., & Joshi, M. (2010). Dry-jet-wet spun polyurethane fibers. I. Optimization of the spinning parameters. *J. Appl. Polym. Sci., 118*(4), 2291-2303.

Reneker, D. H., & Chun, I. (1996). Nanometre diameter fibres of polymer, produced by electrospinning *Nanotechnology, 7* 216 - 223

Richeton, J., Ahzi, S., Vecchio, K. S., Jiang, F. C., & Adharapurapu, R. R. (2006). Influence of temperature and strain rate on the mechanical behavior of three amorphous polymers: Characterization and modeling of the compressive yield stress. *Int. J. Solids Struct., 43*(7), 2318-2335.

Ruan, C., Hu, Y., Jiang, L., Cai, Q., Pan, H., & Wang, H. (2014). Tunable degradation of piperazine-based polyurethane ureas. *J. Appl. Polym. Sci., 131*(19).

Rubina, P. S., Pradeep, K., Yahya, E. C., Lisa, C. d. T., & Viness, P. (2012). Crosslinked electrospun PVA nanofibrous membranes: elucidation of their physicochemical, physicomechanical and molecular disposition. *Biofabrication, 4*(2), 025002.

Sáenz-Pérez, M., Bashir, T., Laza, J. M., García-Barrasa, J., Vilas, J. L., Skrifvars, M., & León, L. M. (2018). Novel shape-memory polyurethane fibers for textile applications. *Text. Res. J., 89*(6), 1027-1037.

Safranski, D. L., Boothby, J. M., Kelly, C. N., Beatty, K., Lakhera, N., Frick, C. P., . . . Griffis, J. C. (2016). Thermo-mechanical behavior and structure of melt blown shape-memory polyurethane nonwovens. *J. Mech. Behav. Biomed. Mater., 62*, 545-555.

Sahoo, S., Kalita, H., Mohanty, S., & Nayak, S. K. (2018). Degradation study of biobased polyester–polyurethane and its nanocomposite under natural soil burial, UV radiation and hydrolytic-salt water circumstances. *J. Polym. Environ., 26*(4), 1528-1539.

Salacinski, H. J., Goldner, S., Giudiceandrea, A., Hamilton, G., Seifalian, A. M., Edwards, A., & Carson, R. J. (2001). The mechanical behavior of vascular grafts: A review. *J. Biomater. Appl., 15*(3), 241-278.

Sánchez, P. F., Brey, E. M., & Briceño, J. C. (2018). Endothelialization mechanisms in vascular grafts. *J. Tissue Eng. Regen. Med., 12*(11), 2164-2178.

Savan, E. K., Paşahan, A., Aksoy, B., Güngör, Ö., Köytepe, S., & Seçkin, T. (2016). Preparation and properties of selective polyurethane films and their use for the development of biomedical dopamine sensor. *Int. J. Polym. Mater. Polym. Biomat., 65*(8), 402-408.

Schriefl Andreas, J., Zeindlinger, G., Pierce David, M., Regitnig, P., & Holzapfel Gerhard, A. (2012). Determination of the layer-specific distributed collagen fibre orientations in human thoracic and abdominal aortas and common iliac arteries. *J. R. Soc. Interface, 9*(71), 1275-1286.

Shah, J. S., Jayson, M. I. V., & Hampson, W. G. J. (1979). Mechanical implications of crimping in collagen fibres of human spinal ligaments. *IMechE, 8*(2).

Sharifpoor, S., Labow, R. S., & Santerre, J. P. (2009). Synthesis and characterization of degradable polar hydrophobic ionic polyurethane scaffolds for vascular tissue engineering applications. *Biomacromolecules, 10*(10), 2729-2739.

Shawon, J., & Sung, C. (2004). Electrospinning of polycarbonate nanofibers with solvent mixtures THF and DMF. *J. Mater. Sci., 39*(14), 4605-4613.

Sheng, J., Zhang, M., Luo, W., Yu, J., & Ding, B. (2016). Thermally induced chemical cross-linking reinforced fluorinated polyurethane/polyacrylonitrile/polyvinyl butyral nanofibers for waterproof-breathable application. *RSC Adv., 6*(35), 29629-29637.

Shi, Q., Wan, K.-T., Wong, S.-C., Chen, P., & Blackledge, T. A. (2010). Do electrospun polymer fibers stick? *Langmuir, 26*(17), 14188–14193.

Shin, Y. M., Hohman, M. M., Brenner, M. P., & Rutledge, G. C. (2001). Electrospinning: A whipping fluid jet generates submicron polymer fibers. *Appl. Phys. Lett., 78*(8), 1149-1151.

Shojaei, A., Li, G., & Voyiadjis, G. Z. (2012). Cyclic viscoplastic-viscodamage analysis of shape memory polymers fibers with application to self-healing smart materials. *J. Appl. Mech., 80*(1), 011014-011014-011015.

Silva, P. E. S., Vistulo de Abreu, F., & Godinho, M. H. (2017). Shaping helical electrospun filaments: A review. *Soft Matter, 13*(38), 6678-6688.

Song, B., Cui, W., & Chang, J. (2011). Study on the effect of inorganic salts on the alignment of electrospun fiber *J. Appl. Polym. Sci., 122* 1047 - 1052

Song, X., Ling, F., Ma, L., Yang, C., & Chen, X. (2013). Electrospun hydroxyapatite grafted poly(l-lactide)/poly(lactic-co-glycolic acid) nanofibers for guided bone regeneration membrane. *Compos. Sci. Technol., 79*, 8-14.

Song, Z., Chiang, S. W., Chu, X., Du, H., Li, J., Gan, L., . . . Kang, F. (2018). Effects of solvent on structures and properties of electrospun poly(ethylene oxide) nanofibers. *J. Appl. Polym. Sci., 135*(5), 45787-n/a.

Soto, G., Castro, A., Vechiatti, N., Iasi, F., Armas, A., Marcovich, N. E., & Mosiewicki, M. A. (2017). Biobased porous acoustical absorbers made from polyurethane and waste tire particles. *Polym. Test, 57*, 42-51.

Sry, V., Mizutani, Y., Endo, G., Suzuki, Y., & Todoroki, A. (2018). Estimation of the longitudinal elasticity modulus of braided synthetic fiber rope utilizing classical laminate theory with the unit N/tex. *Appl. Sci., 8*(7).

Stachewicz, U., Peker, I., Tu, W., & Barber, A. H. (2011). Stress delocalization in crack tolerant electrospun nanofiber networks. *ACS Appl. Mater. Interfaces, 3*(6), 1991-1996.

Steinmann, W., Walter, S., Seide, G., Gries, T., Roth, G., & Schubnell, M. (2011). Structure, properties, and phase transitions of melt-spun poly(vinylidene fluoride) fibers. *J. Appl. Polym. Sci., 120*(1), 21-35.

Stirna, U., Lazdiņa, B., Vilsone, D., Lopez, M. J., Vargas-Garcia, M. d. C., Suárez-Estrella, F., & Moreno, J. (2012). Structure and properties of the polyurethane and polyurethane foam synthesized from castor oil polyols. *J. Cell. Plast., 48*(6), 476-488.

Su, J., Zhang, Q., Wang, P.-C., MacDiarmid, A. G., & Wynne, K. J. (1998). Preparation and characterization of electrostrictive polyurethane films with conductive polymer electrodes. *Polym. Adv. Technol., 9*(6), 317-321.

Sui, T., Baimpas, N., Dolbnya, I. P., Prisacariu, C., & Korsunsky, A. M. (2015). Multiple-length-scale deformation analysis in a thermoplastic polyurethane. *Nat. Commun., 6*(6583).

Sui, T., Salvati, E., Ying, S., Sun, G., Dolbnya, I. P., Dragnevski, K., . . . Korsunsky, A. M. (2017). Strain softening of nano-scale fuzzy interfaces causes Mullins effect in thermoplastic polyurethane. *Sci. Rep., 7*(1), 916.

Sukigara, S., Gandhi, M., Ayutsede, J., Micklus, M., & Ko, F. (2004). Regeneration of Bombyx mori silk by electrospinning. Part 2. Process optimization and empirical modeling using response surface methodology *Polym., 45* 3701 - 3708

Sun, L., Han, R. P. S., Wang, J., & Lim, C. T. (2008). Modeling the size-dependent elastic properties of polymeric nanofibers. *Nanotechnology, 19*, 1-8.

Sunada, T., Kuriyagawa, M., Kawamura, T., & Nitta, K.-h. (2011). Influence of domain structure on the mechanical properties of thermoplastic polyurethane materials. *e-J. Soft Mater., 7*, 8-14.

Sung, G., Kim, S. K., Kim, J. W., & Kim, J. H. (2016). Effect of isocyanate molecular structures in fabricating flexible polyurethane foams on sound absorption behavior. *Polym. Test, 53*, 156-164.

Szczesny, S. E., Driscoll, T. P., Tseng, H.-Y., Liu, P.-C., Heo, S.-J., Mauck, R. L., & Chao, P.-H. G. (2016). Crimped nanofibrous biomaterials mimic microstructure and mechanics of native tissue and alter strain transfer to cells. *ACS Biomater. Sci. Eng.*

Tan, C. J., Andriyana, A., Ang, B. C., & Chagnon, G. (2018). Inelastic deformation of highly aligned dry-spun thermoplastic polyurethane elastomer microfibres. *Mater. Res. Express, 5*(12), 125301.

Tan, C. J., Lee, J. J. L., Ang, B. C., Andriyana, A., Chagnon, G., & Sukiman, M. S. (2019). Design of polyurethane fibers: Relation between the spinning technique and the resulting fiber topology. *J. Appl. Polym. Sci., 0*(0), 47706.

Tang, S. L. P., & Mukhopadhyay, S. K. (2006). Melt-blown lyocell: Influence of solution characteristics on fibre properties. *J. Text. Inst., 97*(1), 39-47.

Tascan, M. (2014). Optimization of process parameters of wet-spun solid PVDF fibers for maximizing the tensile strength and applied force at break and minimizing the elongation at break using the Taguchi method. *J. Eng. Fiber Fabr., 9*(1), 165-173.

Tebyetekerwa, M., & Ramakrishna, S. (2020). What Is next for electrospinning? *Matter, 2*(2), 279-283.

Teo, W. E., Kotaki, M., Mo, X. M., & Ramakrishna, S. (2005). Porous tubular structures with controlled fibre orientation using a modified electrospinning method *Nanotechnology, 16* 918 - 924

Theron, A., Zussman, E., & Yarin, A. L. (2001). Electrostatic field-assisted alignment of electrospun nanofibres *Nanotechnology, 12* 384 - 390

Tijing, L. D., Choi, J.-S., Lee, S., Kim, S.-H., & Shon, H. K. (2014). Recent progress of membrane distillation using electrospun nanofibrous membrane *J. Membr. Sci., 453* 435 - 462

Tomecka, E., Wojasinski, M., Jastrzebska, E., Chudy, M., Ciach, T., & Brzozka, Z. (2017). Poly(l-lactic acid) and polyurethane nanofibers fabricated by solution blow spinning as potential substrates for cardiac cell culture. *Mater. Sci. Eng.: C, 75*, 305-316.

Tonda-Turo, C., Boffito, M., Cassino, C., Gentile, P., & Ciardelli, G. (2016). Biomimetic polyurethane – Based fibrous scaffolds. *Mater. Lett., 167*, 9-12.

Tong, D.-H., & Wu, X.-R. (2014). Analysis of crack opening stresses for center- and edge-crack tension specimens. *Chin. J. Aeronaut., 27*(2), 291-298.

Tong, H.-W., & Wang, M. (2007). Electrospinning of aligned biodegradable polymer fibers and composite fibers for tissue engineering applications. *J. Nanosci. Nanotechnol., 7*(11), 3834-3840.

Uttayarat, P., Perets, A., Li, M., Pimton, P., Stachelek, S. J., Alferiev, I., . . . Lelkes, P. I. (2010). Micropatterning of three-dimensional electrospun polyurethane vascular grafts. *Acta Biomater., 6*(11), 4229-4237.

Vrieze, S. D., Camp, T. V., Nelvig, A., Hagstro¨m, B., Westbroek, P., & Clerck, K. D. (2009). The effect of temperature and humidity on electrospinning *J. Mater. Sci., 44* 1357 - 1362

Wanasekara, N. D., Matolyak, L. E., & Korley, L. T. J. (2015). Tunable mechanics in electrospun composites via hierarchical organization. *ACS Appl. Mater. Interfaces, 7*, 22970-22979.

Wang, B., Liu, W., Zhang, Y., Jiang, Y., Zhang, W. J., Zhou, G., . . . Cao, Y. (2008). Engineering of extensor tendon complex by an ex vivo approach. *Biomaterials, 29*(20), 2954-2961.

Wang, H. B., Michael, E. M., Jared, M. C., Andres, H., Martin, O., Matthew, T. T., & Ryan, J. G. (2009). Creation of highly aligned electrospun poly-L-lactic acid fibers for nerve regeneration applications. *J. Neural Eng., 6*(1), 016001.

Wang, Z., Liu, S., Guidoin, R., & Kodama, M. (2004). Polyurethane vascular grafts with thorough porosity: Does an internal or an external membrane wrapping improve their in vivo blood compatibility and biofunctionality? *Artif. Cells Blood Substit. Biotechnol., 32*(3), 463-484.

Wang, Z., Yu, L., Ding, M., Tan, H., Li, J., & Fu, Q. (2011). Preparation and rapid degradation of nontoxic biodegradable polyurethanes based on poly(lactic acid)-poly(ethylene glycol)-poly(lactic acid) and l-lysine diisocyanate. *Polym. Chem., 2*(3), 601-607.

Wei, X., Xia, Z., Wong, S.-C., & Baji, A. (2009). Modelling of mechanical properties of electrospun nanofibre network. *Int. J. Exp. Comput. Biomech., 1*(1), 45-57.

Weißenborn, O., Ebert, C., & Gude, M. (2016). Modelling of the strain rate dependent deformation behaviour of rigid polyurethane foams. *Polym. Test, 54*, 145-149.

Whelan, A., Duffy, J., Gaul, R. T., O'Reilly, D., Nolan, D. R., Gunning, P., . . . Murphy, B. P. (2019). Collagen fibre orientation and dispersion govern ultimate tensile strength, stiffness and the fatigue performance of bovine pericardium. *J. Mech. Behav. Biomed. Mater., 90*, 54-60.

Whisler, D., & Kim, H. (2015). Experimental and simulated high strain dynamic loading of polyurethane foam. *Polym. Test, 41*, 219-230.

Whitton, A., Flint, D. J., & Black, R. A. (2010). *Development of a compliant electrospun polyurethane vascular graft*.

Wong, C. S., Liu, X., Xu, Z., Lin, T., & Wang, X. (2013). Elastin and collagen enhances electrospun aligned polyurethane as scaffolds for vascular graft. *J. Mater. Sci.-Mater. Med., 24*(8), 1865-1874.

Wong, D., Andriyana, A., Ang, B. C., & Verron, E. (2016). Surface morphology and mechanical response of randomly oriented electrospun nanofibrous membrane. *Polym. Test., 53*(Supplement C), 108-115.

Xia, H., Song, M., Zhang, Z., & Richardson, M. (2007). Microphase separation, stress relaxation, and creep behavior of polyurethane nanocomposites. *J. Appl. Polym. Sci., 103*, 2992-3002.

Xiao, R., Zhu, Q., & Gu, L. (2010). Processing and characterization of polyacrylonitrile/soy protein isolate/polyurethane wet-spinning solution and fiber. *Fibers Polym., 11*(1), 42-47.

Xie, J., Michael, P. L., Zhong, S., Ma, B., MacEwan, M. R., & Lim, C. T. (2012). Mussel inspired protein-mediated surface modification to electrospun fibers and their potential biomedical applications. *J. Biomed. Mater. Res. Part A, 100A*(4), 929-938.

Xu, C. Y., Inai, R., Kotaki, M., & Ramakrishna, S. (2004). Aligned biodegradable nanofibrous structure: a potential scaffold for blood vessel engineering. *Biomaterials, 25*(5), 877-886.

Xue, L., & Greisler, H. P. (2003). Biomaterials in the development and future of vascular grafts. *J. Vasc. Surg., 37*(2), 472-480.

Yang, B., Huang, W. M., Li, C., Lee, C. M., & Li, L. (2003). On the effects of moisture in a polyurethane shape memory polymer. *Smart Mater. Struct., 13*(1), 191-195.

Yang, B., Huang, W. M., Li, C., & Li, L. (2006). Effects of moisture on the thermomechanical properties of a polyurethane shape memory polymer. *Polym., 47*(4), 1348-1356.

Yeh, H.-L., Yeh, H.-Y., & Zhang, R. (1999). A study of negative poisson's ratio in randomly oriented quasi-isotropic composite laminates. *J. Compos. Mater., 33*(19), 1843-1857.

Yi, J., Boyce, M. C., Lee, G. F., & Balizer, E. (2006). Large deformation rate-dependent stress–strain behavior of polyurea and polyurethanes. *Polym., 47*, 319-329.

Yu, E., Zhang, J., Thomson, J. A., & Turng, L. S. (2016). Fabrication and characterization of electrospun thermoplastic polyurethane/fibroin small-diameter vascular grafts for vascular tissue engineering. *Int. Polym. Proc, 31*(5), 638-646.

Yuan, D. X., Zhang, Y., Dong, C., & Sheng, J. (2004). Morphology of ultrafine polysulfone fibers prepared by electrospinning *Polym. Int., 53* (11), 1704 - 1710

Zainal Abidin, N. I., Atrens, A. D., Martin, D., & Atrens, A. (2011). Corrosion of high purity Mg, Mg2Zn0.2Mn, ZE41 and AZ91 in Hank's solution at 37°C. *Corrosion Sci., 53*(11), 3542-3556.

Żenkiewicz, M., Richert, A., Malinowski, R., & Moraczewski, K. (2013). A comparative analysis of mass losses of some aliphatic polyesters upon enzymatic degradation. *Polym. Test, 32*(2), 209-214.

Zhang, C., Yuan, X., Wu, L., Han, Y., & Sheng, J. (2005). Study on morphology of electrospun poly(vinyl alcohol) mats *Eur. Polym. J., 41* 423 - 432

Zhang, J., Woodruff, T. M., Clark, R. J., Martin, D. J., & Minchin, R. F. (2016). Release of bioactive peptides from polyurethane films in vitro and in vivo: Effect of polymer composition. *Acta Biomater., 41*, 264-272.

Zhang, Z., Wang, Z., Liu, S., & Kodama, M. (2004). Pore size, tissue ingrowth, and endothelialization of small-diameter microporous polyurethane vascular prostheses. *Biomaterials, 25*(1), 177-187.

Zhao, P., Jiang, H., Pan, H., Zhu, K., & Chen, W. (2007). Biodegradable fibrous scaffolds composed of gelatin coated poly(ϵ-caprolactone) prepared by coaxial electrospinning. *J. Biomed. Mater. Res. Part A, 83A*(2), 372-382.

Zhao, Y., Miao, X., Lin, J., Li, X., Bian, F., Wang, J., . . . Yue, B. (2017). Coiled plant tendril bioinspired fabrication of helical porous microfibers for crude oil cleanup. *Glob. Chall., 1*(3), 1600021.

Zhou, Z., Yi, Q., Liu, L., Liu, X., & Liu, Q. (2009). Influence of degradation of poly-L-lactide on mass Loss, mechanical properties, and crystallinity in phosphate-buffered solution. *J. Macromol. Sci. Part B, 48*(2), 309-317.

Zhu, L., Dai, J., Chen, L., Chen, J., Na, H., & Zhu, J. (2017). Design and fabrication of imidazolium ion-immobilized electrospun polyurethane membranes with antibacterial activity. *J. Mater. Sci., 52*(5), 2473-2483.

Zhu, Y., Gao, C., He, T., & Shen, J. (2004). Endothelium regeneration on luminal surface of polyurethane vascular scaffold modified with diamine and covalently grafted with gelatin. *Biomaterials, 25*(3), 423-430.

Zhu, Y., Gao, C., Liu, X., & Shen, J. (2002). Surface modification of polycaprolactone membrane via aminolysis and biomacromolecule immobilization for promoting cytocompatibility of human endothelial cells. *Biomacromolecules, 3*(6), 1312-1319.

Zhu, Y., Hu, J., Lu, J., Yeung, L. Y., & Yeung, K.-w. (2008). Shape memory fiber spun with segmented polyurethane ionomer. *Polym. Adv. Technol., 19*(12), 1745-1753.

Zhu, Y., Hu, J., Yeung, L.-Y., Liu, Y., Ji, F., & Yeung, K.-w. (2006). Development of shape memory polyurethane fiber with complete shape recoverability. *Smart Mater. Struct., 15*(5), 1385-1394.

Zhu, Y., Hu, J., Yeung, L.-Y., Lu, J., Meng, Q., Chen, S., & Yeung, K.-w. (2007). Effect of steaming on shape memory polyurethane fibers with various hard segment contents. *Smart Mater. Struct., 16*(4), 969-981.

Zuo, W., Zhu, M., Yang, W., Yu, H., Chen, Y., & Zhang, Y. (2005). Experimental study on relationship between jet instability and formation of beaded fibers during electrospinning *Polym. Eng. Sci.*, 704 - 709

LIST OF PUBLICATIONS AND PAPERS PRESENTED

Publications in Refereed Journals

Tan, C. J., Andriyana, A., Ang, B. C., & Chagnon, G. (2018). Inelastic deformation of highly aligned dry-spun thermoplastic polyurethane elastomer microfibres. *Mater. Res. Express, 5*(12), 125301.

Tan, C. J., Lee, J. J. L., Ang, B. C., Andriyana, A., Chagnon, G., & Sukiman, M. S. (2019). Design of polyurethane fibers: Relation between the spinning technique and the resulting fiber topology. *J. App. Polym. Sci., 136*, 47706.

Tan, C. J., Andriyana, A., Ang, B. C., & Wong, D. (2020). Mechanical deformation and fracture mechanisms of polymeric fibres from the perspective of fractography – A review. Eur. Polym. J., 137, 109924.

Publications in Proceedings

Tan, C. J., Andriyana, A., Ang, B. C., & Chagnon, G. (2017). Mechanical characterization of highly aligned polyurethane microfibers. In Lion A. & Johlitz M. (Eds.), Constitutive models for rubber X (ch. 40). London, CRC Press.